Studies in simplified dynamic modeling and characterization of vehicle suspensions

by

Husain Kanchwala

A dissertation submitted in partial satisfaction
of the requirements for the degree of

Doctor of philosophy

in

Department of Mechanical Engineering

Indian Institute of Technology Kanpur
Kanpur-208016 India

Certificate

This is to certify that the work contained in the thesis entitled "**Studies in simplified dynamic modeling and characterization of vehicle suspensions**" by Husain Kanchwala has been carried out under my supervision and this work has not been submitted elsewhere for a degree.

Dr. Anindya Chatterjee
Professor
Department of Mechanical Engineering
Indian Institute of Technology Kanpur

Kanpur

**Dedicated to
my family**

Acknowledgement

Completing my PhD degree is probably the most rewarding and challenging activity of my life so far. Without the support of my wife and my family completion of this thesis would not be possible. I express my deepest thanks and appreciation to all of them.

I would like to express my gratitude to Dr. Anindya Chatterjee, my thesis advisor, for his guidance, motivation, enthusiasm, and immense support. He taught me academic discipline, technical writing and clarity of presentation. I came from an industrial background and deeply appreciate that my advisor made academics easy for me and encouraged me to work on an industrial research problem which is of my interest.

I am deeply grateful to Dr. N Karuppaiah, Additional Director, National automotive research and infrastructure project, Natrip, Indore for allowing me to use the experimental facilities at Natrip, Indore. At Natrip, Mr. Umesh Raghuwanshi supported me a lot, and apart helped me a great deal in during experimental characterization of suspension bushings. I also sincerely thank Prof. Vinod Pare of Shri G.S. Institute of Technology and Science, Indore, for providing me the Baja ATV to conduct field test experiments. The field testing work would not have been possible without the help of undergraduate students in particular Amit Singh, Jay Pratap and Suraj Mishra who were with me for almost a month during testing.

During my entire course of work Mr. Sagar Bendre of Natrip has helped me a great deal by sharing his expertise in vehicle suspensions modeling, Adams and vehicle testing. I would like to thank Vaibhav Dhar Dwivedi for helping me during calibrating the vehicle instrumentation setup.

I must thank Department of Mechanical Engineering, IIT Kanpur for providing

i

Abstract

   This thesis has four parts.

   In the first part, a theoretical formulation was developed to extend a simple quarter car model to incorporate frame flexibility, inertia effects and other-wheel ground contacts. A simplified Adams model of a vehicle was used to calculate the vehicle body point responses to inputs at four locations. Using the responses obtained from the Adams model, a transfer function matrix was found between ground excitations and vehicle body responses by introducing an unsprung mass model and retaining the suspension properties as free parameters within the formulation. Finally, the transfer function between ground displacements at one wheel and body responses above that wheel, incorporating the effects of the other three wheels with stationary ground contacts, was obtained. We refer to this reduced model as a generalized quarter car model. It is a model of intermediate complexity, of a type that has not been presented in the literature so far.

   The next part of the work includes experiments and develops new theoretical characterization of elastomeric suspension bushings. Four different commercially available bushings were characterized in the frequency domain using an MTS 370.10 elastomer test system at Natrip (National automotive testing, research and infrastructure project), Indore. Empirical models used to describe such frequency-dependent behavior can often be shown to violate some theoretical restrictions like causality. Two new, different, rationally derived, three-parameter models were developed to model the suspension bushings. The models were fitted using the experimental data in frequency ranges such as 1-30 Hz. The fit obtained was good even though the model had relatively few fitted parameters. Such models can be incorporated easily in frequency domain suspension models or models for the full vehicle.

   In the third part, a full vehicle Adams model and also a simplified Adams model were partially validated against field test results. A prototype vehicle manufactured at Shri G. S. Institute of Technology and Science (SGSITS), Indore was used. The vehicle suspensions were characterized using an MTS 850.25 damper test-rig and the vehicle was tested on different test tracks at Natrip, Indore. The vehicle had accelerometers mounted at four wheel axle points and four suspension-to-body attachment points, and the vertical accelerations of these points were recorded. A reasonable correlation was obtained between the experimental and simulation results. Both successful and unsuccessful aspects of the results have been discussed.

   Finally using the above field test data, and with the theoretical formulation developed in the first part, a new Laplace domain transfer function model was fitted to predict the body points' accelerations in response to measured wheel-axle accelerations. This model was further extended to incorporate an unsprung mass model and retain suspension properties as free parameters, thereby serving as an experimental application of the theory developed in the first part of this work. A discussion is given of aspects of the model that match experiments as well as possible sources for observed mismatch between model and experiment.

Contents

List of Figures

List of Tables

Chapter 1

Introduction

This thesis presents simplified dynamic models and characterization experiments for vehicle suspensions and components thereof. Vehicle suspensions are generally modeled using commercial multi-body dynamics packages, but such models are computationally complex. The aim here is to develop models of *intermediate* complexity which can reasonably capture the vehicle dynamic characteristics.

There are four main contributions of this thesis. These are outlined below.

1.1 Generalized quarter car model with frame flexibility and other nonlocal effects

The most widely used model of a vehicle suspension system is the quarter car model (see Figure 1.1). The sprung mass M_s represents a quarter of the vehicle body mass and the unsprung mass M_u represents the mass of one wheel and its suspension. The effective suspension stiffness and damping are denoted by K_s and C_s and the tyre stiffness and damping are represented by K_t and C_t.
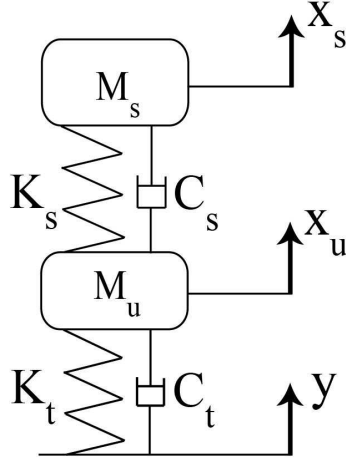
Figure 1.1: Quarter car model.

The vertical vibration to a vehicle using a quarter car model are given by the following governing differential equations of motion [1].

$$M_s\ddot{x}_s + C_s(\dot{x}_s - \dot{x}_u) + K_s(x_s - x_u) = 0 \qquad (1.1)$$

$$M_u\ddot{x}_u - C_s(\dot{x}_s - \dot{x}_u) - K_s(x_s - x_u) + K_t x_u + C_t \dot{x}_t = K_t y + C_t \dot{y}. \qquad (1.2)$$

The quarter car model is the subject of numerous investigations since the invention of the vibration absorber theory by Frahm in 1911 [2]. The first analytical investigation of damping properties of two degree of freedom systems is due to Den Hartog [3].

Since then the quarter car model has been used by numerous researchers to design vehicle suspensions [4, 5]. It contains the most basic features of the real problem.

However, the quarter car model does not incorporate geometric effects of the full car and offers no possibility of studying longitudinal and lateral coupling. It does not incorporate the effect of three ground contacts at other wheels. These effects, in a simplified approach, will be studied in the present thesis.

Dynamic modeling of vehicle suspensions is a part of vehicle design activities.

2

Based on the level of detailing and complexity, mathematical models of suspensions are broadly classified into three types: quarter car [6], half car [7] and full car models [8, 9] (see Figure 1.2).
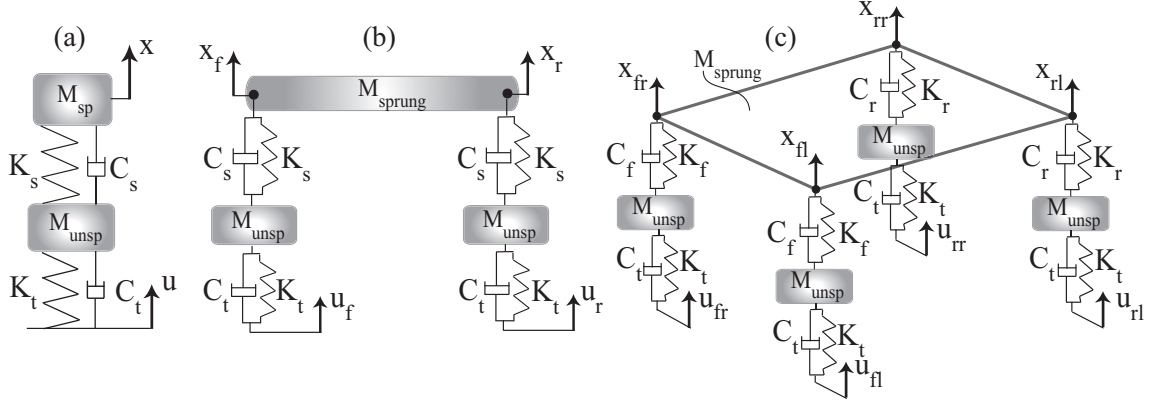
Figure 1.2: Types of car models: (a) quarter car, (b) half car and (c) full car model.

Clearly, the quarter car model accounts for neither the effects of three other wheels and their suspensions nor frame flexibility. The full car model is computationally complex. The half car model is midway in complexity, allows for fore-aft or sideways interaction but not both, and could in principle incorporate frame flexibility.

Although they are popular, quarter car models cannot capture all relevant dynamic effects [10, 11]. There are in fact remarkable differences in ride vibration predictions of various models (quarter car, half car, half car with discrete masses, models with and without frame flexibility) [12]. The engine, passenger CG locations, and frame flexibility influence the vibration response but are not included in the quarter car model.

In the context of the above range of models, the aim here is to develop a *generalized quarter car model* which has *intermediate* complexity and represents the car's dynamics with both reasonable accuracy and low computational effort (Figure 1.3).

3
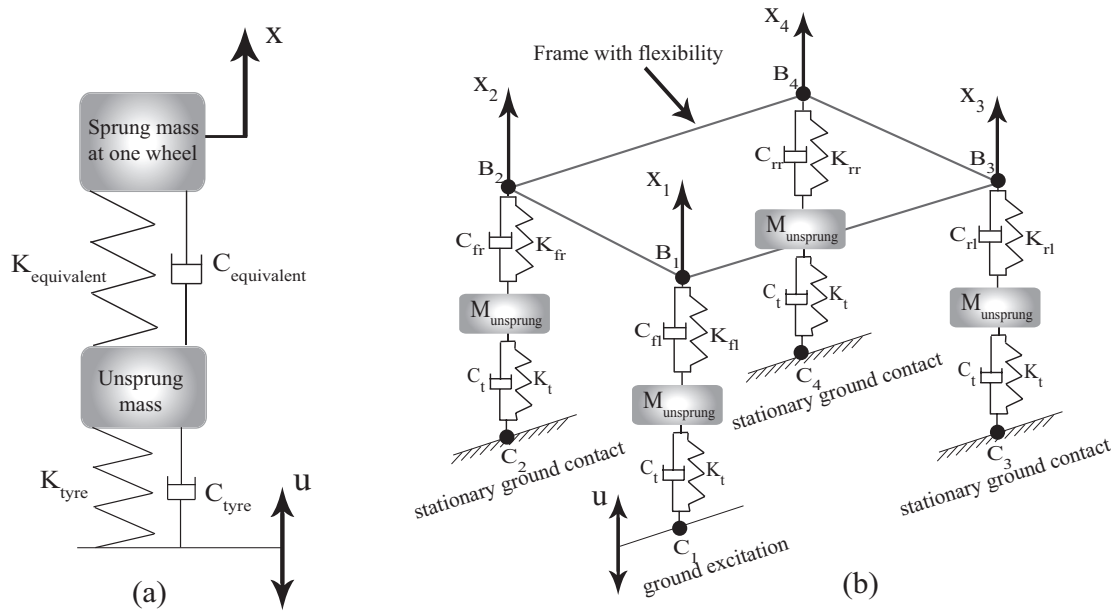
Figure 1.3: (a) Usual quarter car model. (b) Proposed approach: somewhat resembles the quarter car model in that x_1 is computed in response to u, but incorporates complex dynamics of the car including effects of frame flexibility and three other wheel-ground contacts. Note that small rolling and pitching motions of the frame are reflected in corresponding vertical motions of points B_i.
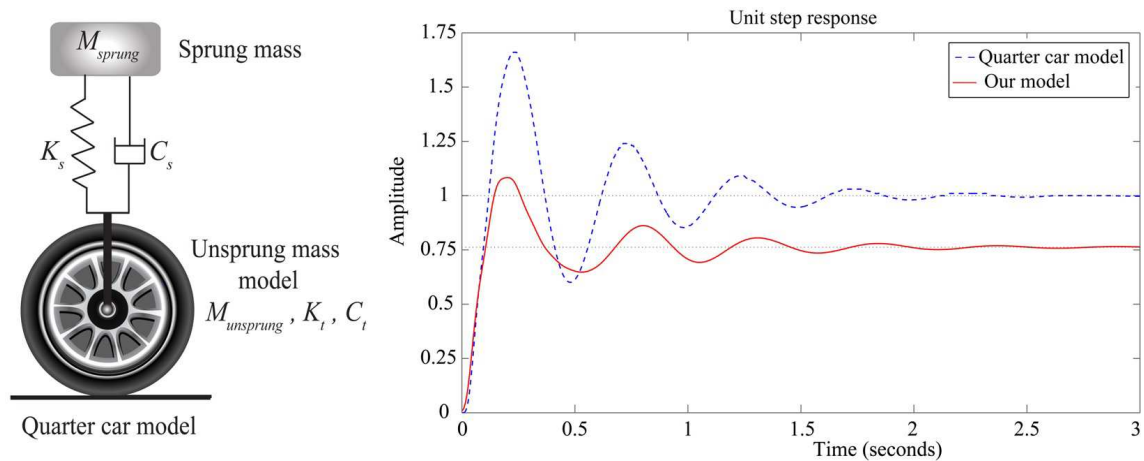
Figure 1.4: Comparison of displacements obtained from usual quarter car model and our model in response to a unit step displacement input at wheel contact point C_1. Both the damping level and steady state response are affected by nonlocal stiffness and dissipation that is captured well by our approach.

As an example of the sort of differences captured by the new proposed approach,

4

the unit step response of the presented model is compared with that of a usual quarter car model (see Figure 1.4). Note in the figure that the value of steady state displacement of a quarter car model for a unit step displacement input will necessarily be unity. In the proposed model the difference observed from unity is strictly due to other-wheel effects.

1.2 Rationally derived models for elastomeric suspension bushings

The second part of this thesis concerns elastomeric bushings of vehicle suspension. These bushings are typically used inside shock absorbers, damper and spring mounts, control arms and bumpstops [13] (see Figure 1.5).
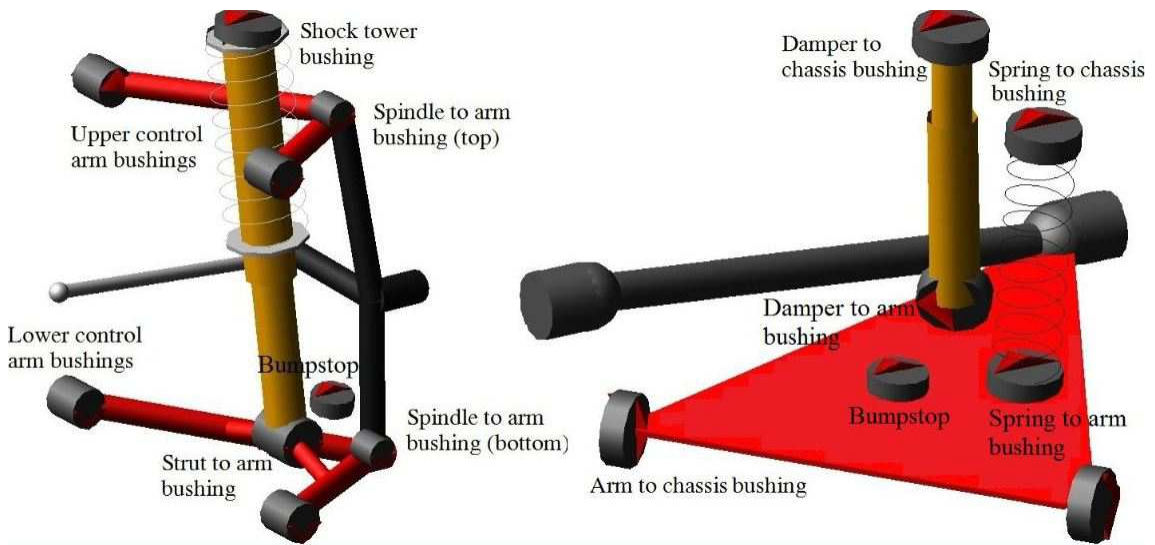
Figure 1.5: Locations of bushings in typical front and rear suspensions of a passenger car.

Accurate material modeling of elastomeric dampers is necessary for reliable vehicle dynamics simulations. Typical existing models for such dampers are empirical in

nature. Empirical fits to experimental data involves several fitted parameters which, if chosen arbitrarily, violate theoretical restrictions derived from causality, linearity, and time-invariance. Here, an asymptotic expansion for Bode's representation of the famous Kramers-Kronig relations is exploited [14, 15, 16]. In the asymptotic expansion, both the leading order term as well as one correction term have been retained. Usually, in the literature, only the leading term is retained. Using this asymptotic expansion, two new mathematical forms that satisfy theoretical restrictions and also fit the experimental data well are proposed. One form has logarithms and power law terms, and is valid if the index in the power law is small. The second form has only logarithmic terms, and satisfies restrictions exactly. Both forms proposed here have three free parameters each, and successfully fit the test data for four different automotive suspension bushings, in the low frequency range ($\sim$ 1-30 Hz). One of the test fits is shown in Figure 1.6.
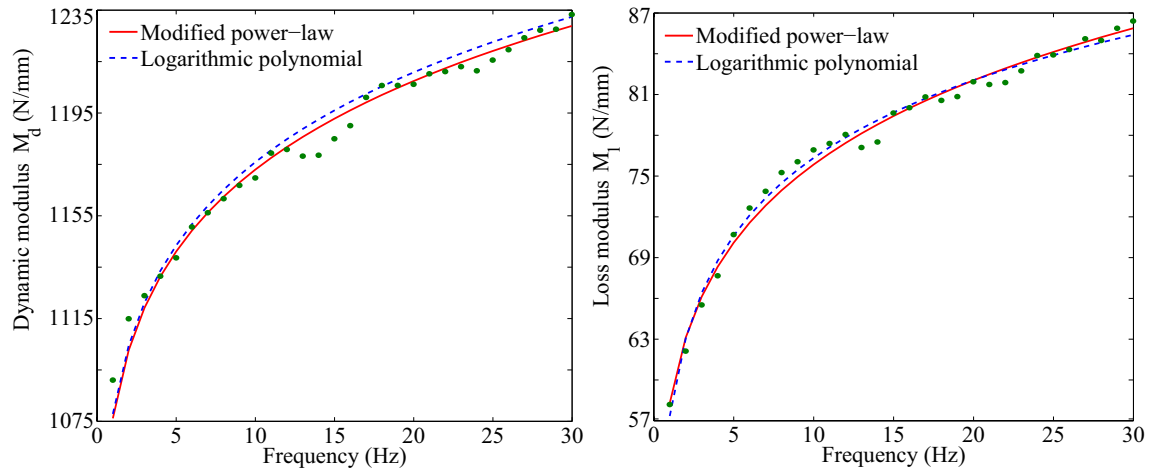
Figure 1.6: Comparison of the dynamic and the loss moduli versus frequency from the modified power law model (solid), the logarithmic polynomial model, (dashed) and experiment (dots) for one of the four suspension bushings.

The frequency response involves both a real and imaginary part, and it is emphasized that both parts have been simultaneously fitted with merely *three* parameters

6

in all. The parsimoniousness of the model indirectly validates the approximations proposed in this part of the work.

1.3 Partial validation of an Adams model against test data

While developing the *generalized quarter car model* an Adams model of the vehicle was used. A practical question remains: to what extent is the Adams model accurate in describing the behavior of an actual vehicle?

To that end, in the third part of this thesis, Adams model correlation with field tests results is presented.

The proposed approach is outlined using a flow chart in Figure 1.7. The individual blocks of the flow chart are described below.

An all terrain vehicle (ATV) prototype was selected for this study as indicated in ① of Figure 1.7. The front and rear suspensions were characterized on an MTS 850.25 damper test-rig at NATRiP[1] (see ②). Using the measured suspension properties, a simplified Adams model of the vehicle was developed. A rigid wheel-road contact kinematic model was developed in step ③. The wheel's vertical displacements from this kinematic contact model were used as inputs to the Adams model.

Next, the vehicle was driven at different speeds on specialized tracks whose displacement profiles are known. Accelerometers were mounted on eight key points, four on the car body where the suspension is attached, and four on wheel axles, as shown in step ④. Vehicle tests were performed on specialized test tracks (two of them are shown in ⑤).

---

[1]National automotive research and infrastructure project, Indore.

From each vehicle test, eight simultaneous time series measurements were obtained corresponding to the vertical accelerations of suspension-to-body attachment points and wheel axle points.

Finally, the field test results were correlated with Adams model simulation in ⑥.
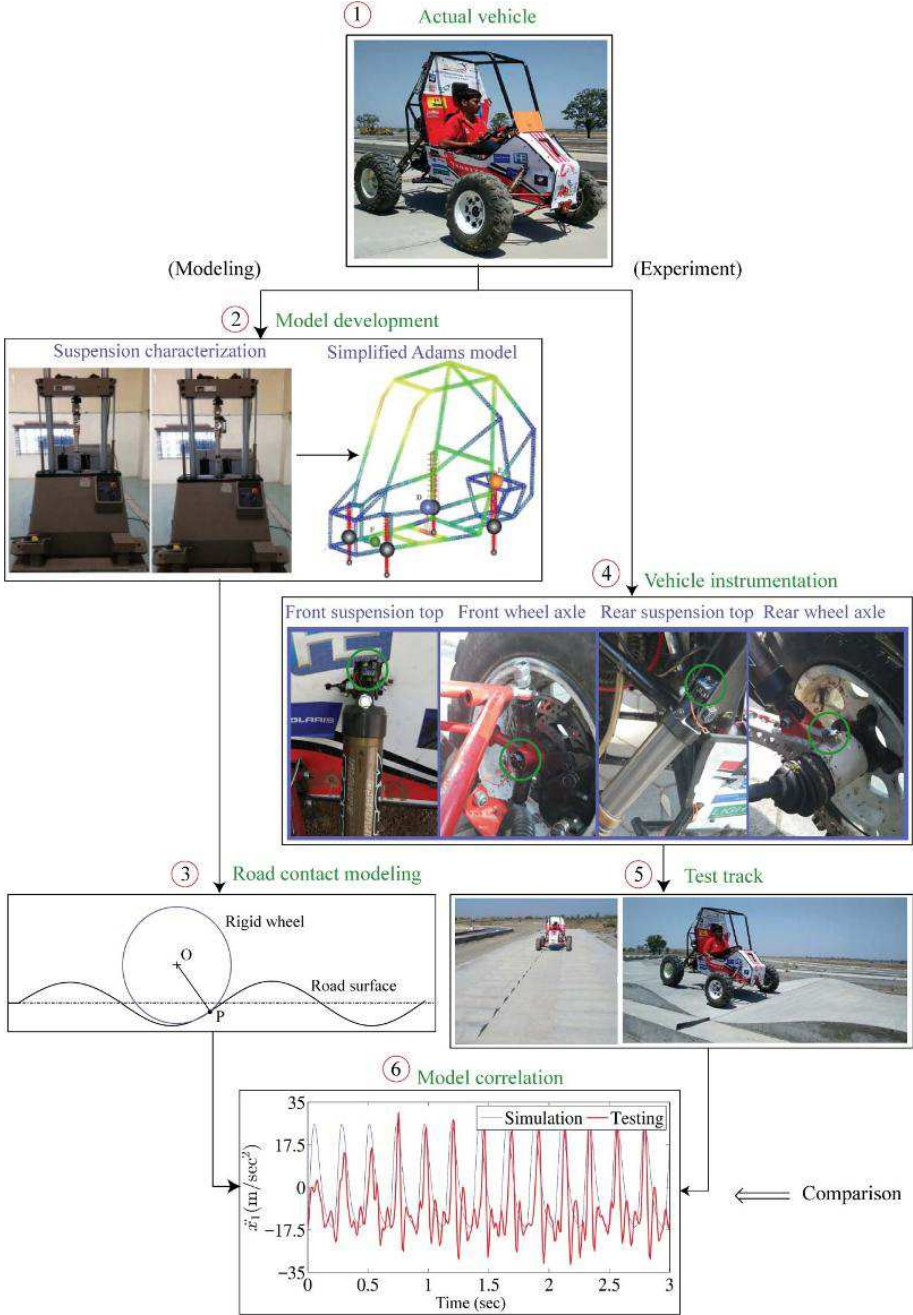
Figure 1.7: Work flow.

We acknowledge that in a typical industrial setup, for detailed validation of Adams models, vehicles are routinely tested on four-post test rigs where base-excitation is applied at four ground-wheel contacts. This kind of testing is time consuming, and requires experienced personnel and specialized equipment. Test track data is used in industry as well, but usually for durability studies, stress analysis, fatigue life estimation and other goals not related to dynamic suspension model validation. In the research literature, field test data has not been used for such partial validation of an Adams model. Since test track measurements can be easily made, the present approach provides an alternative way of model validation. Advantages of the present approach are that it is simpler and that it helps the test engineer think more clearly about some individual sources of vibrations in the accelerometer outputs; these aspects are discussed in the thesis as well.

1.4 Laplace domain reduced order model development using test track data

From the field test acceleration measurements of the all terrain vehicle described in the previous section, a Laplace domain reduced order model of the vehicle is developed in the last part of this thesis.

This Laplace domain model is similar to the generalized quarter car model developed earlier, and may be viewed as a partial experimental implementation of the same ideas.

The modeling approach is discussed using a flow chart in Figure 1.8.
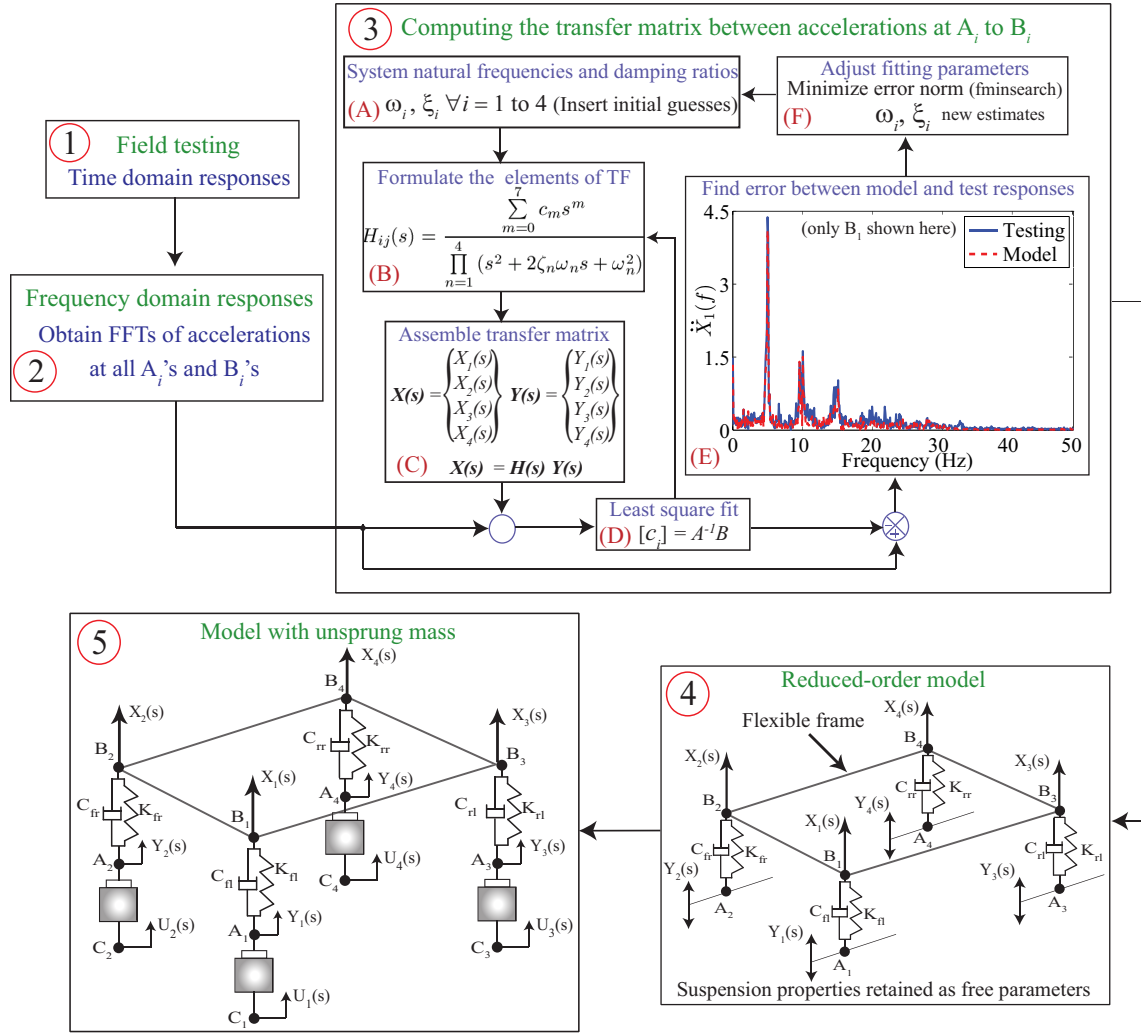
Figure 1.8: Model development using test track data.

To begin with, the test data is obtained from field testing in ① of Figure 1.8. From each vehicle test, eight simultaneous responses corresponding to the vertical accelerations at wheel axles (A_i's) and suspension to body attachment points (B_i's) are obtained. All effects of the car's frame flexibility, mass distribution and the four ground contacts are implicitly reflected in these measured responses. The intention now is to obtain a useful transfer function matrix for the vertical response of the vehicle using this test data. To this end, Fast Fourier Transforms (FFTs) are used

to transform the time domain acceleration data into the frequency domain as indicated in ②. The FFTs are then approximated by an eighth order, strictly proper, transfer function matrix $H(s)$ in ③. Using $H(s)$, a new transfer function matrix with suspension properties treated as free adjustable parameters is obtained in step ④, which facilitates subsequent parameter studies. Finally, the wheel's unsprung mass model is incorporated to obtain a transfer function matrix between ground-excitation at C_i and body displacements at B_i in step ⑤. As a sample of results obtained, model and test responses for one test are compared in Figure 1.9.
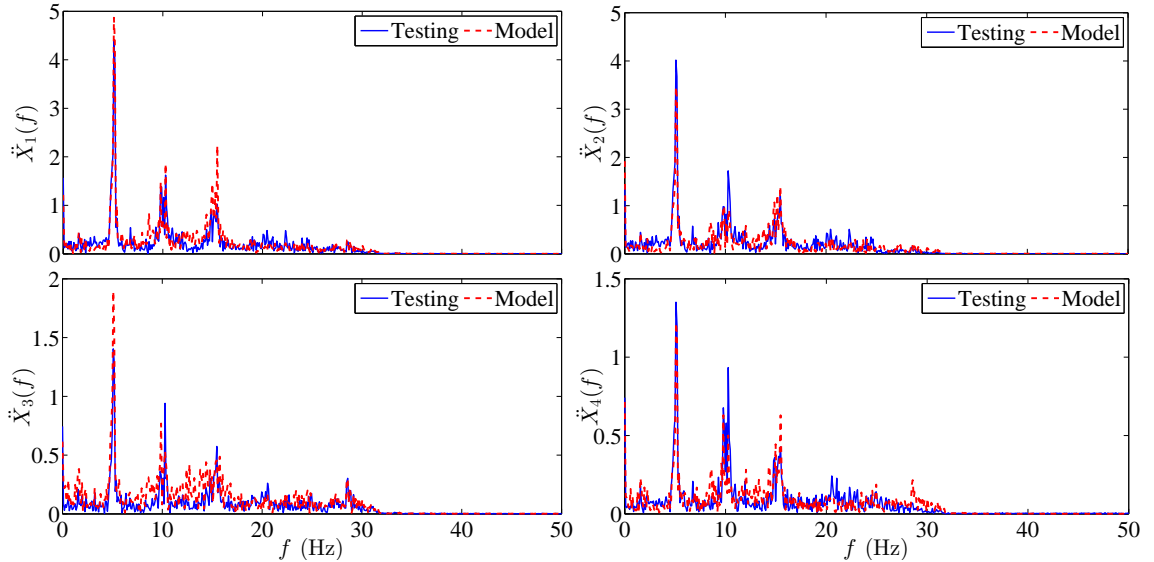
Figure 1.9: Comparison of model and test results for one of the field tests.

It is emphasized that the plotted quantity is not the magnitude of an element of the transfer function matrix. Rather, measured axle accelerometer inputs are used by the model to predict body point accelerations, and the FFT of those predicted quantities is compared with the FFT of measured accelerations at the body point. Possible physical reasons for the observed mismatch are discussed later in the thesis.

1.5 Outline of the thesis

An outline of the rest of the thesis is given here.

The generalized quarter car model of a vehicle's suspension is developed in **Chapter 2**. Two models for vehicle suspension bushings are developed and validated in **Chapter 3**. A simplified Adams model of the vehicle is partially validated against test track data in **Chapter 4**. Finally a reduced order Laplace domain model of the same vehicle's suspension, using the test track data is developed in **Chapter 5**.

In **Chapter 6**, the summary, the major conclusions and some possible direction of future work have been presented.

Chapter 2

A generalized quarter car model with frame flexibility and other nonlocal effects

In this chapter a generalized quarter car model, incorporating frame flexibility and other-wheel ground contacts will be developed. Quarter car models are popular, simple, unidirectional in kinematics, and enable quicker computation than full car models. However, they do not account for three other wheels and their suspensions; nor for the frame's flexibility, mass distribution and damping. We will incorporate all of these effects in this model. The model developed is linear, uses Laplace transforms, involves vertical motions of key points of interest, and has intermediate complexity with improved realism. It uses baseline suspension parameters and responses to step force inputs at suspension attachment locations on the frame. Subsequently, new suspension parameters and unsprung mass compliance parameters are incorporated, for which relevant formulas are developed.

The final expression for the transfer function, between ground displacement and body point response, is approximated using model order reduction. Simple Matlab code is developed that enables quick parametric studies. Finally, parametric studies and wheel hop analysis are performed for a realistic numerical example. Frequency

and time domain responses are obtained which clearly show other wheel effects which are outside the scope of usual quarter car models. The displacements obtained from the quarter car model are compared against this model and show ways in which predictions of quarter car model include errors that can be reduced in this approach.

2.1 Introduction

A vehicle's suspension isolates its occupants from ground disturbances. It achieves a trade-off between ride comfort and vehicle handling. Much research has been carried out on vehicle suspensions [17].

Mathematical models for suspension design are broadly of three types: quarter car [6], half car [7] and full car models [8, 9] (see Figure 2.1).
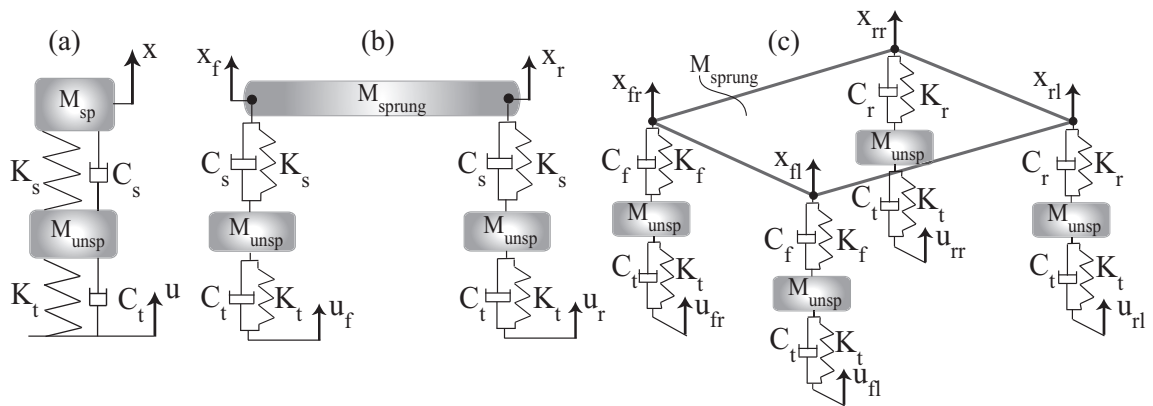
Figure 2.1: Types of car models: (a) quarter car, (b) half car and (c) full car model.

More sophisticated full car models may include the flexibility of the frame. These models have various limitations. The quarter car model accounts for neither the effects of three other wheels and their suspensions nor for frame flexibility. The full car model is computationally complex. The half car model is midway in complexity, allows for fore-aft or sideways interaction but not both, and does not incorporate

14

frame flexibility.

Although they are popular, quarter car models cannot capture all relevant dynamic effects [10, 11]. There are remarkable differences in ride vibration predictions of various models (quarter car, half car, half car with discrete masses, models with and without frame flexibility) [12]. The engine, passenger CG locations, and frame flexibility influence the vibration response and are not included in quarter car model.

In the context of the above range of models, the aim here is to develop a useful modeling approach of *intermediate* complexity, representing the car's dynamics with both reasonable accuracy and low computational effort (see Figure 2.2).
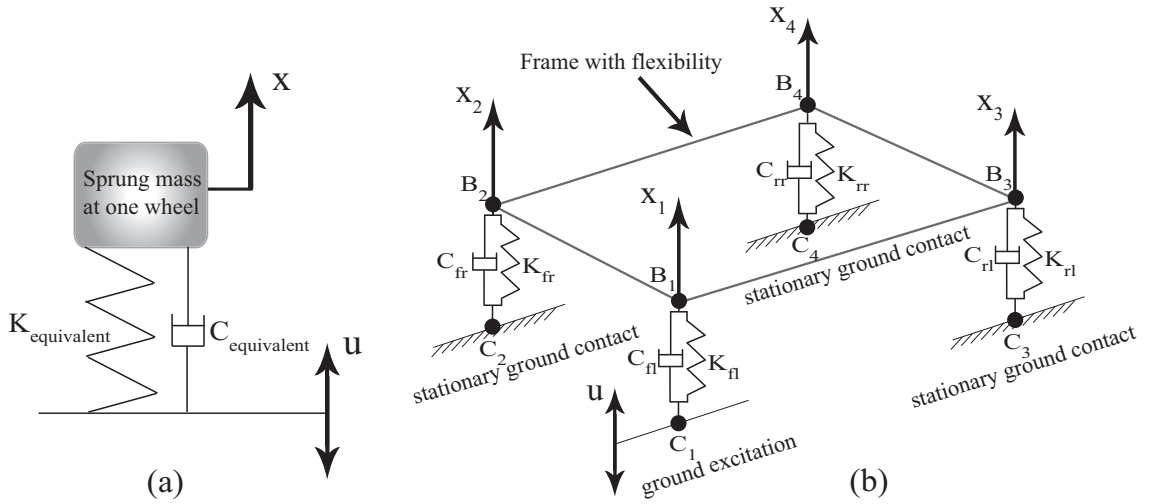
Figure 2.2: (a) Usual quarter car model, with a single sprung mass. (b) Proposed approach: somewhat resembles the quarter car model in that x_1 is computed in response to u, but incorporates complex dynamics of the car including effects of frame flexibility and three other wheel-ground contacts. An unsprung mass is not shown here for simplicity but will be incorporated later. Note here that small rolling and pitching motions of the frame are reflected in corresponding vertical motions of points B_i.

Advantages of the proposed approach over the usual quarter car model go beyond incorporation of frame flexibility and other-wheel effects. In a car, if the front *left* wheel suspension stiffness is changed, the front *right* wheel suspension stiffness will also be changed identically. This effect (symmetric changes at other-wheel locations)

15

is ignored in the usual quarter car model, but incorporated in this approach below. Our model is generalized as it represents the effect of *other* wheels' suspension and is one dimensional in kinematics like a quarter car model: that is why it is named a generalized quarter car model.

Vehicle dynamics can be modeled at different levels of complexity. For instance, in cruise control design the vehicle might be represented as a point mass [18]. For some aspects of handling, a two-wheel bicycle-like model may suffice [19, 20]. A half car model may elucidate braking and stability performance [21, 22]. In this context, the developed approach provides a fundamental extension of the quarter car model, incorporating frame flexibility as well as ground-wheel contacts at three other locations.

Matlab code for obtaining the generalized quarter car model is provided. The code enables a user to perform fairly quick parametric studies. An example of such a parametric study is presented there as well. The role of other wheels, in particular, is seen clearly within our simple modeling framework, emphasizing the advantages of our approach over usual quarter car models.

Lastly, a numerical comparison between a usual quarter car model and our generalized quarter car model is given. As may be expected, the results reveal some inaccuracies in the usual quarter car model which are captured by our model.

2.2 Methodology

The proposed modeling approach is outlined using a flow chart in Figure 2.3.

We start with the actual vehicle in step ① on the flow chart. A realistic vehicle model is developed using MD Adams® [23], as shown in step ②.
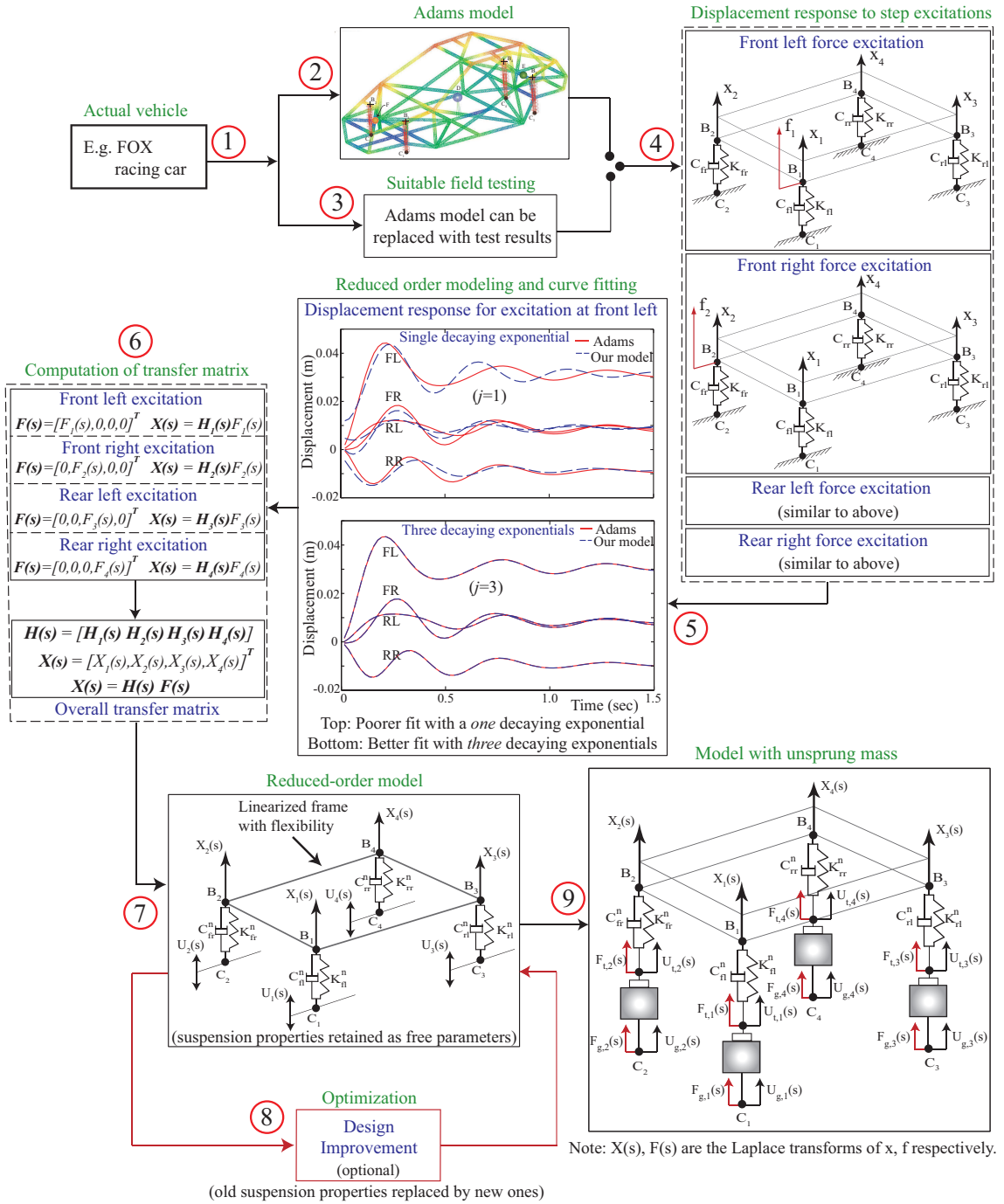
Figure 2.3: Work flow of Chapter 2.

An alternative experimental approach might use direct field testing of a proto-type[1] as shown in ③. In such experiments, applying and then removing forces on

---

[1]This option is explored later in Chapter 5 of this thesis.

chassis points may require less specialized equipment than a full base-excitation test, and this motivates our beginning with force inputs at chassis points B_i as described below.

From the Adams model, the intention is to obtain a useful transfer function matrix for the vehicle. A key point is that subsequent parameter studies should be possible without repeated Adams modeling. To this end, four points on the car body where the suspension is attached (labeled as B_1 through B_4) are identified[2]. In addition to this the ground contact points (labeled as C_1 through C_4) are also identified (see subfigure ④).

Now, four independent sets of responses are calculated sequentially for unit step inputs acting one by one at the four points B_1 through B_4.

For each such step input, the displacement time histories of points B_1 through B_4 are computed numerically[3]. All effects of car flexibility, and the four ground contacts, are implicitly included within these computed responses. The process is indicated schematically in subfigure ④. A total of 16 different time histories are computed in this way.

The above time histories are then approximated using a linear combination of decaying exponentials (plus a constant each). The exponential rates used are the same for all 16 time histories. Sketches of four time histories are shown in subfigure ⑤, which shows also that the approximation can be refined when three decaying exponentials are used. These fitted exponential approximations are Laplace transformed to yield a transfer matrix $H(s)$ between forces and displacements at points

---

[2]If these points are not unique, then representative points can be used.

[3]Mathematically speaking, an impulse or a step input can both be used. For practical testing, a load can be applied and then suddenly taken away, e.g., by cutting a rope, more easily. In simulations, with a step input, velocities remain continuous so numerics are easier. The step input was used for these practical reasons.

B_i (subfigure ⑥).

From $\boldsymbol{H(s)}$, the transfer function matrix between ground-excitation at C_i and body displacements at B_i is computed. A key step here is that the notional suspension parameters of the model in step ④ are now replaced by adjustable parameters in step ⑦. A simple optimization calculation may be conducted on the side if desired, as in step ⑧. Finally, an unsprung mass at each wheel is incorporated in ⑨.

Thus, the proposed modeling approach accounts for frame flexibility and damping, details of mass distribution, as well as interactions of the wheel-suspension of interest with the other three wheels' suspensions, under the simplifying assumption that the dominant ground excitation acts on the wheel of interest. In terms of kinematics, this approach retains much of the simplicity of the quarter car model. Yet, it incorporates more realism and greater scope for parameter studies than the usual quarter car model. At the same time, it is short of the significantly greater complexity of full car models, wherein parameter studies can be more laborious and time consuming.

2.3 Vehicle Model

In this section the vehicle chassis and suspension details will be discussed.

2.3.1 Chassis model

The structural part of the vehicle model used in this study is based on a FOX Silver S2 GT racing car [24, 25] (see Figure 2.4).

The vehicle chassis is made of a roll cage type structure with 1.25 inch SAE 1018 steel pipes of 0.25 inch thickness.

Figure 2.4: FOX racing car S2. Image source: Carlos Bordon's laboratory, University of Seville, Spain. Reproduced with permission.
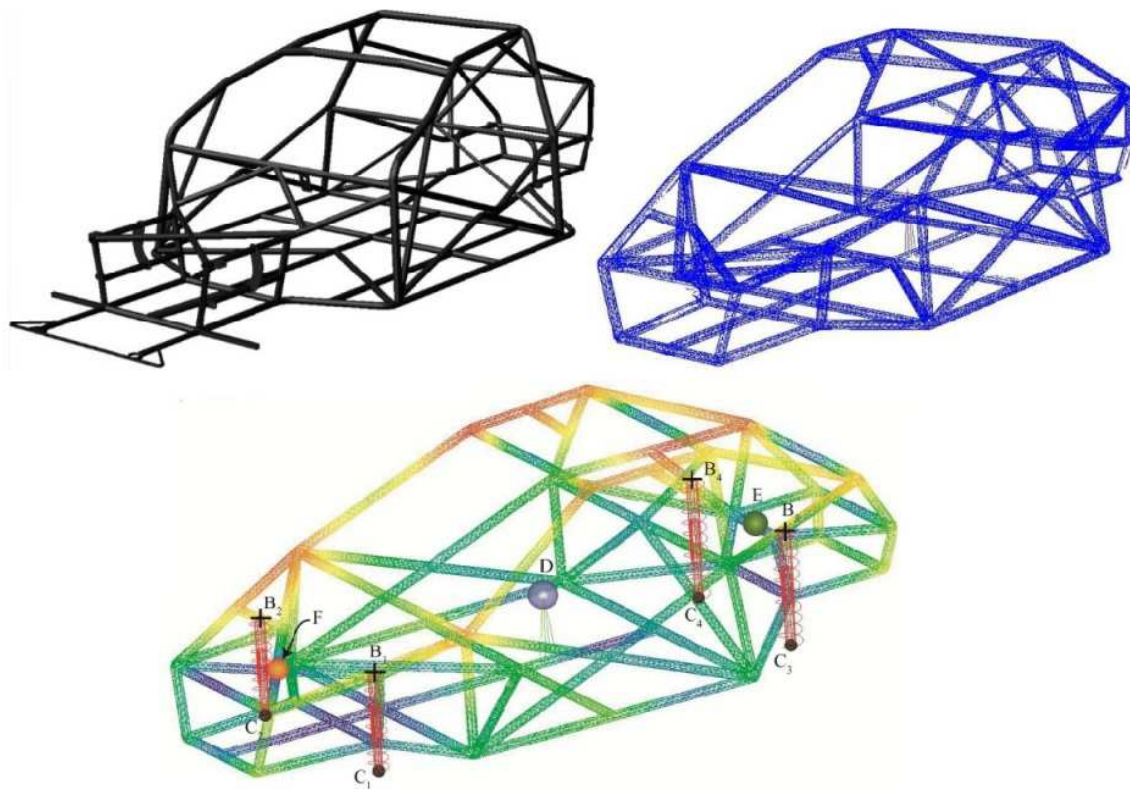
Figure 2.5: Top left: CAD model of the chassis. Top right: FE model of simplified chassis, Bottom: Simplified model of the car with flexible chassis and with suspension assemblies replaced by equivalent spring-dashpots.

20

From the CAD model of the chassis (see top-left of Figure 2.5), a simplified but somewhat similar geometrical model was developed with pipe curvatures removed (Figure 2.5, top-right), and a finite element (FE) model of the latter was developed in Nastran[R] [26]. The FE model had 17369 nodes and 18705 CQUAD4 shell elements[4]. Next, a mathematical model of the vehicle including the suspension was developed in Adams[R]. The FE model of the chassis was imported into Adams from Nastran using Adams/Flex[5].

The four mounting locations B_i were defined as interface nodes. In addition, the model had three more interface nodes denoted D, E and F, corresponding to the center of mass locations of the passengers, some generic payload, and battery, respectively (Figure 2.5, bottom). Three rigid bodies with mass and inertia properties representing the passengers, payload, and battery were attached to these interface nodes[6]. In reality, flexibility and damping in the driver and seat can be significant; and these have indeed been modeled elsewhere, e.g., [27]. These effects were not retained here for simplicity. It will be clear that adding such effects in our approach will simply involve adding some internal modeling details.

2.3.2 Vehicle suspension

The vehicle is equipped with a push rod front and double wishbone rear suspensions (see Figure 2.6).

The effective suspension characteristics were obtained from separate half car

---

[4]Four noded iso-parametric quadrilateral shell elements.

[5]Adams/Flex is an add-on for incorporating a component's flexibility. It uses component mode synthesis through modal superposition. For the present flexible body model first 42 modes were retained.

[6]The rigid bodies have been modeled using spheres in Adams with mass of 300 kg, 100 kg, 100 kg and radius of gyration of 210 mm, 150 mm, 125 mm respectively. The interface nodes are in turn connected to the FE mesh using RBE2 elements, which are used to connect rigid body nodes to a few nodes in a deformable mesh.
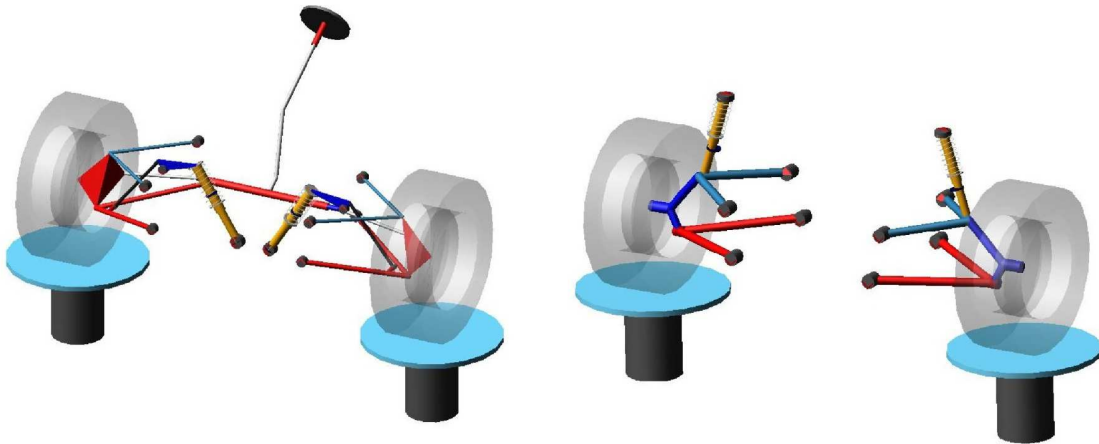
Figure 2.6: Push rod front and double wishbone rear suspensions respectively.

Adams models of the front and rear suspension assemblies. The details of the same are discussed in Appendix A.1. Using those simulations, the suspensions in the full-car model were replaced by four equivalent spring-dashpot pairs between the points B_i and C_i described earlier.

At this stage, the Adams modeling is complete. Forces can be applied to points B_i, and the responses of the vehicle can be computed, as depicted in subfigure ④ in Figure 2.3.

2.4   Reduced order vehicle model

Model order reduction has well-known advantages in large-scale simulation, analysis and control design, and has been extensively studied and used. Designers strive to develop simple models of the physical system. Working with simpler models result in faster and more reliable computations than their higher-order counter parts. Lower order models are also easier to understand and manipulate. Therefore, it is useful to reduce model order while preserving model characteristics that are important to

the application.

The classical techniques for model order reduction are broadly divided as:

1. Modal analysis methods [28]

2. Aggregation methods [29]

3. Frequency domain methods [30]

4. Norm based methods [31]

More recent work on low order modeling in an automotive application (a quarter-car model with realistic suspension details) is reported in [32]. Here, since the displacements responses resembles strongly decaying oscillatory solutions, fitted decaying exponentials will be used for reduced order modeling.

As discussed in Section 2.2, eight key points are selected for reduced order modeling, namely four ground-wheel contacts C_i and four suspension-body attachment points B_i. Consider a set of four numerical responses obtained from Adams for the motions at B_i, in response to a unit step input force (1 KN) at B_1. The numerical responses contain discretely sampled data, at time intervals of $T = 0.02$ seconds in the present case. These are denoted by $x(kT)$, a 4×1 vector containing the displacements of B_1, B_2, B_3 and B_4 at the kth sampling instant[7]. We will approximate these displacement responses using the mathematical form

$$\tilde{x}(t) = R_0 + R_1 e^{-\sigma_1 t}\sin \omega_1 t + R_2 e^{-\sigma_1 t}\cos \omega_1 t + \ldots + R_{2j-1}e^{-\sigma_j t}\sin \omega_j t + R_{2j}e^{-\sigma_j t}\cos \omega_j t,$$

(2.1)

where $\tilde{x}(t)$ is 4×1, the R's are to-be-fitted 4×1 column vectors, and the σ's and

[7]The ADAMS solver used was GSTIFF with integrator SI2 [33].

ω's are fitted real numbers. Equation (2.1) can be written more compactly as

$$\tilde{x}(t) = R_0 + \sum_{k=1}^{j} \left(R_{2k-1} \ e^{-\sigma_k t} \ \sin \omega_k t + R_{2k} \ e^{-\sigma_k t} \ \cos \omega_k t \right).$$

In our calculations, we initially estimated σ's and ω's using a separate simple state space model, but finally refined our fits using nonlinear optimization (see Appendix A.2). These estimates are modified later using Matlab's `fminsearch` to get more refined fits[8]. For fitting σ's and ω's, we work at any time with a set of estimates for these parameters. Given these estimates, the coefficient matrices R_j are fitted by solving the following system of equations in a least squares sense:

$$x(t) = \overbrace{\begin{bmatrix} R_0 & R_1 & R_2 & \ldots & R_{2j-1} & R_{2j} \end{bmatrix}}^{\mathbf{R}}_{4 \times (2j+1)} \overbrace{\begin{bmatrix} 1 \\ e^{-\sigma_1 t} \sin \omega_1 t \\ e^{-\sigma_1 t} \cos \omega_1 t \\ \vdots \\ e^{-\sigma_j t} \sin \omega_j t \\ e^{-\sigma_j t} \cos \omega_j t \end{bmatrix}}^{q(t)}_{(2j+1) \times 1}, \qquad (2.2)$$

or

$$x(t) = \mathbf{R} \ q(t), \qquad (2.3)$$

where $q(t)$ is a vector with a unit entry followed by exponential terms. Equation (2.3) is to be used for several time instants (say $N + 1$)[9], with the left hand side

---

[8] `fminsearch` is an unconstrained nonlinear minimization algorithm in Matlab. For a multivariable function $f(x)$ it starts with an initial guess x0 and attempts to find a local minimum x of the function. The syntax is x = `fminsearch`(fun,x0).

[9] The Adams simulation was performed for 1.5 seconds with a time step T of 0.02 seconds, i.e., $N = 75$.

vectors $x(t)$ stacked side by side to make a large $4 \times (N+1)$ matrix $\mathbf{X}$, and the right hand side vectors $q(t)$ stacked side by side to make a large $(2j+1) \times (N+1)$ matrix $\mathbf{Q}$. Thus,

$$\mathbf{X} = \begin{bmatrix} x(0) & x(T) & \ldots & x(kT) & \ldots & x(NT) \end{bmatrix}_{4 \times (N+1)}$$

$$\text{and} \quad \mathbf{Q} = \begin{bmatrix} q(0) & q(T) & \ldots & q(kT) & \ldots & q(NT) \end{bmatrix}_{(2j+1) \times (N+1)}$$

with Equations (3.17) or (2.3) yielding to

$$\mathbf{X} = \mathbf{R}\,\mathbf{Q}. \tag{2.4}$$

In Equation (2.4), $\mathbf{X}$ is known from simulation (or possibly experiment, if working directly with a prototype), $\mathbf{Q}$ is known in terms of the σ's and ω's, and $\mathbf{R}$ is to be found. Equation (2.4) can be transposed and solved in a least squares sense for given σ's and ω's; and that sum of squares of errors then minimized with respect to the σ's and ω's using an optimization routine (here Matlab's `fminsearch` is used for error norm minimization).

However, for the present application, the above fitting needs to be simultaneously done for independent step force inputs at all suspension-to-body attachment points B_i (16 responses in total). The same exponential rates must be used to fit all 16 responses. Thus, there are four versions of Equation (2.4), one for each individual step inputs at four locations; and these can be stacked vertically in the form

$$
\begin{bmatrix} \mathbf{X}_1 \\ \mathbf{X}_2 \\ \mathbf{X}_3 \\ \mathbf{X}_4 \end{bmatrix}_{16 \times (N+1)} = \begin{bmatrix} \mathbf{R}_1 \\ \mathbf{R}_2 \\ \mathbf{R}_3 \\ \mathbf{R}_4 \end{bmatrix}_{16 \times (2j+1)} \mathbf{Q}_{(2j+1) \times (N+1)}. \tag{2.5}
$$

In Equation (2.5), $\mathbf{Q}$ does not change because the same σ's and ω's are used for all four cases; the left hand side is known (computed or measured); and the matrix of $\mathbf{R}$'s is found in a least squares sense as described above for Equation (2.4).

Fitting results for different numbers of exponentials (i.e., j), are shown in Table 2.1 and Figure 2.7. The fit improves with increasing j, and $j = 3$ gives satisfactory results. Numerical values of various R-vectors are not reported to save space.

From fitted displacement responses, a transfer function matrix between forces and displacements at locations B_i is developed in Section 2.5. Note that, since $\mathbf{X}(t)$ is explicitly fitted using exponentials, finding Laplace transforms $(X(s))$ is simple.

No. of exponentials used (j)	σ	ω
1	3.546	13.894
2	1.708	12.425
	4.452	17.042
3	1.559	12.365
	3.079	17.257
	5.909	16.659

Table 2.1: σ's and ω's obtained for different number of exponentials j. With more freedom, $3.079 \approx 3$ and $5.909 \approx 6$ provide a better fit compared to their average $4.452 \approx 4.5$. Further individual interpretations of these parameters seems difficult and is not attempted here.
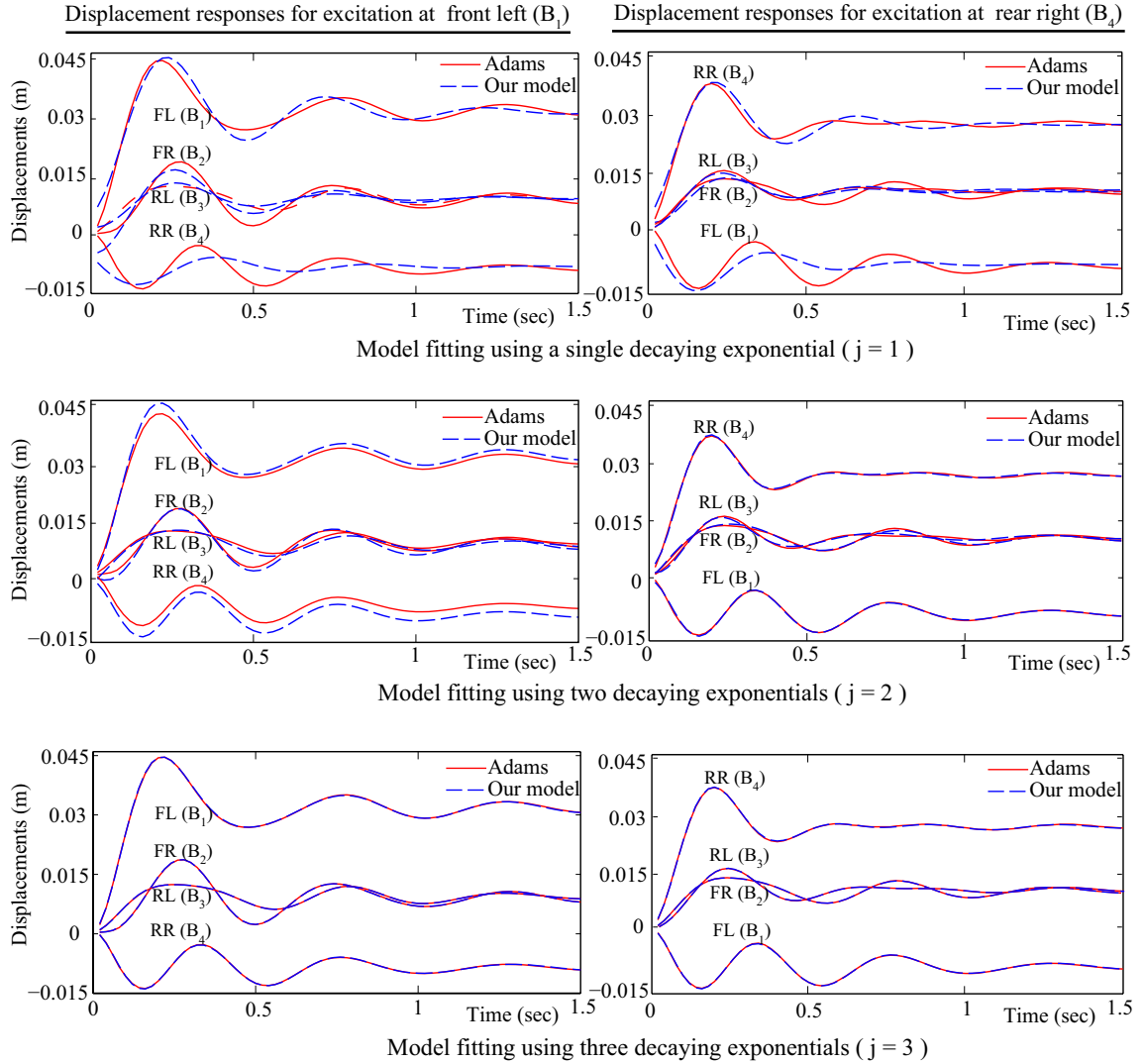
Figure 2.7: Fitted displacement responses for $j = 1, 2$ and 3, for two excitation cases (the other two cases are not shown). The labels are: FR for front right; FL for front left; RR for rear right; and RL for rear left. As seen clearly in the lowermost two plots, the lowest curves on both sides are identical due to the reciprocal theorem [34] applied after Laplace transformation: the response at RR due to forcing at FL equals the response at FL due to forcing at RR. The steady state displacement of the point of application of force is positive in both cases; the displacement at the diagonally opposite point is negative; and the other two displacements are smaller and about the same, because the vehicle approximately rotates about a diagonal line. Finally, displacements at the point of application are much larger than displacements at other locations, as expected.

2.5 Transfer function matrix $H(s)$

Assuming zero initial conditions[10], the Laplace transforms of displacements, $X(s)$, and of forces, $F(s)$, at four points B_i are related linearly as in

$$X(s) = H(s)F(s). \tag{2.6}$$

Equation (2.6) can be expanded as

$$\begin{pmatrix} X_1(s) \\ X_2(s) \\ X_3(s) \\ X_4(s) \end{pmatrix} = \begin{bmatrix} H_{11}(s) & H_{12}(s) & H_{13}(s) & H_{14}(s) \\ H_{12}(s) & H_{22}(s) & H_{23}(s) & H_{24}(s) \\ H_{13}(s) & H_{23}(s) & H_{33}(s) & H_{34}(s) \\ H_{14}(s) & H_{24}(s) & H_{34}(s) & H_{44}(s) \end{bmatrix} \begin{pmatrix} F_1(s) \\ F_2(s) \\ F_3(s) \\ F_4(s) \end{pmatrix}. \tag{2.7}$$

$$\uparrow \qquad \uparrow \qquad \uparrow \qquad \uparrow$$
$$H_1(s) \quad H_2(s) \quad H_3(s) \quad H_4(s)$$

Each element of the above 4×4 matrix is a separate Laplace transform; and individual columns have been named $H_1(s), H_2(s), H_3(s)$ and $H_4(s)$ as shown. For clarity, the procedure for computing $H(s)$ is indicated schematically in Figure 2.8.

First, a step input force is applied at point B_1, with all other input forces equal to zero. The Laplace transform of the force input is then $F_1(s) = \frac{1}{s}$, with $F_2 = F_3 = F_4 = 0$. The corresponding response $X(s)$ is computed analytically from the fitted exponentials as described above; and this same $X(s)$ is then (by Equation (2.6)) equal to $H_1(s)F_1(s)$, whence $H_1(s) = X(s)F_1(s)^{-1} = sX(s)$. In this way, with four successive simulation results, all the columns of $H(s)$ are found.

---

[10]We have assumed zero initial conditions as we are interested in the response of the vehicle under sustained road inputs (disturbances) in which the role of initial conditions rapidly becomes insignificant.
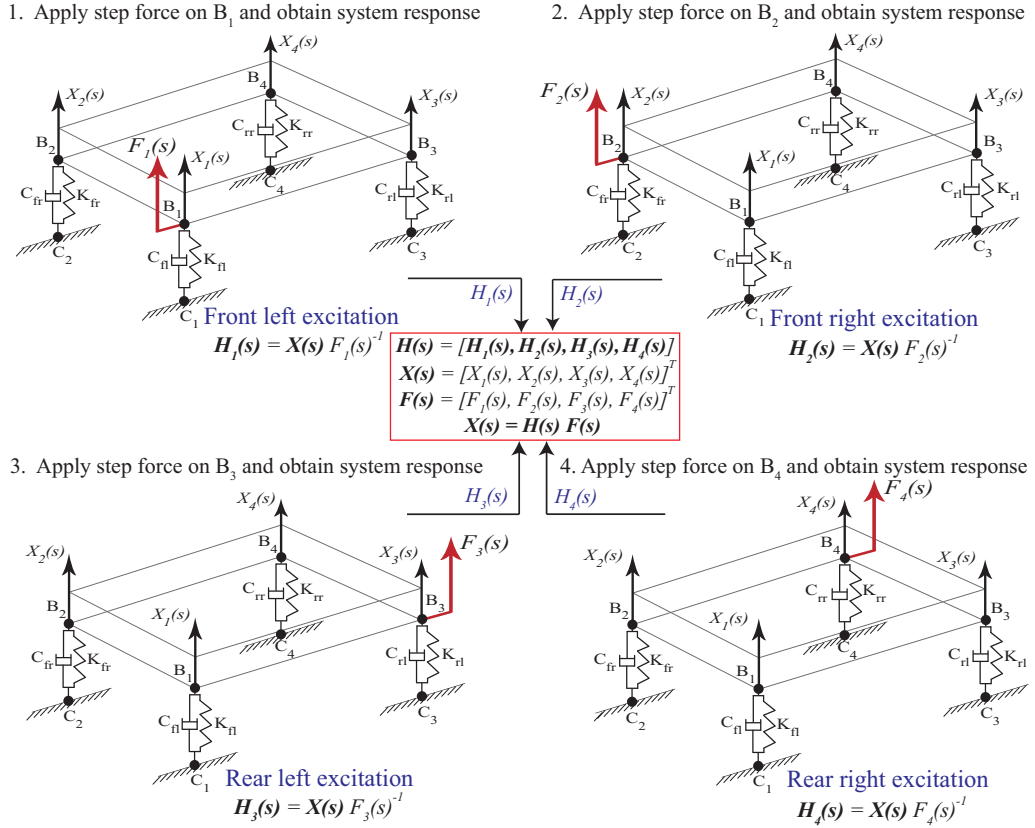
Figure 2.8: Methodology of obtaining transfer function matrix.

We expect from theory that $H(s)$ can be taken as symmetric, as follows.

The linearized dynamics of the vehicle, subjected to vertical forces at four locations (B_i's), can generally be described by a model of the form

$$
\begin{bmatrix} M_{11} & M_{12} \\ M_{12}{}^T & M_{22} \end{bmatrix} \begin{bmatrix} \ddot{x} \\ \ddot{y} \end{bmatrix} + \begin{bmatrix} C_{11} & C_{12} \\ C_{12}{}^T & C_{22} \end{bmatrix} \begin{bmatrix} \dot{x} \\ \dot{y} \end{bmatrix} + \begin{bmatrix} K_{11} & K_{12} \\ K_{12}{}^T & K_{22} \end{bmatrix} \begin{bmatrix} x \\ y \end{bmatrix} = \begin{bmatrix} f \\ 0 \end{bmatrix}. \tag{2.8}
$$

In the above, x represents the vertical displacements at B_1 through B_4, and y represents a possibly very large number of additional unmeasured and unforced degrees of freedom[11]. M and K are *symmetric* mass and stiffness matrices; their symmetry is a

---

[11]The FE model of the chassis has 17369 nodes. Four of them correspond to points B_1 through

consequence of the quadratic form of the kinetic and potential energies in Lagrange's formulation. The damping matrix C is also symmetric in typical formulations. The reason for the symmetry of C is that our dynamic model of the vehicle frame consists of (i) assigned modal damping values for the structure (automatically giving symmetric damping matrices), along with (ii) added discrete dashpots in the suspension, which make symmetric contributions given by Rayleigh's dissipation function [35]. Additionally, and more generally, several other linear damping models can in fact be accurately captured using symmetric matrices, as discussed in e.g., [36, 37].

Taking the Laplace transform of Equation (2.8) we obtain

$$\left(\begin{bmatrix} M_{11} & M_{12} \\ M_{12}{}^T & M_{22} \end{bmatrix} s^2 + \begin{bmatrix} C_{11} & C_{12} \\ C_{12}{}^T & C_{22} \end{bmatrix} s + \begin{bmatrix} K_{11} & K_{12} \\ K_{12}{}^T & K_{22} \end{bmatrix} \right) \begin{bmatrix} X(s) \\ Y(s) \end{bmatrix} = \begin{bmatrix} F(s) \\ 0 \end{bmatrix}, \quad (2.9)$$

rewritten compactly as

$$\begin{bmatrix} G_{11}(s) & G_{12}(s) \\ G_{12}(s)^T & G_{22}(s) \end{bmatrix} \begin{bmatrix} X(s) \\ Y(s) \end{bmatrix} = \begin{bmatrix} F(s) \\ 0 \end{bmatrix}, \quad (2.10)$$

whence, eliminating $Y(s)$, we obtain $X(s) = H(s)F(s)$ with

$$H(s) = \left[G_{11}(s) - G_{12}(s)G_{22}(s)^{-1}G_{12}(s)^T \right]^{-1}, \quad (2.11)$$

which is symmetric. Since $H(s)$ is symmetric, the system obeys reciprocity [34]. As a result, the response at RR (rear-right) due to unit forcing at FL (front-left) equals to the response at FL due to unit forcing at RR, as seen in Figure 2.7.

In the next section we obtain the transfer function matrix $H_n(s)$ between ground

---

B_4. The non-vertical displacements of these four points, and the displacements of all remaining nodes, are unforced and unmeasured degrees of freedom.

excitations at C_i and displacements at B_i.

2.6 Modified transfer function matrix $H_n(s)$

The matrix $H(s)$ relates forces and displacements at points B_i. In determining $H(s)$, a set of baseline suspension properties were used. If the designer wants to change the suspension properties during subsequent simulations, it is not practical to repeat the process of exponential fitting for all design iterations. Instead, $H(s)$ will be modified to incorporate new suspension properties as free parameters.

Subsequently, this modified $H(s)$ will be used to determine a matrix $H_n(s)$ which relates displacement inputs at points C_i to displacements at points B_i.

2.6.1 Incorporating the suspension properties as free parameters

We have initially applied forces $F(s)$ at B_i and obtained $X(s)$ using $H(s)$. The relationship can be formally inverted (displacements to *required additional* forces) as in

$$X(s) = H(s)F(s) \longrightarrow F(s) = H(s)^{-1}X(s). \tag{2.12}$$

To obtain $H_f(s)$, we first imagine detaching the suspensions (spring-dashpots) from the vehicle body, yet applying the same displacements $X(s)$ at points B_i (see Figure 2.9).
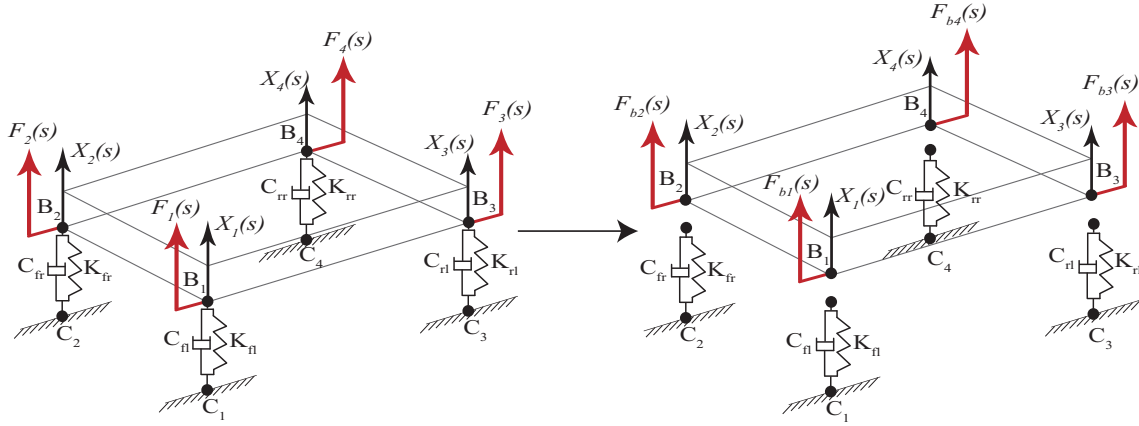
Figure 2.9: Towards finding $H_f(s)$ with suspension properties retained as free parameters.

With suspensions detached, the required additional forces at B_i will change from $F(s)$ to $F_b(s)$ as in

$$F_b(s) = F(s) - D_o(s)X(s), \tag{2.13}$$

where the subscript 'o' denotes 'old' or baseline properties, subscript 'b' denotes 'body', and the diagonal matrix

$$D_o(s) = \begin{bmatrix} K_{fl} + C_{fl}s & 0 & 0 & 0 \\ 0 & K_{fr} + C_{fr}s & 0 & 0 \\ 0 & 0 & K_{rl} + C_{rl}s & 0 \\ 0 & 0 & 0 & K_{rr} + C_{rr}s \end{bmatrix}, \tag{2.14}$$

where in turn $K_{fl}, K_{fr}, K_{rl}, K_{rr}$ are the equivalent stiffnesses and $C_{fl}, C_{fr}, C_{rl}, C_{rr}$ are the corresponding damping coefficients of front left, front right, rear left and rear right wheel-suspension assemblies respectively. We assume for simplicity that the left and right suspension properties are identical (lateral symmetry).

32

Now, if we replace $D_o(s)$ with $D_n(s)$ ('n' denotes 'new' suspension properties)[12], the forces in response to the same $X(s)$ will become (using Equations (2.13) and (2.12))

$$F_n(s) = F_b(s) + D_n(s)X(s) = \left[H(s)^{-1} - D_o(s) + D_n(s) \right] X(s). \qquad (2.15)$$

Thus, upon changing suspension parameters, we obtain a new transfer function $H_f(s)$ to replace the old $H(s)$ as

$$X(s) = \underbrace{\left[H(s)^{-1} - D_o(s) + D_n(s) \right]^{-1}}_{H_f(s)} F_n(s). \qquad (2.16)$$

The matrix $H_f(s)$ obtained above ("f" denoting free parameters), between forces and displacements at B_i, corrects the original $H(s)$ for changed suspension parameters. The baseline and the new suspension properties used in this study are reported in Table 2.2.

Identifier	K_f	K_r	C_f	C_r
Original	25.0 N/mm	30.0 N/mm	0.50 N-s/mm	0.75 N-s/mm
New	23.6 N/mm	34.9 N/mm	0.62 N-s/mm	0.76 N-s/mm

Table 2.2: Original and new suspension parameters.

The transfer function matrix $H_f(s)$ may be useful in future studies where non-linearity is to be introduced in one wheel's suspension. Here, however, we continue our linear formulation and consider ground displacement inputs.

---

[12]The suspension properties used for illustration are given in Table 2.2. The original suspension parameters were obtained from the Adams model of the vehicle (see Appendix A.1). The new suspension parameter values were obtained from a peripheral optimization study (see ⑧ in Figure 2.3) that is not relevant here.

2.6.2 Obtaining the transfer function matrix from ground to body displacements

We now incorporate displacement inputs at ground-contact points C_i (Figure 2.10). To this end, recall the case without ground inputs, i.e., Equation (2.15). If displace-
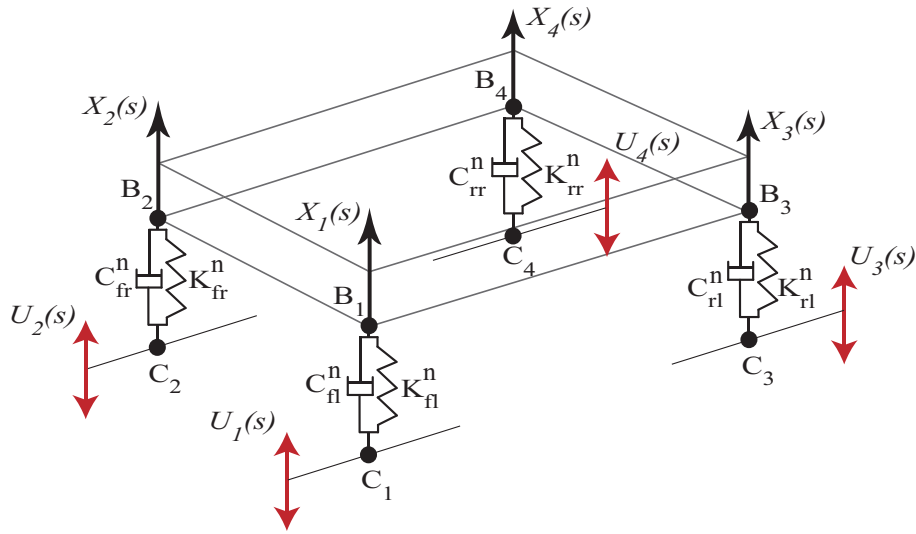
Figure 2.10: Displacement inputs at ground contact points C_i.

ments $U(s)$ are additionally applied to the ground contact points, while holding $X(s)$ constant, then additional forces $D_n(s)U(s)$ are transmitted to the contact points B_i. For $X(s)$ to remain the same in Equation (2.15), we must subtract $D_n(s)U(s)$ from $F_n(s)$. This leads to

$$F_{\text{wgi}}(s) = \left[H(s)^{-1} - D_o(s) + D_n(s) \right] X(s) - D_n(s)U(s), \qquad (2.17)$$

where the 'wgi' subscript stands for 'with ground input.' When there is only base excitation from the ground, and no additional forces are applied, the left hand side

34

above becomes zero and we have

$$X(s) = \underbrace{\left[H(s)^{-1} - D_o(s) + D_n(s) \right]^{-1} D_n(s)}_{H_n(s)} U(s), \qquad (2.18)$$

where $H_n(s)$ is the transfer function matrix between displacements at C_i to B_i ('n' denotes 'new' suspension properties).

2.7 Model with unsprung mass

The term "unsprung mass" is attributed to Healey [38]. It refers to the inertial effects of the suspension, wheels, and other components directly connected to them, rather than the mass supported by the suspension.

We will now incorporate an unsprung mass in our formulation by attributing an effective mass to the wheel[13].

A schematic diagram of one wheel including its unsprung mass is shown in Figure 2.11. The key point is that, due to the nonzero mass, the force from the ground is not transmitted directly through the wheel to the base of the suspension. In terms of Figure 2.11, $F_{g,i} \neq F_{t,i}$.

The ith wheel's suspension now relates four dynamic variables: displacement $U_{g,i}(s)$ and corresponding force $F_{g,i}(s)$ at the true ground contact, and the transmitted displacement and force $U_{t,i}(s)$ and $F_{t,i}(s)$ respectively, at the suspension base point (these replace the points called C_i above). In other words, $U_{t,i}(s)$ is the same as the ith component of displacement $U(s)$ in Equation (2.18).

---

[13]Sometimes point masses are also added to the body points B_i, but that does not affect our procedure.
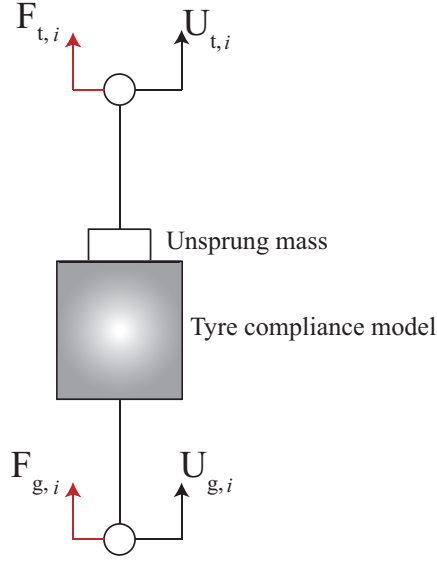
Figure 2.11: Schematic diagram representing dynamic compliance of ith wheel including its unsprung mass. Here, $U_{t,i}(s)$ corresponds to base displacement $U(s)$ in Equation 2.18.

These forces and displacements are related by

$$\begin{bmatrix} F_{g,i}(s) \\ F_{t,i}(s) \end{bmatrix} = \underbrace{\begin{bmatrix} T_{11}(s) & T_{12}(s) \\ T_{21}(s) & T_{22}(s) \end{bmatrix}}_{\text{Tyre's dynamic compliance}} \begin{bmatrix} U_{g,i}(s) \\ U_{t,i}(s) \end{bmatrix}, \tag{2.19}$$

where $i = 1, 2, 3, 4$ for front left, front right, rear left, and rear right wheel respectively. It is clear that these individual suspensions' dynamic compliances are unaffected by phenomena at other wheels. Considering the front left wheel we have

$$F_{t,1}(s) = D_{n,11}(s)(X_1(s) - U_{t,1}(s)) \tag{2.20}$$

From Equations (2.19) and (2.20), we obtain

$$D_{n,11}(s)(X_1(s) - U_{t,1}(s)) = T_{21}(s)U_{g,1}(s) + T_{22}(s)U_{t,1}(s),$$

36

which yields

$$U_{t,1}(s) = (D_{n,11}(s)+T_{22}(s))^{-1}D_{n,11}X_1(s)-(D_{n,11}(s)+T_{22}(s))^{-1}T_{21}(s)U_{g,1}(s). \quad (2.21)$$

Equation (2.21) is of the form

$$U_{t,1}(s) = \bar{A}_1(s)X_1(s) - \bar{B}_1(s)U_{g,1}(s). \quad (2.22)$$

Four versions of above equation, one for each wheel, can be assembled in matrix form as

$$U_t(s) = \underbrace{\begin{bmatrix} \bar{A}_1(s) & 0 & 0 & 0 \\ 0 & \bar{A}_2(s) & 0 & 0 \\ 0 & 0 & \bar{A}_3(s) & 0 \\ 0 & 0 & 0 & \bar{A}_4(s) \end{bmatrix}}_{A(s)} X(s) - \underbrace{\begin{bmatrix} \bar{B}_1(s) & 0 & 0 & 0 \\ 0 & \bar{B}_2(s) & 0 & 0 \\ 0 & 0 & \bar{B}_3(s) & 0 \\ 0 & 0 & 0 & \bar{B}_4(s) \end{bmatrix}}_{B(s)} U_g(s).$$

$$(2.23)$$

From Equation (2.18), noting that $U_t(s) \equiv U(s)$, we have

$$U_t(s) = H_n^{-1}(s)X(s), \quad (2.24)$$

which finally yields

$$X(s) = \left[A(s) - H_n^{-1}(s)\right]^{-1} B(s)U_g(s) = G(s)U_g(s), \quad (2.25)$$

where $U_g(s)$ is the actual base excitation from the true ground-contact point. As a check we may note that if the tyres' compliance is set to zero, then in Equation

(5.22) we must have $A(s) = 0$ and $B(s) = I$ (the identity matrix), whence Equation (2.25) reduces to Equation (2.18).
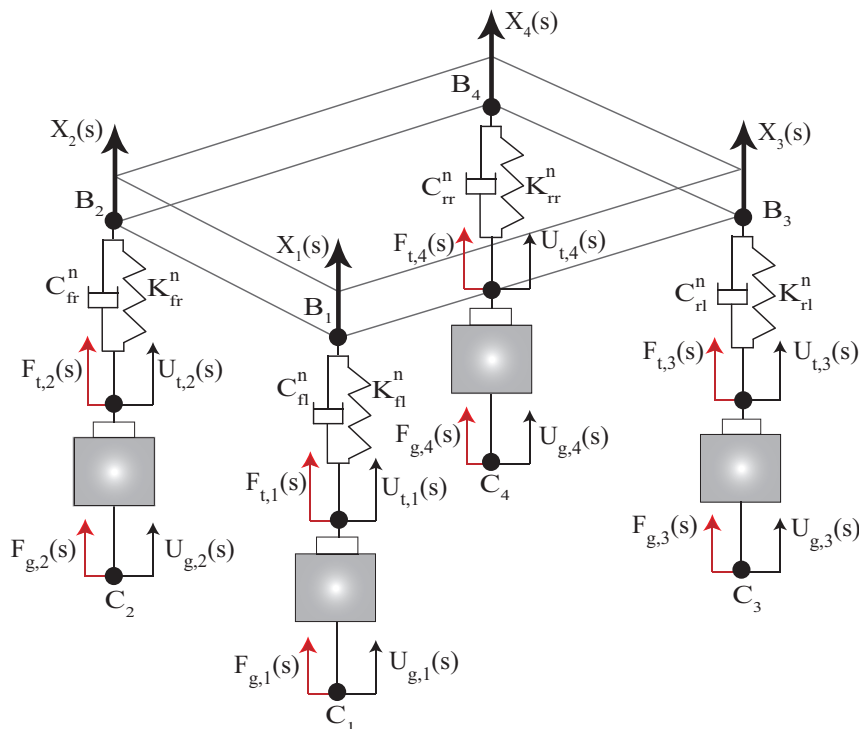
Figure 2.12: Car model with unsprung mass.

The resulting car model is shown schematically in Figure 2.12. Superficially, it looks like a full car model, but it is restricted in various ways. For example, the motion kinematics at the body points B_i is purely vertical. Moreover, the development of the model is based on individual attention to one-dimensional behaviors of individual wheels' suspensions. A desirable practical use of this model lies in setting input ground displacements at three wheels to zero, and taking the appropriate scalar diagonal element of $G(s)$ in Equation (2.25), to obtain the resulting quarter car model for the wheel of interest, while incorporating chassis flexibility and other-wheel effects to a useful extent.

For practical work, the matrix manipulations leading to Equation (2.25) lead to long analytical expressions that can be simplified without sacrificing accuracy as

shown below.

2.8 Model order reduction of the final transfer function matrix $G(s)$

Model order reduction of $G(s)$ leads to obvious computational simplifications. A reduced order model is obtained earlier in section 2.4 to obtain $H(s)$ by direct exponential fitting using three pairs of decaying sines and cosines ($j = 3$ in Table 2.1) plus an added constant. Consequently, each element of $H(s)$ is a transfer function with both numerator and denominator of 6th order. The subsequent matrix operations with $H(s)$, as described in Equations (2.12) through (2.18), can be done symbolically in Matlab. The matrix $H_n(s)$ of Equation (2.18) has elements of 28th order, which is quite large.

Finally, $H_n(s)$ is itself modified using Equations (2.19) through (2.25) to incorporate an unsprung mass compliance model (see Table 2.3), leading to a more realistic vehicle transfer function matrix $G(s)$ as in Equation (2.25).

Identifier	M_u (unsprung)	K_t (tyre)	C_t (tyre)
Front	45 kg	250 N/mm	0.05 N-s/mm
Rear	50 kg	275 N/mm	0.06 N-s/mm

Table 2.3: Parameter values used in the unsprung mass compliance model. Note that the unsprung mass is small compared to the total sprung mass (548 kg in our case); the stiffness is large and the damping is small compared to the suspension parameters of Table 2.2. The unsprung mass values used are high for conventional wheels. These values are used for clearer demonstration later, and are representative of wheels with hub motors.

The elements of $G(s)$ are of 36th order. One of them is reproduced for illustration in Appendix A.4. Such complicated expressions can be simplified for easier use. For demonstration purpose the model order reduction of one diagonal element of $G_n(s)$,

e.g., $G_{n,11}(s)$ (for the front left wheel) will be done.

Since $G_{n,11}(s)$ is a 36$^{\text{th}}$ order transfer function, its equivalent time domain model will have 36 states, given by, $[x_1(t), \dot{x}_1(t), \ddot{x}_1(t), \ldots, x_1{}^{(36)}(t)]$. Different reduced order models were developed using Matlab's built-in function `balred`[14].

Figure 2.13 shows that a 6$^{\text{th}}$ order approximation $G_{red}(s)$ preserves the model characteristics accurately. Frequency response and time domain step-input response of reduced order $G_{red}(s)$ and full order $G_{n,11}(s)$ are compared in Figure 2.14. The match is good in the frequency range plotted (up to 100 Hz). In particular, on a logarithmic scale, differences are seen only where response itself is negligibly small.

There are three peaks in the bode plot of Figure 2.14. The first and second peaks correspond to the front and rear suspension natural frequencies (1.8 and 2.6 Hz) and the third peak represents the wheel hop frequency (10.3 Hz).

2.9 Recipe for Matlab implementation of our model

Finally, the Matlab code for simple implementation of the entire procedure for obtaining the generalized quarter car model, beginning from the original Laplace transforms of Equation (2.7) is provided. Assuming lateral symmetry, only $H_1(s)$ and $H_3(s)$ need to be specified, corresponding to inputs at front left and rear left respectively. Additionally, due to reciprocal relations, in fact only the last two elements of $H_3(s)$ need to be specified[15]. In addition to these, the user must also specify baseline suspension stiffness and damping properties, in case these are to be changed later.

---

[14]The details about `balred` function are given in Appendix A.3. Note that while using `balred` the option of matching the DC gain and phase should be used.

[15]In terms of the code below, `H3(1)` is the same as `H1(3)` by symmetry of H (reciprocal theorem), and `H3(2)` is the same as `H2(3)` for the same reason. But `H2(3)` is the rear left response to front right forcing, which by lateral symmetry of the car is identical to rear right response to front left forcing, namely `H1(4)`.
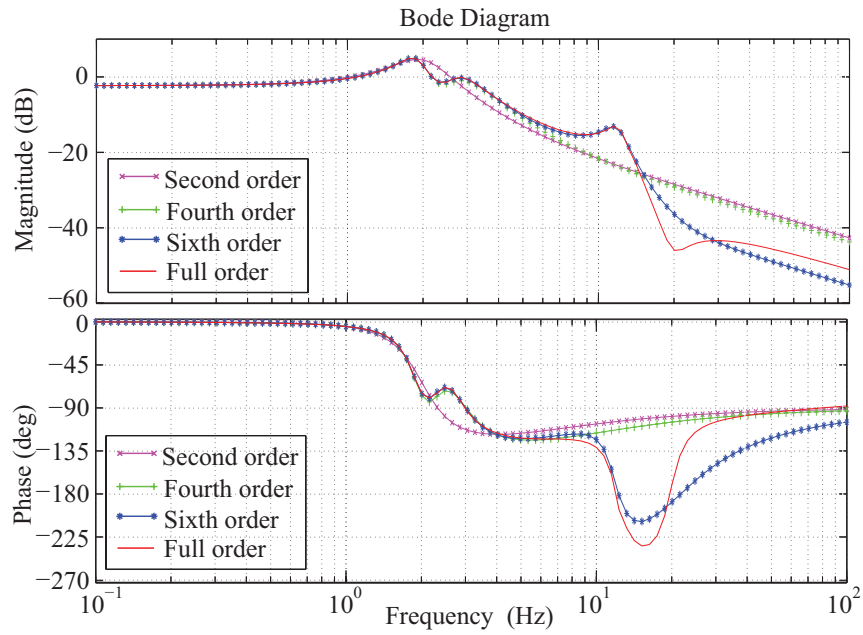
Figure 2.13: Bode plot comparison of reduced order models against the full order model.
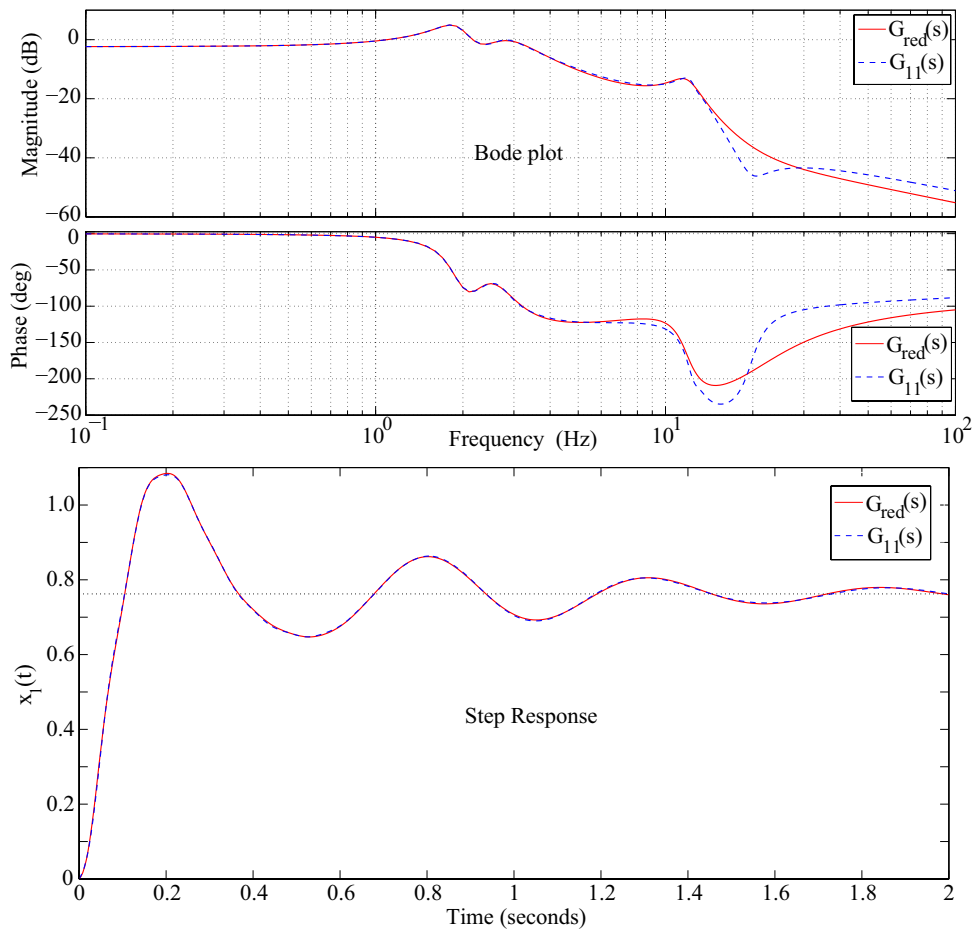
Figure 2.14: Comparison of frequency domain response (Bode plot: top) and time domain response (step response: bottom) of the reduced order $G_{red}(s)$ (solid) and the original $G_{11}(s)$ (dashed) transfer function model.

41

Given the above information, the following Matlab code uses new suspension stiffness and damping properties, unsprung mass and tyre compliance properties (stiffness and damping), as well as the desired order of the final reduced order model. The code returns the reduced order model $G_{red}(s)$; compares the frequency response (Bode plot) and the time domain step response of $G_{red}(s)$ with the original $G_{11}(s)$ to help the user decide if a higher order approximation is needed. The user can change suspension properties at will and can simulate response to other excitations beyond a simple step input, if desired.

The transparent algorithmic approach for obtaining the above approximation to the quarter car response, accounting for vehicle flexibility and unsprung mass as well as other wheel effects, is the main contribution of this chapter.

Matlab code

```
% Declare 's' to be symbolic (Note: with s symbolic, we can define
% quantities like 0.2(s-1)/(s+3), save them, load them, etc.)

syms s

% Load 4x1 transfer function matrices H1(s) and H3(s) respectively

load H1.mat; load H3.mat;

% Assemble H(s):
H = [H1(1) H1(2) H3(1) H1(4);
     H1(2) H1(1) H3(2) H1(3);
     H1(3) H1(4) H3(3) H3(4);
     H1(4) H1(3) H3(4) H3(3)];

% Enter baseline (old) suspension properties (Table 2)
K_f = 25; K_r = 30; C_f = 0.5; C_r = 0.75;

% Diagonal old suspension property matrix Do(s)
Do = diag([K_f+C_f*s; K_f+C_f*s; K_r+C_r*s; K_r+C_r*s]);

% Modifications begin (change below as needed)
% Input new suspension properties (Table 2)
```

```matlab
K_fn = 23.6; K_rn = 34.9; C_fn =.62; C_rn =.76;

% Diagonal new suspension property matrix Dn(s)
Dn = diag([K_fn+C_fn*s; K_fn+C_fn*s; K_rn+C_rn*s; K_rn+C_rn*s]);

% Obtaining modified transfer function matrix Hn(s) (Eq. 18)
Hn = ((H^-1-Do+Dn)^-1)*Dn;

% Input unsprung mass model parameters
M_uf = 45; M_ur = 50;

% Input tyre stiffness and damping
K_tf = 250; C_tf = 0.05; K_tr = 275; C_tr = 0.06;

% Assembling the diagonal unsprung mass matrix
M_unsp = diag([M_uf, M_uf, M_ur, M_ur]);

% Diagonal tyre compliance matrix Dt(s)
Dt = diag([K_tf+C_tf*s; K_tf+C_tf*s; K_tr+C_tr*s; K_tr+C_tr*s]);

% Obtaining A(s) and B(s) as defined in Equation (23)
C = M_unsp*s^2+ Dn + Dt; % Intermediate calculation quantity
A = C^-1*Dn; B = -C^-1*Dt;

% Obtaining the final transfer function matrix G(s) (Eq. 25)
G = (A-Hn^-1)^-1*B;

% Reducing order of G_11(s) for excitation only at front left wheel
[Num, Den] = numden(G(1,1));
N1 = double(coeffs(Num)); N = flipud(N1);
D1 = double(coeffs(Den)); D = flipud(D1);

% Building the transfer function from num and den coeffs
G_11 = tf(N,D);

% Defining balred options
opt = balredOptions('StateElimMethod','MatchDC');

% Input the desired reduced model order
n=6;

% Obtaining reduced order transfer function G_red(s)
G_red = balred(G_11,n,opt);
```

```
% Extracting reduced order transfer function coefficients
[N_red, D_red] = tfdata(G_red,'vec');

% Dropping 6th order numerator term to obtain a strictly proper TF
N_red = N_red(2:end); G_red = tf(N_red, D_red);

% Comparing the bode plots and the step response
figure(1) bode(G_red,'r',G_11,'--');
figure(2) step(G_red,'r',G_11,'--',2)
```

The above Matlab code takes only a few seconds to run on an ordinary desktop PC. It enables easy parametric studies. Two potential applications of our model will be discussed in the next section.

2.10 Applications of our model

The first is a study of the effect of suspension parameters and second involves wheel hop.

2.10.1 Parametric study of suspension

Here we consider the effects of varying three different parameters.

Front stiffness

The front suspension stiffness is increased by 25 and then 50 percent from its baseline value $K_f^n = 23.6$ N/mm (Table 2.2). The corresponding frequency and time domain responses are compared in Figure 2.15.

As the suspension stiffness increases, the peak overshoot in the unit step response increases because of the reduction in effective damping. More interestingly, note that the steady state displacement changes slightly as well. In all three cases considered, the steady state displacement is close to 0.8. For a quarter car model, the steady
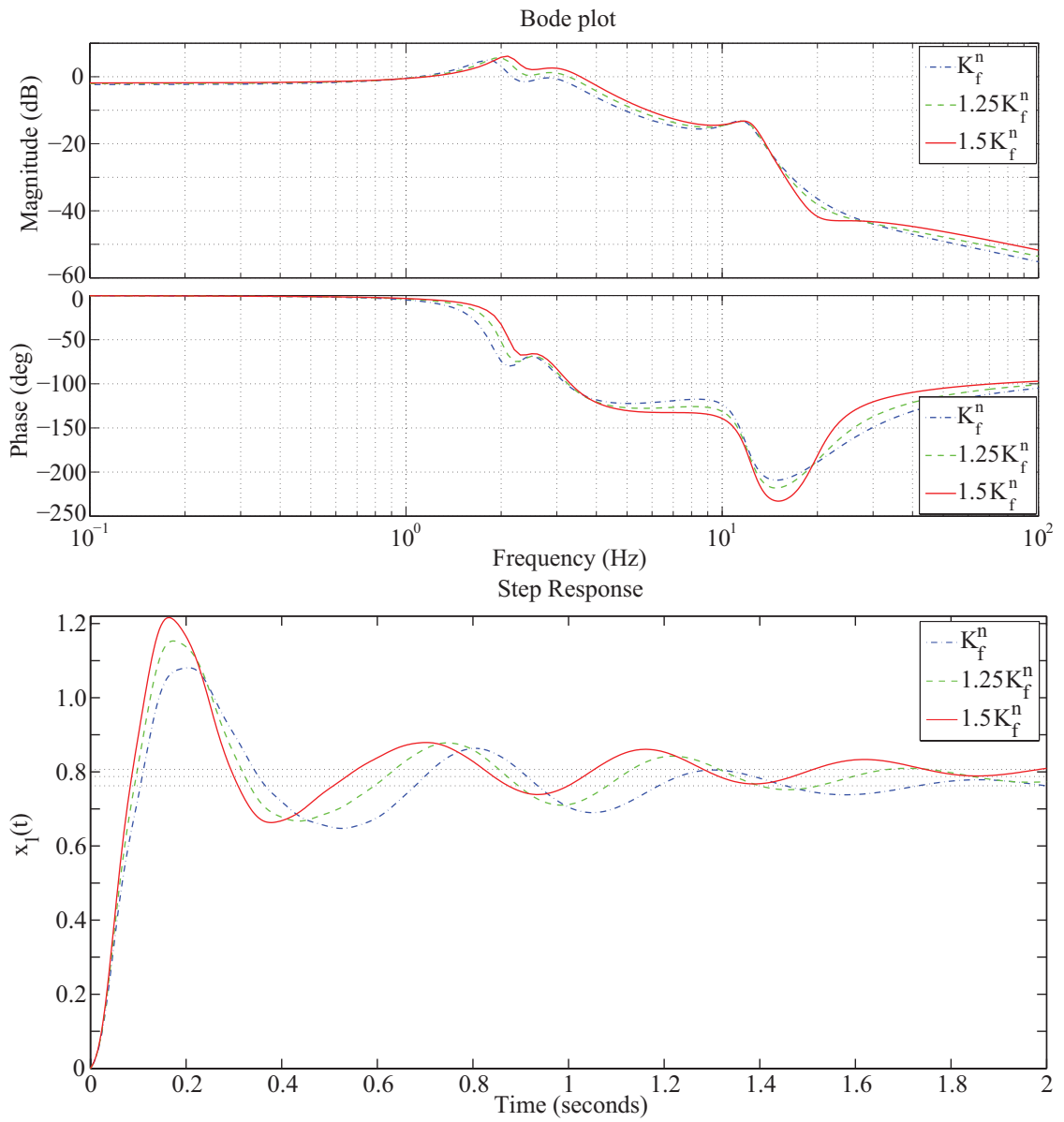
Figure 2.15: Comparison of frequency domain response (Bode plot: top) and time domain response (step response: bottom) for different values of front suspension stiffness.

state displacement in response to a unit step displacement input is unity independent of the stiffness. The difference from unity is a strictly an other-wheel effect.

Front damping
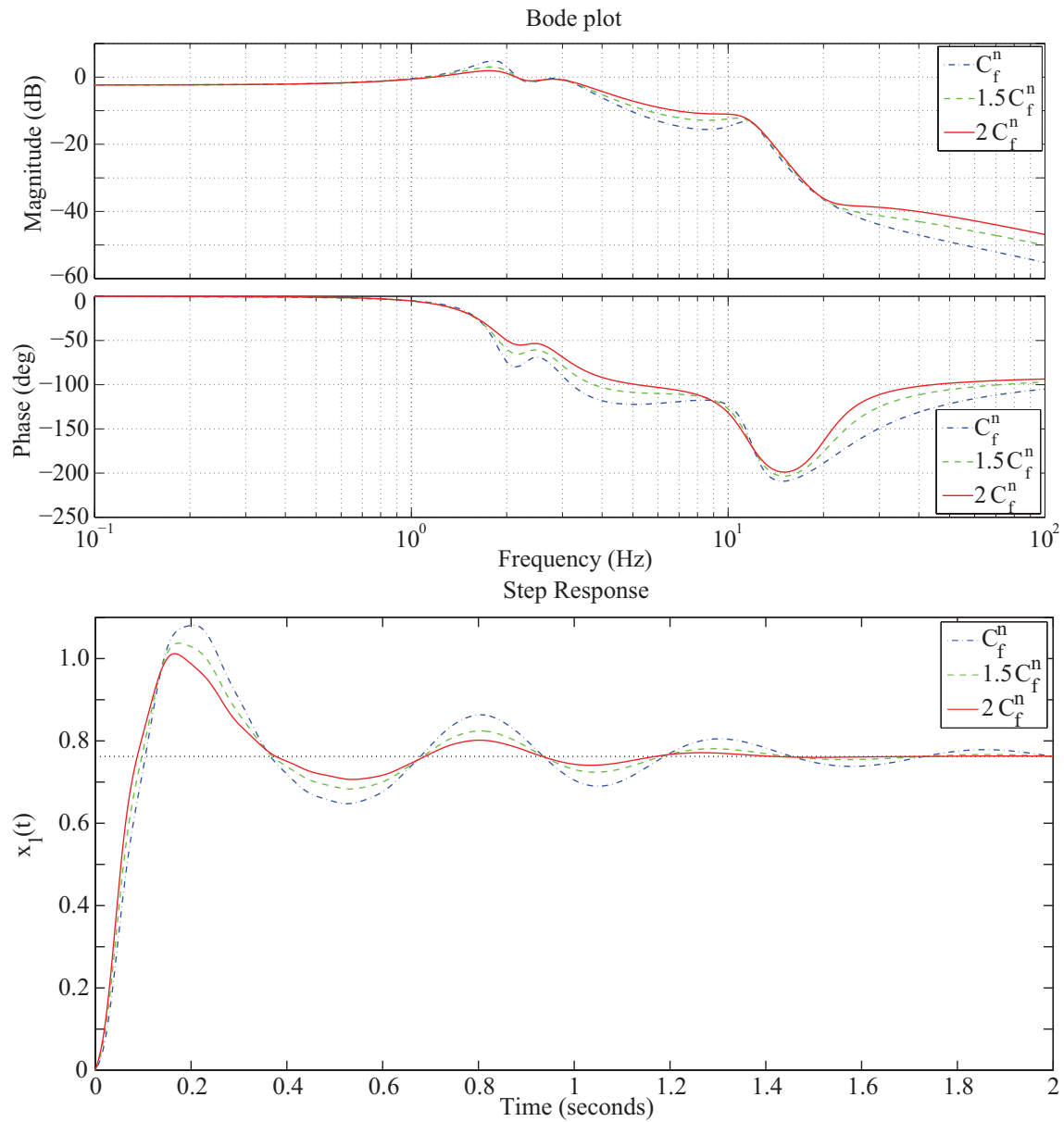
Figure 2.16: Comparison of frequency domain response (Bode plot: top) and time domain response (step response: bottom) for different levels of front suspension damping.

The front suspension damping coefficient is increased by 50 and then 100 percent

from its baseline value $C_f^n = 0.62$ N-s/mm (Table 2.2). The corresponding frequency and time domain responses are compared in Figure 2.16. With increase in damping, the resonant peak in the Bode plot gets suppressed, and transients in the step response die out faster, as expected.

Rear damping

Finally, the rear suspension damping coefficient is increased by 50 and then 100 percent from its baseline value $C_r^n = 0.76$ N-s/mm (see Table 2.2). The corresponding frequency and time domain responses are compared in Figure 2.17.

As damping increases, the second resonant peak in the Bode plot gets suppressed and the step response shows small changes as well.

This is again because of the other-wheel effects, which are not observed in a usual quarter car model.

Note also that there is no change in the steady state displacement due to changes in damping: this shows that these automated approximation methods above retain the "DC gain" behavior correctly.
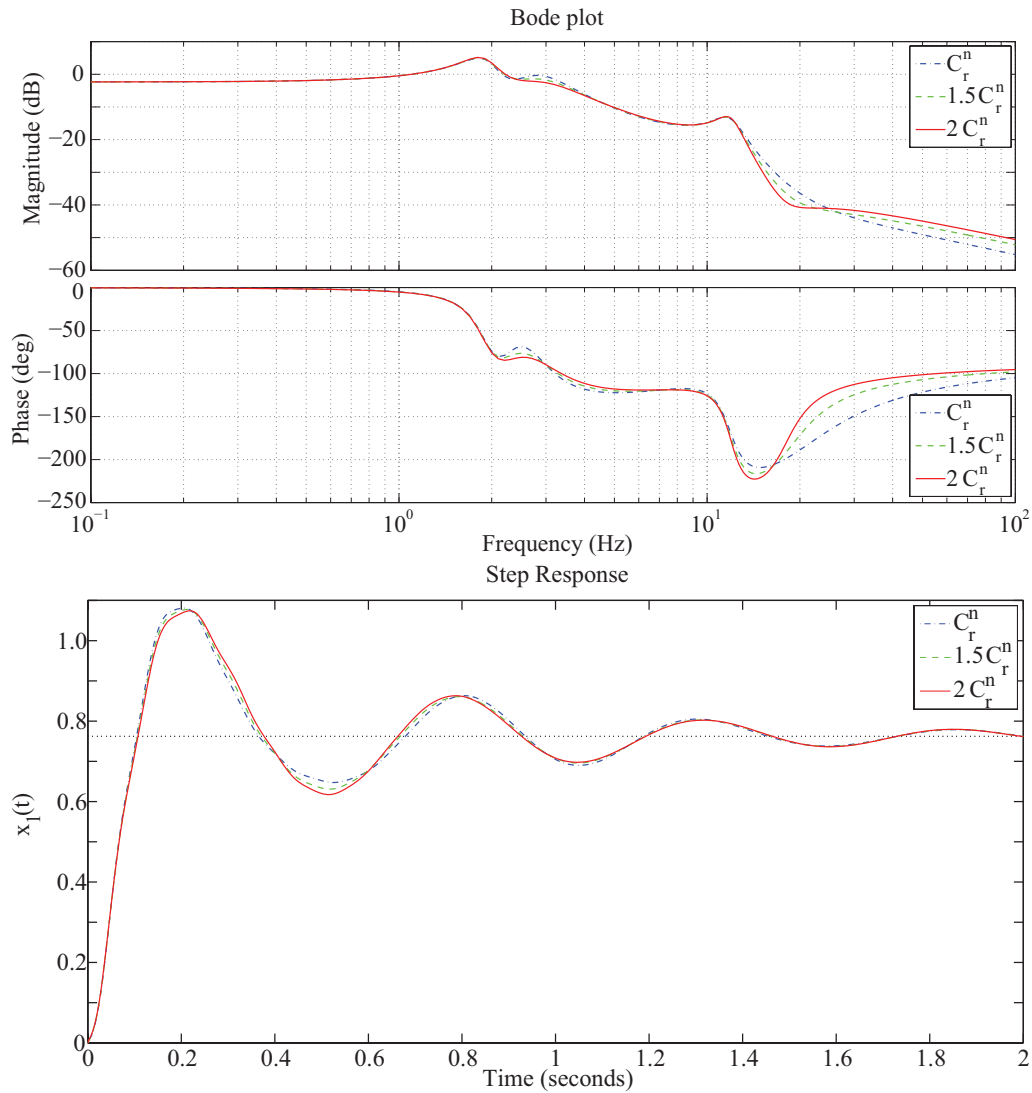
Figure 2.17: Comparison of frequency domain response (Bode plot: top) and time domain response (step response: bottom) for different values of rear suspension damping coefficients.

2.10.2 Effect of wheel hop

Wheel hop is a strong vertical oscillation of the wheels of a car, i.e., a response dominated by motion of the unsprung mass. The particular frequency at which wheel hop may be dominant depends on suspension parameters and unsprung mass but not significantly on vehicle mass. Here the effect of varying the unsprung mass

is examined.

The unsprung mass is generally much smaller than the sprung mass, so in a simplified quarter car analysis the sprung mass is held stationary while estimating the wheel hop frequency [39] (see Figure 2.18).
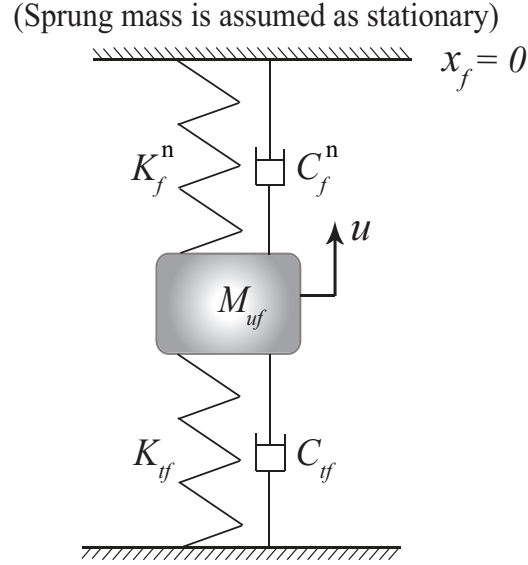
Figure 2.18: Demonstration of wheel hop.

Mimicking that approach in this system, for the front left wheel, the total restoring stiffness is $K_{tf} + K_f^{\mathrm{n}}$, where the tyre stiffness K_{tf} is usually much larger than the suspension stiffness K_f^{n}. In this way, an approximate equation of motion for the free vibration of the front wheel assembly is

$$M_{uf}\,\ddot{u} + (C_{tf} + C_f^{\mathrm{n}})\dot{u} + (K_{tf} + K_f^{\mathrm{n}})u = 0, \qquad (2.26)$$

where u is the corresponding unsprung mass displacement.

The wheel hop frequency is thus estimated to be

$$\omega_n \approx \frac{1}{2\pi}\sqrt{\frac{K_{tf} + K_f^{\mathrm{n}}}{M_{uf}}}. \qquad (2.27)$$

The FOX vehicle that motivates this numerical example is equipped with in-hub wheel motors (see Figure 2.19), and so the unsprung mass is a bit higher than for conventional wheels [16]

Figure 2.19: The vehicle is equipped with Kelly 72V - 7KW wheel hub motors (left) weighing 46 kg each which leads to an overall front and rear unsprung mass of 60 kg and 65 kg respectively (see Table 2.3). The hub motor assembly on one of the wheels is shown on the right. Image source: Kelly controls LLC [40].

We now study the effect of varying the unsprung mass. Results are given in Table 2.4 and Figure 2.20.

Unsprung mass M_{uf}	Quarter car model (Equation (2.27))	Our model (From poles of $G_{red}(s)$)
33.75 kg (75% of baseline)	14.3 Hz	13.2 Hz
45 kg (baseline)	12.4 Hz	11.8 Hz
56.25 kg (125% of baseline)	11.1 Hz	10.9 Hz

Table 2.4: Comparison of wheel hop frequencies estimated from Equation (2.27) and obtained from our model $G_{red}(s)$.

---

[16]Naturally, the higher unsprung mass due to wheel hub motors can affect the dynamics, but our procedure remains unaffected.
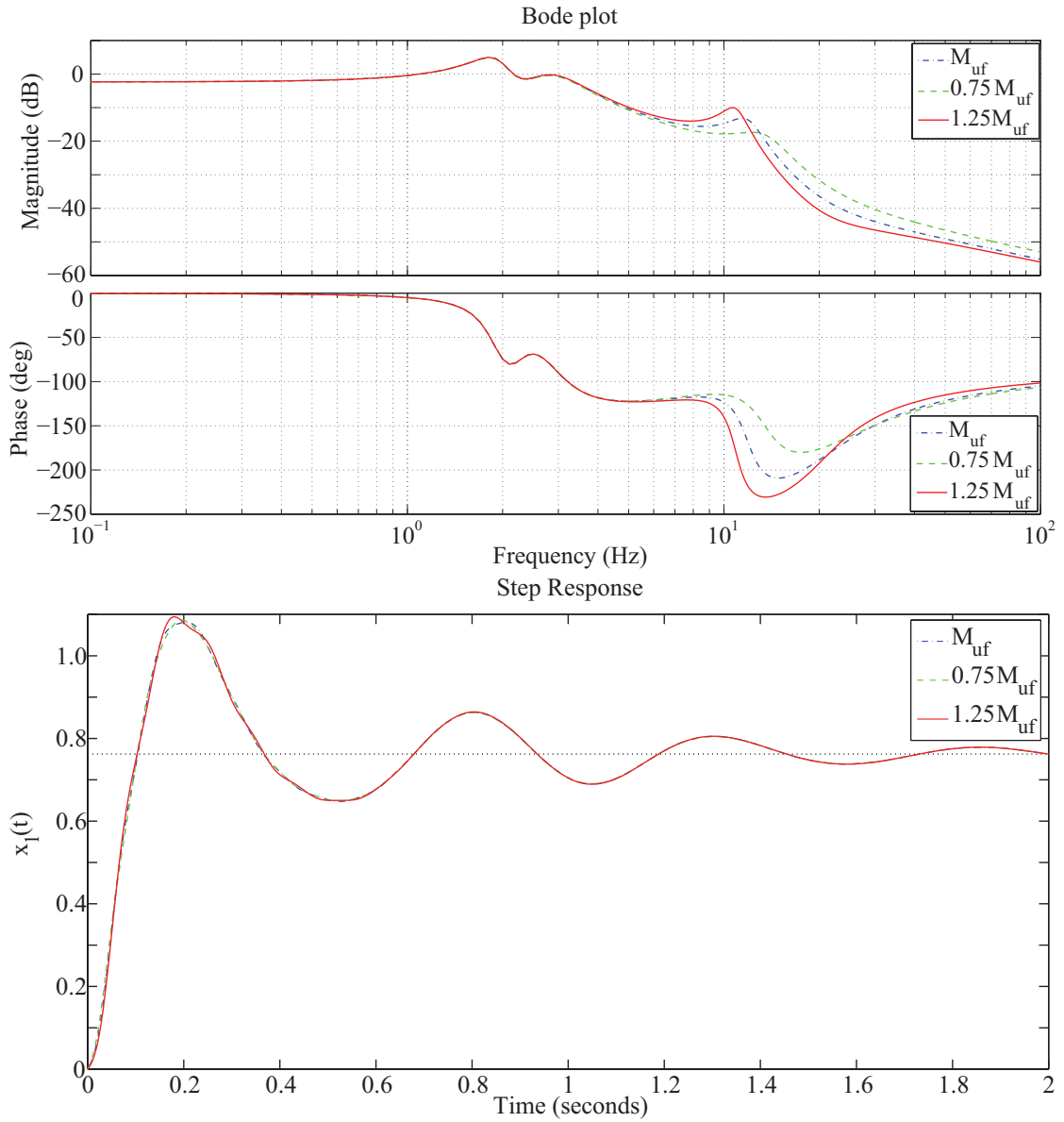
Figure 2.20: Comparison of frequency domain response (Bode plot: top) and time domain response (step response: bottom) for different values of the unsprung mass.

It was observed that in each case, the actual frequency corresponding to poles of $G_{red}(s)$ is slightly lower than the frequency estimated using Equation (2.27). The actual poles are expected to be slightly lower because of both damping as well as small motions of the sprung mass. Thus, it is seen that wheel hop effects on the body motion are also captured easily by the present approach.

2.11 Further comparison of our model with the quarter car model

Finally, the unit step response of this model is compared with that of a quarter car model (see Figure 2.21).
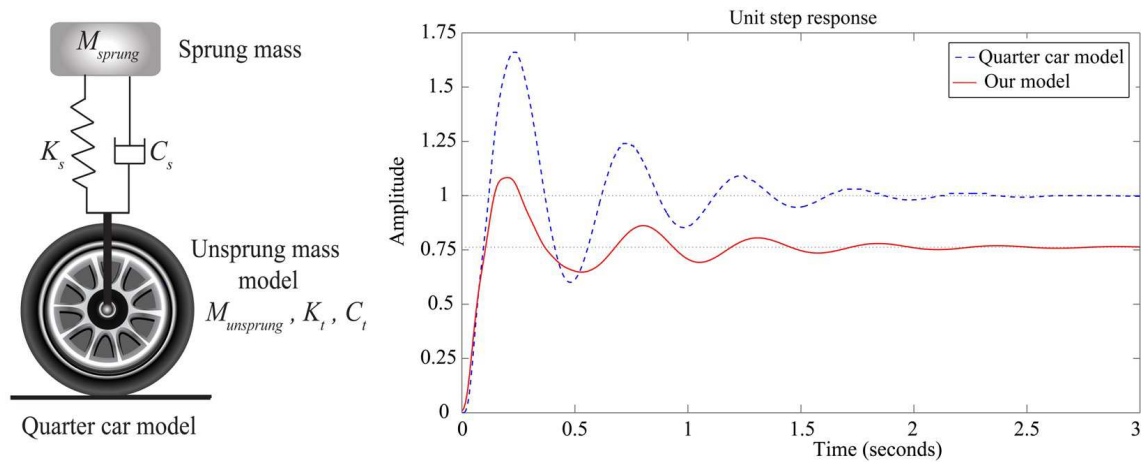
Figure 2.21: Comparison of displacements obtained from usual quarter car model and our model in response to a unit step displacement input at wheel contact point C_1. Both the damping level and steady state response are affected by nonlocal stiffness and dissipation that is captured well by our approach.

Note here that the value of steady state displacement of a quarter car model for a unit step displacement input will necessarily be unity. In the proposed model the difference observed from unity is strictly due to other-wheel effects[17]. The front left suspension to body point B_1's displacement $x_1(t)$ is used for comparison. The parameters for building the quarter car model are reported in Table 2.5. The vehicle total sprung mass is 548 kg. There is almost equal mass distribution between front and rear wheels and the vehicle is assumed to be symmetric about its center line.

---

[17]When the spatial frequencies are low (long wavelengths on the road), the 3 wheels fixed and one wheel forced assumption will not be valid and the standard quarter car model will be better. Our approach is better when spatial correlations are poor, and spatial wavelengths are small, like one wheel going over an isolated bump or pothole.

Therefore, the sprung mass in the quarter car model is taken to be $548/4 = 137$ kg.

M_{sprung} (kg)	$M_{unsprung}$ (kg)	K_s N/mm	K_t N/mm	C_s N-s/mm	C_t N-s/mm
137	45	23.6	250	0.62	0.05

Table 2.5: Quarter car model parameters.

2.12 Concluding remarks

The vehicle dynamics research literature includes many studies of vehicle suspensions under the quarter-car or half-car simplifications. Here, we have proposed a fairly simple way to incorporate vehicle mass, flexibility and damping effects, as well as the effects of stationary ground contacts at other wheels. In this way, our approach is of intermediate complexity, between quarter-car or half-car models on one hand and full-car models on the other. Some obvious differences between usual quarter-car model predictions and our more realistic approach can be seen easily, e.g., in unit step input responses (see Figure 2.21). An examiner of this thesis has observed that just like our 'generalized quarter car model', one could posit a 'generalized half car model' that is 2 input 2 output, but including the effect of other wheels. But this would not be quite as single input single output system, so not as compeling.

We have also provided simple Matlab code which makes it easy for a user to carry out the full range of computations, beginning with Laplace-transformed step-force input responses from two forcing locations.

In our approach the usual suspension parameters are retained as free parameters to enable semi-detailed comparative studies in the design stage. The model can also

be used for the analysis of wheel hop.

In future work, it should be possible to extend or adapt this formulation to incorporate test results in place of initial simulation results; to incorporate more sophisticated unsprung mass models; and also, if there is a need, to incorporate nonlinearities in the local-wheel suspension (where displacements are largest), while retaining linear behavior at other locations.

Chapter 3

Rationally derived models for elastomeric suspension bushings: theory and experiment

Elastomers find applications in diverse areas of vibration and noise control [41, 42], including structural vibrations [43], as seismic dampers in civil engineering [44]. They are widely used in automotive industry in powertrain mounts, exhaust hanger mountings, body and engine mounts and suspensions [13]. Particularly in suspensions these are used in shock absorber bushings, control arm bushings and bumpstops (see Figure 3.1). Therefore, accurate modeling of elastomers is necessary for reliable vehicle dynamics simulations.

In the last chapter, a model of vehicle suspensions was developed. In this chapter a frequency domain material model for automotive suspension bushings will be developed. As both the suspension and the bushing models are developed in the frequency domain, these can be assembled together to accurately predict the vehicle response to vertical disturbances.

Linear, causal, and time-invariant viscoelastic material response models are of practical interest in modeling elastomeric bushings. Many of these existing material models are empirical in nature. Empirical fits to experimental data involves several
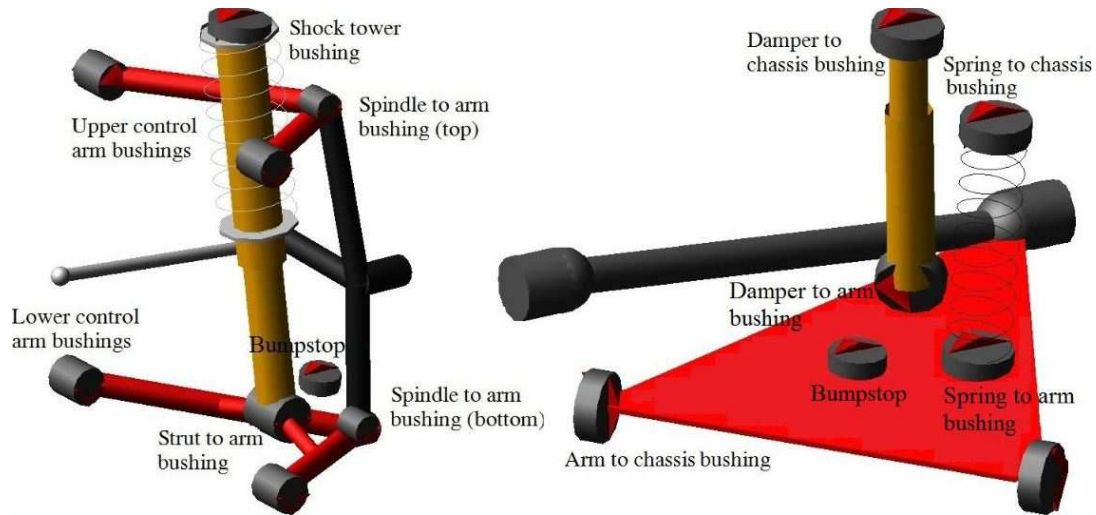
Figure 3.1: The locations of suspension bushings in a typical front and rear suspension of a passenger car.

fitted parameters which, if chosen arbitrarily, violate theoretical restrictions derived from causality, linearity, and time-invariance. Here, an asymptotic expansion for Bode's representation of the famous Kramers-Kronig relations [14, 16] is considered. In the asymptotic expansion the leading order term and one correction term has been retained. Two new mathematical forms that satisfy theoretical restrictions and also fit the experimental data well are proposed. Both forms proposed here have three free parameters each. One form has logarithms and power law terms, and is valid if the index in the power law is small. The second form has only logarithmic terms, and satisfies restrictions exactly. Both forms successfully fit our test data for four different automotive suspension bushings, in the low frequency range (1-30 Hz). The first form, with a power law, is more complicated but fits the data slightly better. Since the frequency response involves both a real and imaginary part, simultaneously fitting both parts well with merely three parameters validates the approximations proposed in this model.

3.1 Introduction

Elastomers are viscoelastic, exhibiting both elastic and damping properties, often referred to simply as dynamic properties. These dynamic properties depend on temperature and frequency. Temperature dependence is captured by the classical shift factor approach [45, 46][1].

The temperature dependence of dynamic properties are not considered here for simplicity, and the suspension bushings were tested at a controlled room temperature. For frequency dependence of dynamic properties, a complex and frequency-dependent modulus of elasticity is used [46], as in

$$M^*(\omega) = \underbrace{M_{\mathrm{d}}(\omega)}_{\text{Elastic or dynamic modulus}} + i \underbrace{M_1(\omega)}_{\text{Loss modulus}} . \tag{3.1}$$

These frequency-dependent complex moduli (dynamic modulus $M_{\mathrm{d}}(\omega)$ and loss modulus $M_1(\omega)$) fully characterize the viscoelastic material within the linear regime [47, 48].

A summary of the main approaches used for linear systems which are relevant to our work will be presented. Subsequent sections will present the experimental data, new theory, and results.

3.2 Theory

Different kinds of viscoelastic models are available in the literature. These models are broadly classified into four main categories.

---

[1]Using temperature-dependence data of 17 polymers, Williams, Landel, and Ferry derived the famous WLF equation which estimates the elastomer properties at temperatures other than those for which the material was tested using a temperature shift factor.

3.2.1 Standard Linear Solid (SLS) models

In this approach, stress-strain or force-deformation behaviors are assumed to obey differential equations of the form

$$\sum_{n=0}^{N} a_n \frac{d^n \sigma(t)}{dt^n} = \sum_{m=0}^{M} b_m \frac{d^m \varepsilon(t)}{dt^m}.$$ (3.2)

Special cases of the above are the Maxwell and the Kelvin-Voigt models, which in turn lead to some generalizations thereof (see Figure 3.2).

These generalizations seem intuitively simple, but have many fitted parameters [49]. This approach will not be pursued in this work.
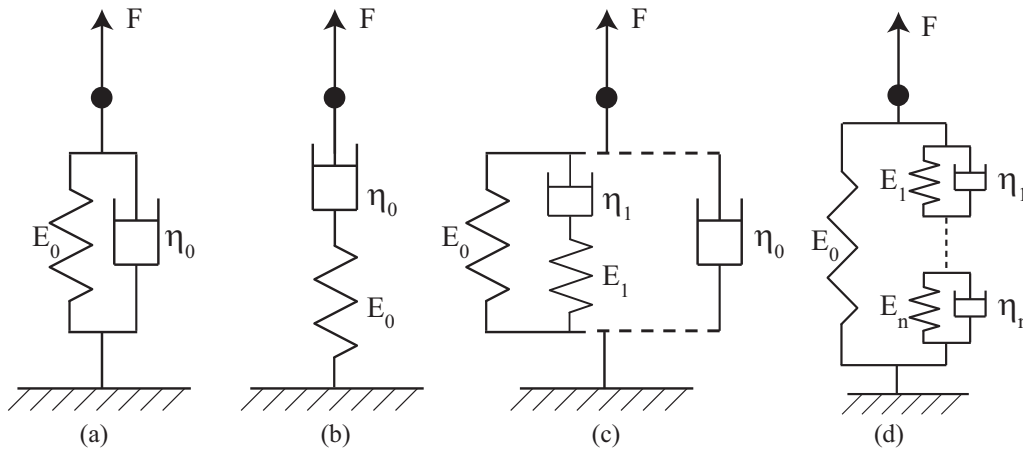
Figure 3.2: Different types of Standard linear solid models: (a) Kelvin Voigt model (b) Maxwell model (c) Generalized Maxwell model (d) Generalized Voigt model.

3.2.2 Prony series based models

These models use a series of exponentials to describe the linear viscoelastic material characteristic functions (stress relaxation and creep), as in

$$E(t) = E_\infty + \sum_{i=1}^{n} E_i \exp\left(\frac{-t}{\tau_i}\right), \tag{3.3}$$

where E_∞ = long-term modulus and τ_i = relaxation time. The parameters (Prony coefficients) in the series are fitted from relaxation or creep test data [50]. This approach requires difficult experimentation, and is not directly usable with frequency-domain test data.

3.2.3 Fractional order models

An interesting and powerful approach based on fractional calculus was proposed by Bagley and Torvik [51], wherein the regular derivatives are replaced by fractional-order differential operators D^α defined as

$$D^\alpha[\varepsilon(t)] = \frac{1}{\Gamma(1-\alpha)} \frac{d}{dt} \int_0^t \frac{\varepsilon(\tau)}{(t-\tau)^\alpha} \, d\tau, \ 0 < \alpha < 1. \tag{3.4}$$

Fractional order models have succeeded in describing the behavior of many viscoelastic materials using relatively few fitted parameters in the frequency domain [52]. A single simple equation may be enough to describe dynamic characteristics over a large range of frequencies, e.g.,

$$\sigma(t) = E_0\varepsilon(t) + E_1 D^\alpha[\varepsilon(t)]. \tag{3.5}$$

59

Taking the Fourier transform of Equation (3.5), denoted by "hats" as in $\mathcal{F}[\cdot] = \widehat{\cdot}$, a power law representation can be obtained that is easy to use in the frequency domain as,

$$\widehat{\sigma}(\omega) = E_0 \widehat{\varepsilon}(\omega) + E_1 (i\omega)^\alpha \widehat{\varepsilon}(\omega). \tag{3.6}$$

The empirical success of such power law models (and some generalizations, see [53]) is appreciable and such a power law behavior will be incorporated in the proposed model.

3.2.4 Dynamic mechanical characterization

Dynamic Mechanical Analysis (DMA) is a frequency-domain testing technique for which standard commercial equipment is available (e.g., [54]). Sinusoidal loading at a sequence of frequenci es is applied to the test specimen and the steady-state displacement amplitude and phase are recorded for each frequency. In the frequency domain, the general linear relationship can be written as (recall Equation (3.1)),

$$\widehat{\sigma}(\omega) = M^*(\omega) \, \widehat{\varepsilon}(\omega) = (M_{\mathrm{d}}(\omega) + i M_1(\omega)) \, \widehat{\varepsilon}(\omega). \tag{3.7}$$

For each individual frequency the following amplitude-phase relation may also be written:

$$\sigma(t) = \sigma_0 \sin(\omega t), \quad \varepsilon(t) = \varepsilon_0 \sin(\omega t - \delta), \tag{3.8}$$

where the phase δ as well as both σ_0 and ε_0 can be thought of as functions of frequency, depending on the specific test conditions (load controlled with σ_0 prescribed, or displacement controlled with ε_0 prescribed). Combining the above two equations,

the following condition can be deduced:

$$M_{\mathrm{d}}(\omega) = \frac{\sigma_0(\omega)}{\varepsilon_0(\omega)} \cos \delta(\omega); \qquad M_1(\omega) = \frac{\sigma_0(\omega)}{\varepsilon_0(\omega)} \sin \delta(\omega). \tag{3.9}$$

3.2.5   Transfer function in the Laplace domain

If the test specimen is linear and time invariant, and starts from zero initial conditions, then its transfer function in the Laplace domain is given by $H(s)$ in

$$L_\sigma(s) = H(s) L_\varepsilon(s), \tag{3.10}$$

where $L_\sigma(s)$ denotes the Laplace transform of $\sigma(t)$, $L_\varepsilon(s)$ denotes the Laplace transform of $\varepsilon(t)$, and s is the Laplace variable. Although $H(s)$ can be complicated, it must have *real coefficients*.

If the test specimen is subjected to sinusoidal loading, say with $\varepsilon(t)$ of the form $e^{i\omega t}$ (either real or imaginary parts can be taken later; and a similar calculation can be done if the test is load controlled), then the Laplace transform of the *steady-state* stress response is given by [55]

$$L_\sigma(s) = \frac{H(i\omega)}{s - i\omega},$$

when transient parts of the response have decayed to zero, it can be shown that consistency with Equations (3.7) through (3.9) requires

$$H(i\omega) = M_{\mathrm{d}}(\omega) + i M_1(\omega).$$

It is important to note here that the left hand side above comes from the Laplace

61

domain transfer function (and so must have *real* coefficients), and the right hand side comes from frequency domain testing.

It follows that substituting $\omega = s/i$ in the DMA test fit must necessarily yield functions of s with *real* coefficients. It is this necessary consistency condition on the DMA test fit that leads to a *theoretical* reduction in the number of fitted parameters, which will be exploited below.

3.2.6 Other required frequency-domain theory

Finally, the contributions from some classical theoretical analyses of frequency-domain or spectral methods [56, 57] are used. The use of these methods in viscoelasticity is generally attributed to Kuhn [58]. The intent of the analysis is to relate causality and dispersion (see also [59]). As discussed before the elastic and damping properties of a viscoelastic material can be characterized in the frequency domain by the complex modulus of elasticity (see Equation 3.1). The viscoelastic materials are assumed as linear for low amplitudes of excitation, moreover, they are causal in time domain (see Figure 3.3). Causality, which means that the specimen's response does not anticipate the excitation, implies the Kramers-Kronig relations, which find use in various fields like electromagnetism [14], optics [61], acoustics [62] and electronics [16]. The relations are

$$M_{\mathrm{d}}(\omega) - M_0 = \frac{2}{\pi} \int_0^\infty \frac{\omega' M_1(\omega')}{\omega^2 - \omega'^2} \, d\omega', \tag{3.11}$$

$$M_1(\omega) = -\frac{2}{\pi} \int_0^\infty \frac{\omega[M_{\mathrm{d}}(\omega') - M_0]}{\omega^2 - \omega'^2} \, d\omega', \tag{3.12}$$
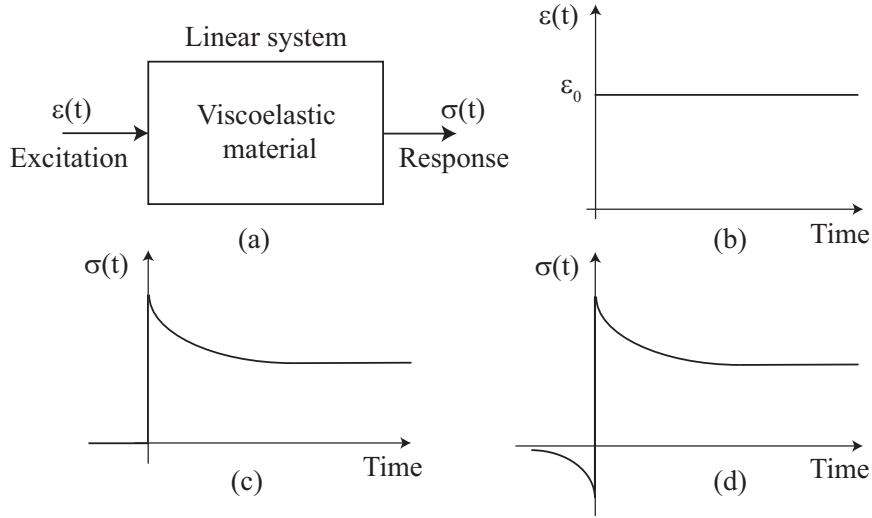
Figure 3.3: (a) Viscoelastic material treated as a linear system (b) Excitation (c) Causal response (d) Non-causal response. Image source [60].

where M_0 is the limiting value of the dynamic modulus at high ("infinite") frequency. A detailed proof of the above dispersion relations are given in Appendix B.1.

Furthermore Equation (3.12), under a change of variables with a subsequent series expansion, and under the assumption of being far from resonances and in a region of somewhat slow changes, leads to the following:

$$M_1(\omega) = \frac{\pi}{2}\omega\frac{dM_{\rm d}(\omega)}{d\omega} + \frac{\pi^3}{24}\left(\omega\frac{dM_{\rm d}(\omega)}{d\omega} + 3\omega^2\frac{d^2M_{\rm d}(\omega)}{d\omega^2} + \omega^3\frac{d^3M_{\rm d}(\omega)}{d\omega^3}\right) + \cdots \quad (3.13)$$

Some details of the derivation of Equation (3.13), with more terms in the expansion, are given in Appendix B.2. This Equation (3.13) will be used below as well.

This concludes the summary of the background theory of linear systems that is needed for the present work.

Now experimental characterization of these bushings will be discussed.

63

3.3 Experimental characterization of bushings

For material characterization, two specimens each of four different commercially available bushings are tested. These are aftermarket (non-OEM) bushings used in the suspension mountings of passenger cars presently sold in India. The makes and models of the corresponding vehicles are not mentioned because the aim is to demonstrate the test, theory, and fitting procedures only. The bushings (one each) are shown in Figure 3.4.

Figure 3.4: Suspension bushings used for dynamic mechanical characterization.

In order to test these suspension bushings, they have to be mount on the test-rig. For this various fixtures have to be made depending on the shape and size of the bushings. The details of the test rig, fixture, and the dimensional drawings of these bushings are given in Appendix B.3.

64

In actual application, these suspension bushings are loaded with the sprung mass distributed on individual suspensions. In order to roughly represent operational conditions, static preloads were applied on the bushings corresponding to the sprung mass loads they might encounter in the field (see first row of Table 3.1).

Identifier	①	②	③	④
Preload	3434 N	2943 N	3188 N	4905 N
Frequency range	1-30 Hz	1-30 Hz	1-25 Hz	1-50 Hz

Table 3.1: Preload details and frequency ranges of different suspension bushings used for testing.

For dynamic material characterization an MTS 370.10 elastomer test system was used (see Figure 3.5).

Bushing 1   Bushing 2   Bushing 3   Bushing 4
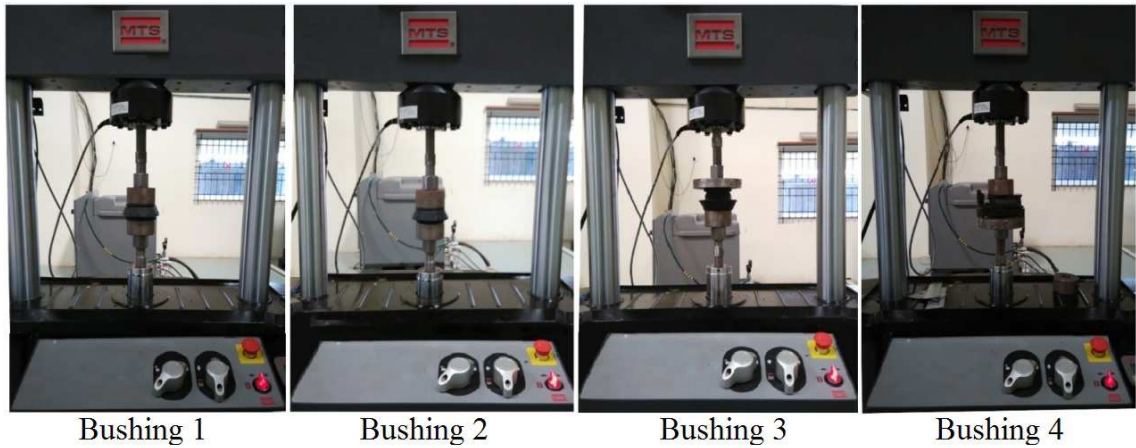
Figure 3.5: Suspension bushings characterization on MTS 370.10 elastomer test-rig at a room temperature of 20°C (Image Source: NATRiP, Indore [63]).

The test-rig was configured for elastomeric specimens in the frequency range 0.1-200 Hz, with a maximum force capacity of 15 KN.

A sinusoidally varying displacement with amplitude of 1 mm (peak to peak) was applied on the bushings. Displacement and resulting force are both recorded as time

signals. In addition, the dynamic modulus $M_d(\omega)$ and the loss modulus $M_1(\omega)$ are also directly reported by the system. Tests were performed at various frequencies with a frequency interval of 1 Hz (see second row of Table 3.1).

As indicated in section 3.2.3, simple power law models are popular for characterizing viscoelastic materials. A *pure* power law implies constant phase. In this context, the primary result from our tests was that the phase angle δ varies by several percent over the frequency range studied (see Figure 3.6), and so models that are not pure power laws have to be developed.
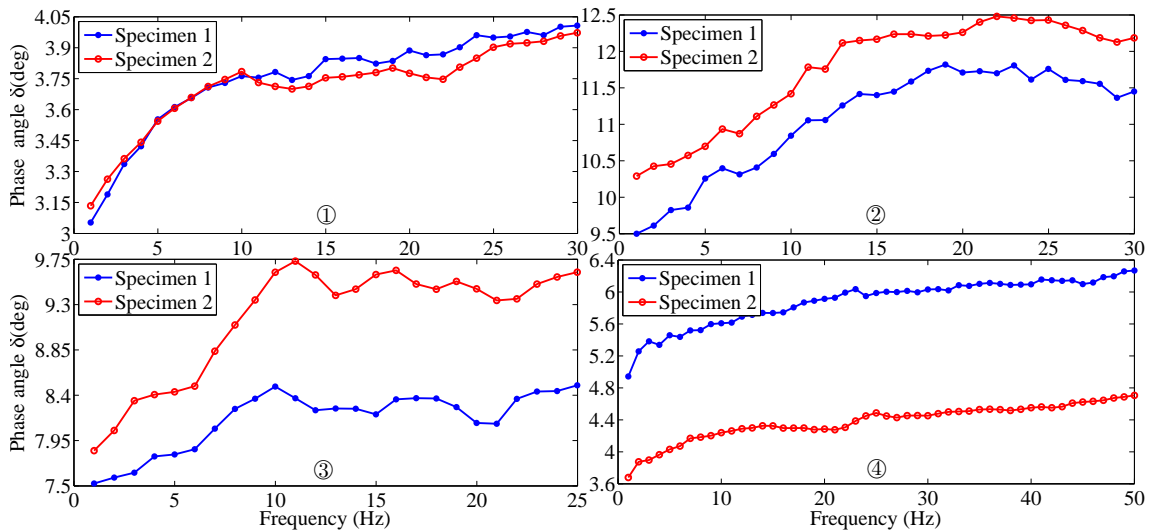
Figure 3.6: Phase angle versus frequency characteristics of the different bushings used in our experimental study. There is variability of several percent in the phase; and variability between two nominally identical bushings as well. Note that our focus here is not on manufacturing consistency. Our intent is to see how far linear theory applies to a *given* test specimen. Thus, we view these results as simply coming from eight different bushings.

New models of this type (not pure power laws), based on the background given in the introduction, are the main theoretical contribution of this work.

3.4 Modeling approach

In Equation (3.13), the leading order term is simply

$$M_1(\omega) = \frac{\pi}{2}\omega\frac{dM_{\mathrm{d}}(\omega)}{d\omega}. \tag{3.14}$$

Equation (3.14) yields

$$\tan\delta(\omega) = \eta(\omega) = \frac{\pi}{2}\frac{d[\log M_{\mathrm{d}}(\omega)]}{d[\log\omega]}. \tag{3.15}$$

The above simple result is widely quoted (e.g., [16, 60, 64]). It says a constant loss factor ($\eta = \tan\delta$) implies a straight line plot of the dynamic modulus versus frequency on log-log axes, i.e., a power law.

In the experimental data, however, it has been noted that there is some systematic variation in the phase angle δ (see Figure 3.6). To incorporate this variation in a rationally derived theory, a two-term expansion is considered as

$$M_1(\omega) = \frac{\pi}{2}\omega\frac{dM_{\mathrm{d}}(\omega)}{d\omega} + \frac{\pi^3}{24}\left(\omega\frac{dM_{\mathrm{d}}(\omega)}{d\omega} + 3\omega^2\frac{d^2 M_{\mathrm{d}}(\omega)}{d\omega^2} + \omega^3\frac{d^3 M_{\mathrm{d}}(\omega)}{d\omega^3}\right). \tag{3.16}$$

In order to fit the experimental data two different functional forms have been considered. One is a power law with logarithmic multiplying terms; the other is a polynomial on logarithmic axes. The requirements of consistency with the basic theory above will lead to restrictions on fitting parameters, thereby yielding more parsimonious models (with fewer free parameters).

3.4.1 Modified power-law model

Prompted by the equidimensional nature of Equation (3.16) a modified power law model is proposed, given by

$$M_{\mathrm{d}}(\omega) = \left(A_0 + A_1 \log \omega + A_2 (\log \omega)^2\right) \omega^\beta, \tag{3.17}$$

where A_0, A_1 and A_2 are the coefficients of a truncated logarithmic polynomial and β is a fractional power, making four fitted parameters in all. From Equation (3.16) the corresponding loss modulus $M_1(\omega)$ is obtained.

As Equation (3.16) is linear, it allows the computation of corresponding loss modulus $M_1(\omega)$ in three steps.

1. The first term, $A_0 \omega^\beta$ in Equation (3.16) gives

$$\left[\frac{1}{24}\pi\,\beta\left(12 + \pi^2\beta^2\right)\right]A_0\omega^\beta. \tag{3.18}$$

2. The second term, $(A_1 \log \omega)\,\omega^\beta$ in Equation (3.16) gives

$$\left[\frac{1}{24}\pi\left(12\,\beta + \pi^2\beta^3\right)\log\omega + \frac{1}{24}\pi\,\omega^\beta\left(12 + 3\,\pi^2\beta^2\right)\right]A_1\omega^\beta. \tag{3.19}$$

3. Finally, the third term, $(A_2(\log \omega)^2)\,\omega^\beta$ in Equation (3.16) gives

$$\left[\left(\frac{1}{2}\pi\,\beta + \frac{1}{24}\pi^3\beta^3\right)(\log\omega)^2 + \left(\frac{1}{4}\pi^3\beta^2 + \pi\right)\log\omega + \frac{1}{4}\pi^3\beta\right]A_2\omega^\beta. \tag{3.20}$$

$M_1(\omega)$ is then obtained by adding the above three terms, which are rearranged

68

as

$$M_1(\omega) = \left(B_0 + B_1 \log \omega + B_2(\log \omega)^2\right) \omega^\beta, \tag{3.21}$$

where the coefficients B_0, B_1 and B_2 are given by

$$
\begin{aligned}
B_0 &= \left(\frac{1}{2}\pi\beta + \frac{1}{24}\pi^3\beta^3\right)A_0 + \left(\frac{1}{2}\pi + \frac{1}{8}\pi^3\beta^2\right)A_1 + \left(\frac{1}{4}\pi^3\beta\right)A_2 \\
B_1 &= \left(\frac{1}{2}\pi\beta\right)A_1 + \frac{1}{24}\left(\pi^3\beta^3 + \frac{1}{4}\pi^3\beta^2 + \pi\right)A_2 \\
B_2 &= \left(\frac{1}{2}\pi\beta + \frac{1}{24}\pi^3\beta^3\right)A_2.
\end{aligned}
\tag{3.22}
$$

It is clear that, even with $M_1(\omega)$ determined as above, there are still only four fitting parameters, namely A_0, A_1, A_2, and β. Also while deriving Equation (3.16), an allowance was made for a nonzero M_0 and the causality condition was applied to $[M_\mathrm{d}(\omega') - M_0]$. Thus, M_0 remains an additional free parameter, and there are a total of five parameters to be fitted.

Using Equations (3.17) and (3.21), the complex modulus $M^*(\omega)$ is given by

$$M^*(\omega) = M_0 + \left(A_0 + A_1 \log \omega + A_2(\log \omega)^2\right) \omega^\beta + i\left(B_0 + B_1 \log \omega + B_2(\log \omega)^2\right) \omega^\beta$$

$$\tag{3.23}$$

Now the equivalence between descriptions based on Fourier and Laplace transforms is invoked. The FRF can be represented in the Laplace domain (as discussed in section 3.2.5) by substituting $\omega = \dfrac{s}{i}$, in Equation (3.23) to obtain

$$M^*\left(\frac{s}{i}\right) = M^*\left(se^{\frac{-i\pi}{2}}\right) =$$

$$
M_0 + s^\beta e^{\frac{-i\pi\beta}{2}} \left(\underbrace{\{A_2 + iB_2\}}_{\text{I}}(\log s)^2 + \underbrace{\{(A_1 + \pi B_2) + i(B_1 - \pi A_2)\}}_{\text{II}}\log s \right.
$$

$$
\left. + \underbrace{\left\{\left(A_0 - A_2\pi^2/4 + B_1\pi/2\right) + i\left(-A_1\pi/2 + B_0 - B_2\pi^2/4\right)\right\}}_{\text{III}} \right) \tag{3.24}
$$

Since the right hand side above <u>must have real coefficients</u>, the phases of each of the three terms, labelled I, II and III respectively, must be $\dfrac{\pi\beta}{2}$.

The above necessary consistency condition will limit the number of free parameters further. This consistency condition enforced for such a purpose has not been seen in any of the related literature.

Term I of Equation (3.24) gives

$$
\tan^{-1}\left(\frac{B_2}{A_2}\right) = \frac{\pi\beta}{2} \tag{3.25}
$$

Substituting the value of B_2 from Equation (3.22) in (3.25) gives

$$
\tan\frac{\pi\beta}{2} = \frac{\pi\beta}{2}\left(1 + \frac{\pi^2\beta^2}{12}\right) \tag{3.26}
$$

The right hand side above is simply the truncated Taylor series of the left hand side for small β. A small verifying calculation along similar lines using Equation (3.14) yields a correspondingly truncated version of Equation (3.26), namely

$$
\tan\frac{\pi\beta}{2} = \frac{\pi\beta}{2}. \tag{3.27}
$$

Since both conditions, Equations (3.26) and (3.27), are derived from the truncated Equations (3.16) and (3.14) respectively, these conditions are satisfied so long as β

70

is small compared to unity. Term I has nothing more to contribute[2].

Term II of Equation (3.24) gives

$$\frac{B_1 - \pi A_2}{A_1 + \pi B_2} = \frac{\pi \beta}{2}, \tag{3.28}$$

which on simplification yields

$$A_2 = \frac{2}{\pi^2 \beta} A_1. \tag{3.29}$$

Thus, the parameter A_2 is not arbitrary after all; it is known in terms of A_1.

Finally, term III of Equation (3.24) gives

$$\frac{B_0 - \frac{\pi}{2} A_1 - \frac{\pi^2}{4} B_2}{A_0 + \frac{\pi}{2} B_1 - \frac{2}{\pi^2 \beta} A_1} = \frac{\pi \beta}{2}, \tag{3.30}$$

whence

$$A_1 = \frac{4\pi^4 \beta^3}{24\, \pi^2 + 14\, \pi^4 \beta^2 - 96 + \pi^6 \beta^4} A_0, \tag{3.31}$$

showing that the parameter A_1 is also known in terms of A_0. Therefore, there remain only three fitting parameters, namely A_0, β and M_0. The modified power law model is finally given by

$$M_{\mathrm{d}}(\omega) = M_0 + \left(A_0 + A_1 \log \omega + A_2 (\log \omega)^2\right) \omega^\beta \tag{3.32}$$

$$M_1(\omega) = \left(B_0 + B_1 \log \omega + B_2 (\log \omega)^2\right) \omega^\beta, \tag{3.33}$$

where B_0, B_1 and B_2 are given by Equation (3.22), and also A_2 and A_1 are given by Equations (3.29) and (3.31) respectively.

---

[2]Note that Equation (3.27) alone might be misleading, suggesting a sequence of discrete values of β; but in conjunction with Equation (3.26) it seems clear that in fact β should be small.

It is important to note here that although there remain only three free parameters, the dependence of the final formula on these parameters is complicated and needs to be derived from theory; it cannot be guessed.

These parameters will be fitted using the dynamic and loss modulus data obtained from testing, and the results will be discussed in Section 3.5. Now a different, and somewhat simpler model will be considered.

3.4.2   Logarithmic polynomial model

In the previous section, it was concluded that for the asymptotic approximation to be valid, the fractional power β should be small. The Equation (3.25) is in fact exactly satisfied for $\beta = 0$. This case will be explored here, in the form:

$$M_{\mathrm{d}}(\omega) = A_0 + A_1 \log \omega + A_2 (\log \omega)^2. \tag{3.34}$$

Again, by linearity, the three terms of Equation (3.34) will be separated and subsequently substituted into Equation (3.16), to obtain independent contributions to the form of $M_1(\omega)$.

1. First term, A_0 drops out upon differentiation in Equation (3.16).

2. Substituting the second term, $A_1 \log \omega$, in Equation (3.16) yields $\dfrac{\pi}{2} A_1$.

3. Substituting the final term, $A_2 (\log \omega)^2$, in Equation (3.16) yields $\pi A_2 \log \omega$.

Adding up the individual contributions above gives

$$M_1(\omega) = \pi \left(\frac{A_1}{2} + A_2 \log \omega \right). \tag{3.35}$$

Notice that the dynamic modulus at infinity, namely M_0, can be included in A_0 with no consequence to obtain

$$M^*(\omega) = A_0 + A_1 \log \omega + A_2 (\log \omega)^2 + i\pi \left(\frac{A_1}{2} + A_2 \log \omega \right). \tag{3.36}$$

Again the equivalence between the frequency response and Laplace domain representations gives

$$M^*(se^{-i\frac{\pi}{2}}) = A_0 + A_1\left(\log s - i\frac{\pi}{2}\right) + A_2\left(\log s - i\frac{\pi}{2}\right)^2 + i\left(\frac{\pi}{2}A_1 + \pi A_2\left(\log s - i\frac{\pi}{2}\right)\right),$$
(3.37)

which simplifies to an expression where the coefficients are real already:

$$A_0 + A_1 \log s + A_2\left(\frac{\pi^2}{4} + (\log s)^2\right).$$
(3.38)

Thus, there are no further restrictions and the model is

$$M_{\mathrm{d}}(\omega) = A_0 + A_1 \log \omega + A_2(\log \omega)^2$$
(3.39)

$$M_1(\omega) = \pi\left(\frac{A_1}{2} + A_2 \log \omega\right),$$
(3.40)

with three fitted parameters, namely A_0, A_1 and A_2.

These parameters will also be fitted using the dynamic and loss modulus test data. Note that two models have been proposed: (a) Equations (3.32) and (3.33) with added constraints on parameters, and (b) Equations (3.39) and (3.40) with no constraints on parameters. Both models have three independent fitted parameters each. The first model is mathematically more complicated. It is not clear in advance which model will fit the data better.

3.5   Model fitting results

The model fitting results are presented here.

Both models were fitted by minimizing the sum of squares of a logarithmic error:

74

$$J = \sum_{\omega} \left[\left(\log \frac{M_\mathrm{d}(\omega)_\mathrm{model}}{M_\mathrm{d}(\omega)_\mathrm{testing}} \right)^2 + \left(\log \frac{M_1(\omega)_\mathrm{model}}{M_1(\omega)_\mathrm{testing}} \right)^2 \right], \qquad (3.41)$$

where the sum is over all frequencies for which data was collected (see Table 3.1).

The above error norm was used since the imaginary parts (M_1) are typically much smaller than the real parts (M_d), yet it is necessary to seek good representations for both of them. For minimizinbg the error norm, Matlab's built-in function `fminsearch` is used. The fitted parameters are reported in Table 3.2.

Bushing	Specimen	Modified power-law			Logarithmic polynomial		
		A_0	β	M_0	A_0	A_1	A_2
①	1	529.720	0.056	485.635	1019.674	26.861	2.625
	2	649.802	0.048	355.167	1002.370	28.931	2.304
②	1	855.702	0.090	44.132	904.701	59.552	13.658
	2	894.934	0.089	-54.369	839.987	61.474	14.078
③	1	517.930	0.060	-109.340	413.357	26.932	3.069
	2	365.390	0.078	23.210	389.852	24.116	4.086
④	1	441.464	0.060	132.586	576.690	23.094	2.758
	2	433.754	0.050	185.934	620.944	20.043	1.770

Table 3.2: Fitted parameters for both models, and all eight bushings. Note that β, the index of the power is small, as required by Equation (3.26), i.e., for the approximation to be valid. Moreover, $A_0 + M_0$ from the modified power-law model approximately equals A_0 of the logarithmic polynomial model, as expected upon comparing Equations (3.17) and (3.39) for small β.

Graphical results of model fitting for all of these bushings are shown in Figures 3.7 through 3.13. Load-deflection loops at several frequencies are also shown therein[3]. It is seen that in each case, both models fit the data well. The low frequency fit for bushing 2 is the poorest of all (see Figure 3.10), with fits at other frequencies being

---

[3] We have observed what <u>may</u> be an oscillatory behavior in the response curves, superimposed on the mean variation we have captured. We have been unable to develop a rational defensible theory for this, and have treated those fluctuations as some combination of modeling and experimental error. We have captured the mean behavior.

fairly good. The modified power law model appears slightly superior overall, though both models have the same number of fitted parameters.
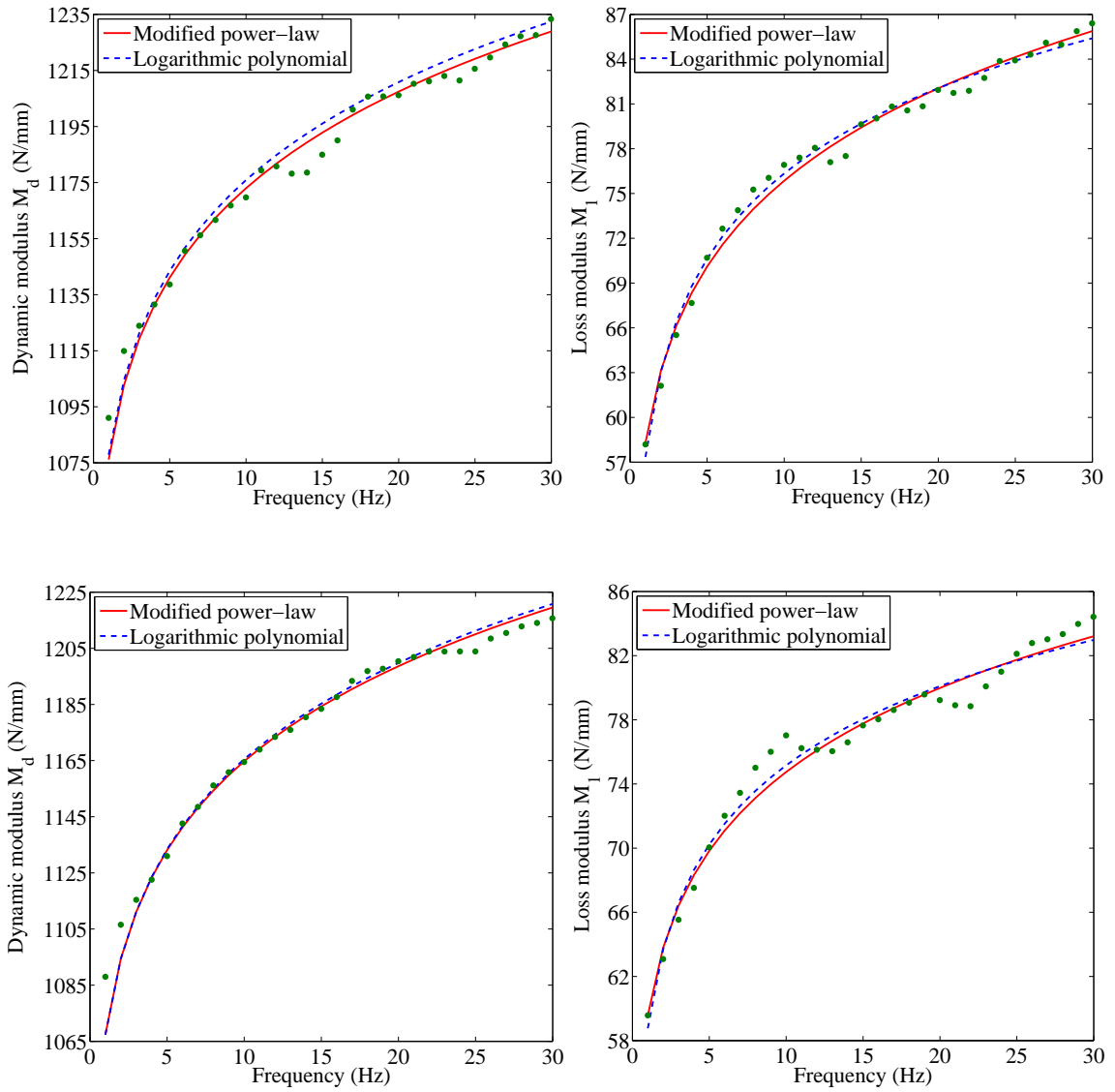
Figure 3.7: Comparison of the dynamic and the loss moduli versus frequency from the modified power law model (solid), the logarithmic polynomial model, (dashed) and experiment (dots) for first specimen (top) and second specimen (bottom) of bushing 1.
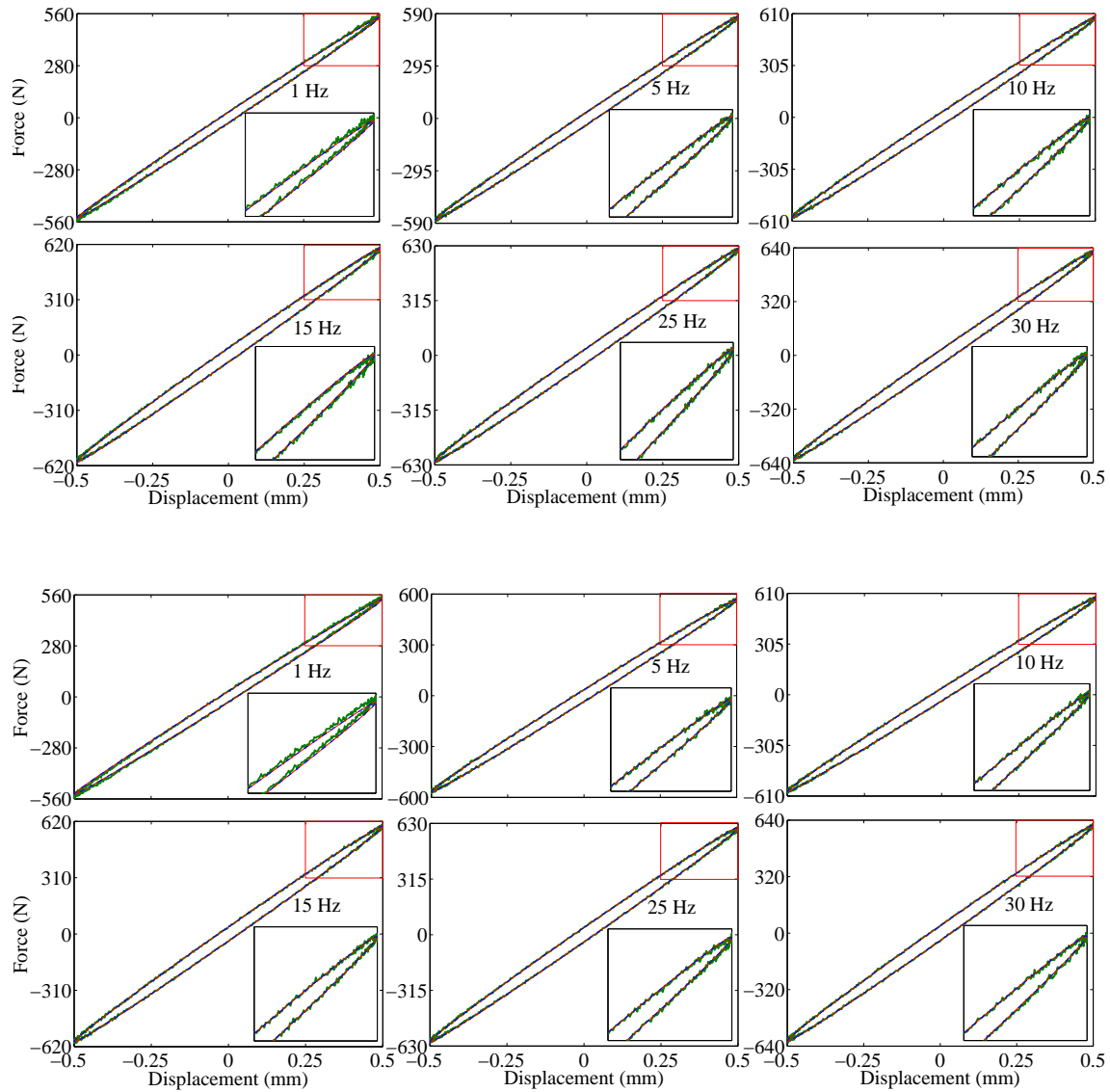
Figure 3.8: Load-displacement hysteresis loops at different frequencies: modified power law model (solid), logarithmic polynomial model (dashed), and experiment (thick), for the first specimen (top) and the second specimen (bottom) of bushing 1. The zoomed-in trajectories are also shown for each frequency. Note that the aspect ratios of these elliptical loops are similar but not identical; this is because (recall Figure 3.6) the phase $\delta(\omega)$ is roughly, but not exactly, constant. Capturing this small variation in $\delta(\omega)$ using rationally derived models with a small number of parameters was the main purpose of this work.
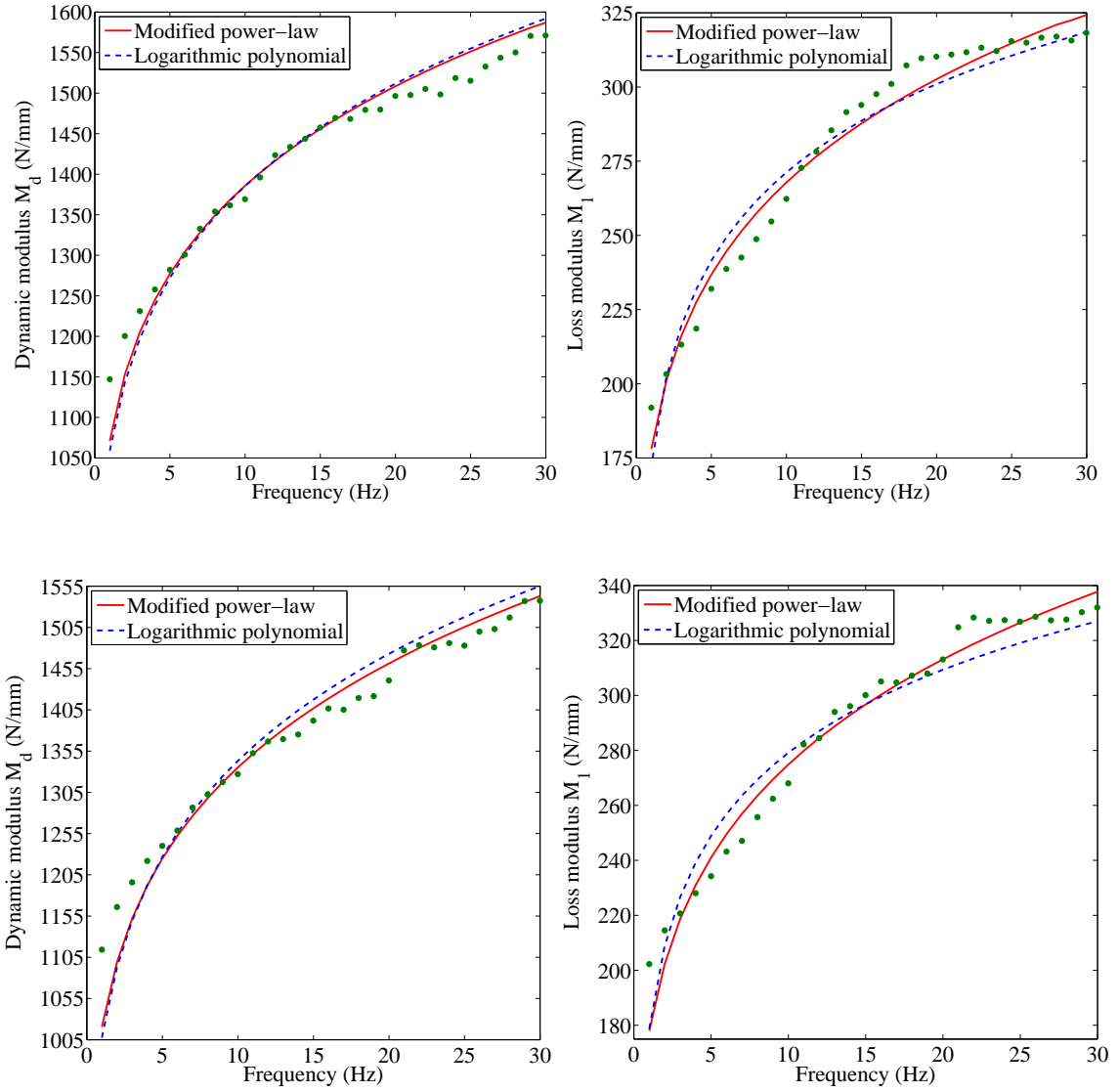
Figure 3.9: Comparison of the dynamic and the loss moduli versus frequency from the modified power law model (solid), the logarithmic polynomial model, (dashed) and experiment (dots) for first specimen (top) and second specimen (bottom) of bushing 2.
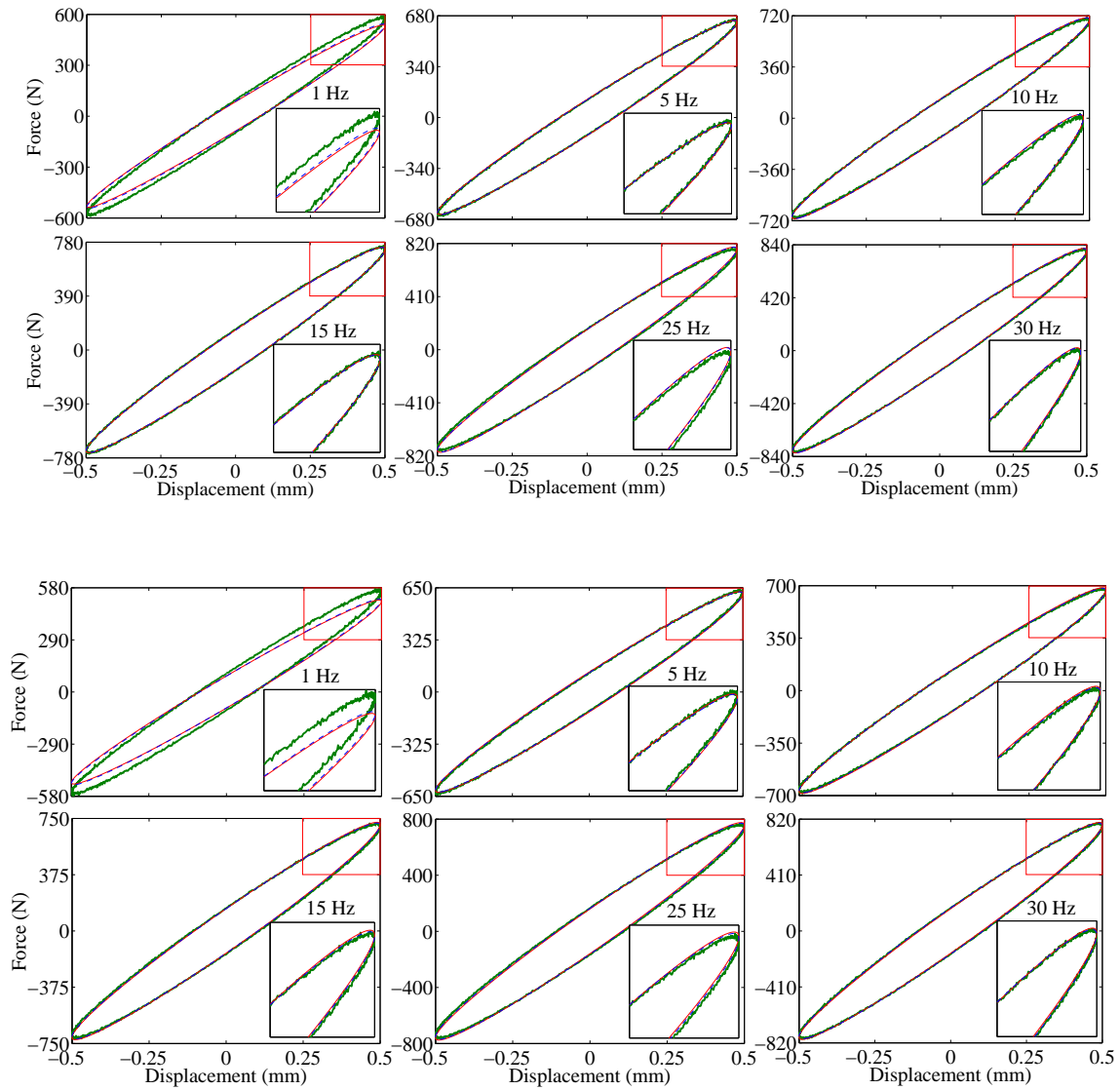
Figure 3.10: Load-displacement hysteresis loops at different frequencies: modified power law model (solid), logarithmic polynomial model (dashed), and experiment (thick), for the first specimen (top) and the second specimen (bottom) of bushing 2. The zoomed-in trajectories are also shown for each frequency.The low-frequency match is poor (poorest of all).
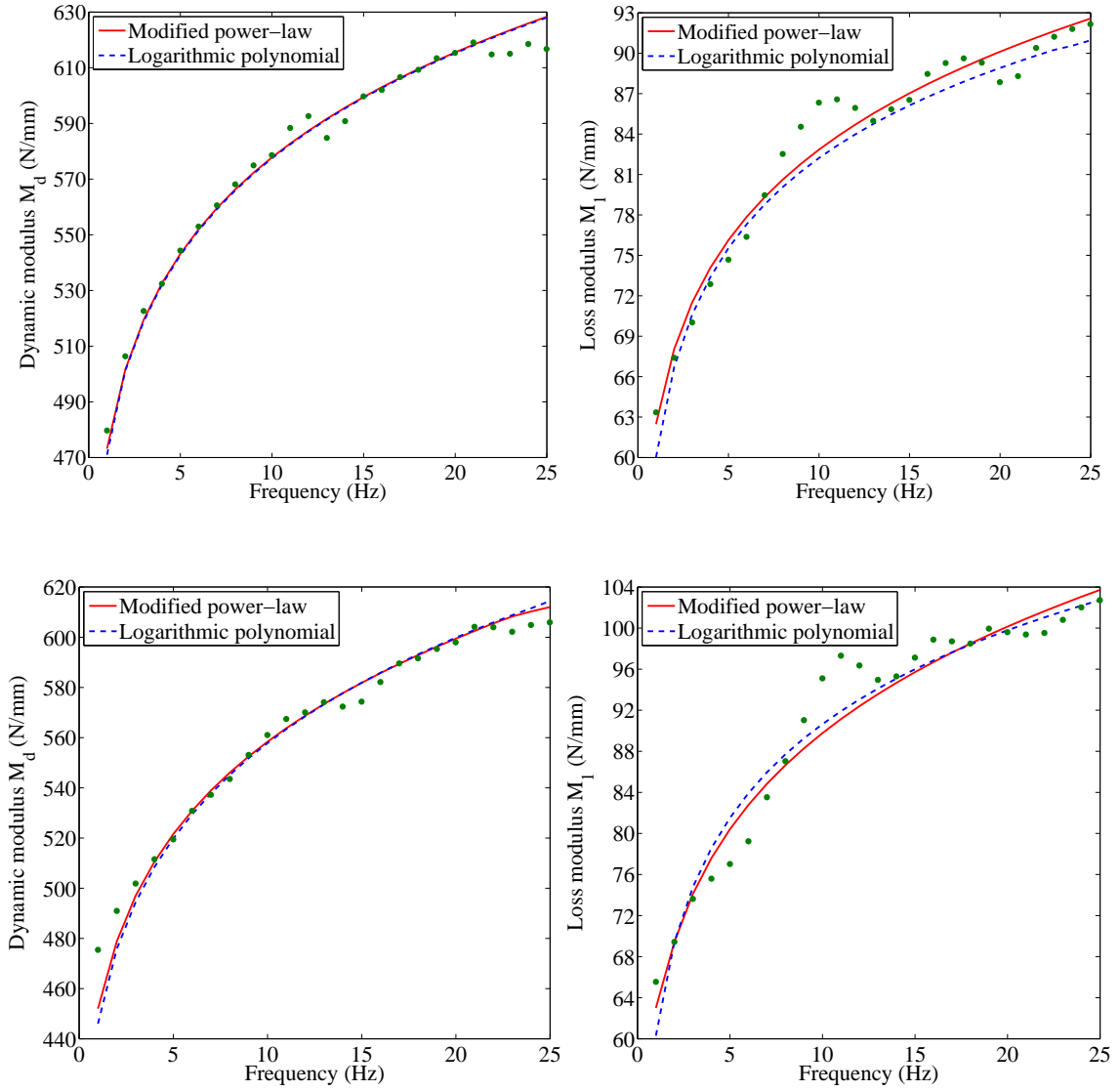
Figure 3.11: Comparison of the dynamic and the loss moduli versus frequency from the modified power law model (solid), the logarithmic polynomial model, (dashed) and experiment (dots) for first specimen (top) and second specimen (bottom) of bushing 3.
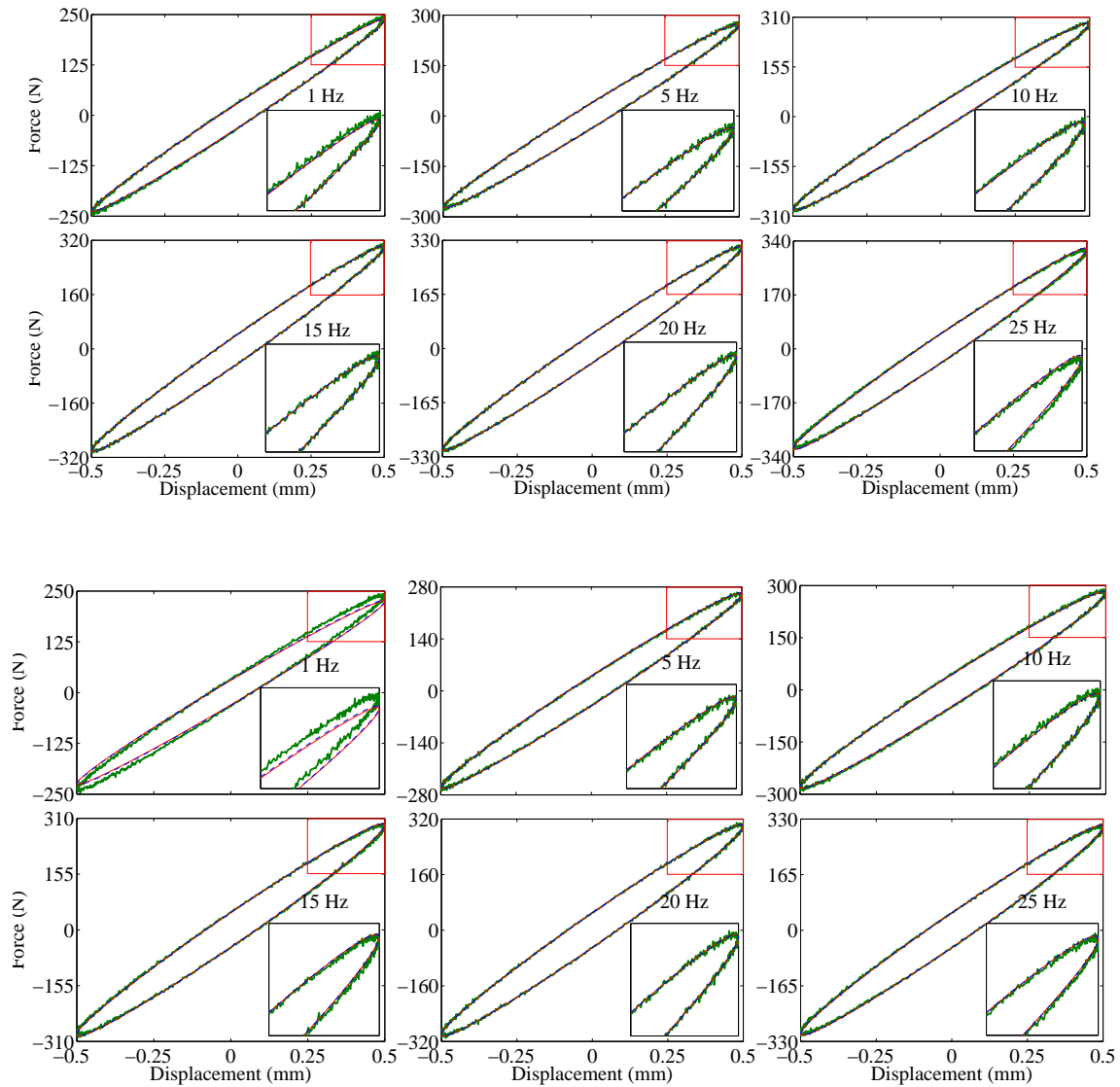
Figure 3.12: Load-displacement hysteresis loops at different frequencies: modified power law model (solid), logarithmic polynomial model (dashed), and experiment (thick), for the first specimen (top) and the second specimen (bottom) of bushing 3. The zoomed-in trajectories (red-box) are also shown for each frequency. The match is nearly perfect, with loops overlapping within plotting accuracy.
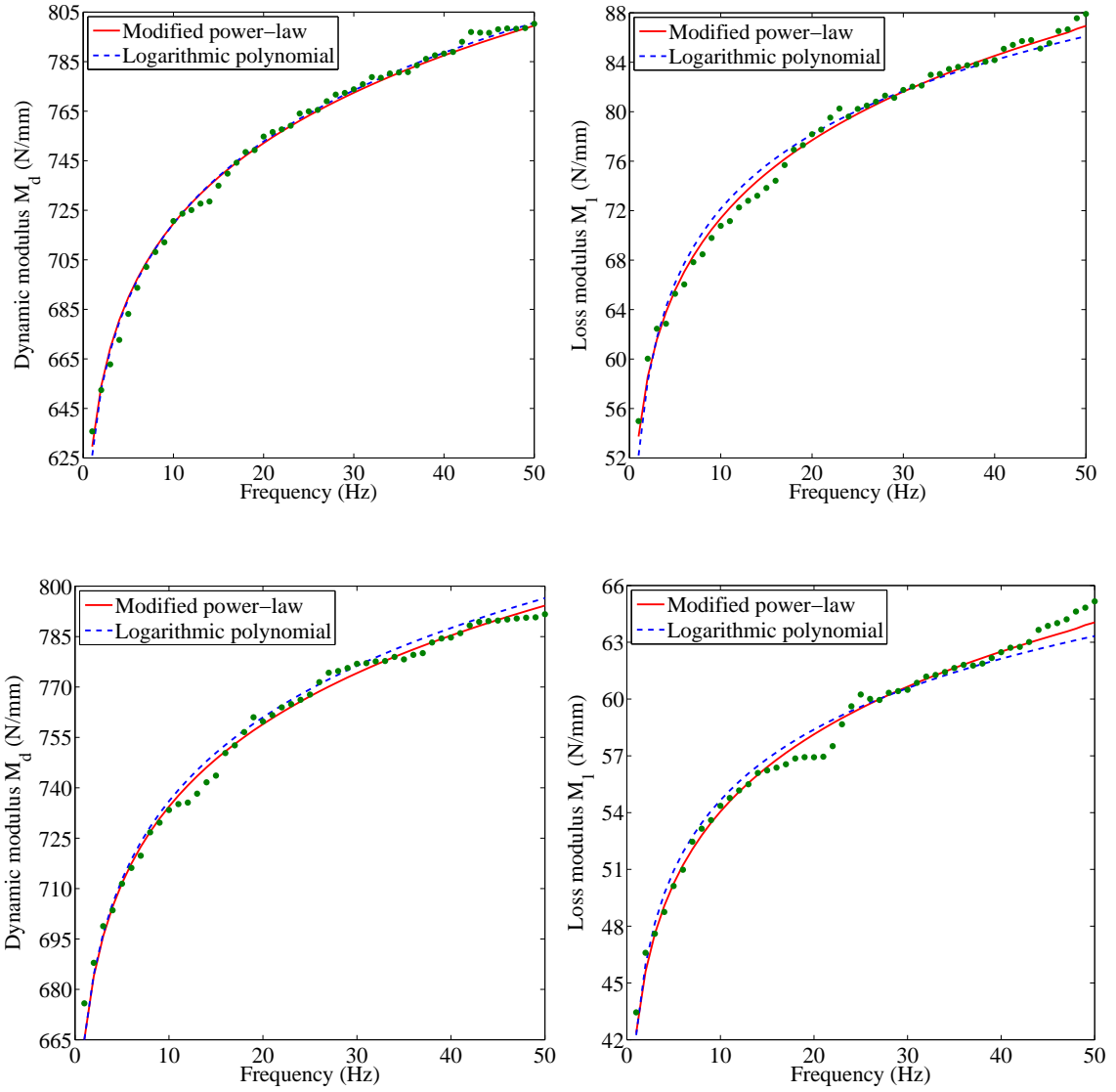
Figure 3.13: Comparison of the dynamic and the loss moduli versus frequency from the modified power law model (solid), the logarithmic polynomial model, (dashed) and experiment (dots) for first specimen (top) and second specimen (bottom) of bushing 4.
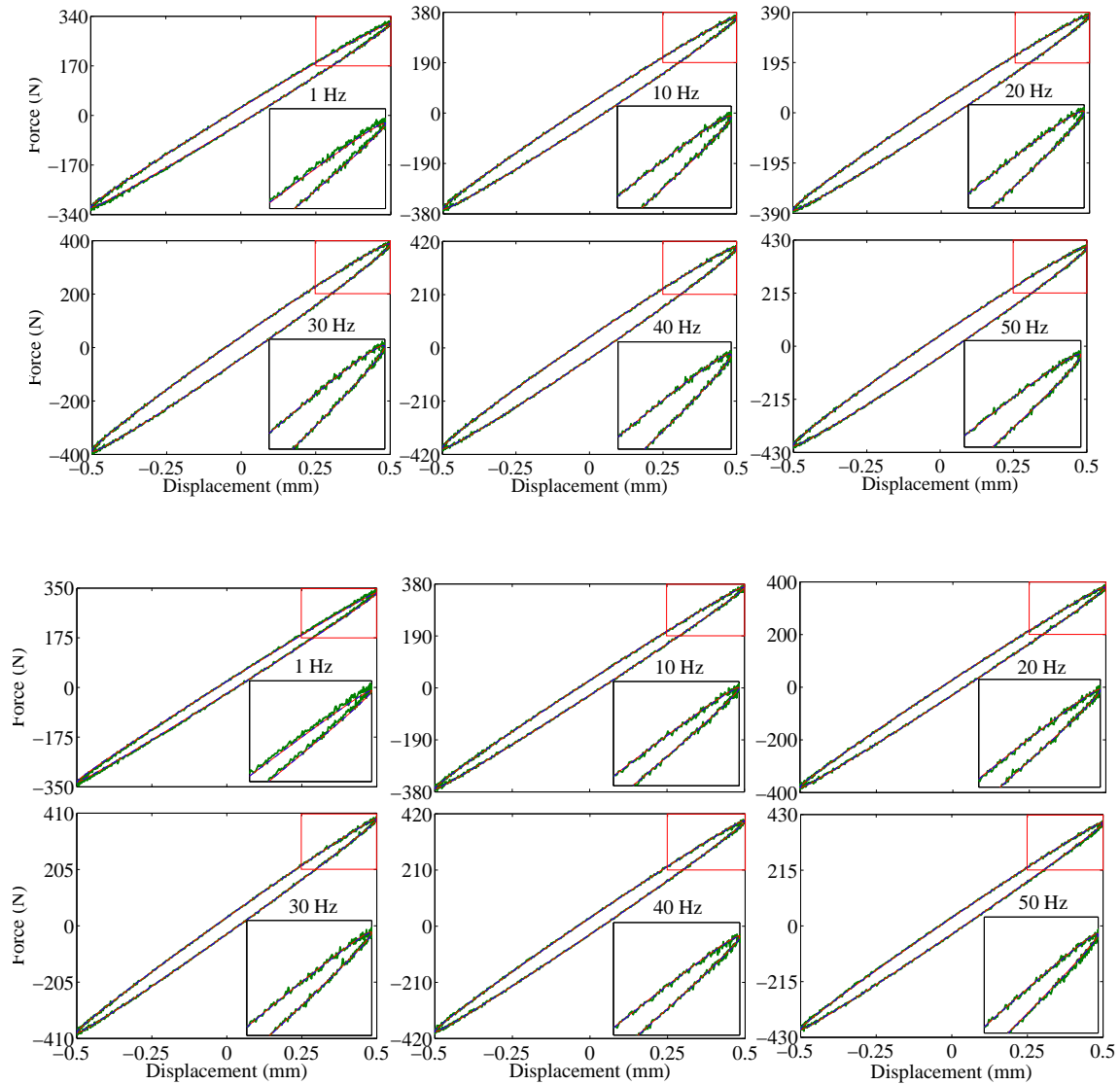
Figure 3.14: Load-displacement hysteresis loops at different frequencies: modified power law model (solid), logarithmic polynomial model (dashed), and experiment (thick), for the first specimen (top) and the second specimen (bottom) of bushing 4. The zoomed-in trajectories (red-box) are also shown for each frequency. The match is nearly perfect, with loops overlapping within plotting accuracy.

3.6 Comparison with other models: accuracy and theoretical restrictions

To model the frequency dependent properties of elastomeric vibration isolators researchers have developed lumped parameter models with fractional damping elements [65], reduced order models using Laplace domain approaches [66] and models using dynamic material characterization [67]. These models do not entirely satisfy the theoretical restrictions imposed by causality, linearity and necessity of real coefficients in Laplace domain descriptions. Moreover, the models available in the literature have many fitting parameters as opposed to a few (*three*) parameters in our model.

In order to further emphasize the merits and success of our modeling approach, we have compared it against the original fractional order Kelvin-Voigt model proposed by Bagley and Torvik (see Equation (3.6)) [51]. This fractional order model also has three fitting parameters, and satisfies some theoretical restrictions, but it does not satisfy the higher-order expansion of the Kramers-Kronig relation given by Equation (3.16); and it gives a poorer fit.

In this section we will compare fitting results from our model with that of the three parameter fractional Kelvin Voigt model which satisfies the theoretical restrictions [51], and with the four parameter improved fractional order model of [68] which is empirical and does not satisfy theoretical restrictions.

3.6.1 Fractional order Kelvin-Voigt model

The model is:

$$M_d(\omega) = E_0 + E_1 \cos\left(\frac{\alpha\pi}{2}\right)\omega^\alpha; \quad M_1(\omega) = E_1\omega^\alpha \sin\left(\frac{\alpha\pi}{2}\right). \qquad (3.42)$$

This model has three fitting parameters namely, E_0, E_1 and α.

3.6.2 Four parameter improved fractional order model

The model is:

$$M_d(\omega) = E_0 \left\{ 1 + \frac{k\left[\cos\left(\frac{\alpha\pi}{2}\right)\omega^\alpha\tau^\alpha + \omega^{2\alpha}\tau^{2\alpha}\right]}{1 + 2\cos\left(\frac{\alpha\pi}{2}\right)\omega^\alpha\tau^\alpha + \omega^{2\alpha}\tau^{2\alpha}} \right\};$$

$$M_1(\omega) = E_0 \frac{k\sin\left(\frac{\alpha\pi}{2}\right)\omega^\alpha\tau^\alpha}{1 + 2\cos\left(\frac{\alpha\pi}{2}\right)\omega^\alpha\tau^\alpha + \omega^{2\alpha}\tau^{2\alpha}} \qquad (3.43)$$

This model has four fitting parameters namely, E_0, k, τ and α.

These models are fitted to the data for the first bushing specimen, and the fitting results are compared against the modified power law model in Figure 3.15.

The fit from our rationally derived model is distinctly superior. The fitting parameters of these models and their respective logarithmic error norms J are reported in Table 3.3. The value of J is smallest for the modified power law model.
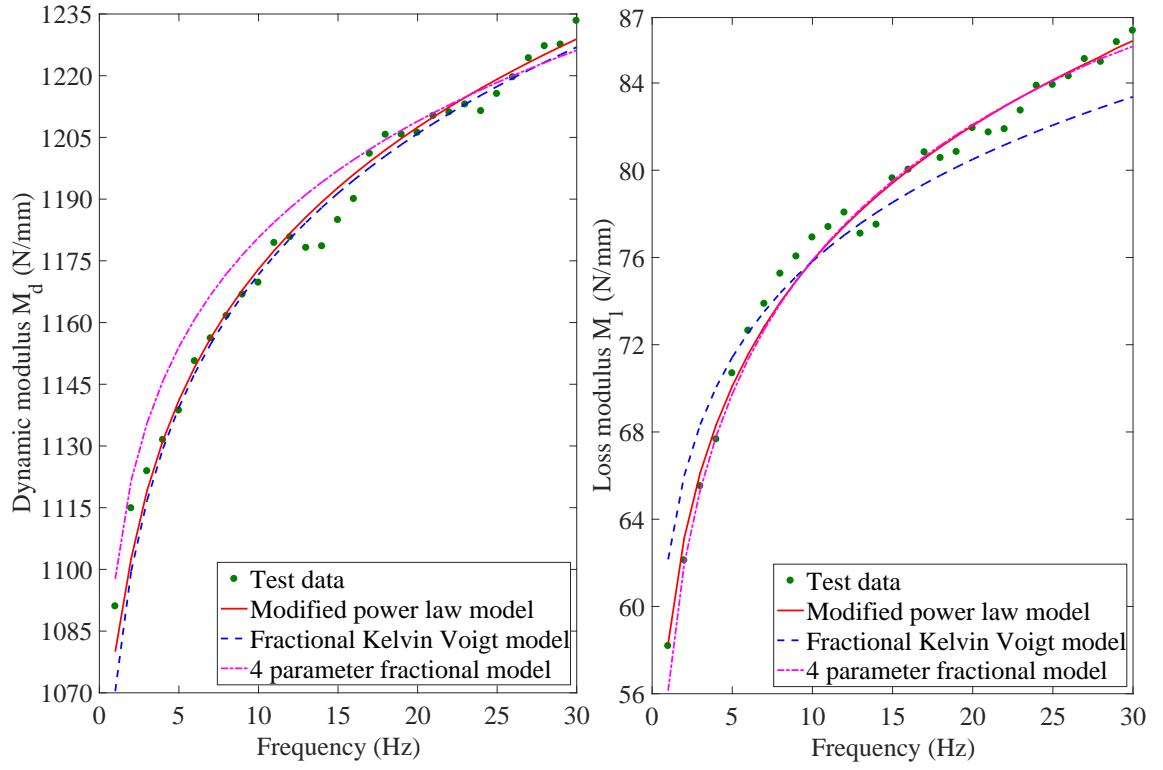
Figure 3.15: Comparison of dynamic and loss moduli versus frequency from the modified power law model (solid-red), fractional Kelvin-Voigt model (dashed-blue), 4 parameter improved fractional model (dash-dot magenta), and experiment (dots-green): first specimen of bushing ①.

Identifier	Parameters	Values	J
Modified power-law	M_0, A_0 and β	485.64, 529.72 and 0.06	0.05
Fractional Kelvin-Voigt	E_0, E_1 and α	615.72, 392.49 and 0.09	0.14
4 parameter fractional KV	E_0, k, τ and α	899.72, 1.82, 8.2e-6 and 0.19	0.07

Table 3.3: Fitting parameters of different models and their respective error norms J.

3.7 Concluding remarks

Elastomeric dampers show frequency dependent behavior. In the literature, fractional power law fits to this behavior have been proposed and found to be accurate as well. However, the *mathematical form* of the empirical fits used have not been fully consistent with linear systems theory. This work has provided a new and useful contribution in that direction. In particular, by ensuring consistency between (a) formulas based on causality, (b) an asymptotic expansion for a regime with slow variations, (c) frequency domain descriptions, and (d) the necessity of real coefficients in Laplace domain descriptions, two useful simple mathematical forms with just three fitted parameters each have been derived. Experiments with aftermarket automotive bushings have shown that both these mathematical forms can fit the data well. Of these, the modified power law model has more complicated expressions, but fits the data slightly better than does the logarithmic polynomial model.

It is acknowledged that, unlike some models which address very large frequency ranges (e.g., [53, 69]), here a more limited frequency range (about one and a half decades) is considered. However, the selected frequency range is relevant for automotive suspension dynamics simulations, and the small number of fitted parameters along with the consistency with background linear theory makes the two proposed models attractive for practical applications in vehicle dynamics.

Chapter 4

Partial validation of an Adams model for a prototype using test track data

In Chapter 2, an Adams model of a vehicle was used to develop a Laplace domain representation of a generalized quarter-car model. A practical question remains, viz, to what extent is the Adams model accurate in describing the behavior of an actual vehicle?

To that end, in this chapter, Adams model development and subsequent field testing of an instrumented vehicle will be discussed. The Adams model simulation results will in this way be partially validated against the test track data. The vehicle used here is a prototype available in Indore, and is not the vehicle of Figure 2.4, so the Adams model is to be built afresh.

For detailed validation of an Adams model for suspension design, a vehicle is generally tested on a four-post test rig and base-excitation is applied at four ground-wheel contacts. This kind of testing is expensive, time consuming, and requires both experienced personnel and specialized equipment. Sometimes, test track data is used in industry as well, but usually for durability studies, stress analysis, fatigue life estimation and other goals not related to dynamic suspension model validation.

In the research literature, as far as I know, field test data has not been used for partial validation of an Adams model as undertaken in this chapter. Since test track measurements can be easily made by using a few accelerometers and a data acquisition system, no other sophisticated equipment is needed.

The two main activities involved in this chapter, therefore, are model development and field testing. These are outlined using a flow chart in Figure 4.1. The individual parts of the flow chart are described below.

An all terrain vehicle (ATV) prototype was selected for this study (see ①). The front and rear suspensions were characterized on an MTS 850.25 damper test-rig at NATRiP (see ②). Using the measured suspension properties, a simplified Adams model of the vehicle was developed. A rigid wheel-road contact kinematic model was developed in step ③. The wheel displacements from this kinematic contact model were used as inputs to the Adams model.

Next the vehicle was driven at different speeds on specialized tracks whose displacement profiles are known. Similar to the approach in Chapter 2, eight key points were identified: four on the car body where the suspension is attached, and four on wheel axles. Accelerometers were mounted on these points as indicated by circles in step ④. Vehicle tests were performed on specialized test tracks (two of these tracks are shown in ⑤). From each vehicle test, eight simultaneous time series measurements were obtained corresponding to the vertical accelerations at body points and wheel axle points.

Finally, the field test results were correlated with Adams model simulation results in ⑥.
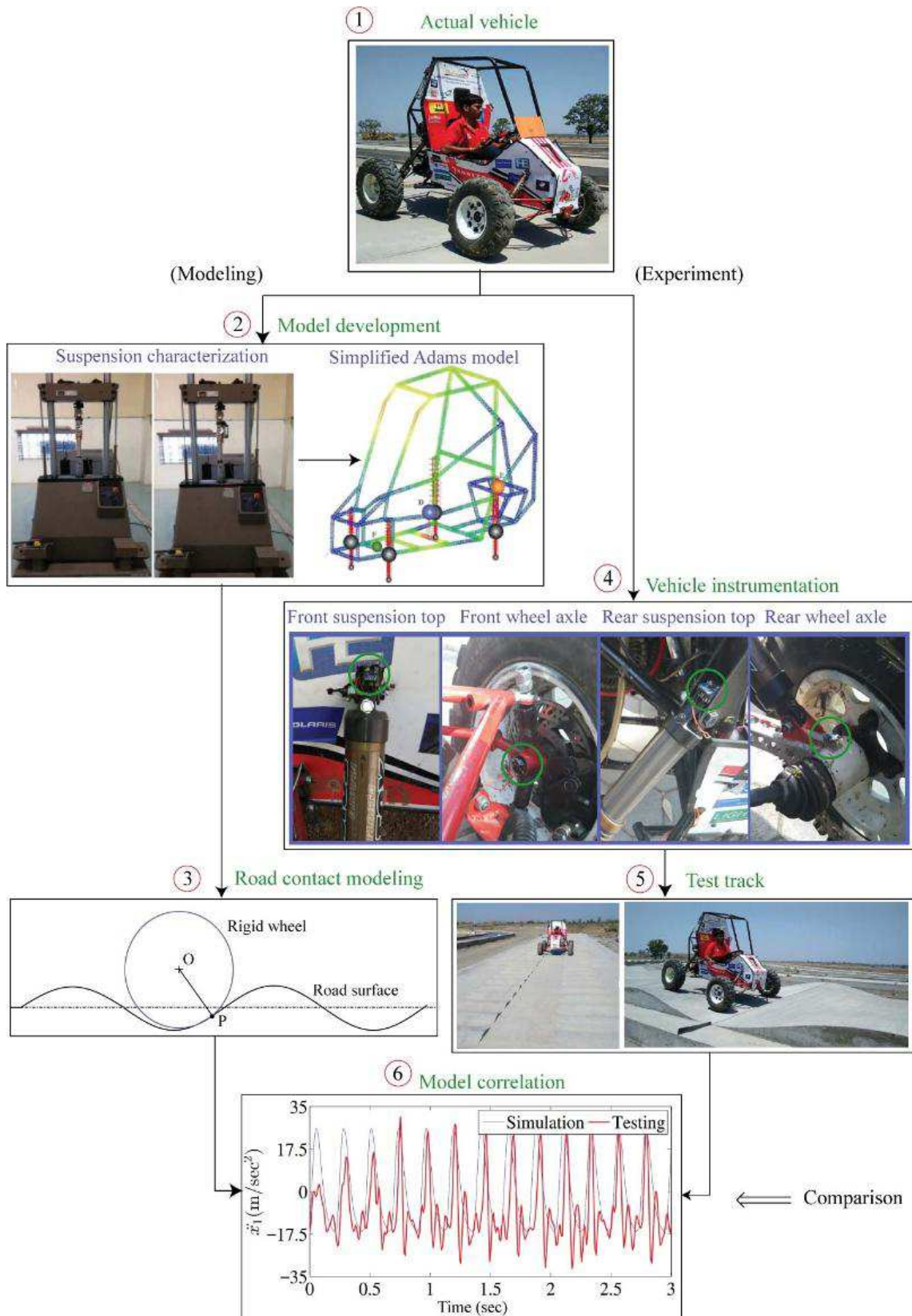
Figure 4.1: Work flow of this chapter.

In the rest of this chapter, the above mentioned activities will be described in detail.

4.1 Vehicle model development in Adams

4.1.1 Vehicle suspension

The ATV is shown in Figure 4.2.

Figure 4.2: All terrain vehicle used for field testing. Photograph obtained from Welding Engineering Laboratory of Mechanical Engineering Department, SGSITS, Indore [70]. Reproduced with permission.

The vehicle was fabricated by undergraduate students of Shri G.S. Institute of Technology and Science (SGSITS), Indore[1].

The vehicle has a double wishbone front suspension and a semi-trailing arm rear suspension. The front and rear suspensions are equipped with FOX pneumatic shock absorbers. The suspension properties of these shock absorbers need to be estimated before developing the Adams model.

The front suspensions have Float 3 and the rear suspensions have Float 3 EVOL

---

[1]Further details about the vehicle are available in a design report [71].

("extra volume") R shocks respectively[2](see Figure 4.3 (a)). These suspensions use
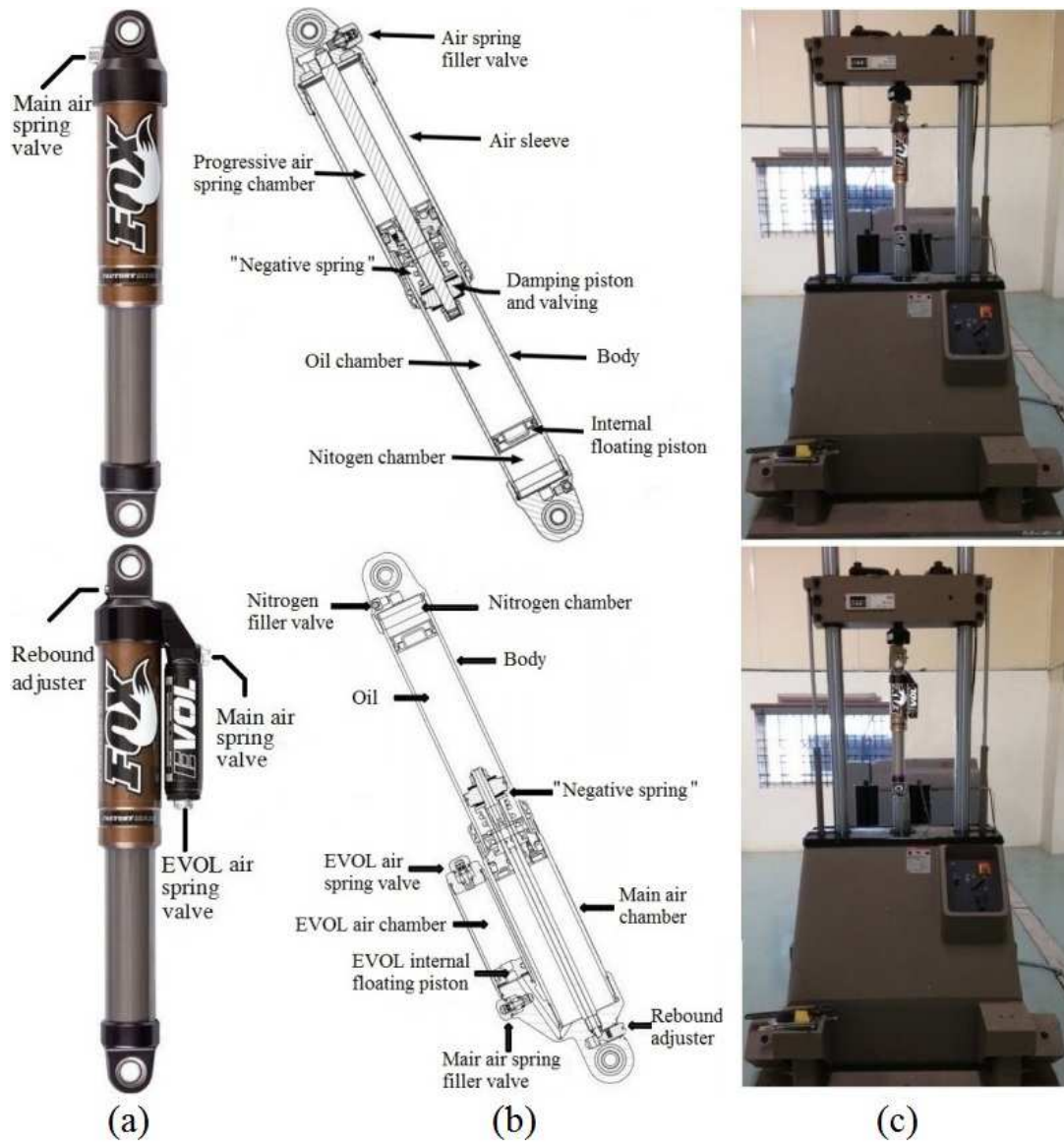
Figure 4.3: (a) Front and rear Fox suspensions; (b) Schematic diagram showing the constructional details (adapted from [72, 73]); (c) Suspension component characterization on MTS 850.25 damper test-rig at vehicle dynamics lab facility of NATRiP, Indore [63].

progressive air springs whose stiffness can be adjusted by changing the air pressure. Underneath the air spring chamber is a damper consisting of an oil chamber and a high pressure nitrogen gas chamber separated by an internal floating piston. In

---

[2]Further details about these Fox suspensions and their tuning procedure is given in their operational manuals [72, 73]

addition to these features, there is also an EVOL ("extra volume") chamber and rebound adjuster in the rear suspension. The constructional details of the suspensions are given in Figure 4.3(b) The suspensions were characterized on an MTS 850.25 damper test-rig at NATRiP, Indore (see Figure 4.3(c))[3].

To obtain suspension stiffness characteristics, a sinusoidal displacement is applied at a frequency of 0.1 Hz and the peak force is measured. The actuator stroke of the test rig is limited to 100 mm, and the sinusoidal displacement amplitude is varied from 5 mm to 100 mm in steps. Force versus displacement characteristics of front and rear suspension are shown in Figure 4.4.
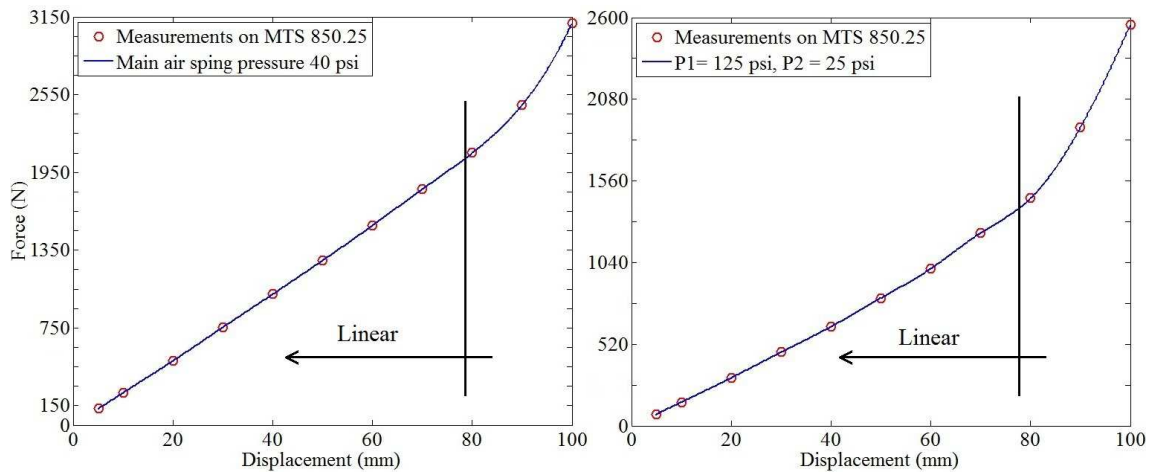
Figure 4.4: Force versus displacement characteristics of front suspensions (main pressure = 40psi) and rear suspensions (EVOL pressure, P1 = 125psi; main pressure, P2 = 25psi).

For the given pressure setting and in the useful range of suspension travel, these characteristics are seen to be linear. The suspension damping properties were not measured in this study, but obtained from damper charts in [72, 73]. Suspension component properties used in the Adams model for both front and rear suspensions are reported in Table 4.1.

---

[3]The test rig details are available in [74].

S. No.	Identifier	K_{front}	K_{rear}	C_{front}	C_{rear}
1.	Suspension	25 N/mm	15 N/mm	1.50 N-s/mm	1.36 N-s/mm
2.	At wheels	10.5 N/mm	6.5 N/mm	0.63 N-s/mm	0.59 N-s/mm

Table 4.1: 1. Typical values of suspension component properties obtained from suspension characterization. 2. Equivalent suspension properties at wheels, obtained after multiplying by the square of the motion ratios.
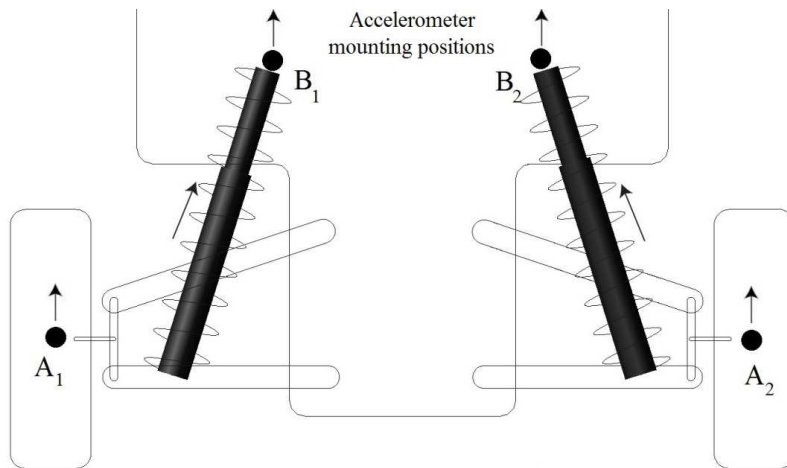
Figure 4.5: Accelerometer mounting positions and definition of motion ratio.
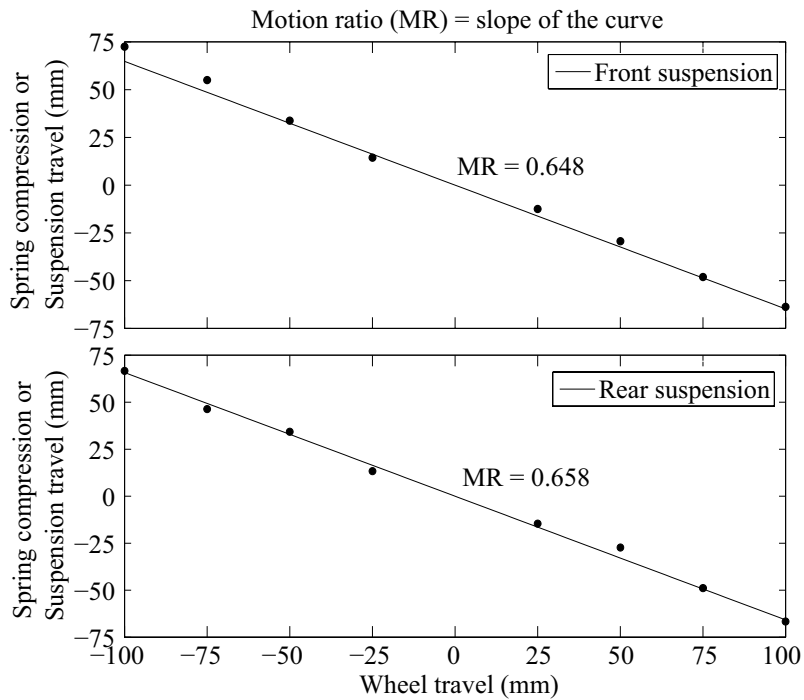
Figure 4.6: Motion ratio characteristics of front and rear suspensions respectively.

Note in Figure 4.5 that the suspension compression is not equal to the wheel travel. Later, in the Adams model, the suspension spring and dampers will be purely vertical. Such a simplification is routinely made in many industrial studies. The advantage is that the complications of the linkages in Figure 4.5 are avoided. The price paid is that suspension component stiffness and damping must be multiplied by a motion ratio (squared); see Figure 4.6. The motion ratios were experimentally obtained by raising/lowering the wheel of interest and measuring the spring compression/extension. Note in Figure 4.5 that the suspension compression is not equal to the wheel travel. Later, in the Adams model, the suspension spring and dampers will be purely vertical. Such a simplification is routinely made in many industrial studies. The advantage is that the complications of the linkages in Figure 4.5 are avoided. The price paid is that suspension component stiffness and damping must be multiplied by a motion ratio (squared); see Figure 4.6. The motion ratios were experimentally obtained by raising/lowering the wheel of interest and measuring the spring compression/extension.

Using these suspension properties, (i) a full vehicle Adams model and (ii) a simplified Adams model similar to the one developed in chapter 2 were developed.

4.1.2   Adams model

The vehicle chassis is made of a roll cage type structure. The roll cage structural details are given in Table 4.2.

Material	CS	Diameter	Thickness	Yield and ultimate strength
Steel AISI 4130	Circular	31.75 mm	1.65 mm	721 MPa and 760 MPa

Table 4.2: Physical and material properties of the roll cage pipe structural members. The material properties were measured by the ASTM A370-2012 tensile test and the material test certificate is available in [75].

From the full vehicle Adams model (see ① in Figure 4.7), a parasolid model of the vehicle chassis is obtained as shown in ② below (see ADAMS/Exchange [76]). A simplified but somewhat similar geometrical model was built and a finite element (FE) model of the latter was developed in Nastran as shown in ③ below.

The FE model was then imported into Adams. The four mounting locations B_i were defined as interface nodes. In addition, the model had three more interface nodes denoted D, E and F, corresponding to the center of mass locations of the driver, engine and battery respectively (see ③ in Figure 4.7). Three rigid bodies with mass and inertia properties representing the driver, engine-driveline assembly and battery were attached to these interface nodes[4].

The driver weight is 65 kg and the driver inertia properties were obtained from [77, 78]. The battery has dimensions (in mm) $240 \times 175 \times 175$ with mass 15 kg; using these values, the corresponding inertia properties were calculated and used. Finally the engine and driveline mass is 40 kg and the inertia properties were obtained from the CAD assembly of the engine, transmission and gearbox (see Figure 4.8) [71].

Four spring-dashpot pairs with the equivalent suspension properties (see Table 4.1) are attached between points B_i on the car body and unsprung masses at wheel axle A_i. The unsprung masses are further connected by springs and dashpots representing tyre properties to ground contact points C_i. The unsprung mass and tyre properties are listed in Table 4.3.

The above Adams model will be partially validated against test results.

---

[4]These interface nodes are in turn connected to the FE mesh using RBE2 elements, which connects rigid body nodes to a few nodes in the deformable mesh.
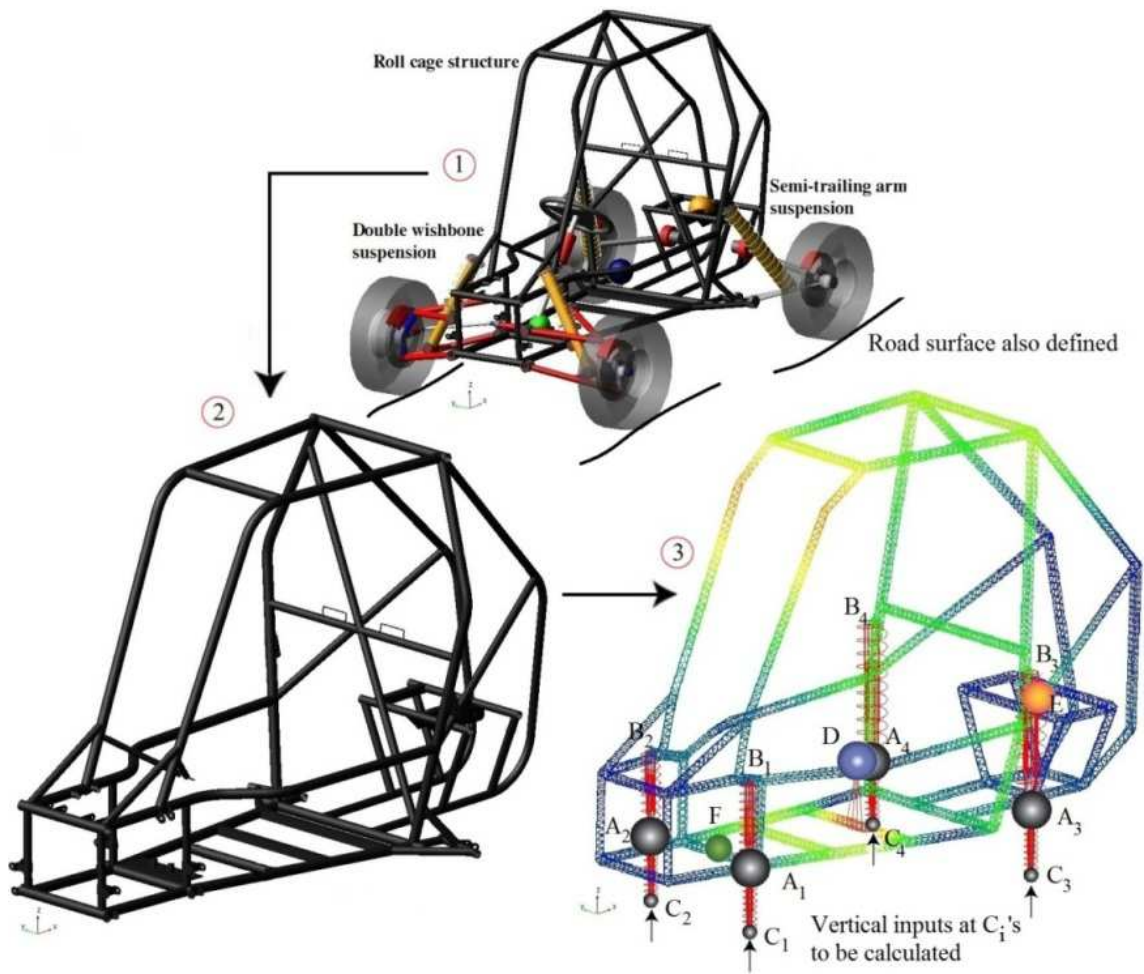
Figure 4.7: ①: Full vehicle model in Adams. The road surface is also defined for the full vehicle simulation. ②: Parasolid model of the chassis obtained from the full car Adams model. ③: FE model of the simplified chassis with pipe curvatures removed. The displacement inputs are given to wheel contact points C_i.

Identifier	M_u (unsprung)	K_t (tyre)	C_t (tyre)
Front	15 kg	40 N/mm	0.2 N-s/mm
Rear	12.5 kg	40 N/mm	0.2 N-s/mm

Table 4.3: The vehicle is equipped with 22x7-10 BKT W207 ATV tires [79] in all four wheels, but the front wheel has greater mass because of a brake assembly. Moreover, ATV tyres use low inflation pressures (typically 7 psi) and have low stiffness and high damping compared to typical commercial tyres.
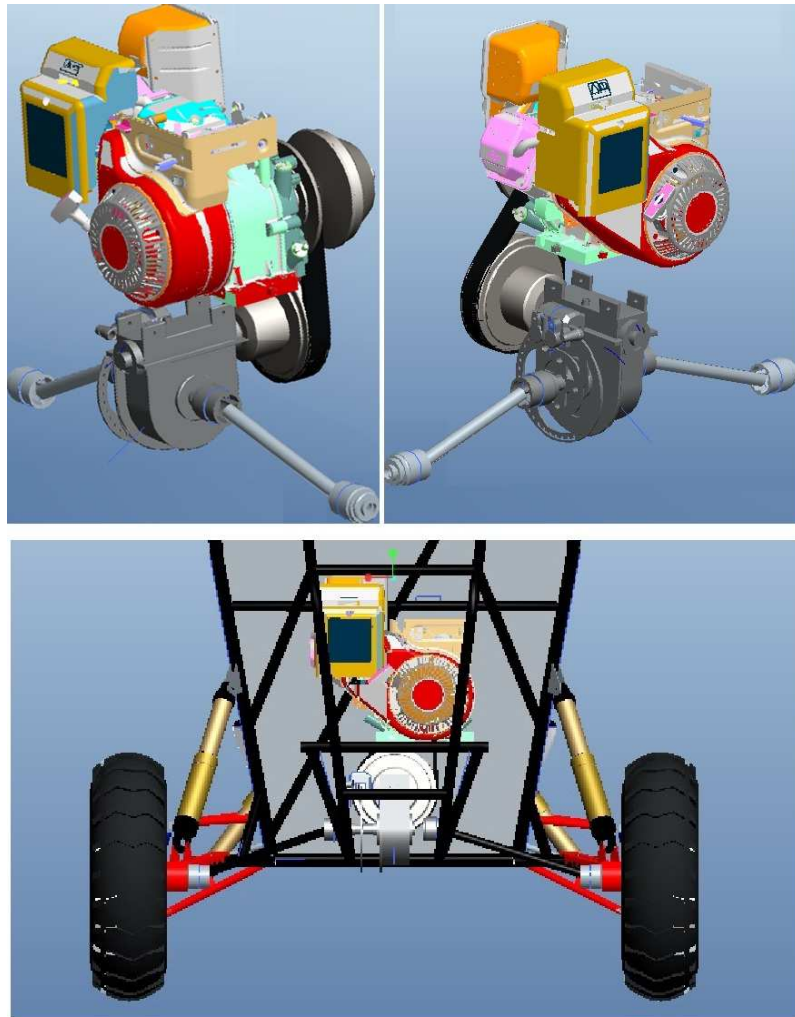
Figure 4.8: CAD model assembly showing engine, transmission and gearbox. This assembly was used to calculate the inertia properties.

4.1.3   Road contact kinematic model

The road surface geometry has to be converted into an equivalent vertical input to be applied at the wheel-ground contact points C_i of the simplified Adams model. We will use a road contact kinematic model that calculates the effective wheel displacements for the continuous displacement tracks (see Table 4.4).

Since the half-wavelength of the sinusoidal tracks is comparable to the tire diameter, although the road profile is sinusoidal the actual *displacement input* to the wheel is not sinusoidal. The ground excitation at each wheel contact point C_i is calculated approximately using a rigid-wheel kinematic model as discussed below.

Consider a rigid wheel going over a sinusoidal track as shown in Figure 4.9(a). The track amplitude is A, wavelength is L and tire radius is R. The coordinates of wheel center O is $(\bar{x}, \bar{y})$ and the coordinates of the wheel-ground contact point P is (x, y).

From geometrical considerations

$$x = \bar{x} + R\sin\theta, \tag{4.1}$$

$$y = A\sin\left(\frac{2\pi x}{L}\right), \tag{4.2}$$

$$\frac{dy}{dx} = \tan\theta. \tag{4.3}$$

Differentiating Equation (4.1) gives

$$\dot{x} = \dot{\bar{x}} + R\dot{\theta}\cos\theta, \tag{4.4}$$
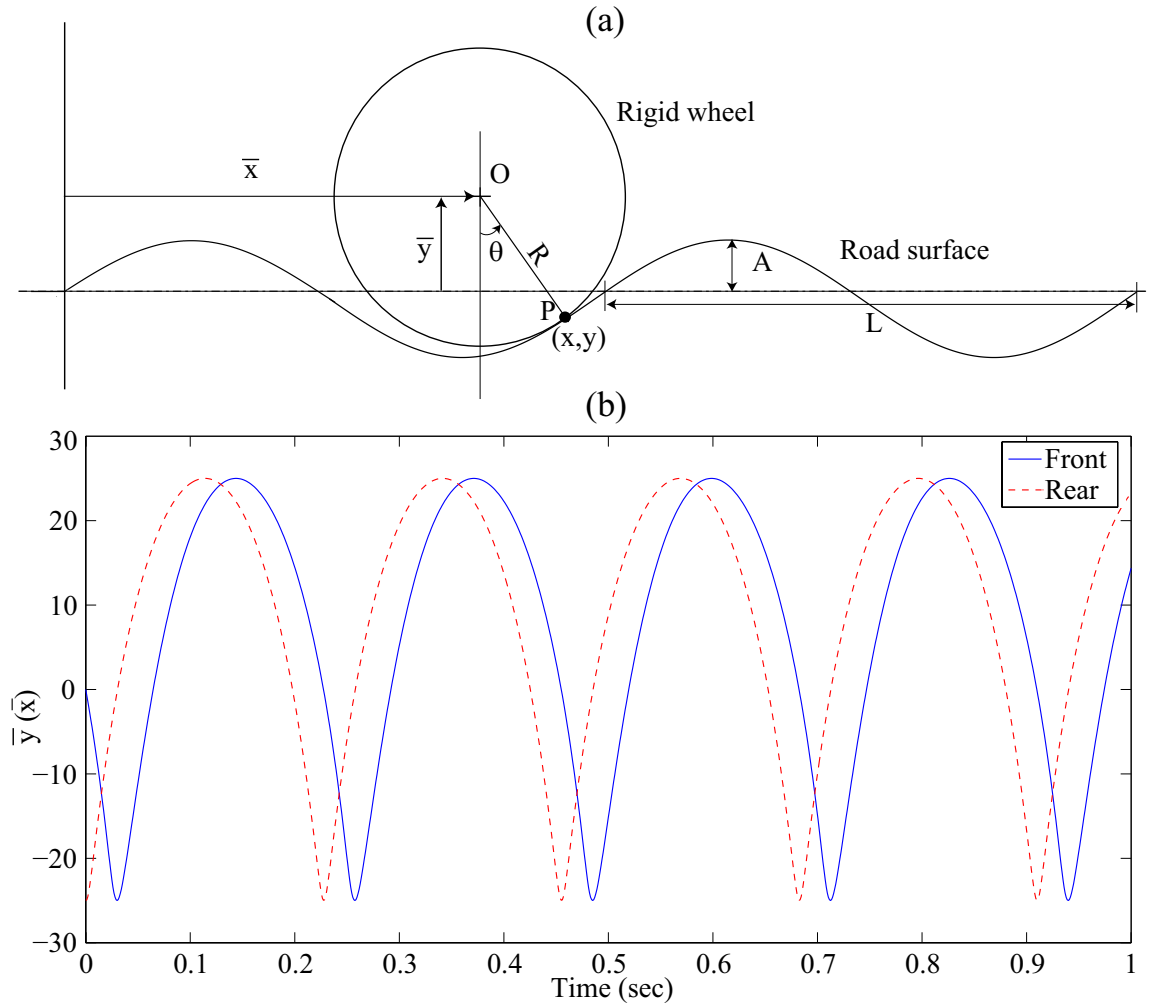
Figure 4.9: (a) Kinematics of a rigid wheel going over a sinosuidal road; (b) The road displacement input acting on the wheel contact point P as seen at O.

where $\dot{\bar{x}}$ is the vehicle longitudinal velocity (v). Substituting Equation (4.2) in (4.3) and differentiating the same gives

$$\dot{\theta} = -A \left(\frac{2\pi}{L}\right)^2 \sin\left(\frac{2\pi x}{L}\right) \dot{x} \cos^2\theta \qquad (4.5)$$

Using Equations (4.4) and (4.5) yields

$$\dot{x} = \frac{v}{1 + AR\cos^3\theta \left(\frac{2\pi}{L}\right)^2 \sin\left(\frac{2\pi x}{L}\right)}; \quad \dot{\theta} = \frac{-Av\left(\frac{2\pi}{L}\right)^2 \sin\left(\frac{2\pi x}{L}\right)\cos^2\theta}{1 + R\cos^3\theta A\left(\frac{2\pi}{L}\right)^2 \sin\left(\frac{2\pi x}{L}\right)} \qquad (4.6)$$

101

Equation (4.6) is solved numerically in Matlab using `ode45` with initial conditions $x = \bar{x} = \frac{L}{4}, \theta = 0$ at $t = 0$. A typical solution is shown in Figure 4.9(b)[5].

This type of computed ground excitations are used as a cubic spline inputs [80] to Adams for all simulations.

In this approach for calculating the displacement input, two things are neglected: the deformation of the wheel, and the shifting location of the contact force on the wheel. In the Adams simulation, the computed displacement input is simply applied at points C_i (see ③ in Figure 4.7). Note that the accelerometers used for field testing measure only vertical accelerations; so, to the extent that the longitudinal acceleration of the vehicle causes pitching oscillations, the present approach fails to capture them. Incorporation of such effects could be attempted in future work.

In addition to the displacement input computed above, wheel compliance and damping need to be assigned in the Adams model before final simulation. These quantities were estimated from the tyre inflation pressure based on data for similar tires in [81]. The stiffness and damping values used for model development are 40 N/mm and 0.2 N-s/mm respectively. Note that the tyre compliance is a lot smaller than the suspension compliance, so small errors in the compliance estimates have tiny effects.

4.2   Vehicle testing

The vehicle needs to be instrumented before performing field testing. We have used the capacitor-based ADXL326 accelerometers (a total of eight) for vehicle testing. These are triple axis accelerometers but only the Z-axis output is used for measuring

---

[5]This road displacement input is for the vehicle running at a speed of 9.5 kmph on high severity washboard track.

vertical accelerations. The data acquisition system consists of a FAT32 Micro SD card module and an Arduino ATMega328P micro-controller board. These systems are compatible with a breadboard, making it easy to connect them together and power the circuit by a standard 9V battery.

The accelerometers need to be calibrated before use. The accelerometer details and the calibration procedure followed are given in Appendix C.1.

The accelerometers were mounted at points B_i and A_i using magnetic mounting strips; see Figure 4.10(left). The data acquisition system is mounted on the vehicle dashboard; see Figure 4.10(right).
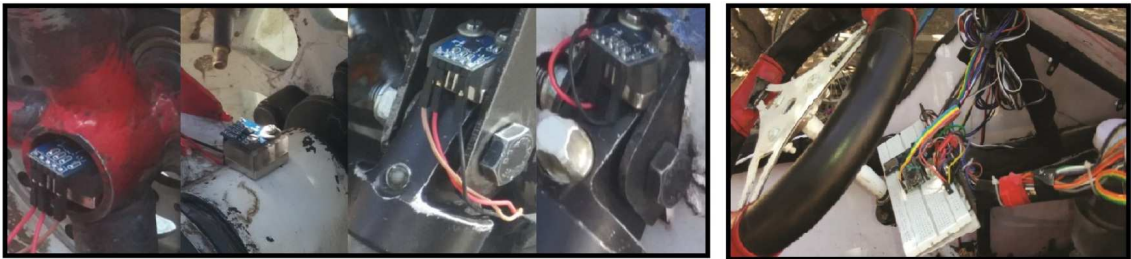
Figure 4.10: Left: Accelerometers mounted at A_i's and B_i's; Right: Data acquisition system mounted on the vehicle dashboard.

Next the instrumented vehicle was tested on various specialized tracks at the test track facility of NATRiP, Indore (see Figure 4.11).
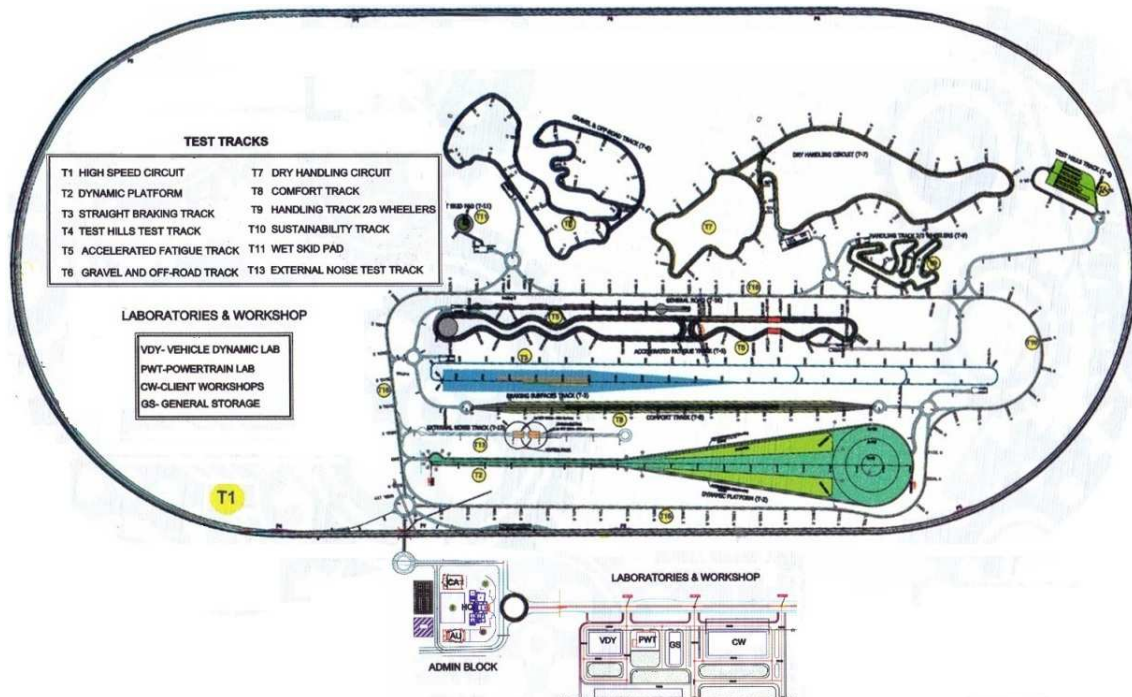
Figure 4.11: A plan view of NATRAX proving ground facility of NATRiP, India [63].

Some of the testing tracks used for this study are shown in Figure 4.12. These test tracks are broadly classified into two categories:

1. Continuous displacement input tracks:

   These are sinusoidal tracks having a simple displacement profile suited for direct and deterministic simulation. The tracks selected under this category are washboard, one-sided washboard, herringbone, sine sweep, and chassis-twist track. The track details are shown in Table 4.4.

2. Discontinuous displacement input tracks:

   These are tracks with non-deterministic and transient displacement inputs. The tracks selected under this category are rough road, cobblestone and Belgian pave. Apart from these tracks other test conditions were prepared in

the university (SGSITS, Indore) which are half sine bump, step bump, and one-sided half sine bump.

Figure 4.12: Some of the sinusoidal and rough tracks considered for study.

S. No.	Track	Severity	Amplitude (mm)	Pitch (mm)
1.	Washboard	Low	15	400
		High	25	600
2.	One-sided washboard	Low	15	400
		High	25	600
3.	Herringbone	Low	10	500
		Medium	15	600
		High	20	800
4.	Chassis twist	Low	150	2000
		Medium	175	3000
		High	200	4000
5.	Sine sweep	-	15	400-600 in 24 m

Table 4.4: Track details of continuous displacement tracks.

Now the test results will be presented along with the Adams simulation results.

4.3 Test results

The test results for various tracks and its correlation with the Adams simulation results of the vehicle developed in section 4.1.2 will be discussed in this section. This both validates (at least partially) our Adams modeling approach and ensures that the vehicle instrumentation gives satisfactory results.

The test data was acquired at a sampling frequency of 100 Hz. For subsequent comparisons with Adams model, the test data is filtered using a low pass filter with cut-off frequency of 30 Hz using Matlab's `designfilt` command.

4.3.1 Continuous displacement input tracks

Washboard track

There are two sinusoidal washboard tracks of different pitch and amplitudes (see Figure 4.13).

Figure 4.13: Low severity (left) and high severity (right) washboard tracks respectively.

The vehicle test details are given in Table 4.5.

Speed	Low severity	High severity
Low	7.5 kmph	11 kmph
High	9.5 kmph	13 kmph

Table 4.5: Test details on two washboard tracks.

A discussion of the test response of the front left wheel axle A_1 and the corresponding response of the suspension-to-body attachment point B_1, for a low speed test on a low severity washboard track, is now given as a typical example of test results.

The wheel displacement input is obtained from the rigid-road contact model and is applied at wheel contact point C_1 (see Figure 4.14).
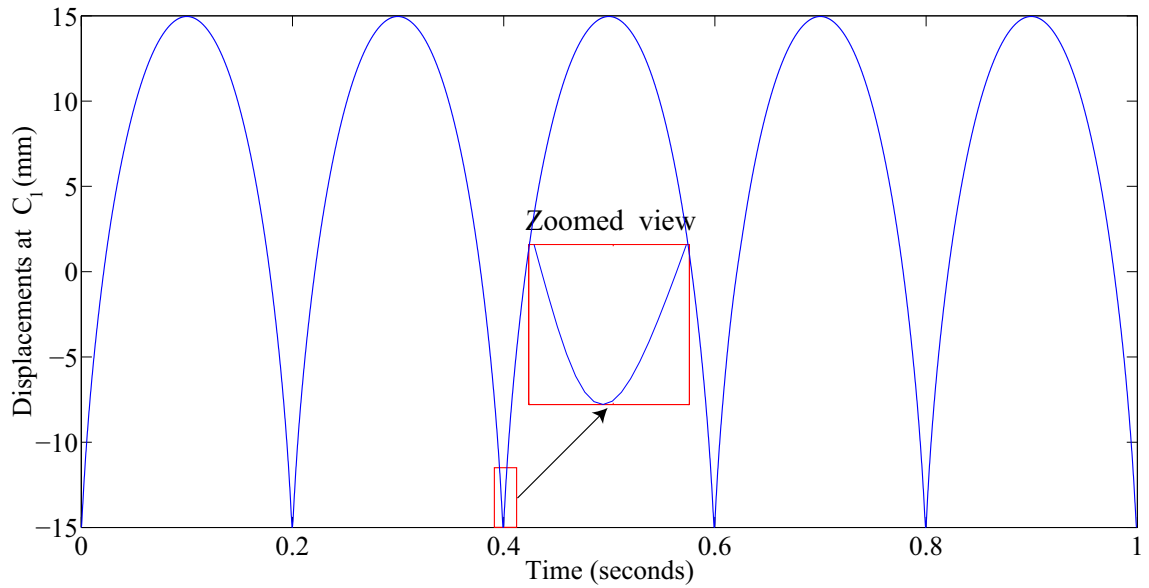
Figure 4.14: Ground displacement input at C_1 given to the Adams model (see ③ in Figure 4.7).

Corresponding to the wheel input there is an axle response and there is a body point response. These responses will be studied sequentially because once the axle

response has been determined subsequently the match or lack thereof with the body response is a matter of the Adams model only and the wheel inputs no longer have any role to play. The axle response at A_1 obtained from the Adams model is compared with the field test results as shown in Figure 4.15. We observe that the
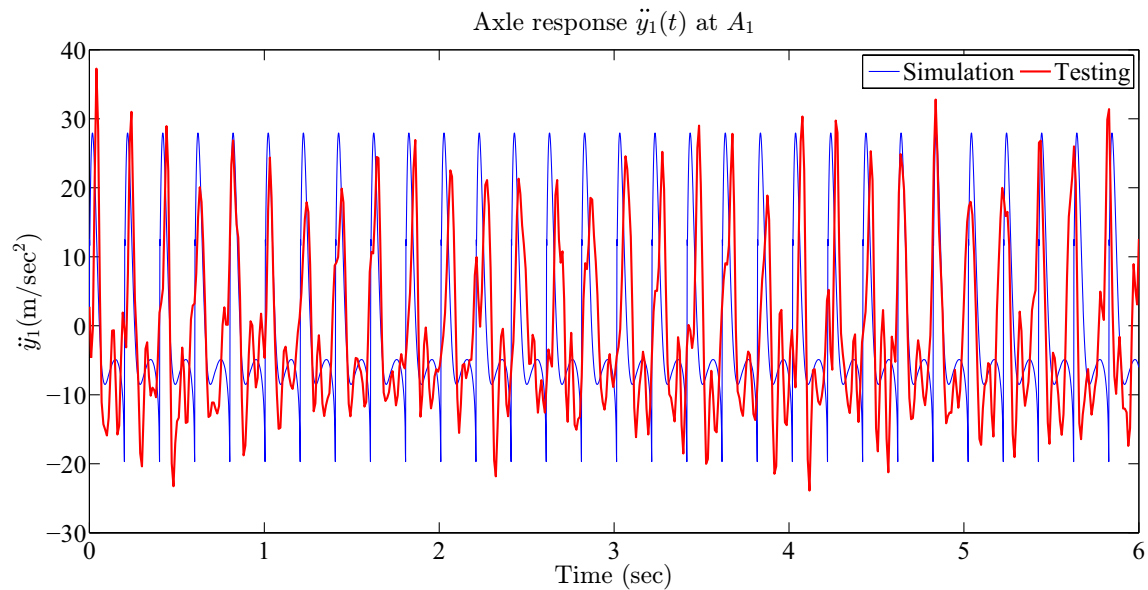
Figure 4.15: Response $\ddot{y}(t)$ of front left axle A_1. The thicker line shows test data[6].

widths of the periodic responses are correct on the whole, the peaks are comparable; the rapid oscillations near the bottom are not fully captured, as expected. The forward speed of the vehicle does show some variation that is not captured in the present approach. On the whole, the wheel compliance and damping is reasonably captured by the model as seen by peak widths and amplitudes.

In the same Adams simulation, the body point responses were also computed. The body point response at B_1 obtained from Adams model is compared with field test results in Figure 4.16, as another typical example of the set of results obtained.

---

[6]There is apparently a low frequency fluctuation in amplitude and phase. This could be due to a slight asymmetry in suspension parameters, a somewhat weak excitation of a roll mode, or even an approximately periodic fluctuation in the forward speed of the vehicle during testing.
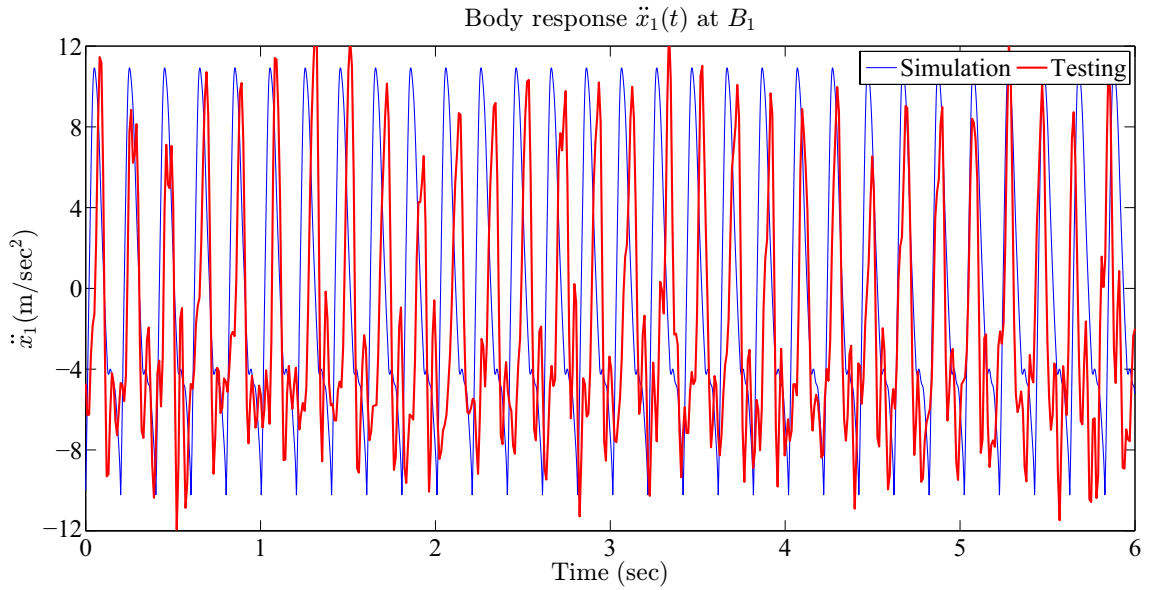
Figure 4.16: Response $\ddot{x}(t)$ of suspension to body attachment point B_1. The thicker line shows test data.

Here too, the peak heights and the widths are roughly matched by the simulation. This shows that the Adams model reasonably correlates with the field test measurements. We conclude that the inertial and compliance properties of the overall vehicle model are fairly accurate.

All other simulation results obtained with the same model parameters are given in subsequent figures to show that the quality of the match with the field test responses remains about the same for several test tracks.

Various road inputs given to the Adams model using the rigid tire-ground contact kinematic model are shown in Figures 4.17 and 4.18.

In subsequent figures, where test results are compared against the Adams model, accelerations of body points B_1 through B_4 are denoted by $\ddot{x}_1(t)$ through $\ddot{x}_4(t)$, and the accelerations of wheel axle points A_1 through A_4 are denoted by $\ddot{y}_1(t)$ through $\ddot{y}_4(t)$. The thicker lines show test data.

Figure 4.19 shows the comparison of simulation and test results of low speed test on low severity washboard track. The peak heights and the peak widths match reasonably well.

Figure 4.20 shows the comparison of simulation and test results of high speed test on low severity washboard track. The peak heights and the peak widths match reasonably well.

Figure 4.21 shows the comparison of simulation and test results of low speed test on high severity washboard track. The peak heights and the peak widths match reasonably well for the acceleration responses of the wheel axle points A_1 and A_2. The peak locations of the simulation and the test responses at A_3 and A_4 tend to deviate after 1.5 seconds. The peak widths of the test responses of the body points B_i are narrower than that observed in the simulation. One possible reason for the mismatch being pronounced in this test case is that the forward speed fluctuates more in this test as the track displacement amplitude is higher, and it is not possible to maintain a constant low speed. Such fluctuations in forward speed could, e.g., set up pitching oscillations that the Adams model would not capture under purely vertical base excitation.

Figure 4.22 shows the comparison of simulation and test results of high speed test on high severity washboard track. The peak heights and the peak widths match reasonably well.

Figure 4.17: Ground displacement inputs given to the Adams model for low and high speed tests on low severity washboard track.

Figure 4.18: Ground displacement inputs given to the Adams model for low and high speed tests on high severity washboard track.

111
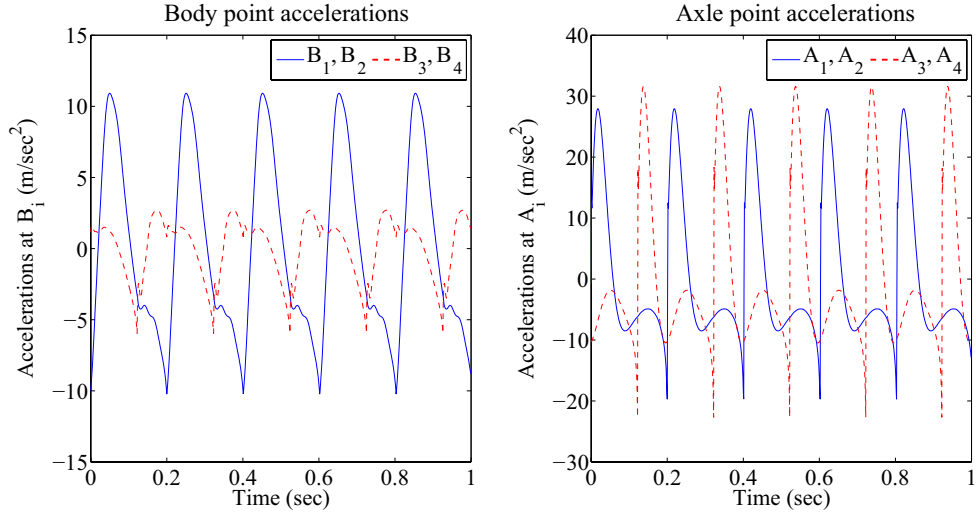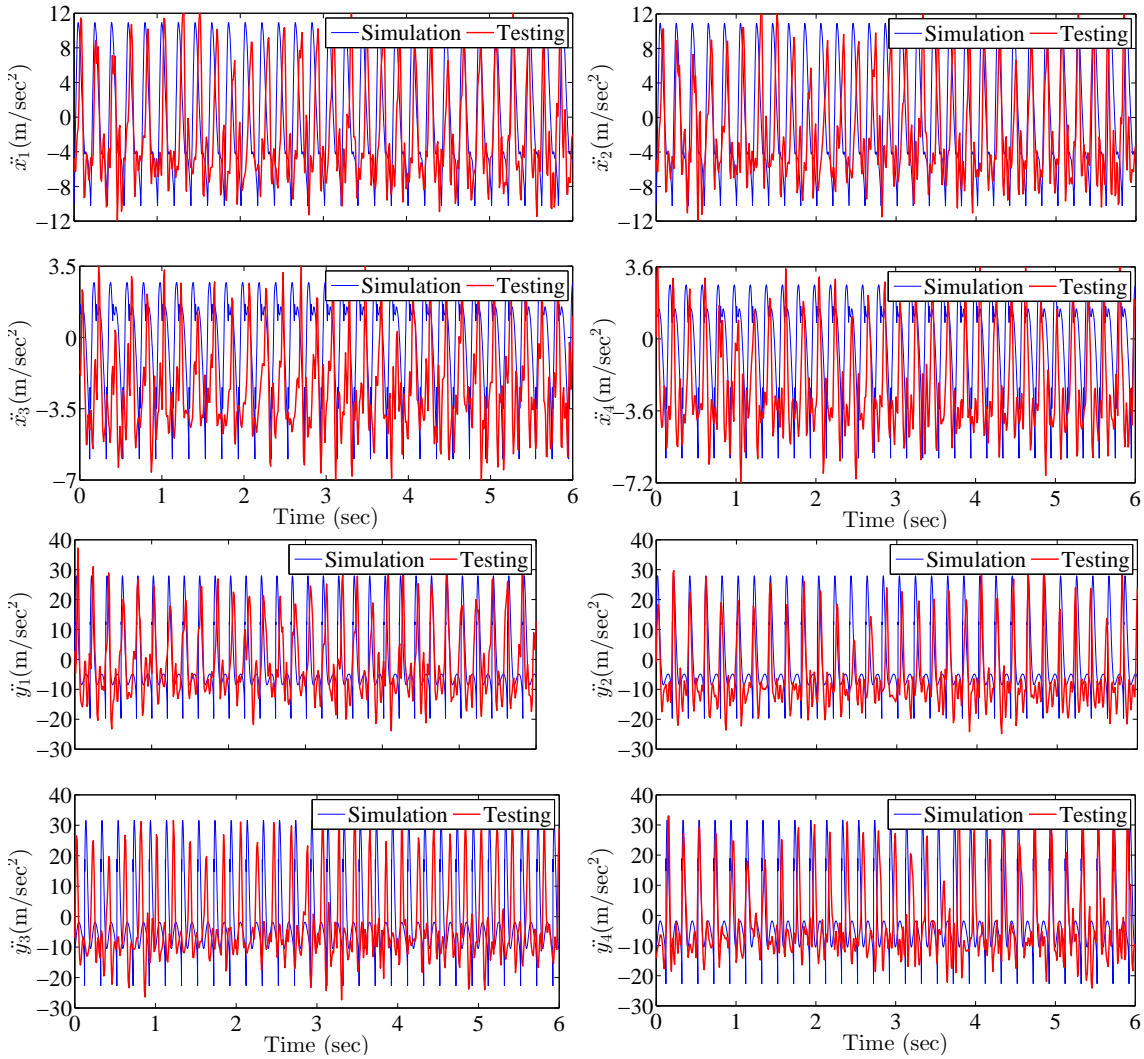
Figure 4.19: Results of low speed test on low severity washboard track.
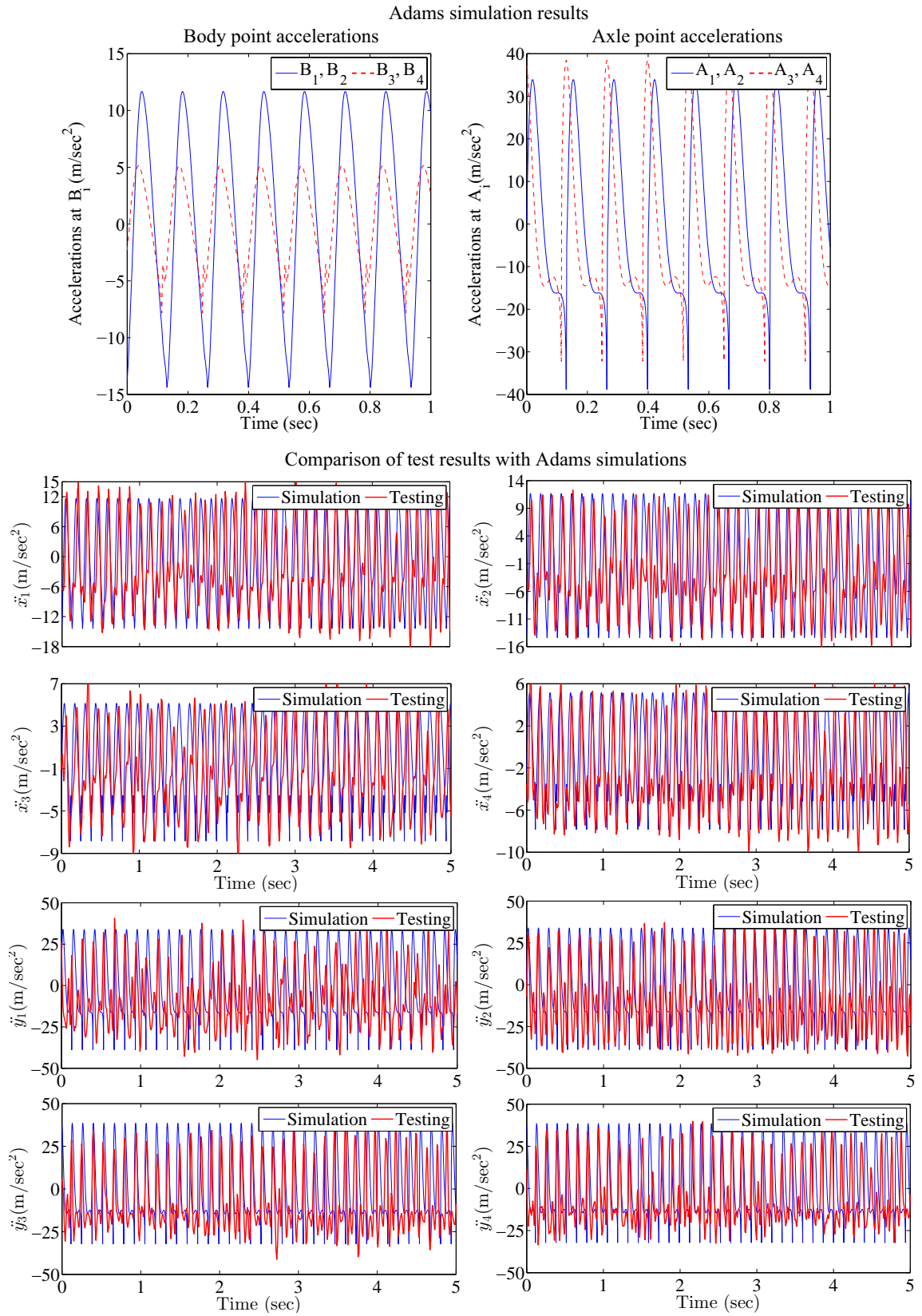
Figure 4.20: Results of high speed test on low severity washboard track.
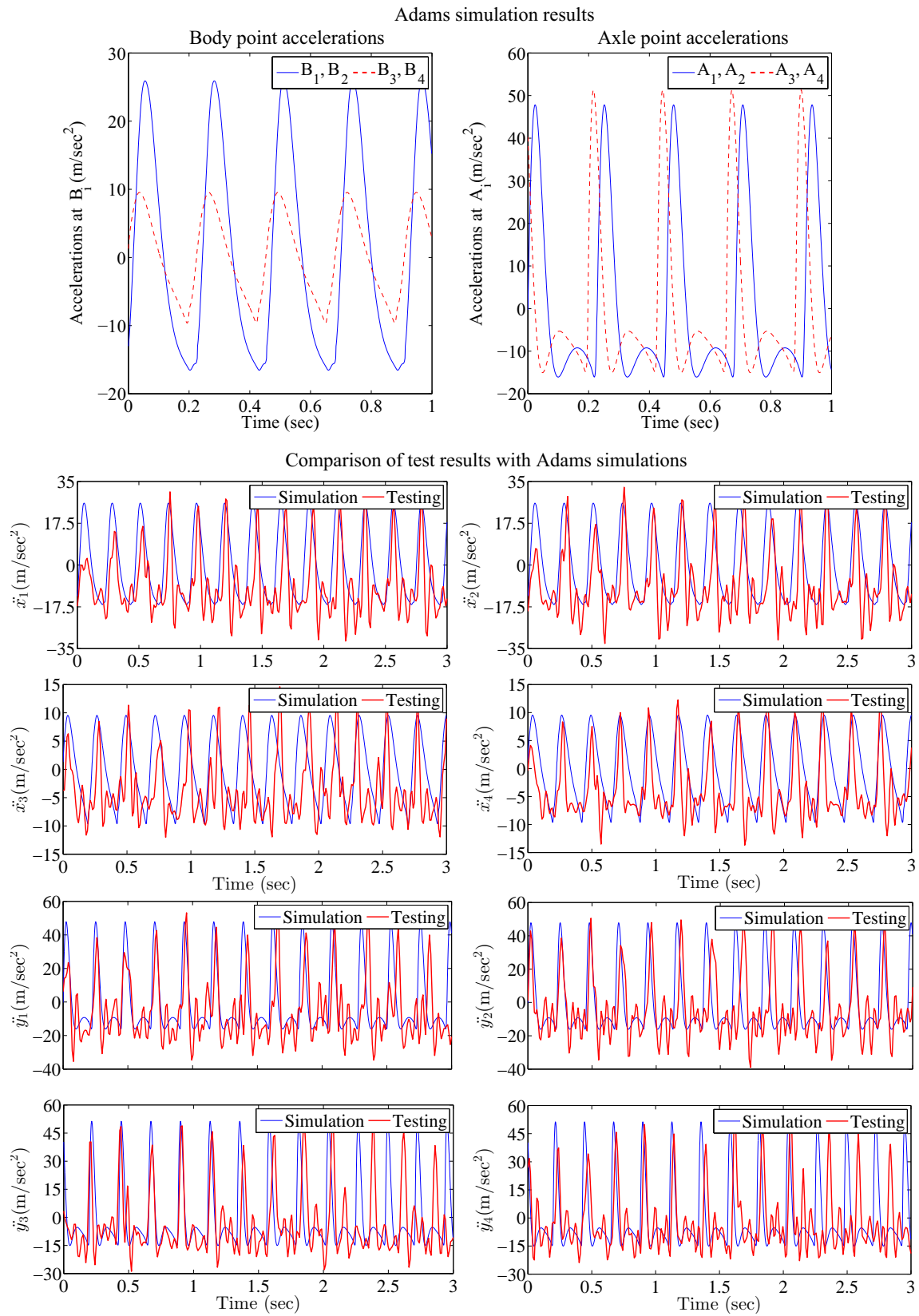
Figure 4.21: Results of low speed test on high severity washboard track.
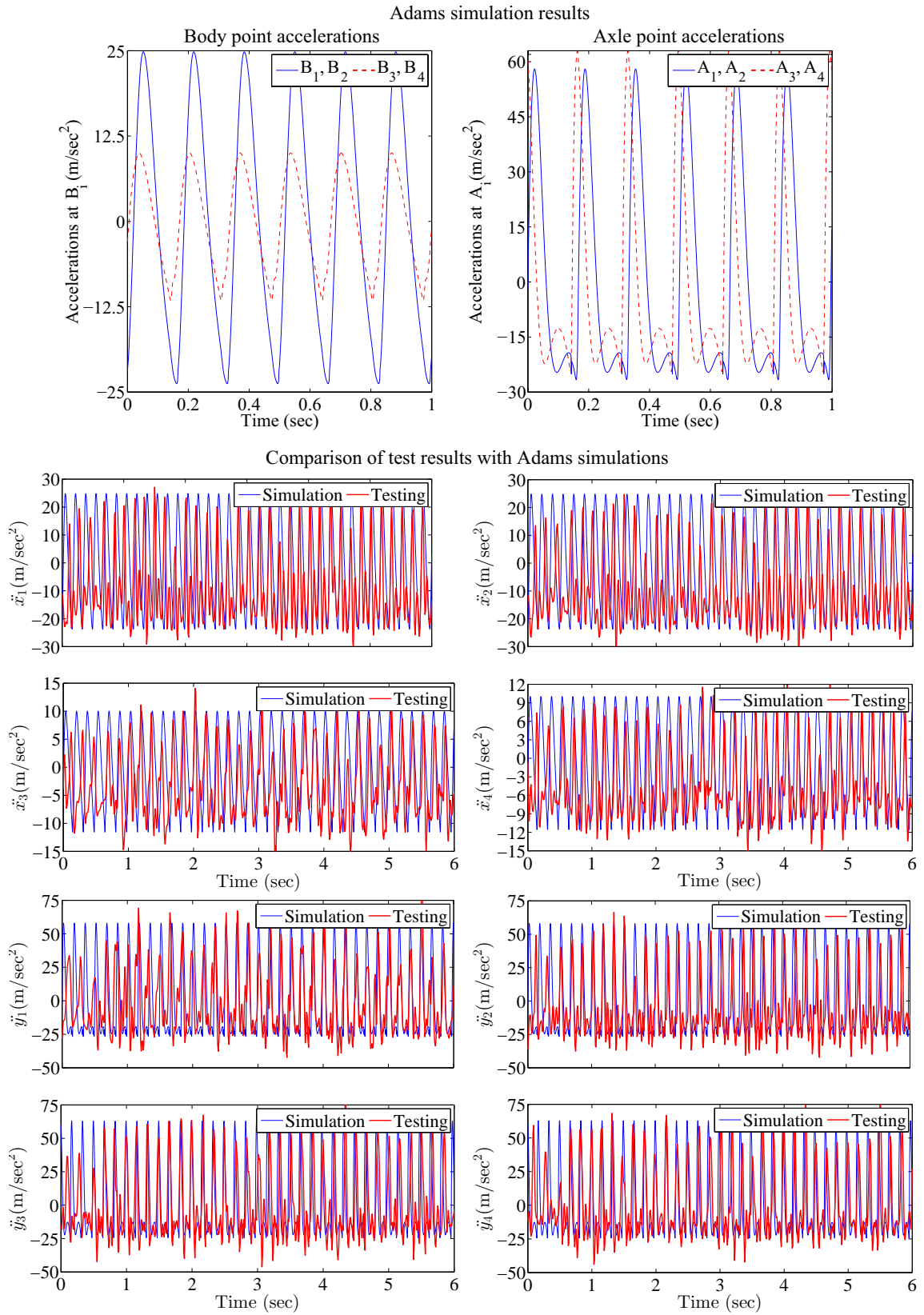
Figure 4.22: Results of high speed test on high severity washboard track.

Herringbone track

In the herringbone track the sinusoidal bumps are inclined at an angle of 20 degrees across the width of the track (see Figure 4.23).
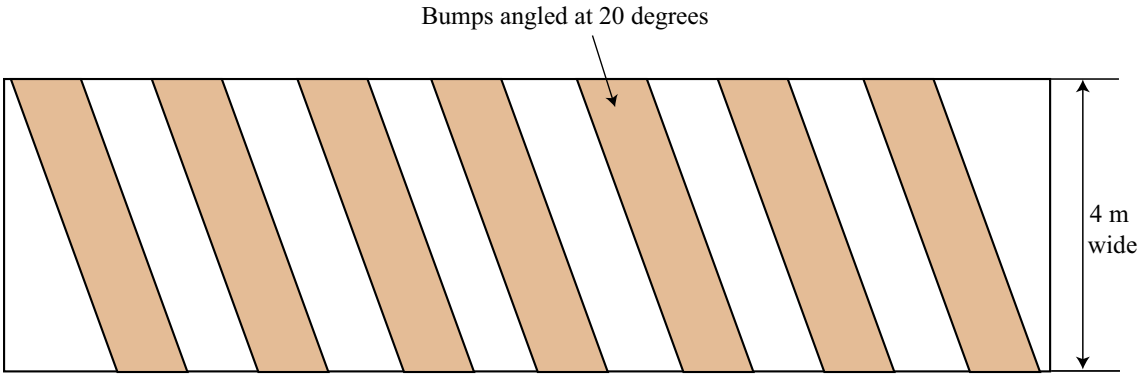
Figure 4.23: Schematic layout of the herringbone track.

There are three herringbone tracks with low, medium, and high severity respectively as shown in Figure 4.24.

Figure 4.24: Low severity (left), medium severity (middle) and high severity (right) herringbone tracks respectively.

The vehicle test details are given in Table 4.6.

Speed	Low severity	Medium severity	High severity
Low	9 kmph	21 kmph	14 kmph
High	14 kmph	25 kmph	19 kmph

Table 4.6: Test details on different herringbone tracks.

116

The road inputs for the left and the right wheels are no longer identical. These displacement inputs are calculated using the rigid tire-ground contact model (see Equation 4.6) and subsequently given to the Adams model as shown in Figures 4.25 through 4.27.

In subsequent figures, where test results are compared against the Adams model, accelerations of body points B_1 through B_4 are denoted by $\ddot{x}_1(t)$ through $\ddot{x}_4(t)$, and the accelerations of wheel axle points A_1 through A_4 are denoted by $\ddot{y}_1(t)$ through $\ddot{y}_4(t)$. The thicker lines show test data.

Figures 4.28 and 4.29 show the comparison of simulation and test results of low and high speed tests on low severity herringbone track. The peak heights and the peak widths match well on the whole. The left and right wheels no longer experience identical inputs. Note that the time series measurements of all eight accelerometers are presented for the same 5 seconds.The match is reasonably good.

Figures 4.30 and 4.31 shows the comparison of simulation and test results of low and high speed tests on medium severity herringbone track. The peak widths match reasonably well. We note that the peak heights of the left body points B_1 and B_3 are relatively less than the right body points B_2 and B_4. One possible reason for the mismatch is that the medium severity herringbone track is not exactly straight but it has a curvature (see Figure 4.24). Also, since the bumps do not hit the right and left wheels simultaneously, there is no symmetry in the right and left-side responses of the vehicle.

Figures 4.32 and 4.33 shows the comparison of simulation and test results of low and high speed tests on high severity herringbone track. The match between simulation and test results is poorest of all. The main reason for the mismatch, in my opinion, is that on high severity tracks the rigid wheel-ground kinematic model is

117

no longer accurate. The wheel displacements predicted by the model are relatively higher than the actual wheel displacements because the tyre compliance plays a role. Also, the suspension properties tend to deviate from the linear characteristics as used in the Adams model.
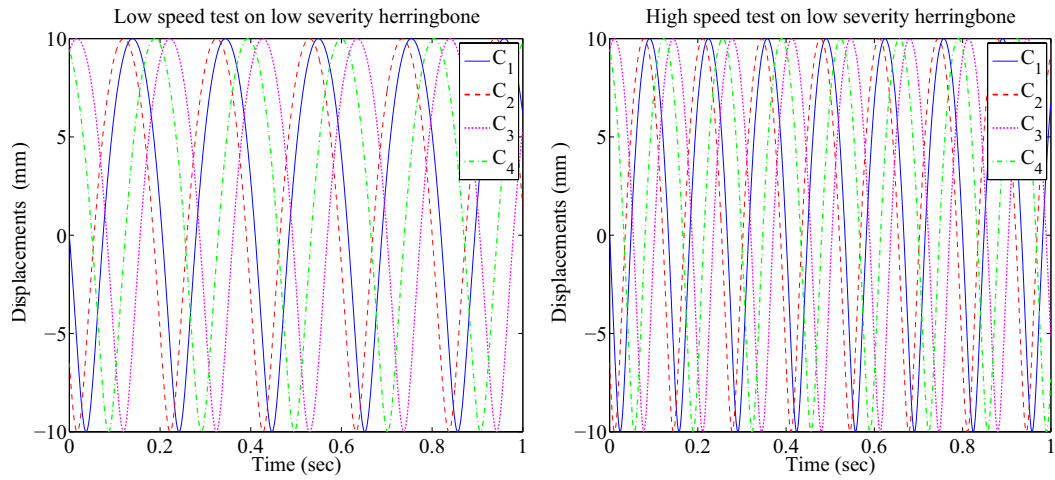
Figure 4.25: Ground displacement inputs given to the Adams model for low and high speed tests on low severity herringbone track.
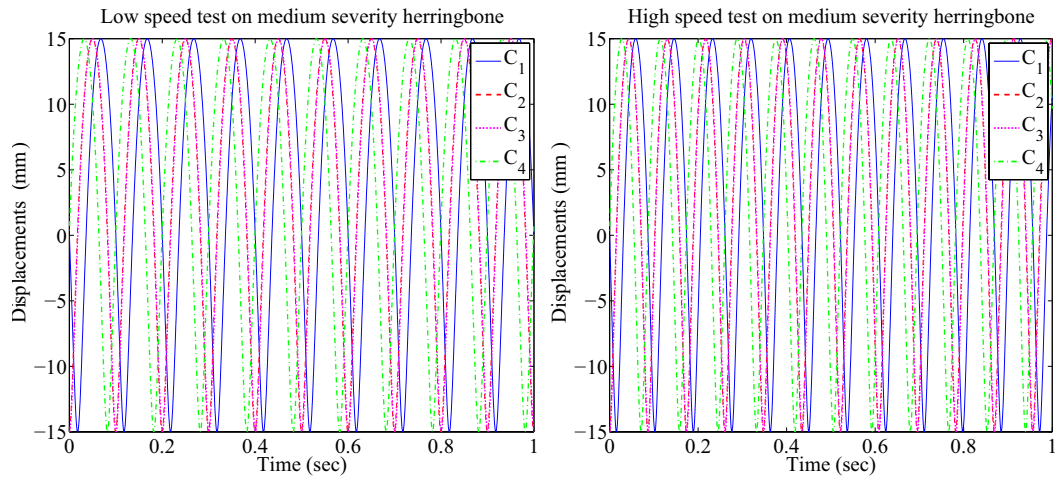
Figure 4.26: Ground displacement inputs given to the Adams model for low and high speed tests on medium severity herringbone track.
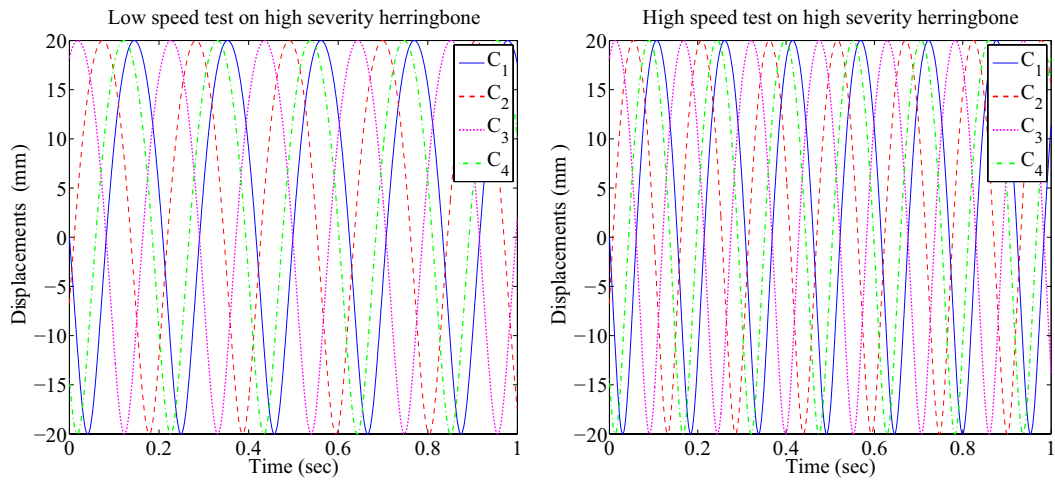
Figure 4.27: Ground displacement inputs given to the Adams model for low and high speed tests on high severity herringbone track.
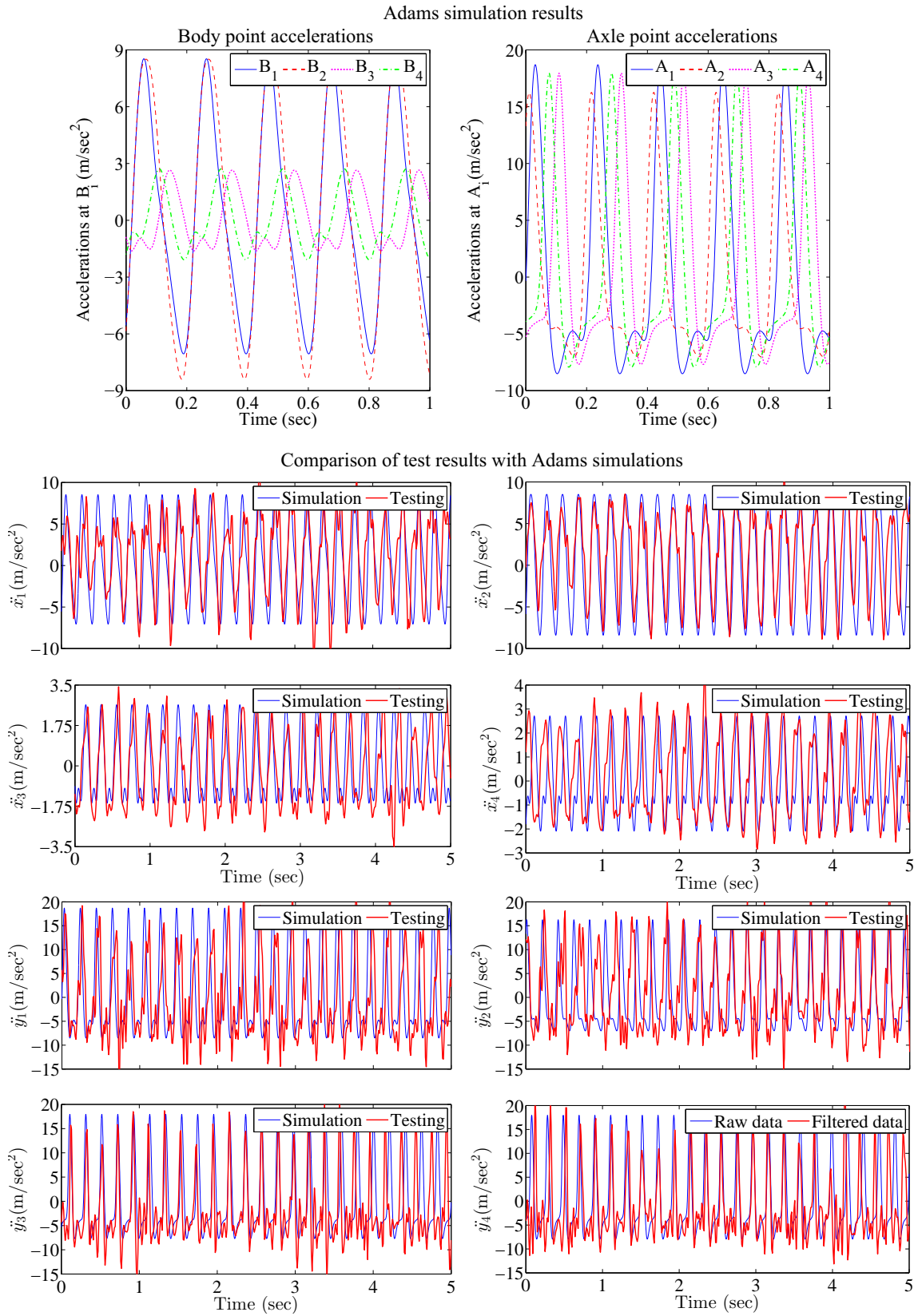
Figure 4.28: Results of low speed test on low severity herringbone track.
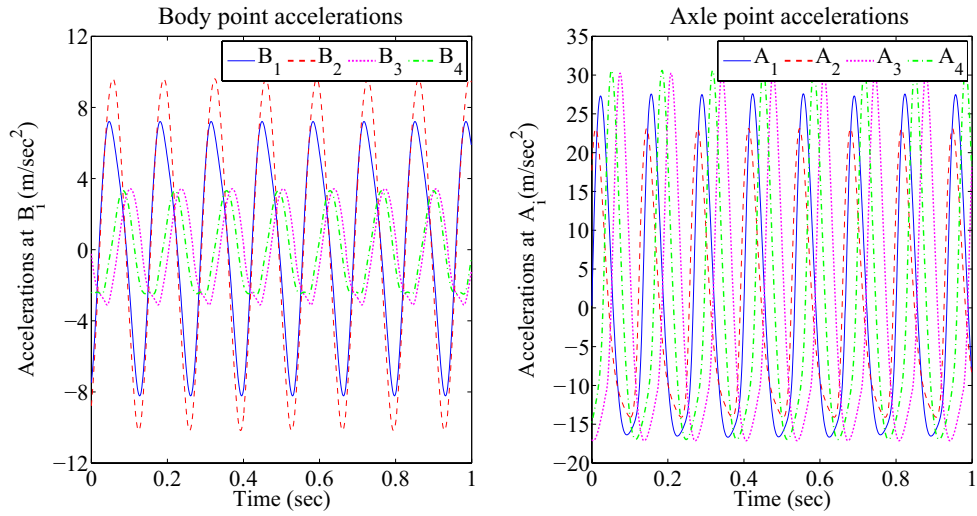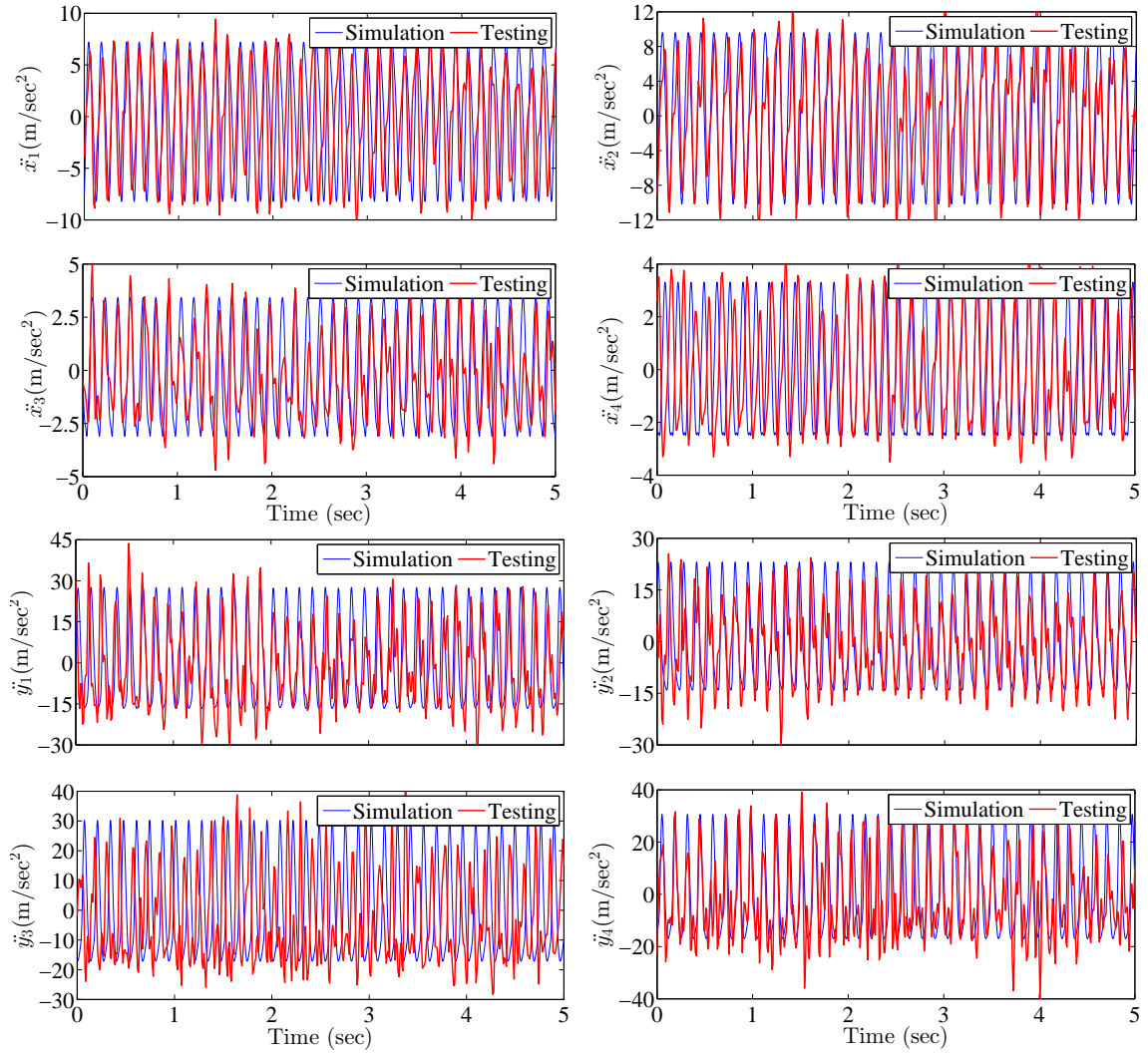
Figure 4.29: Results of high speed test on low severity herringbone track.
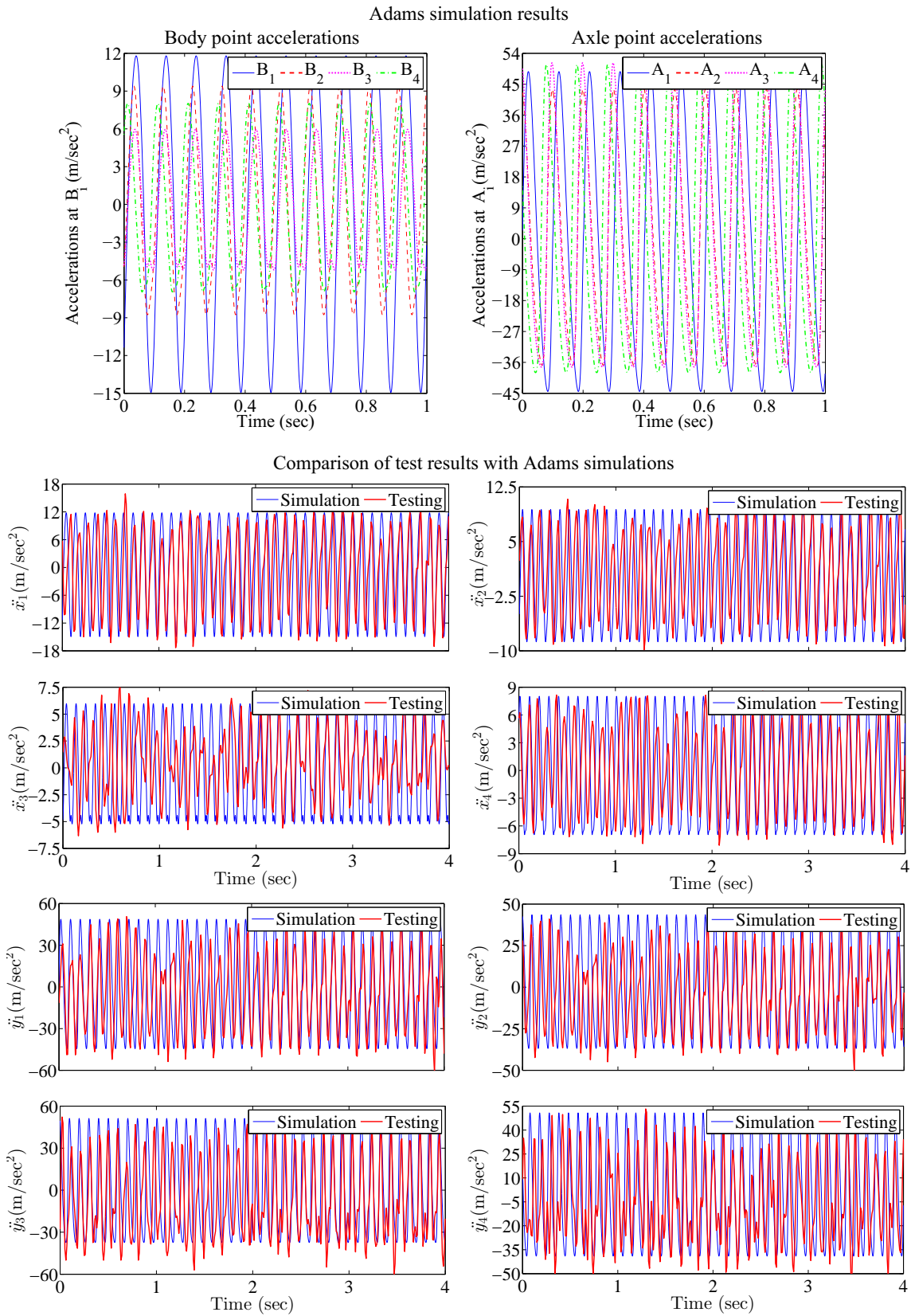
Figure 4.30: Results of low speed test on medium severity herringbone track.
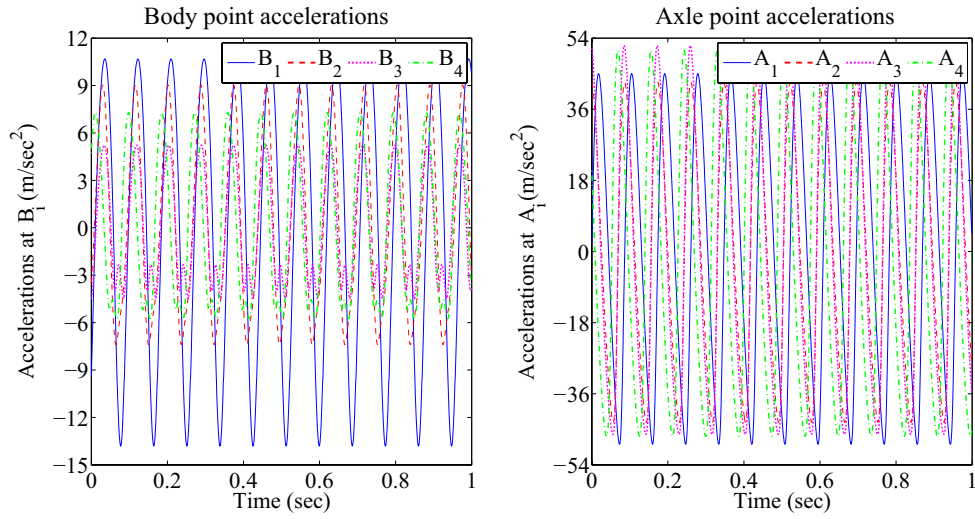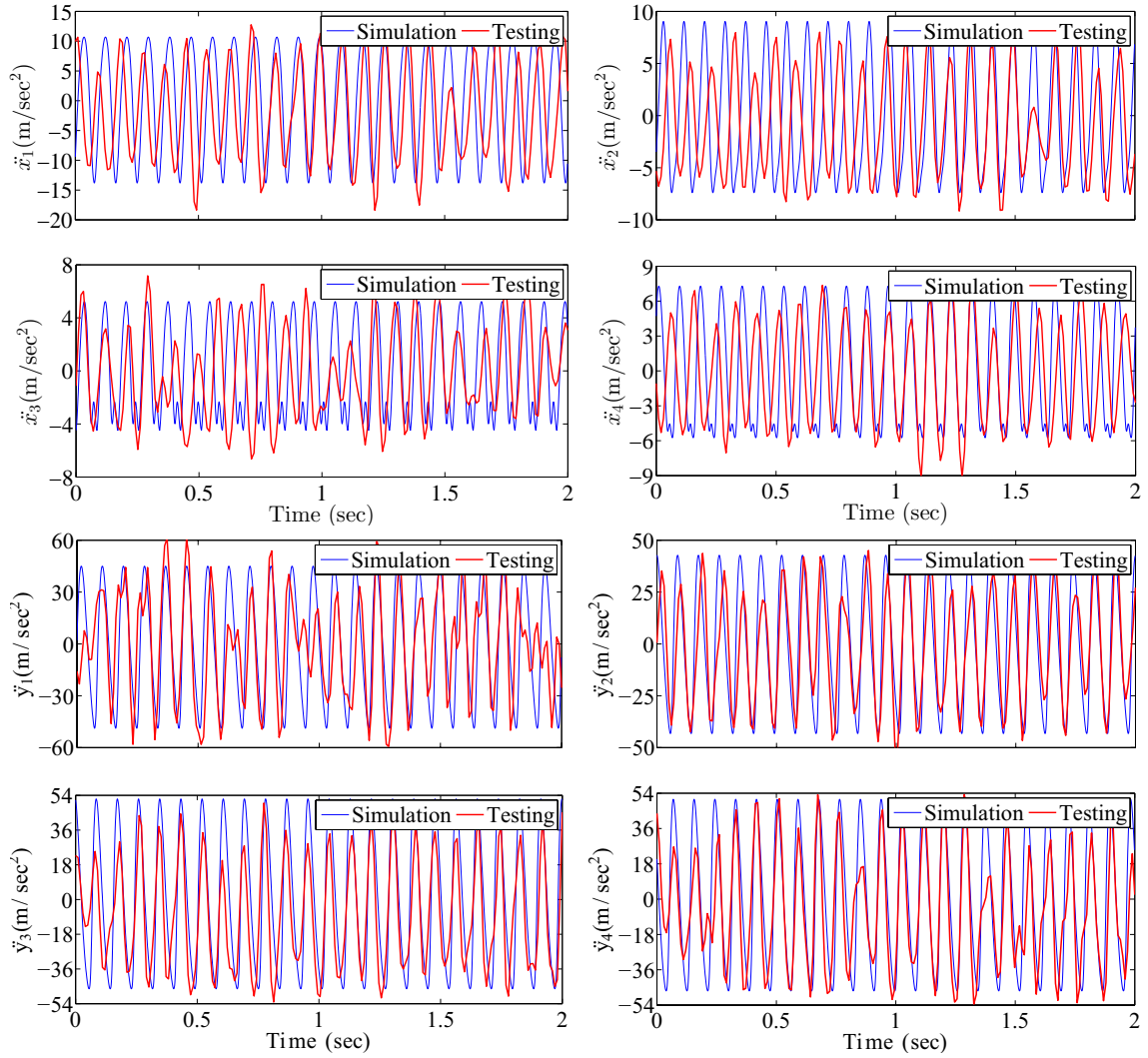
Figure 4.31: Results of high speed test on medium severity herringbone track.
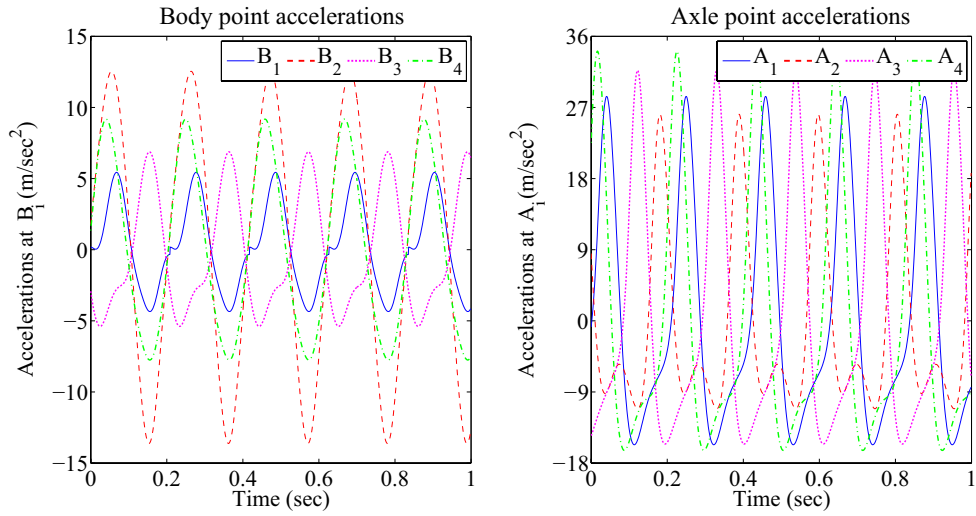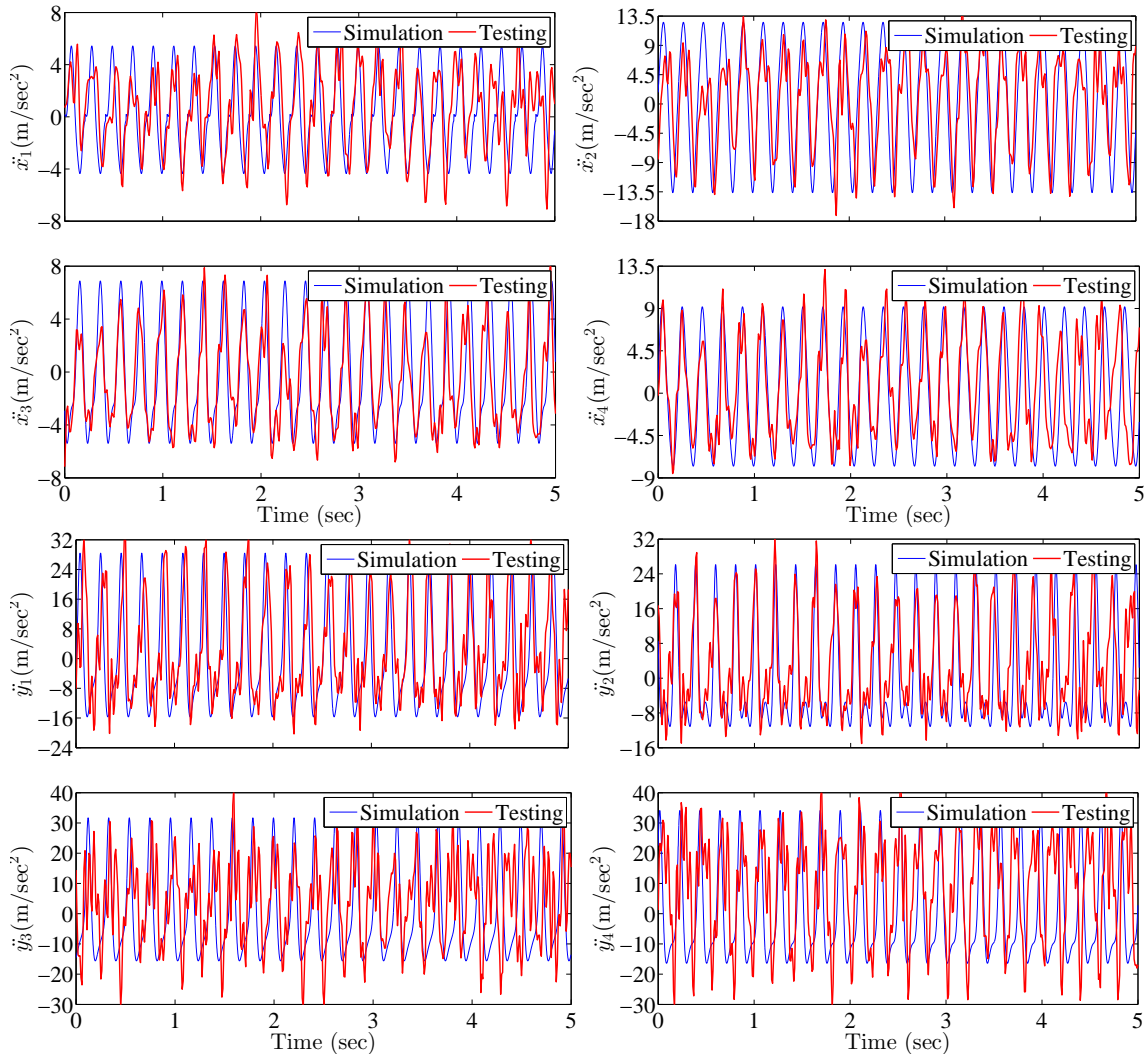
Figure 4.32: Results of low speed test on high severity herringbone track.

124
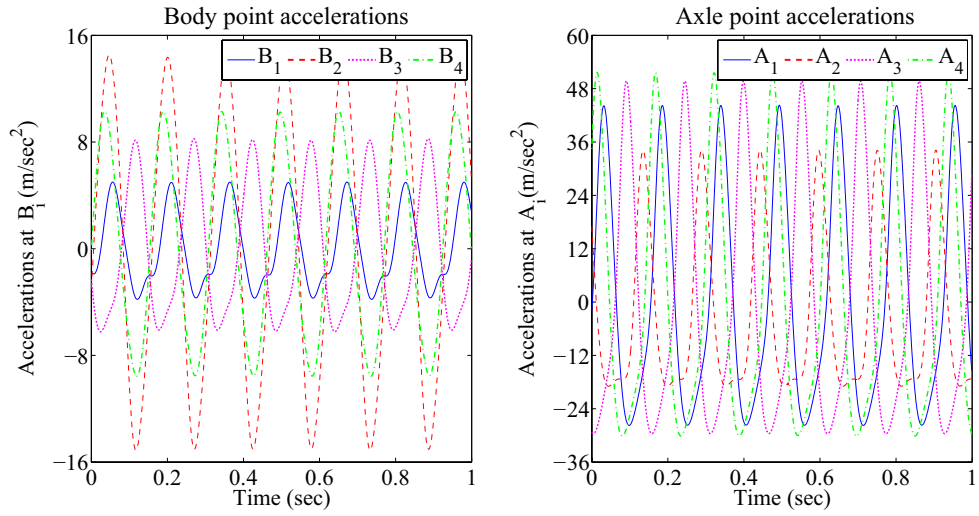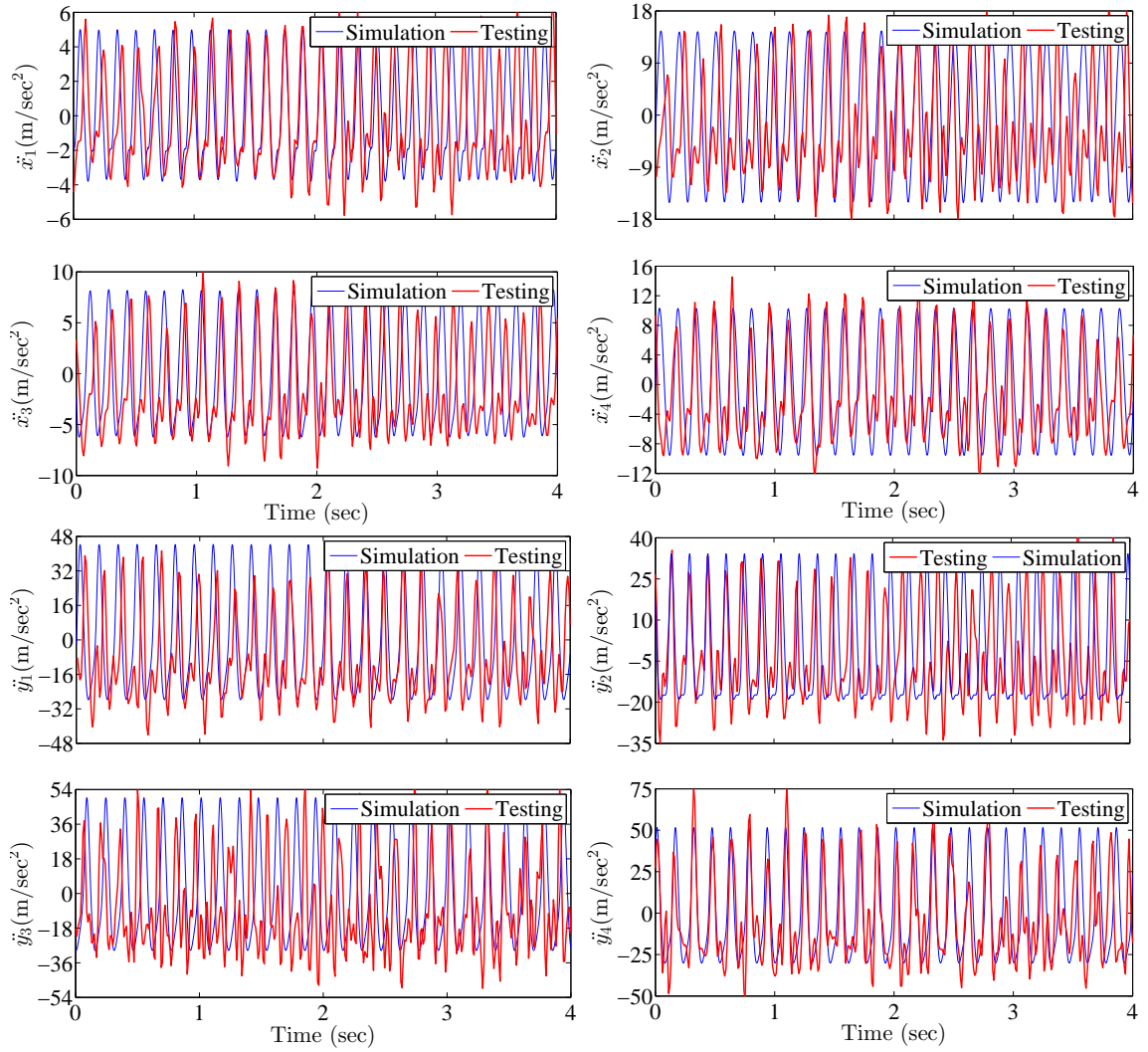
Figure 4.33: Results of high speed test on high severity herringbone track.

Chassis twist track

The chassis twist track is a 4 m wide track. The left and right track ends are sinusoids that are separated in phase by π radians, i.e., the peak at the left end and the valley at the right end occur at the same longitudinal position of the road. The track surface is prepared by the linear interpolation of these two end profiles (ruled patch [82]). The track schematic is shown in Figure 4.34.
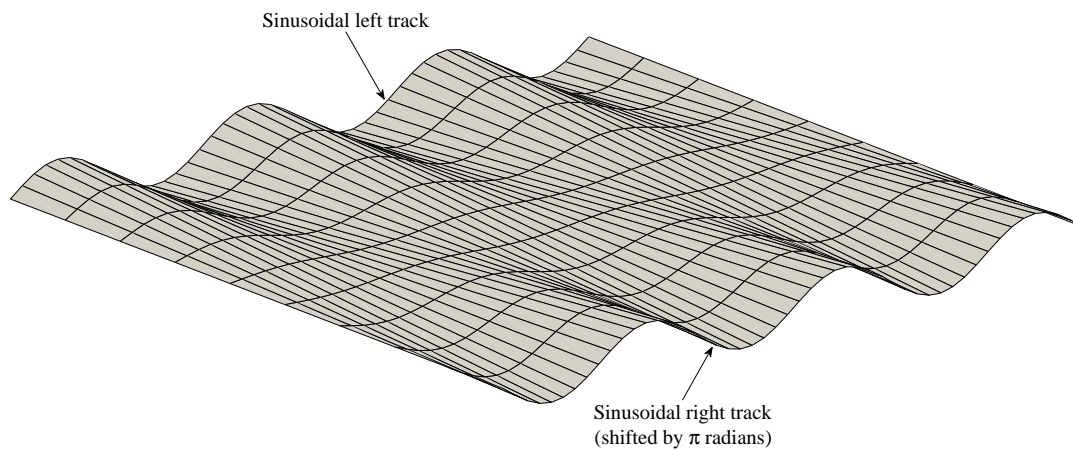
Figure 4.34: Schematic layout of the twist track.

There are three chassis twist tracks of different amplitudes and wavelengths as shown in Figure 4.35. The test details are given in Table 4.7.

Figure 4.35: Low severity (left), medium severity (middle) and high severity (right) chassis twist test tracks respectively.

126

Speed	Low severity	Medium severity	High severity
Low	7.5 kmph	6.5 kmph	5.5 kmph
High	15.5 kmph	21.5 kmph	14.5 kmph

Table 4.7: Details of vehicle testing on different chassis twist tracks.

The vehicle is driven at the left side of the track and the corresponding road inputs given to the Adams model are shown in Figures 4.37 through 4.39.

In subsequent figures, where test results are compared against the Adams model, accelerations of body points B_1 through B_4 are denoted by $\ddot{x}_1(t)$ through $\ddot{x}_4(t)$, and the accelerations of wheel axle points A_1 through A_4 are denoted by $\ddot{y}_1(t)$ through $\ddot{y}_4(t)$. The thicker lines show test data.

Figures 4.40, 4.42 and 4.44 show the comparison of simulation and test results of low speed test on low, medium and high severity chassis twist tracks. The peak heights and the peak widths match but there is a high frequency response in addition to the main low frequency response in all of these three tracks. The underlying source of this frequency component of around 10 Hz may be the CVT (continuously varying transmission).

The reason behind this speculation is that the vehicle speed on all of these three tracks is in the range of 5-7 kmph. The high frequency response is approximately at 10 Hz. The engine runs approximately at 1800 rpm. The CVT was used with a reduction ratio of 3, i.e., 600 rpm or 10 Hz.

Figures 4.41 and 4.43 show the simulation and test results of high speed tests on low and medium severity twist track. The peak heights and the peak widths match reasonably well.

Figure 4.36: Briggs and Stratton engine coupled with a CVT. Image source: Vehicle design report [71].

Figure 4.45 shows the simulation and test results of high speed tests on high severity twist track. The peak heights and the peak widths roughly match but here also tyre compliance plays a role (recall Figure 4.9(a)). Moreover in this track the suspensions behave nonlinearly as the input displacement amplitude is 200 mm.
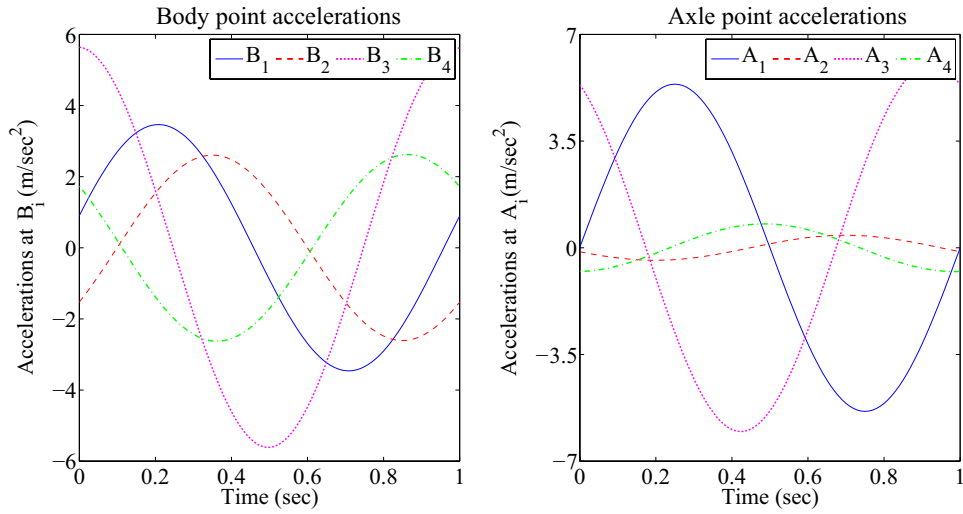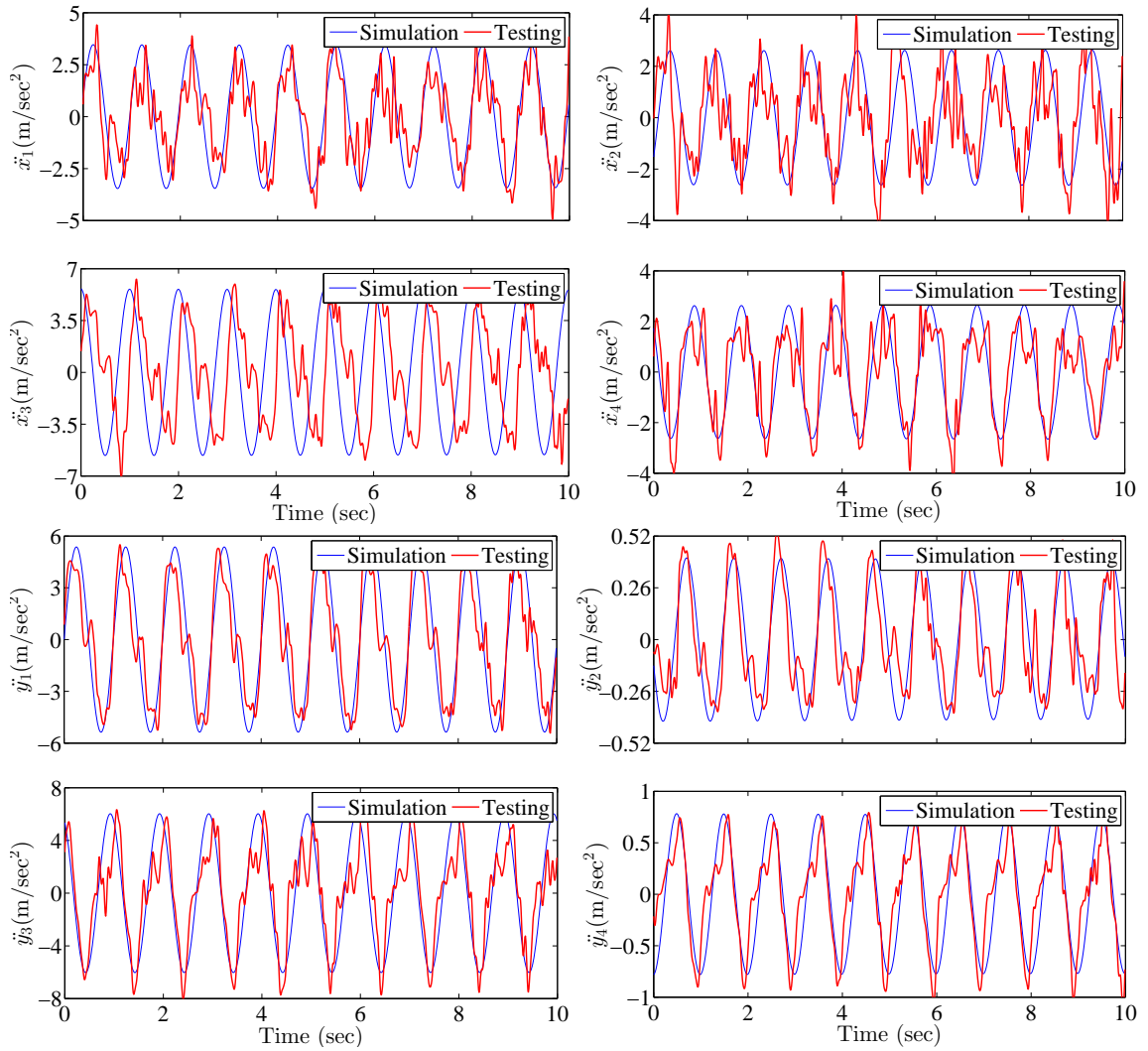
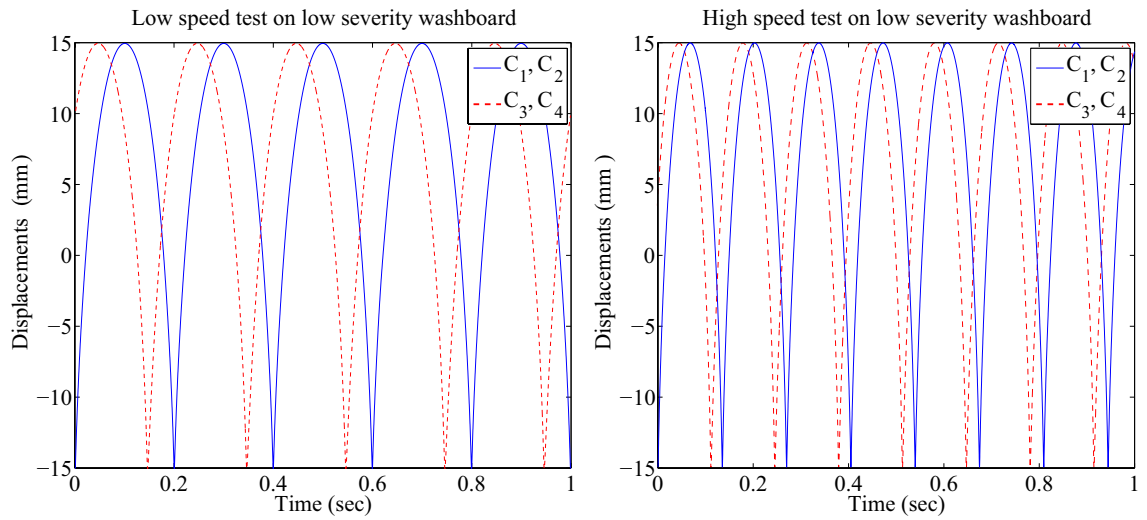Figure 4.40: Results of low speed test on low severity chassis twist track.
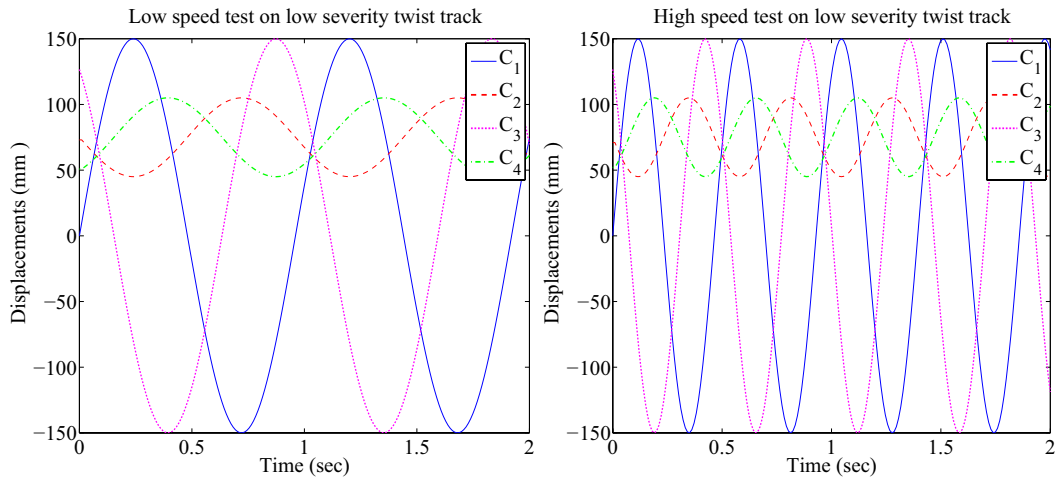
Figure 4.37: Ground displacement inputs given to the Adams model for low and high speed tests on low severity twist track respectively.
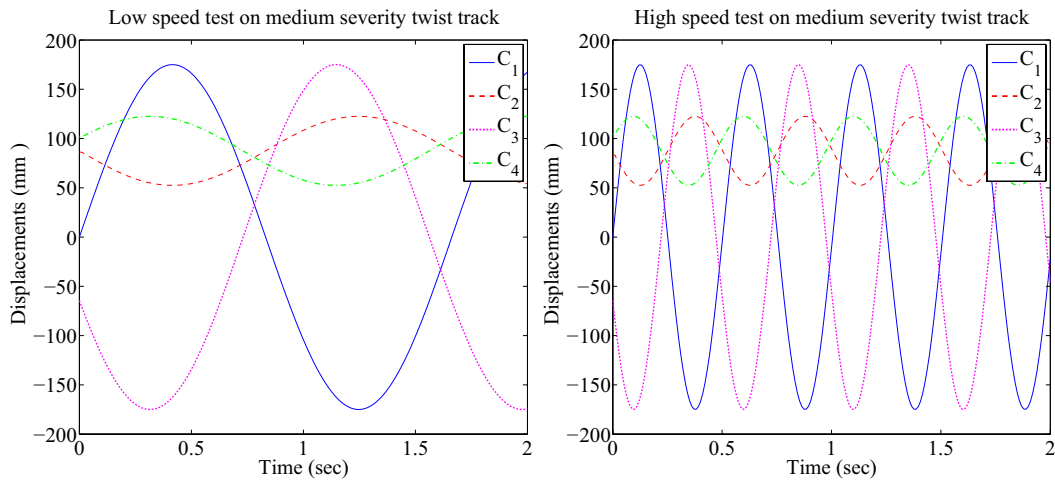
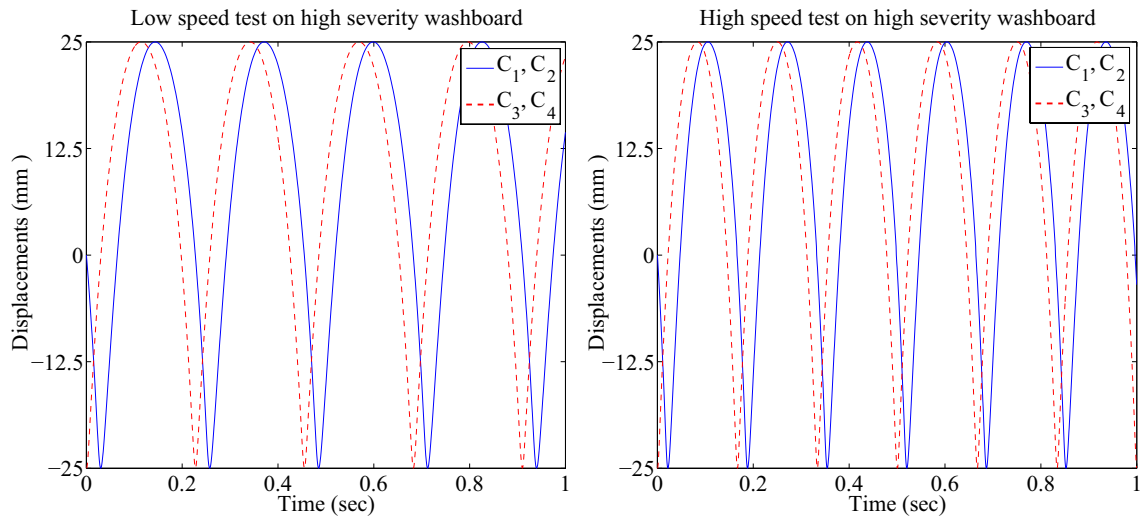Figure 4.38: Ground displacement inputs given to the Adams model for low and high speed tests on medium severity twist track respectively.
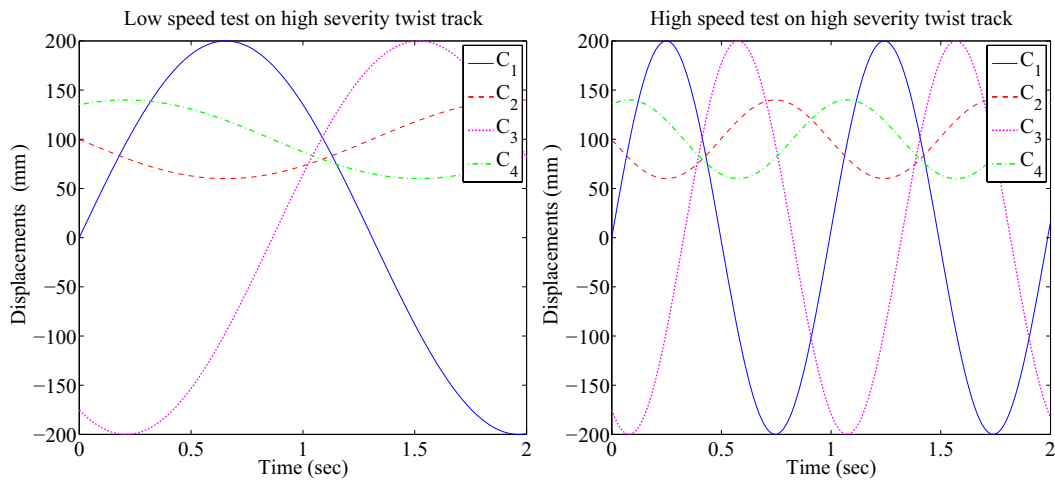
Figure 4.39: Ground displacement inputs given to the Adams model for low and high speed tests on high severity twist track respectively.
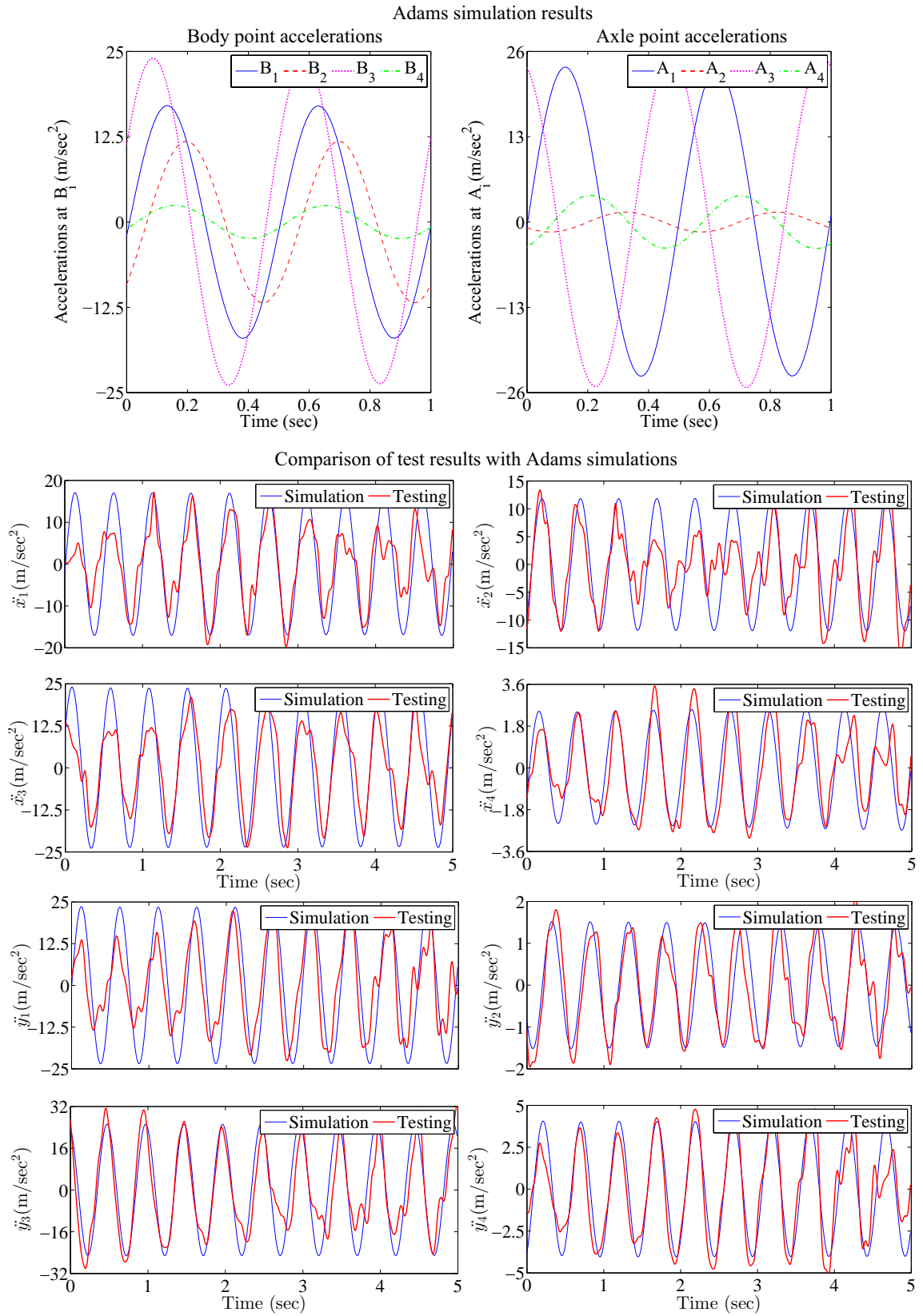
Figure 4.41: Results of high speed test on low severity chassis twist track.
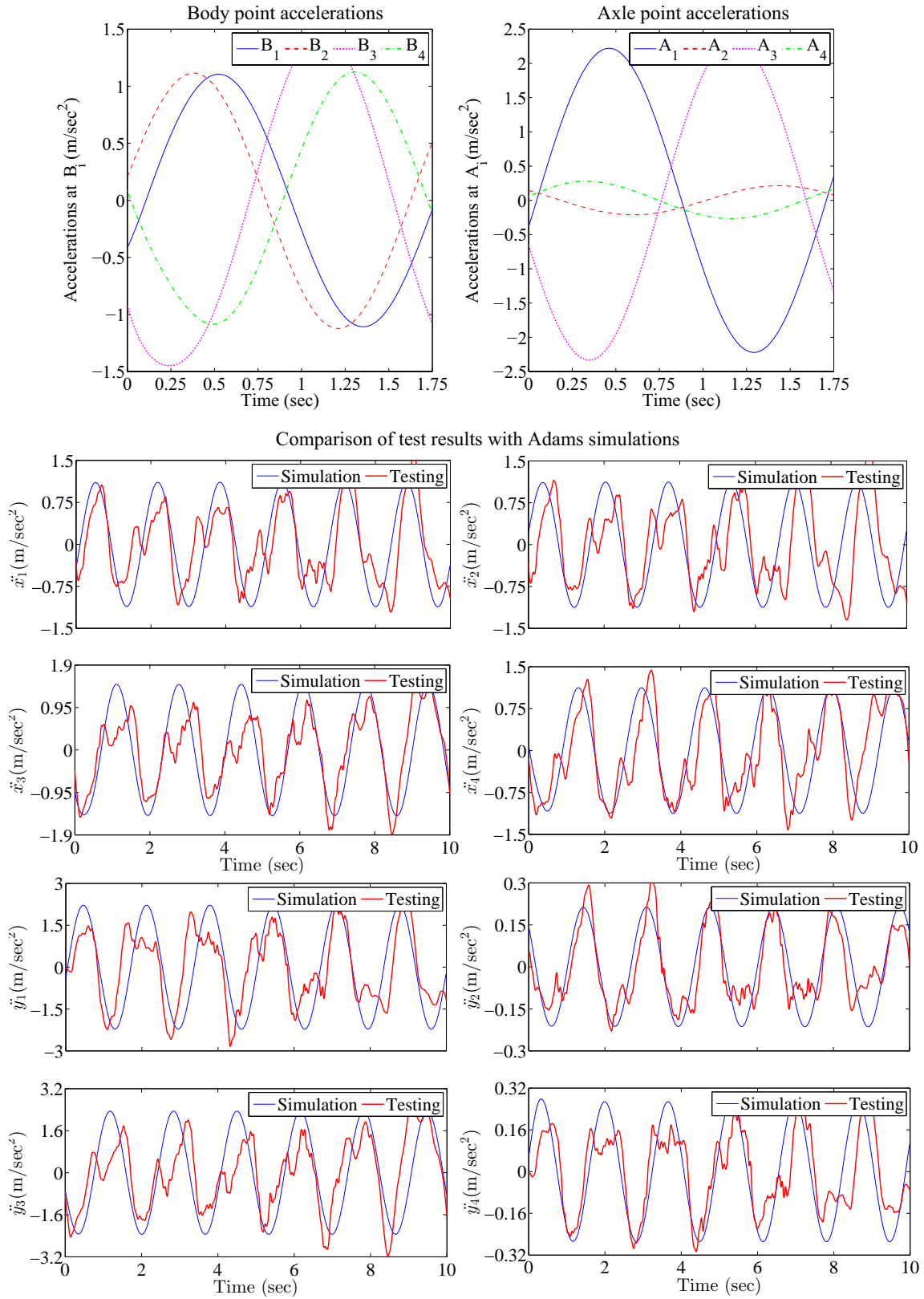
Figure 4.42: Results of low speed test on medium severity chassis twist track.

132
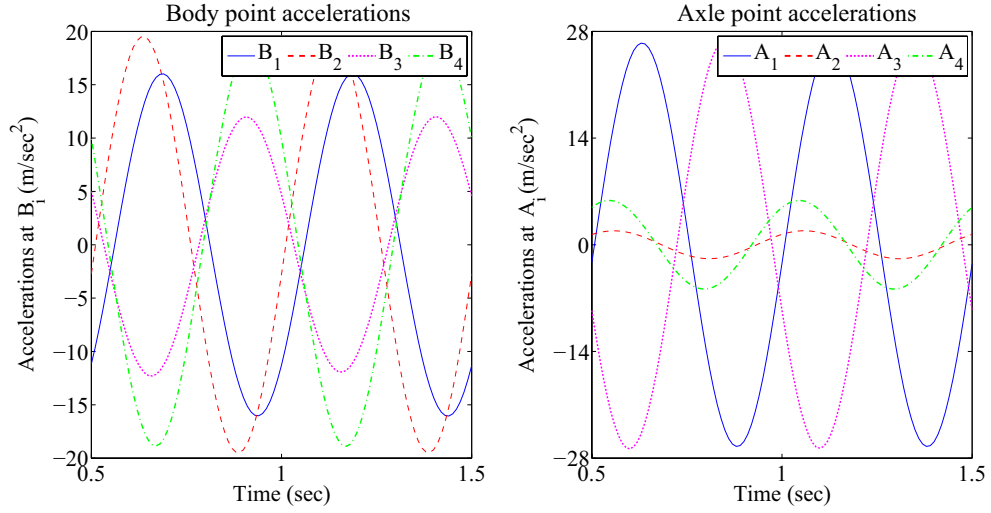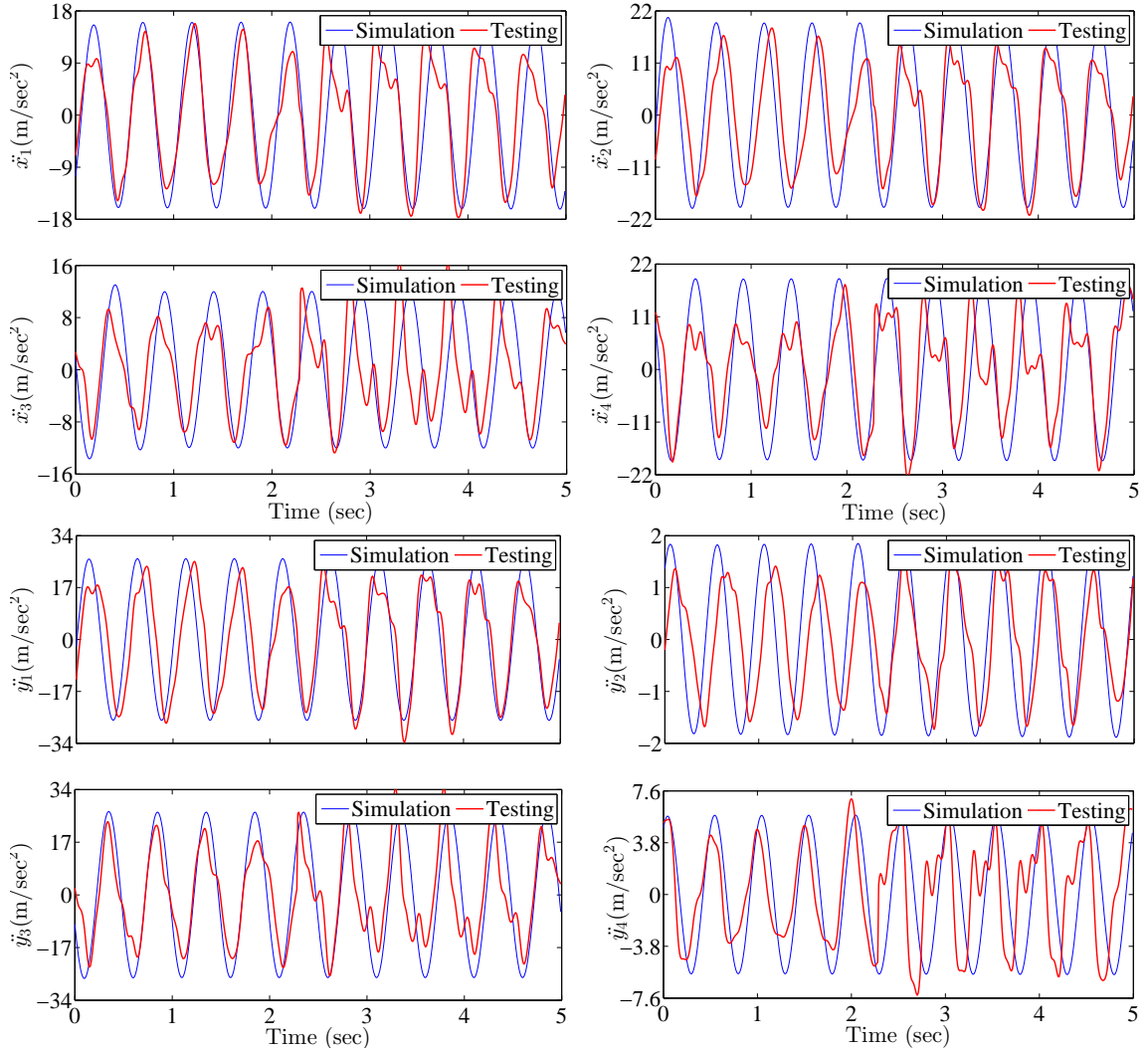
Figure 4.43: Results of high speed test on medium severity chassis twist track.
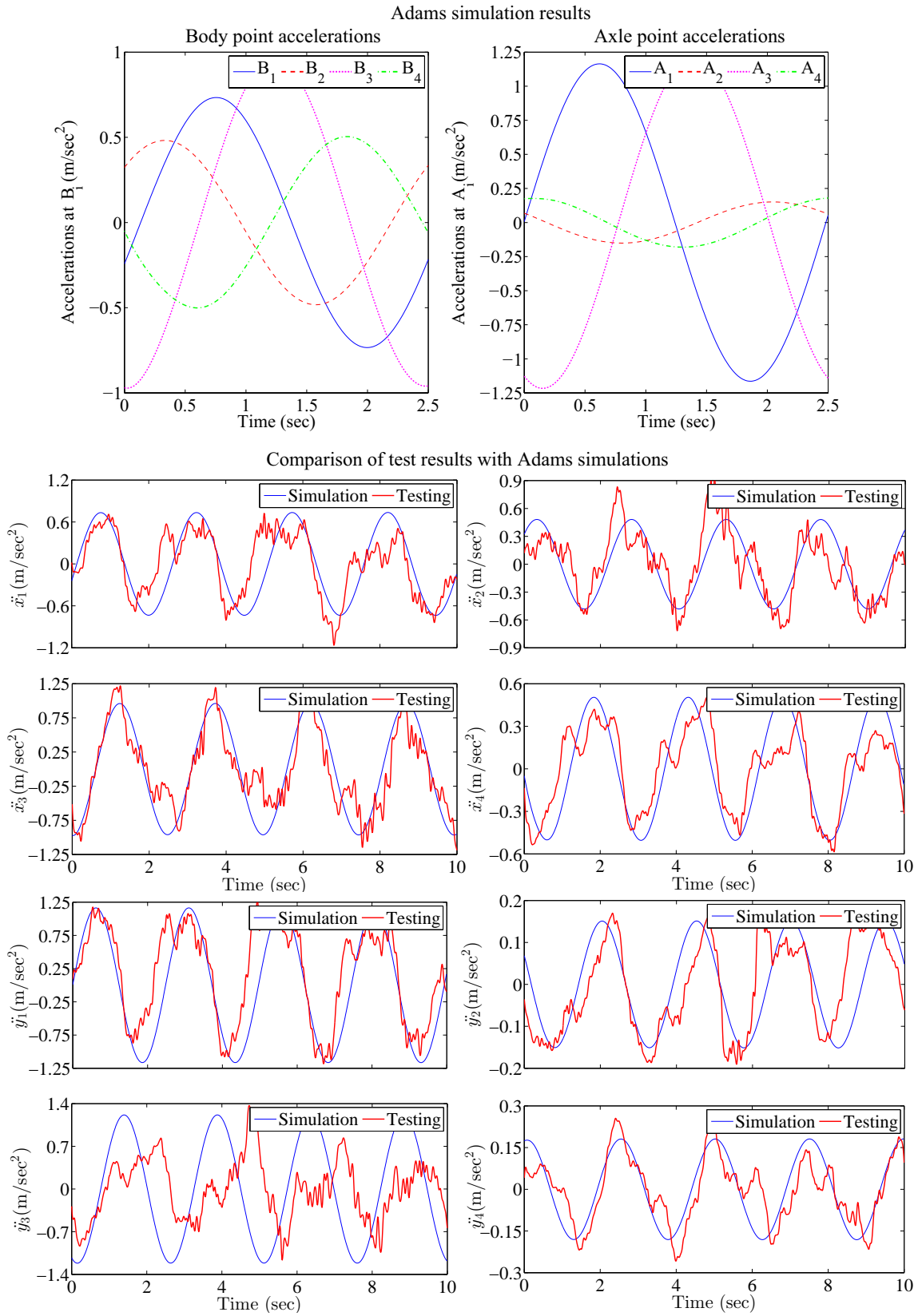
Figure 4.44: Results of low speed test on high severity chassis twist track.
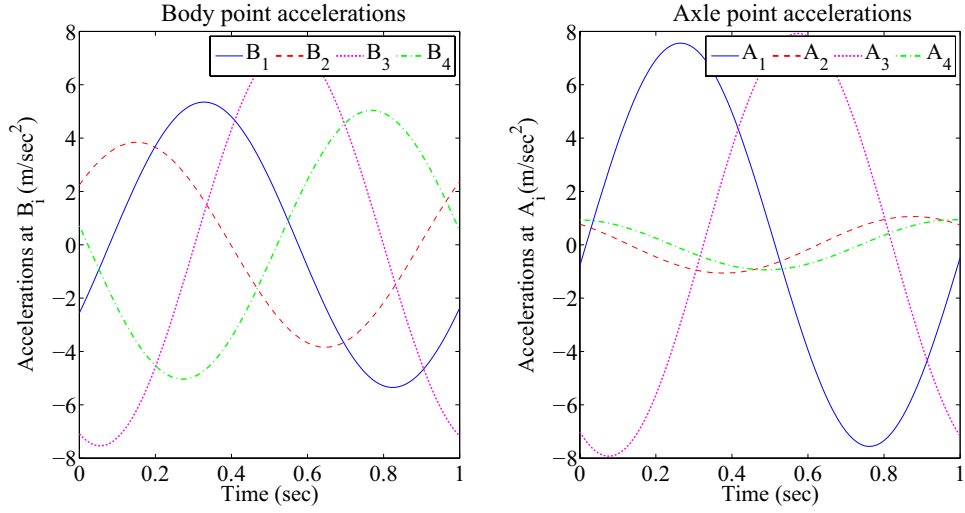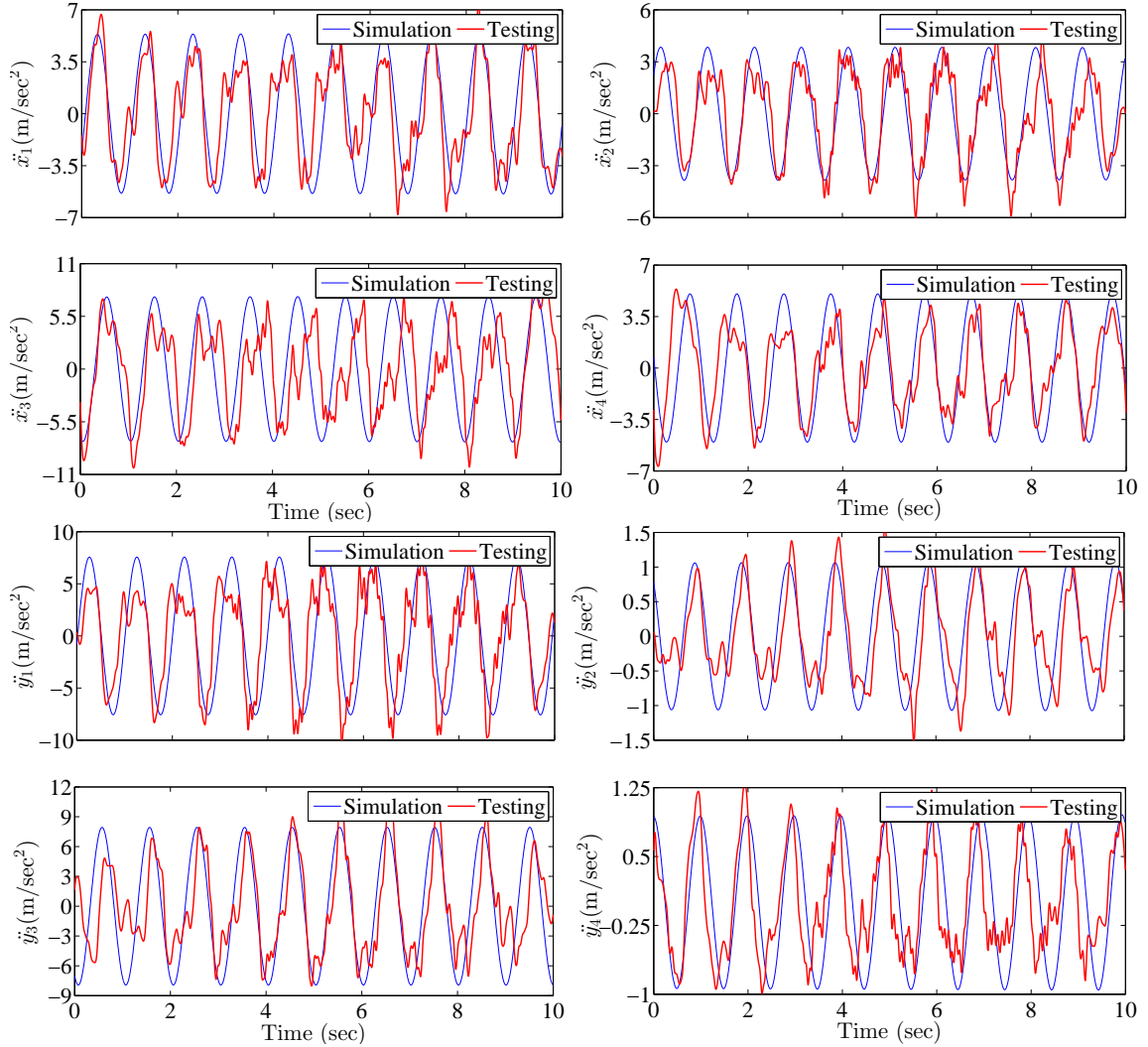
Figure 4.45: Results of high speed test on high severity chassis twist track.

One-sided washboard track

We now present the results for a test on washboard track where the ground excitation acts only on the left wheels. There are two one sided washboard tracks with low severity and high severity as shown in Figure 4.46. The vehicle tests were performed on these two tracks at speeds on 7 kmph and 13 kmph respectively.

Figure 4.46: Low (left) and high severity (right) one-sided washboard tracks.

The road inputs given to the Adams model are shown in Figure 4.47.

In subsequent figures, where test results are compared against the Adams model, accelerations of body points B_1 through B_4 are denoted by $\ddot{x}_1(t)$ through $\ddot{x}_4(t)$, and the accelerations of wheel axle points A_1 through A_4 are denoted by $\ddot{y}_1(t)$ through $\ddot{y}_4(t)$. The thicker lines show test data.

In this track there is a substantial mismatch between the Adams simulation results and test track measurements. It is because of the limitations of the Adams model.

In this track the vehicle suffers rocking motions. The vehicle mass is 220 kg while the driver weight is 75 kg. In this types of vehicle, driver inertia plays an

important role which is not adequately captured in Adams model. Moreover the driver provides a resistance to the vehicle rocking motion and there is a coupling between driver and seat and driver and steering wheel which provides a torsional stiffness which is not present in the Adams model.

This kind of modeling can be done as a part of future research work.
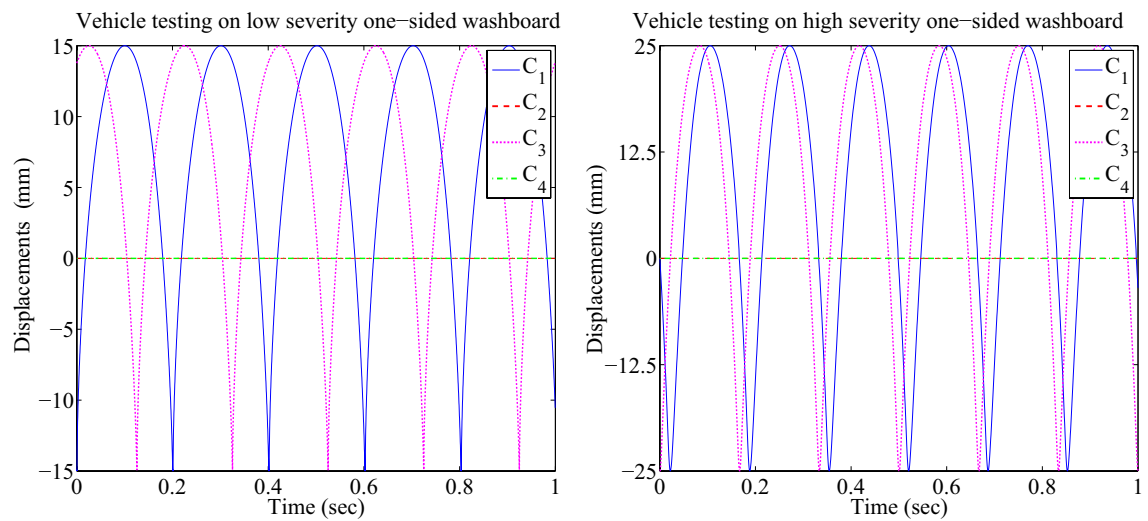
Figure 4.47: Ground displacement inputs given to the Adams model for vehicle testing on low and high severity one-sided washboard track respectively.
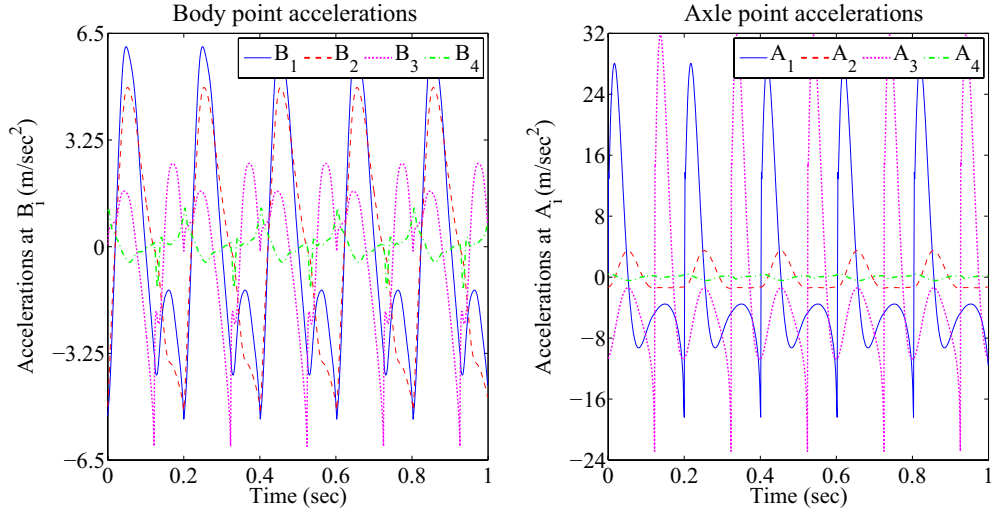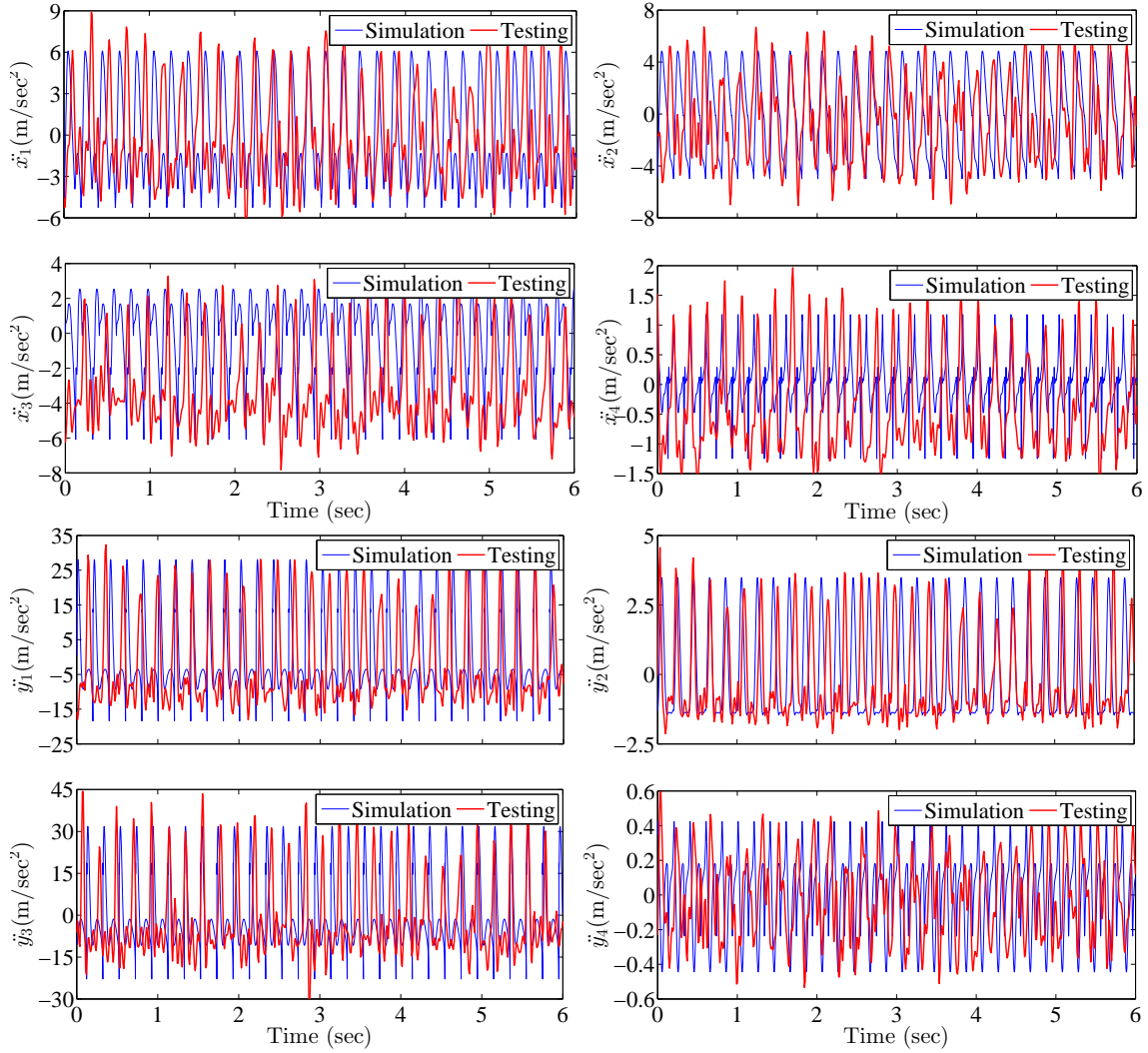
Figure 4.48: Results of low speed test on low severity one-sided washboard track.
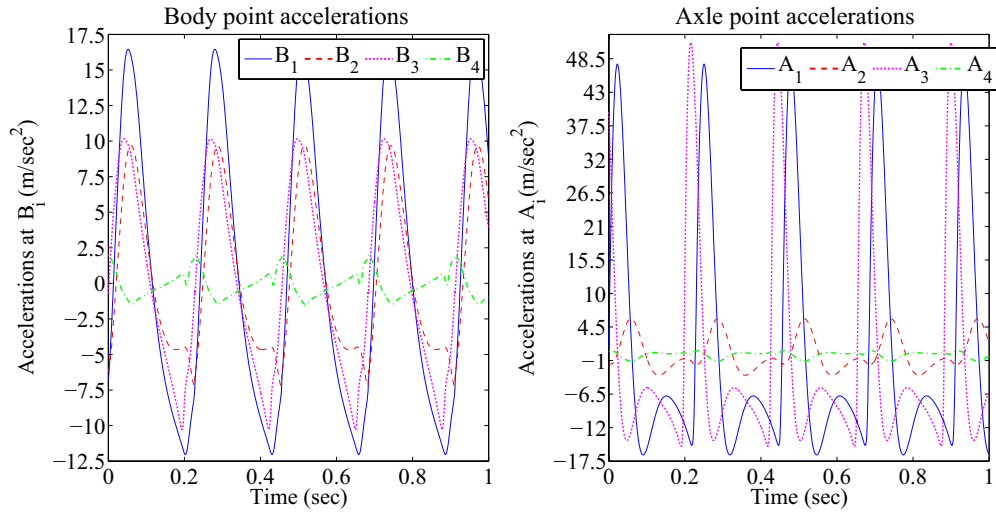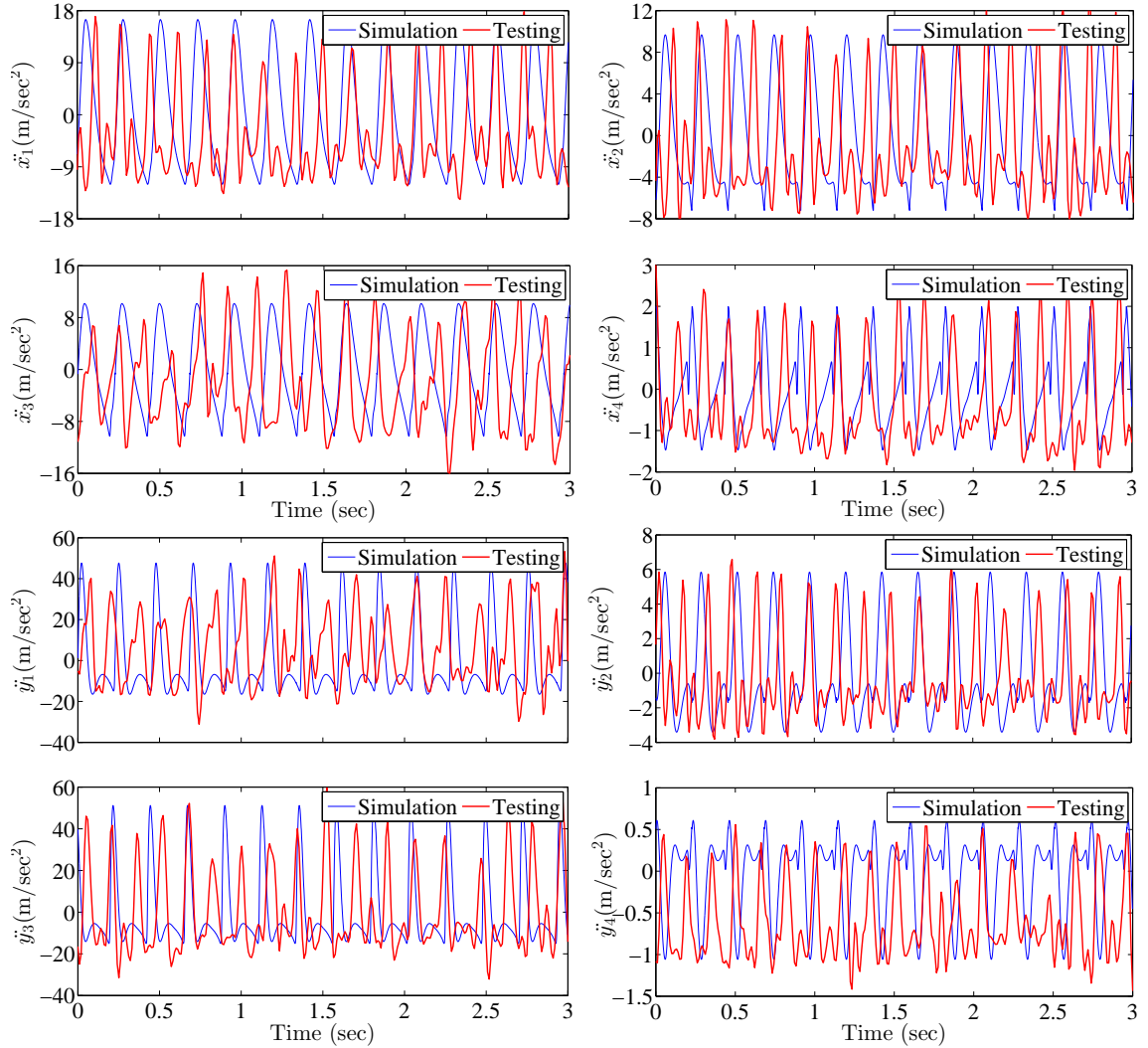
Figure 4.49: Results of low speed test on high severity one-sided washboard track.

Belgian pave track: stochastic model

The Belgian pave track is often used to evaluate vehicle ride comfort when traversing over random terrains [83]. Its surface is made up of cobbles firmly cemented together; see Figure 4.50.

Figure 4.50: Vehicle testing at Belgian pave test track.

The track width is 4 m. The elevations of different track points are measured at intervals of 150 mm in longitudinal and 250 mm in lateral directions, providing 16 sets of measurement data. The data was provided to me by NATRiP.

Such road profiles are often characterized by their power spectral density (PSD)[7] [84]. From the 16 sets of road elevation data, the displacement PSDs have been obtained using the `pwelch` function in Matlab. In order to model the pave track, the ISO 8608 road model is used [85]. It uses a two parameter spectrum to generate a road profile $Z(x)$ given by

$$S_Z(\Omega) = C \left(\frac{\Omega}{\Omega_0} \right)^{-w}, \tag{4.7}$$

---

[7]PSD is the square of the elevation of road points distributed over wave number (cycles/m).

where Ω is the spatial angular frequency, $\Omega_0 = 1$ rad/m, degree of unevenness C, and waviness w are fitting parameters. These parameters were fitted from the 16 road PSDs and are reported in Table 4.8.

C	w
$6.7\text{e} - 4$	1.36

Table 4.8: Fitting parameters of the ISO 8608 road model

The displacements corresponding to this road profile were applied to the four ground wheel contact points X_i (see Figure 4.7).

The vehicle test is conducted on the pave track at a speed of 12 kmph and results are shown in Figure 4.51.
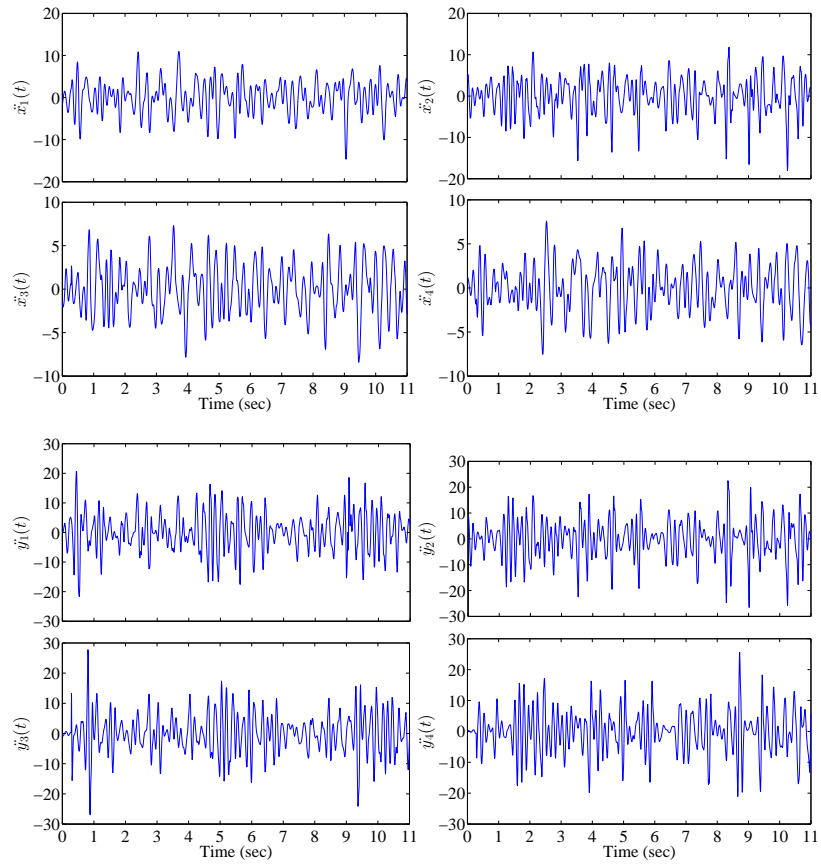
Figure 4.51: Test results for vehicle testing on pave track.

The Adams simulation results for the acceleration responses of front left and rear left body points B_1 and B_3 are compared with the test results in the frequency domain in Figure 4.52. The Adams model matches the test data quite well for frequencies upto 10 Hz.
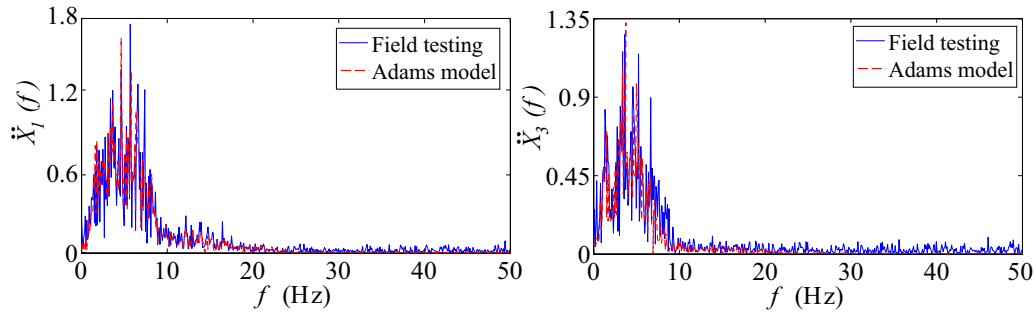
Figure 4.52: Comparison of acceleration FFT magnitudes at body points B_1 and B_3.

4.3.2 Tracks requiring full vehicle simulation

We now consider tracks that are rougher and cannot be described by using simple expressions. A full vehicle model developed earlier in Section 4.1 is to be used for simulation and meshed models of some of the tracks need to be prepared. These tracks are discussed below.

Rough road track

The rough road track is used for evaluating the rough terrain mobility and structural endurance of all-terrain vehicles. This track is primarily used to test the durability of chassis, suspension, steering, axles, differential locks, mountings, etc. under accelerated conditions. Sometimes this track is also used to find the relative movement between chassis and wheels to evaluate the vehicle ride comfort.

Figure 4.53: Left: rough road track. Right: Vehicle on rough road track.

In Figure 4.53 the track may appear smooth; but the RMS values of the displacement of this track is even higher than the RMS values of Belgian pave track.

A meshed model of the track was prepared, and for the test result correlation a full vehicle Adams model was used. From the road profile measurements[8], a meshed model of the road was prepared in Nastran and the corresponding road data file was used in Adams (see Figure 4.54).

The road surface is defined by specifying z values corresponding to nodes on a triangular mesh. The road surface was modeled using Autodesk Inventor® (see Figure 4.55(a)) and transferred to Nastran which in turn generated a road data file to be used for full vehicle simulation in Adams as shown in Figure 4.55(b).

---

[8]The elevations of all road points were measured in a grid size of 150mm×250mm for the entire rough road track.
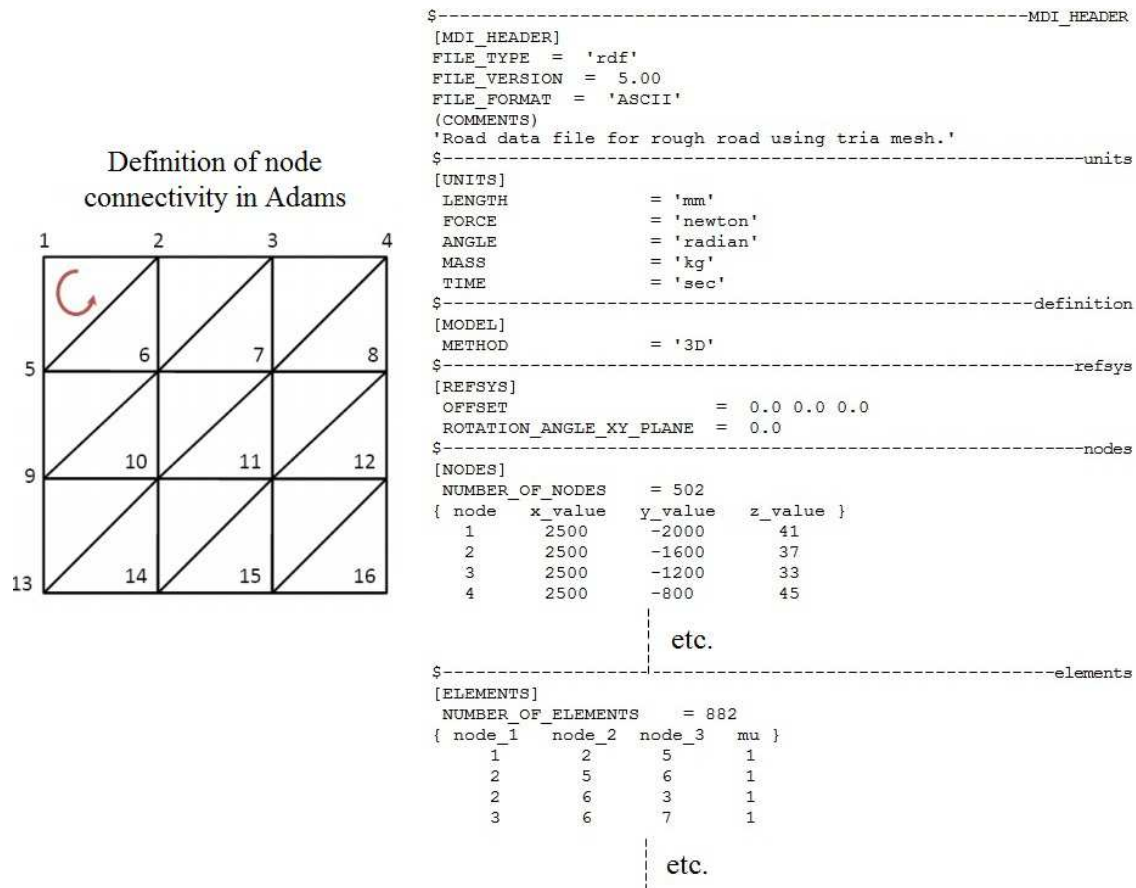
Figure 4.54: Left: 3D mesh definition in Adams. Right: Portion of rough road data file.
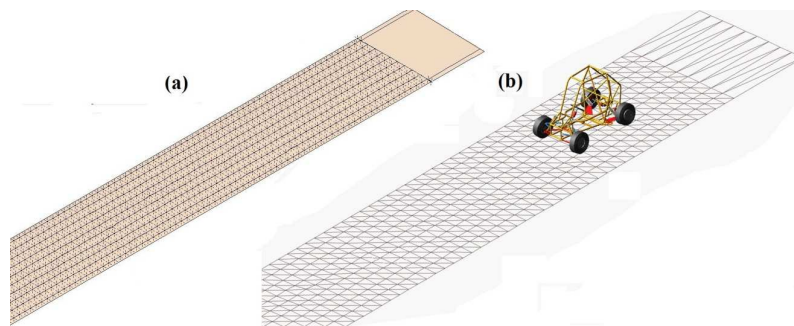
Figure 4.55: (a) Rough road surface modeling in Autodesk Inventor; (b) Simulation of vehicle running on rough road track in Adams Car.

The simulation results and the test results are not shown on the same plot because of the random-like nature of inputs. Instead qualitative aspects of the data like peak width, heights, and variability are compared visually. The vehicle test is

performed at a speed of 15 kmph. The simulation and test results for body point and axle point accelerations are compared in Figure 4.56 and 4.57.
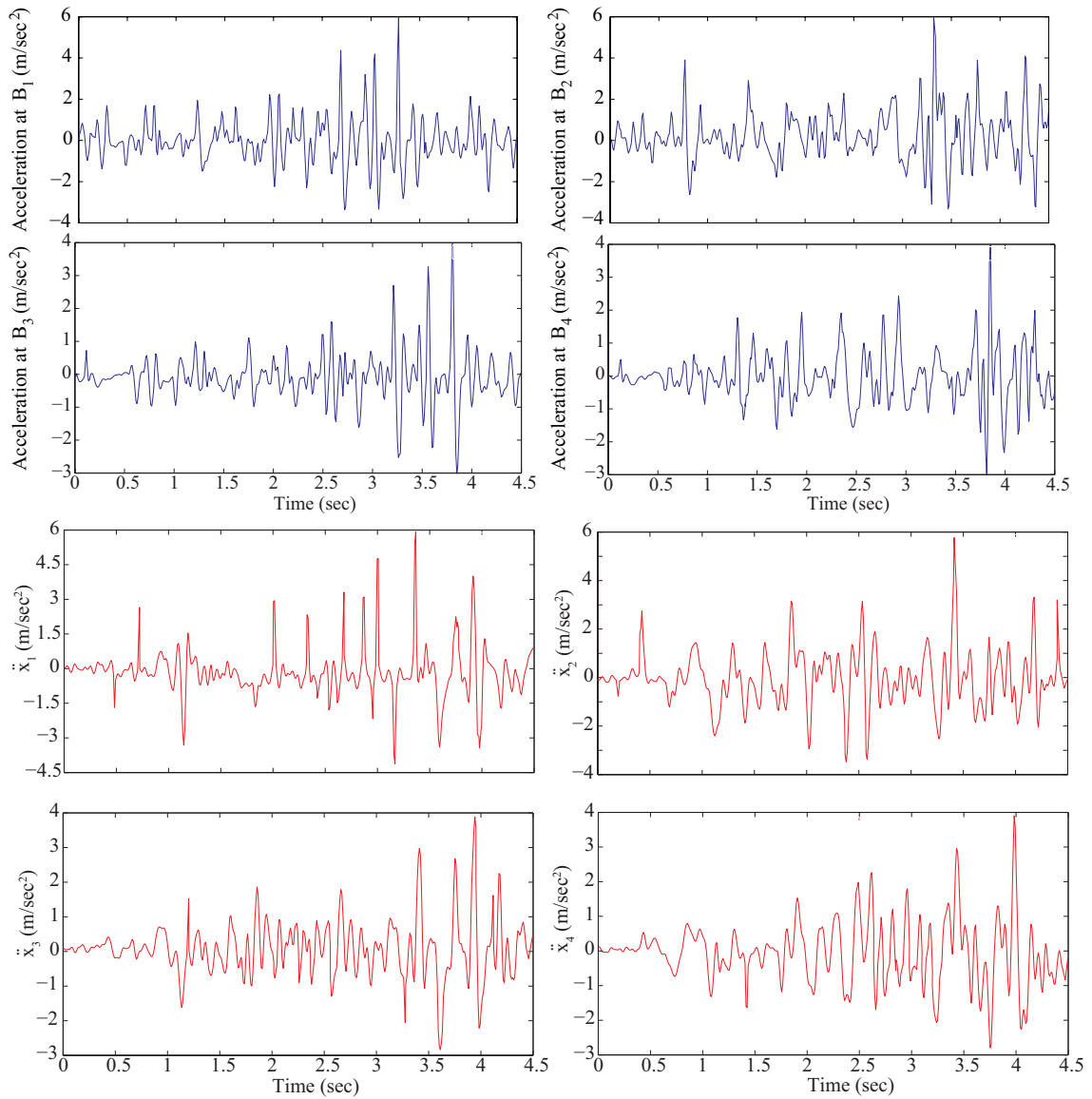
Figure 4.56: Comparison of simulation (top) and test results (bottom) of vehicle testing on rough road track.
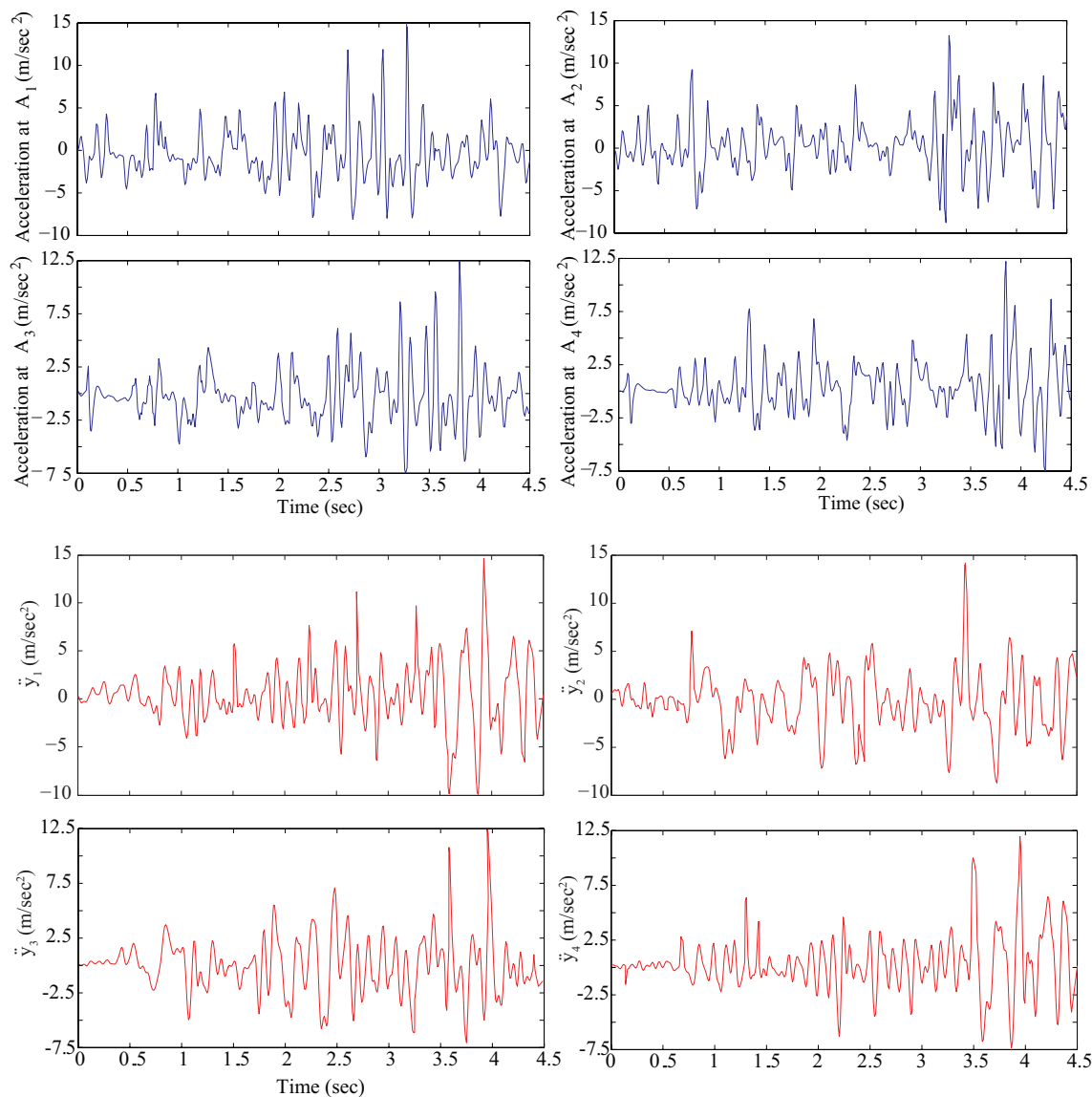
Figure 4.57: Comparison of simulation (top) and test results (bottom) of vehicle testing on rough road track.

From the simulation and test results it is observed that, roughly speaking, the peak heights, the statistical fluctuations, and the typical spacings between different peaks are quite similar. To this extent the vehicle response on rough road track is reasonably captured by the full vehicle Adams model with no change in model parameters.

Cobblestone track

This track is used for performing the accelerated durability testing, in order to access the fatigue life of a vehicle's suspension by performing repeated tests under standard conditions. It consists of different types of stones embedded in the pavement at predetermined locations (see Figure 4.58).

Figure 4.58: Left: cobblestone track. Right: Vehicle running on cobblestone track.

As was done for the rough road track, here also the road surface was modeled using Autodesk Inventor® (see Figure 4.59), is subsequently meshed using "tria" (triangular) elements in Nastran, and the generated road data file was used in Adams.

Figure 4.59: Top: Dimension details of different types of stones used in the cobblestone track. Bottom: Cobblestone track modeled in Autodesk Inventor.

For the cobblestone track, too, a full vehicle model in Adams is used for test correlation (see Figure 4.60).

Figure 4.60: (a) simulation of vehicle running on cobblestone track in Adams Car; (b) zoomed-in wireframe image showing the road mesh.

The vehicle test is performed at a speed of 25 kmph. The simulation and test results are compared in Figures 4.61 and 4.62.

148

Figure 4.61: Comparison of simulation (top) and test (bottom) results for vehicle running on cobblestone track.
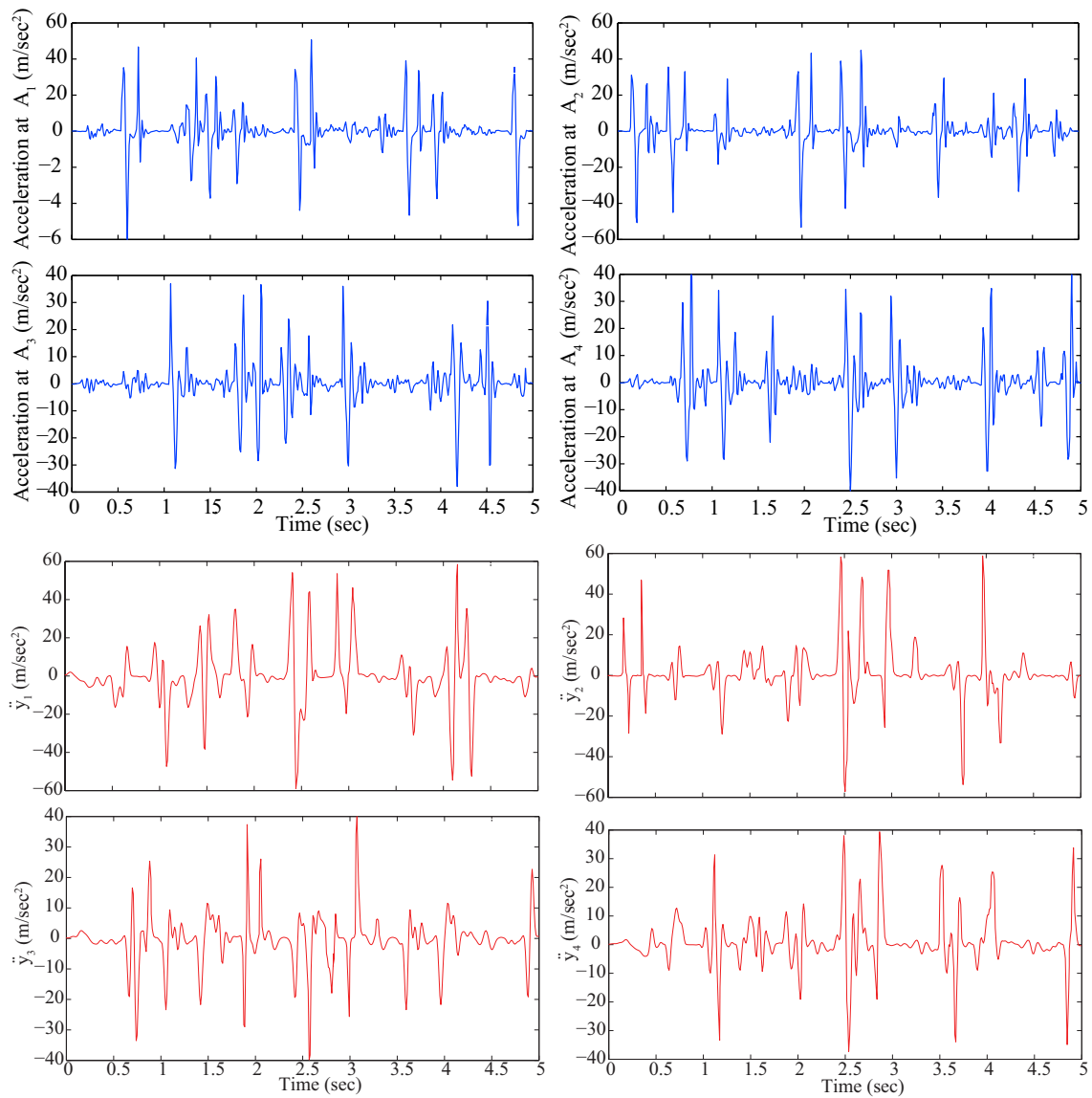
Figure 4.62: Comparison of simulation (top) and test (bottom) results for vehicle running on cobblestone track.

By comparing the simulation and field test results it has been observed that, roughly speaking, the peak heights, the statistical fluctuations and the typical spacings between different peaks are similar. To this extent the vehicle response on cobblestone track is reasonably captured by the full vehicle Adams model with no change in model parameters.

Sine sweep track

This is a sinusoidal track with varying wavelength. The wavelength changes from 400 mm to 600 mm in 24 meters (see Figure 4.63).

Figure 4.63: Left: sinesweep track (the decreasing wavelength is visible); Right: vehicle on the sinesweep track.

The idea behind frequency sweep testing is to excite a vehicle, driven at constant speed, with increasing (or decreasing) frequency. It excites the vehicle with a specified frequency sweep to detect and solve squeak and rattle (S & R) issues.

The vehicle test is conducted at a speed of 10.5 kmph. The sine-sweep track has been prepared using the 3D road builder interface in Adams Car [86]. The full vehicle model is used for simulation (see Figure 4.64).
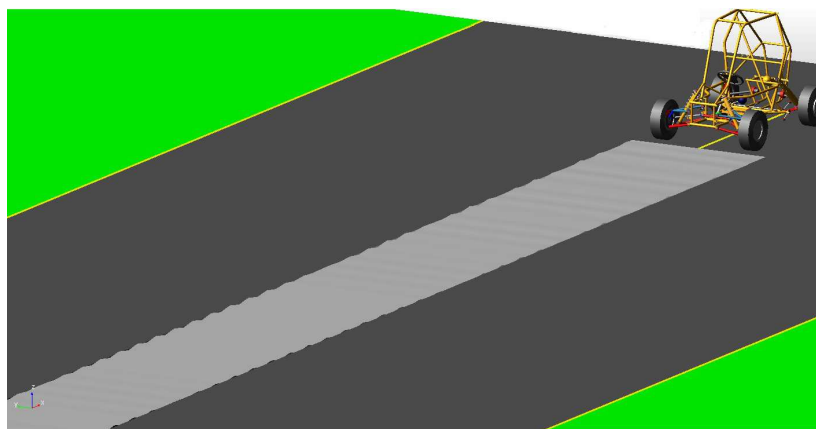
Figure 4.64: Vehicle running on sine-sweep track in Adams Car.

The test results are compared against the Adams model in Figure 4.65.
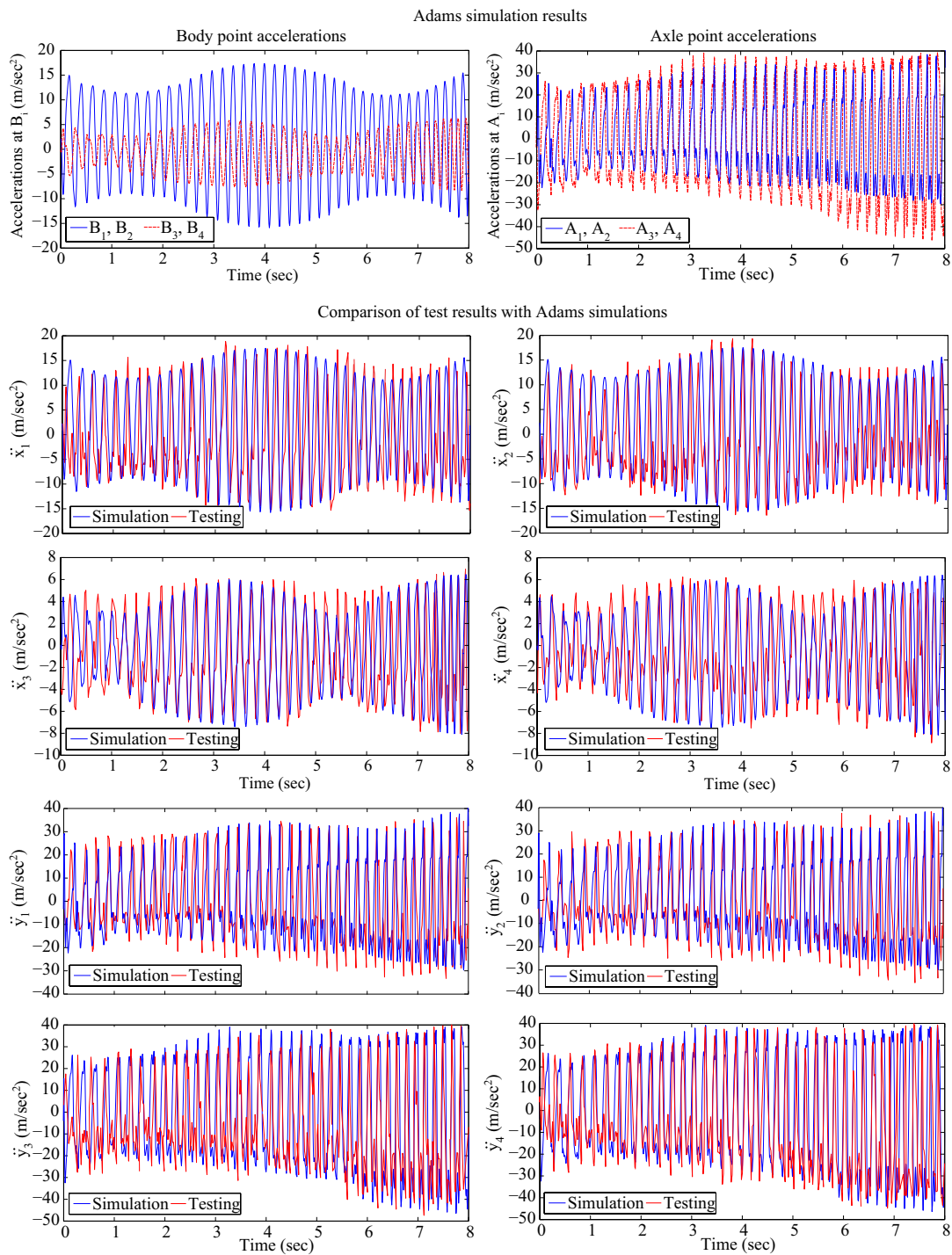
Figure 4.65: Results of vehicle testing on sine sweep track.

The full vehicle model reasonably matches the field test results with the peak heights matching and the peak widths comparable. The modulation in the amplitude of the response is reasonable captured as well.

4.3.3 Other tests conducted at SGSITS, Indore

Some other tests, not requiring test tracks, were conducted at SGSITS¡ Indore with help from students of that institute[9].

Half sine bump

The vehicle is driven over a bump of length 1000 mm and amplitude 200 mm (see Figure 4.66).

Figure 4.66: Left: bump dimensions. Right: vehicle traversing over the bump.

The full vehicle simulation was performed in Adams Car as shown in Figure 4.67.
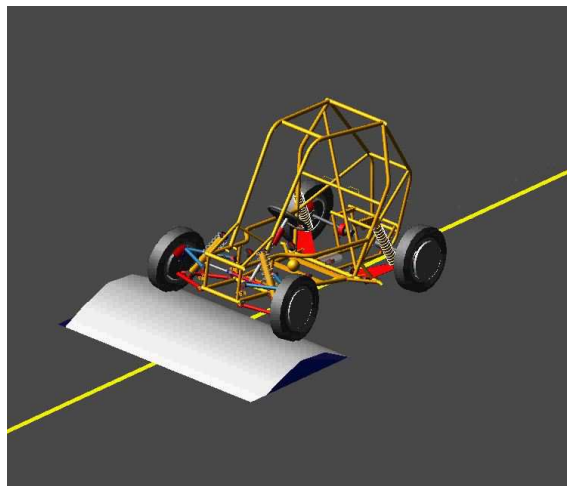
Figure 4.67: Full vehicle simulation on half sine bump track.

---

[9]Mr. Amit Singh helped in preparing test conditions and Mr. Jap Pratap drove the vehicle.

Two tests were conducted at 7 kmph and 15 kmph respectively. The test results are shown in Figures 4.68 and 4.69. It is seen that for this transient case, the qualitative match is excellent and the quantitative match is reasonable.
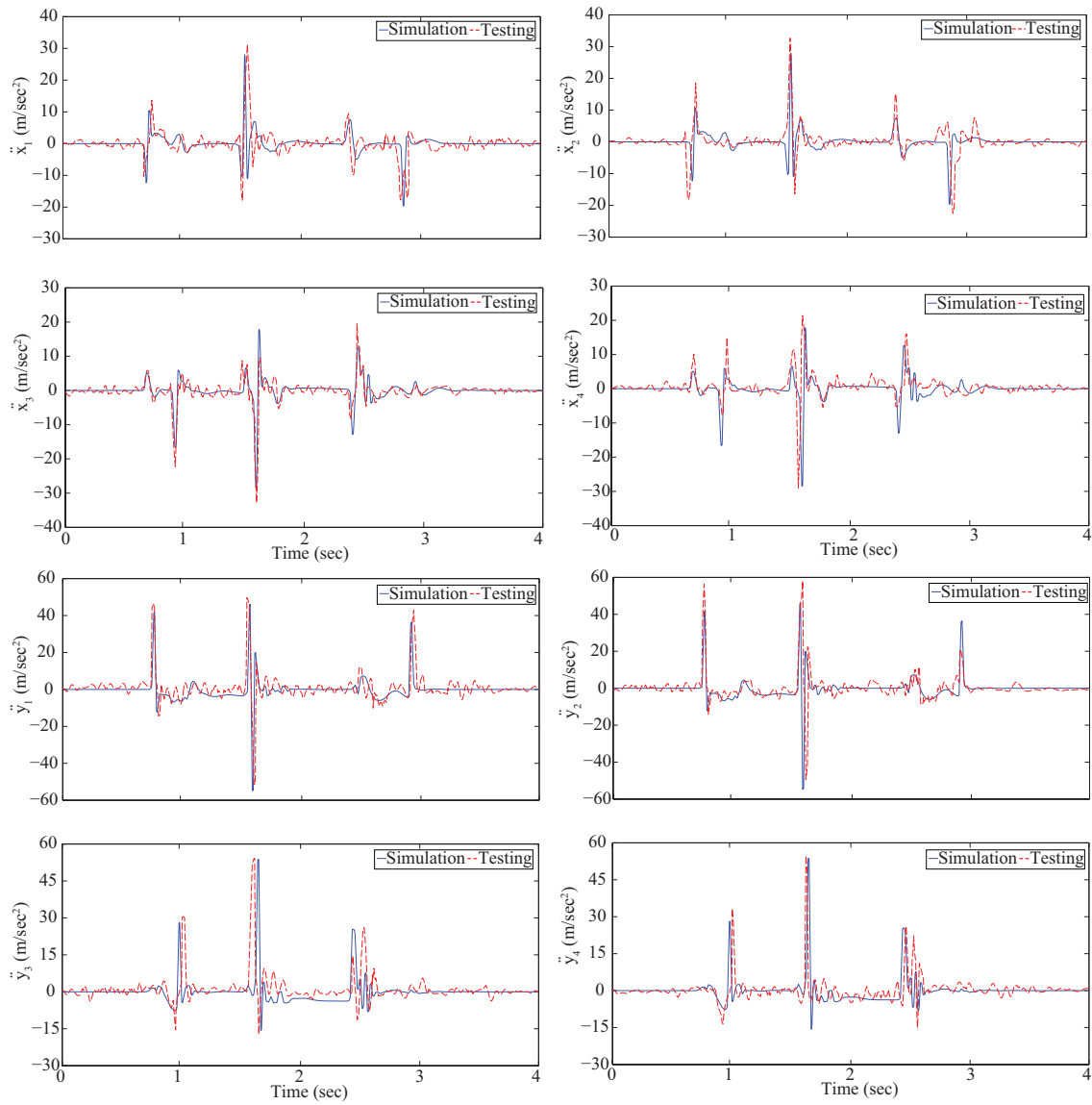
Figure 4.68: Results of vehicle testing on half sine bump track (speed 7 kmph).
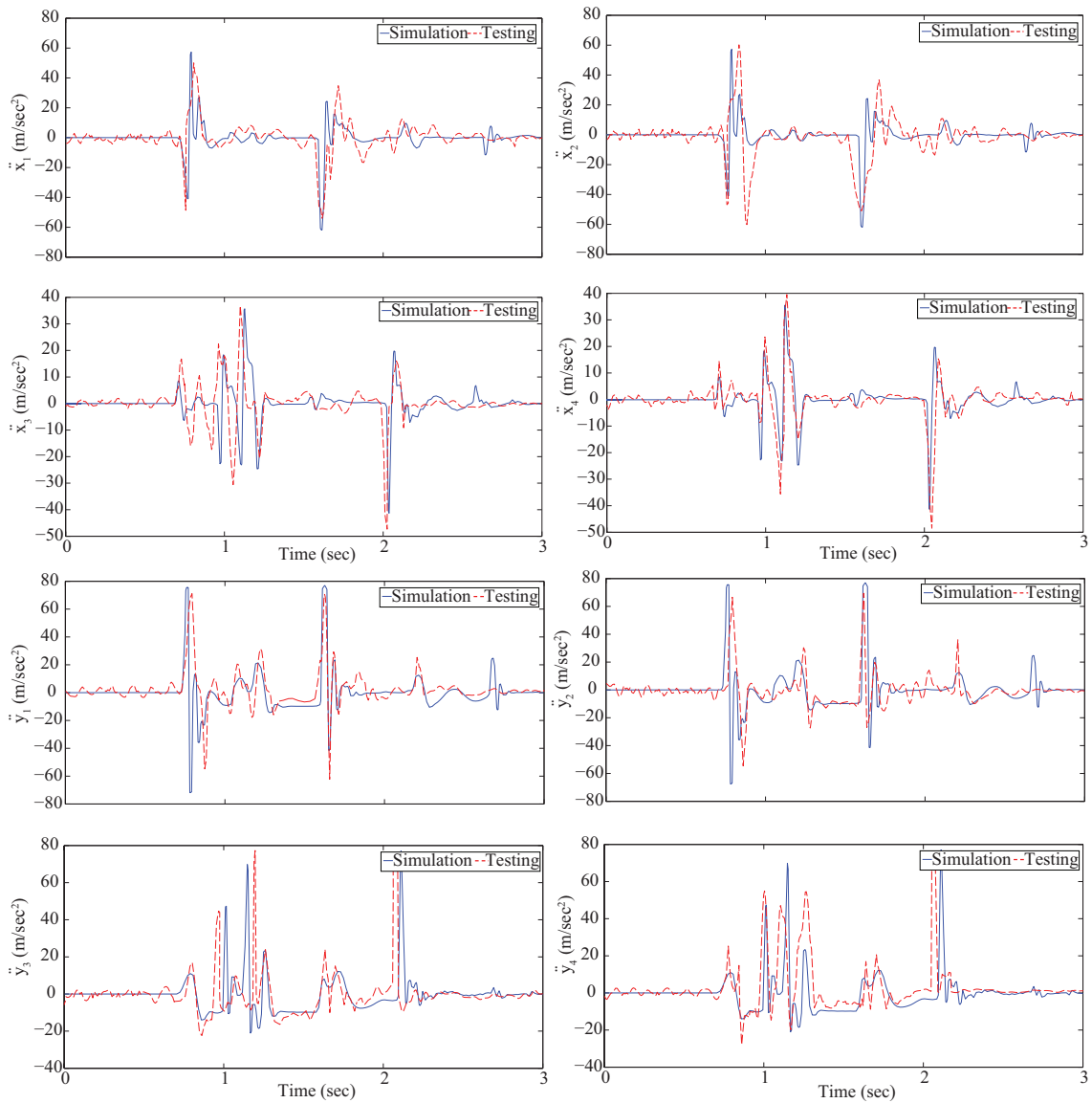
Figure 4.69: Results of vehicle testing on half sine bump track (speed 15 kmph).

Single sided half sine bump track

This test is same as the half sine bump track but here only the right wheels go over the bump (see Figure 4.70). Two tests are conducted at speeds 5 kmph and 12 kmph. The test results are shown in Figures 4.72 and 4.73.
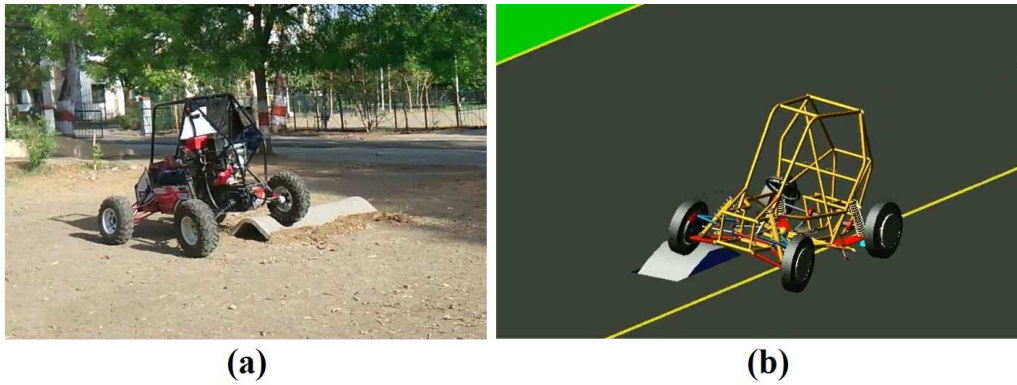
Figure 4.70: (a) Right wheels traversing over the bump; (b) vehicle simulation in Adams.

Step bump track

In this test the vehicle traverses over a sharp step bump (see Figure 4.71). The bump height is 80 mm and width is 200 mm. The vehicle test is conducted at 15 kmph. The test results are shown in Figure 4.74.
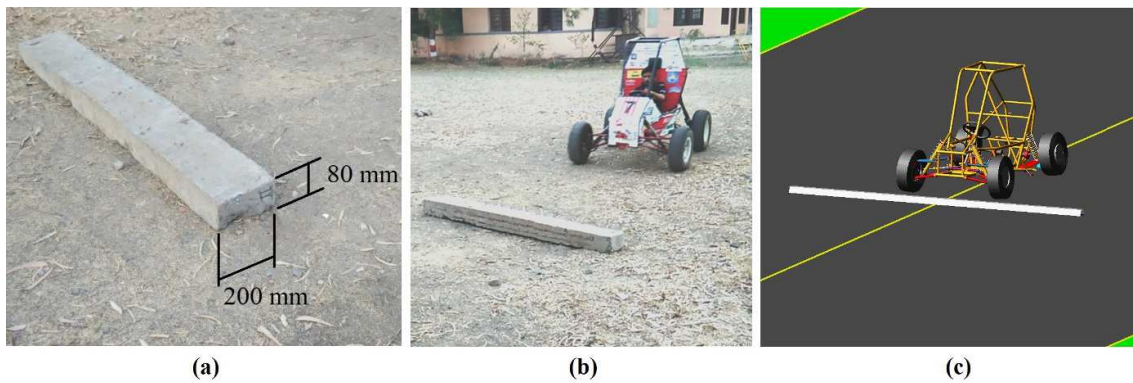
Figure 4.71: (a) Bump dimensions; (b) vehicle testing; (c) Adams simulation.

Again in Figures 4.72, 4.73 and 4.74 it is seen that, the qualitative match is excellent and the quantitative match is reasonable.
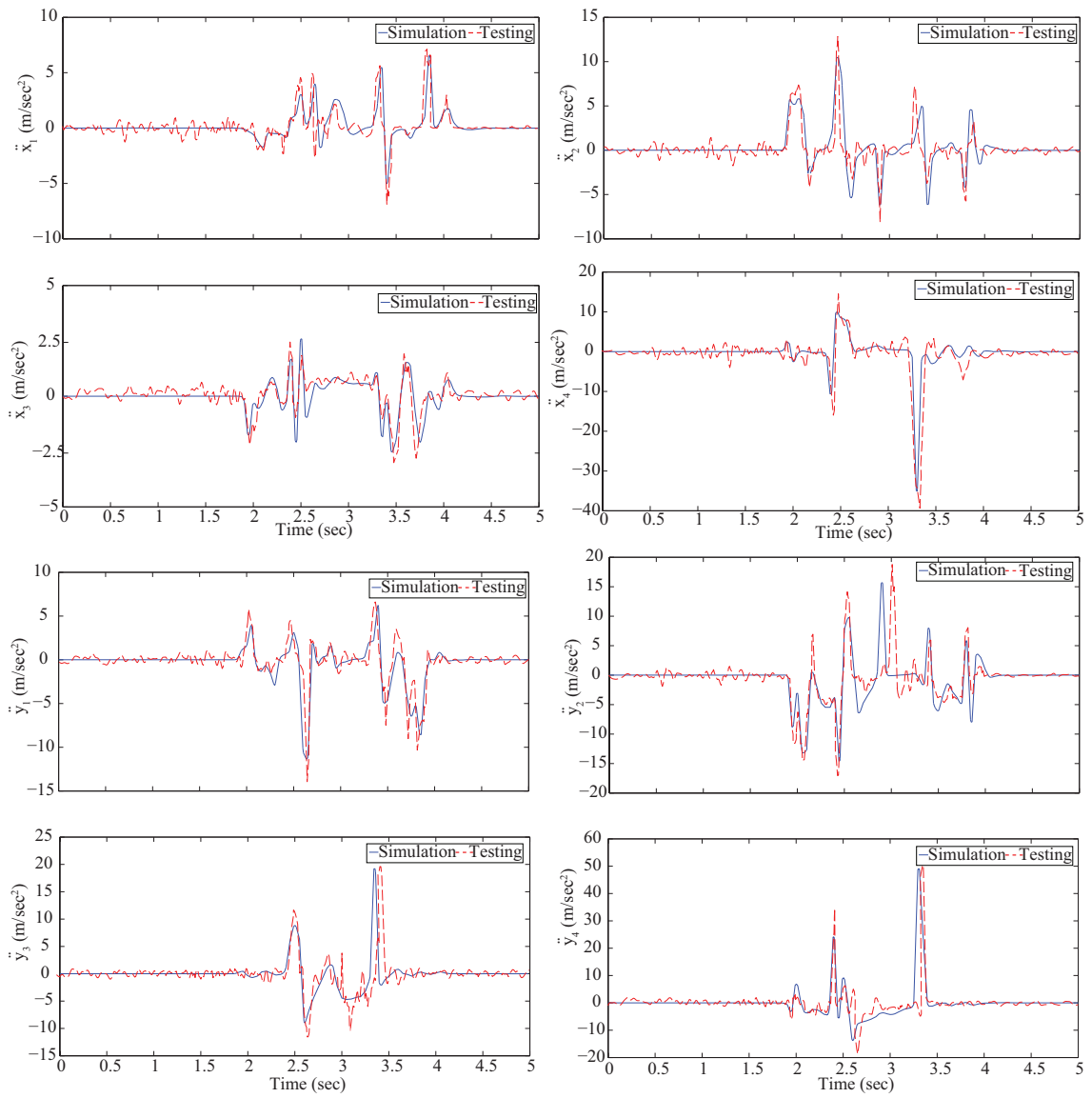
Figure 4.72: Results of vehicle testing on half sine single bump track (speed 5 kmph).
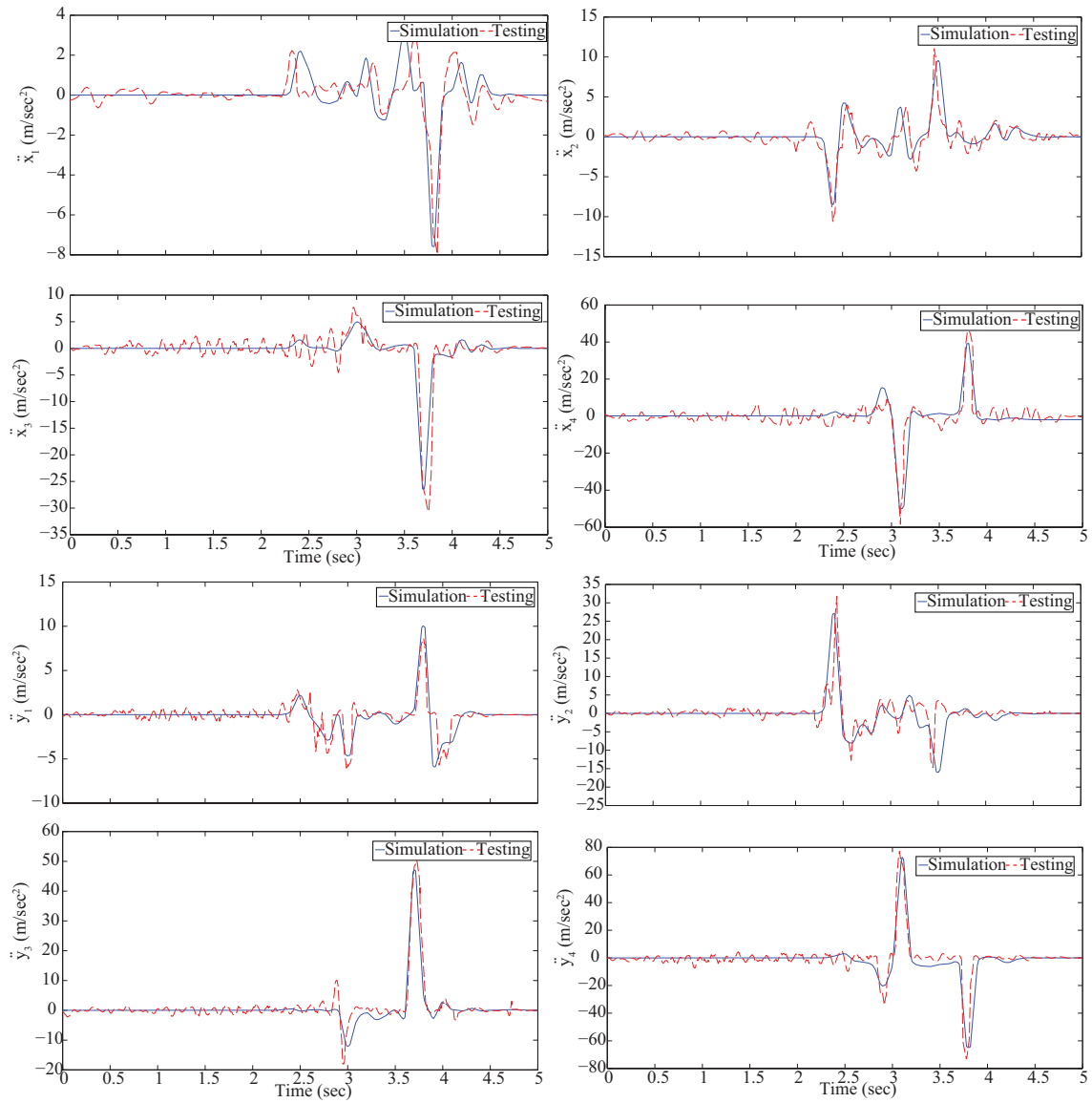
Figure 4.73: Results of vehicle testing on half sine single bump track (speed 12 kmph).
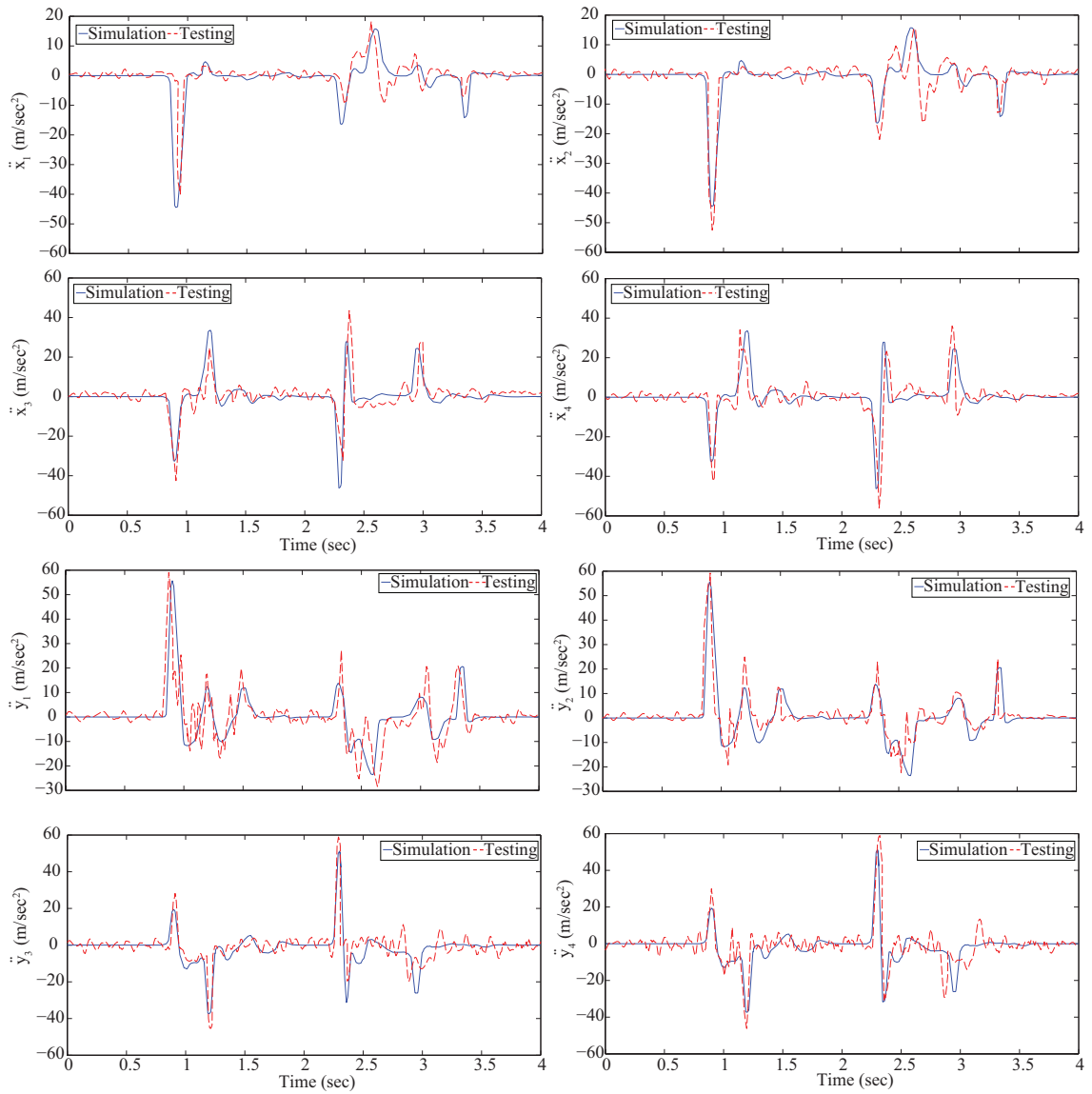
Figure 4.74: Results of vehicle testing on step bump track (speed 15 kmph).

This completes the vehicle testing and Adams model validation portion of this thesis. The test data acquired is also used to develop a reduced order Laplace domain model of the vehicle in the succeeding chapter.

4.4 Concluding remarks

A partial validation of the Adams model for an ATV against the field test results, was presented in this chapter. Such a simplified model is able to capture the essential vertical suspension dynamic characteristics. The present approach of using test track data to partially validate the model is a practical contribution presenting an inexpensive option that nevertheless provides useful information and insights. It gives the user an alternative approach for situations where a conventional four post test setup is not available. The simulation results match the experimental results reasonably well for several tests spanning a wide range of operating conditions.

In some of the tests, there is a mismatch between the Adams model results and field test measurements, essentially because of the limitations of the Adams model. Some possible reasons for the mismatch are listed below.

1. The displacement inputs used in simulations are possibly smoother than the actual wheel displacements because of small-scale roughness on the road surface.

2. When the vehicle moves on the track, there are longitudinal accelerations. These accelerations cause pitching oscillations which cause vertical accelerations in the frame, and these oscillations are not captured by the Adams model with purely vertical base excitations.

3. The forward speed of the manually driven vehicle does show some variation, which leads low frequency modulation in the response, not captured in the Adams simulation.

4. The vehicle does not have a differential, so wheel slip may occur on uneven

tracks. In the Adams model, the displacements given to the wheel contact points C_i are calculated from idealized theory with no wheel slip.

5. The test tracks are curved at many places (see Figure 4.75). This causes lateral dynamics and wheel slip.

Figure 4.75: Certain cases when the track geometry is not straight.

6. On the one-sided washboard tracks, the vehicle undergoes rocking motions. In the actual field test there is a torsional coupling between the driver, seat and the steering wheel, which affects vehicle rocking motions. This aspect is absent from the Adams model.

7. One possible cause of high frequency vibrations is transmission coupling, which is not modeled in Adams at all.

8. The shifting location of actual groung-wheel contact was not modeled.

161

9. In the real vehicle there are other unmodeled effects like backlash, loose joints, nonlinearity, etc. which are absent from the Adams model.

Nevertheless, the overall good match of the axle point accelerations suggest that the wheel compliance and damping is reasonably captured by the model; and the degree of match obtained in the body point acceleration suggests that the Adams model reasonably captures the effects of mass distribution, inertia effects, other wheel effects, frame flexibility and damping.

Our simplified Adams model will be used in the succeeding chapter to get initial estimates of system natural frequency and damping in a Laplace domain reduced order model of the vehicle.

Chapter 5

Laplace domain model development using test track data

Detailed field testing of an all terrain vehicle was described in the preceding chapter. Using the same field-test measurement data, a Laplace domain reduced order model of the vehicle will be developed in this chapter. This model is similar to the generalized quarter car model developed earlier in Chapter 2, and may therefore be viewed as a partial experimental implementation of the same ideas. While developing the generalized quarter car model in Chapter 2, it was pointed out that either a mathematical model of the vehicle or the actual vehicle prototype can be used. The latter option is investigated here.

5.1   Introduction

The proposed modeling approach is discussed using a flow chart in Figure 5.1.

The individual blocks of the flow chart are described below.

To begin with, the test data is obtained from field testing as described in the preceding chapter, in ① of Figure 5.1.

1 Field testing

Time domain responses

2 Obtain FFTs of accelerations at all B_i and A_i

$\ddot{X}_1(f)$ — Frequency (Hz)

$\ddot{Y}_1(f)$ — Frequency (Hz)

3 Computing the transfer matrix between accelerations at A_i to B_i

System natural frequencies and damping ratios

(A) $\omega_i, \xi_i \ \forall i = 1$ to 4 (Insert initial guesses)

Adjust fitting parameters
Minimize error norm (fminsearch)

(F) ω_i, ξ_i new estimates

Formulate the elements of TF

$$H_{ij}(s) = \frac{\sum\limits_{m=0}^{7} c_m s^m}{\prod\limits_{n=1}^{4} (s^2 + 2\zeta_n \omega_n s + \omega_n^2)}$$

(B)

Find error between model and test responses

(only B_1 shown here) —— Testing --- Model

$\ddot{X}_1(f)$ — Frequency (Hz)

(E)

Assemble transfer matrix

$$X(s) = \begin{Bmatrix} X_1(s) \\ X_2(s) \\ X_3(s) \\ X_4(s) \end{Bmatrix} \quad Y(s) = \begin{Bmatrix} Y_1(s) \\ Y_2(s) \\ Y_3(s) \\ Y_4(s) \end{Bmatrix}$$

(C) $X(s) = H(s) \ Y(s)$

Least square fit
(D) $[c_i] = A^{-1}B$

5 Model with unsprung mass

$X_4(s)$, B_4, C_{rr}, K_{rr}, $Y_4(s)$
$X_2(s)$, B_2, $X_1(s)$, B_1, $X_3(s)$, B_3
C_{fr}, K_{fr}, A_4, $U_4(s)$, C_{rl}, K_{rl}
A_2, $Y_2(s)$, C_{fl}, K_{fl}, C_4, $Y_3(s)$, A_3
C_2, $U_2(s)$, A_1, $Y_1(s)$, C_3, $U_3(s)$
C_1, $U_1(s)$

4 Reduced-order model

Flexible frame

$X_4(s)$, B_4, C_{rr}, K_{rr}, $Y_4(s)$
$X_2(s)$, B_2, $X_1(s)$, B_1, $X_3(s)$, B_3
C_{fr}, K_{fr}, A_4, C_{rl}, K_{rl}
$Y_2(s)$, C_{fl}, K_{fl}, $Y_3(s)$
A_2, $Y_1(s)$, A_1, A_3

Suspension properties retained as free parameters

Figure 5.1: Work flow of Chapter 5.

From each vehicle test, eight simultaneous responses corresponding to the vertical accelerations at wheel axles A_i's and suspension to body attachment points B_i's are obtained. All effects of the car's frame flexibility, mass distribution and the four ground contacts are implicitly included in these measured responses. The intention now is to obtain a useful transfer function matrix for the vertical response of the vehicle using this test data. To this end, Fast Fourier Transforms (FFTs) are used to transform the time domain acceleration data to the frequency domain as indicated in ②. The FFTs are then approximated by an eighth order, strictly proper, transfer function matrix $H(s)$ in ③. This $H(s)$ represents the dynamics of the car body, and the suspension is to be modeled separately (see section 5.3 in Chapter 5). Using $H(s)$, a new transfer function matrix with suspension properties treated as free adjustable parameters is obtained in step ④, which facilitates subsequent parameter studies without repeated vehicle testing. Finally, the wheel's unsprung mass model is incorporated to obtain a transfer function matrix between ground-excitation at C_i and body displacements at B_i in step ⑤. This last part of the formulation follows Chapter 2 closely and may be viewed as an implementation of the same.

Details of the abovementioned experimental work follow.

5.2   Test data

The test data from continuous displacement tracks will be used for model development. A total of 18 vehicle tests were performed on different sinusoidal tracks as reported in Table 5.1. These tests were performed at different speeds. The test speeds were selected so that the full set of test conditions covers a broad range of frequencies.

Track	Speed	Low severity	Medium severity	High severity
Washboard	Low	7.5	-	11
	High	9.5	-	13
Herringbone	Low	9	21	14
	Medium	14	25	19
Chassis twist	Low	7.5	6.5	5.5
	High	15.5	21.5	14.5
One-side washboard	Low	7	-	13

Table 5.1: Speed details of vehicle testing on various tracks. All speeds are in kmph[1].

Since there are variations in speed and other effects as described in the previous chapter, the actual frequency content is rich (for instance, see Figure 5.2).
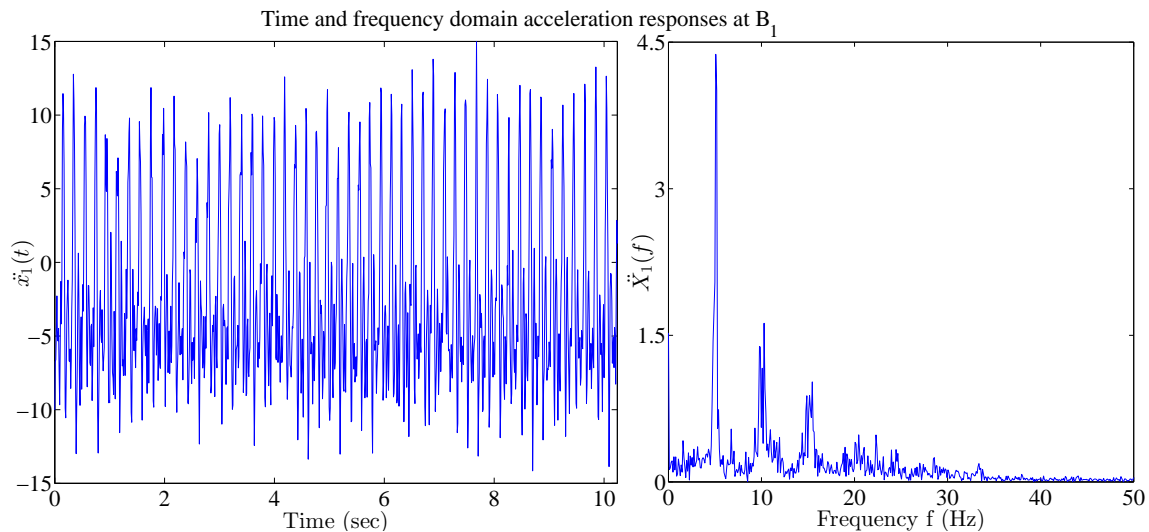
Figure 5.2: Time and frequency domain respresentations of the acceleration response of body point B_1 for a low speed test on low severity washboard track.

Over 18 test conditions, as will be seen, enough data is available for useful model

---

[1]The vehicle is driven on the tracks at "low" and "high" speeds. These are qualitative and imprecise labels based on perception, and the reader should look at the absolute numerical quantities for precise information.

development.

The vertical accelerations of points B_i's and A_i's were obtained from each vehicle test. Next, these time domain acceleration responses ($\ddot{x}_i(t)$ and $\ddot{y}_i(t)$) were transformed to the frequency domain responses ($\ddot{X}_i(f)$ and $\ddot{Y}_i(f)$) by taking the fast Fourier transforms (FFTs)[2]. The vertical acceleration data was recorded at a sampling frequency of 100 Hz, therefore the frequency content of the FFT signals ranged over 0-50 Hz. Subsequently, digital filtering was done to cut off frequencies above 30 Hz.

The frequency domain responses are vertically stacked to obtain eight big column vectors $\ddot{\boldsymbol{X}}_{\boldsymbol{i}}(\boldsymbol{f})$ and $\ddot{\boldsymbol{Y}}_{\boldsymbol{i}}(\boldsymbol{f})$ containing the accelerations at points B_i and A_i from all eighteen vehicle tests given by

$$\ddot{\boldsymbol{X}}_{\boldsymbol{1}}(\boldsymbol{f}) = \begin{bmatrix} \boxed{\ddot{X}_1(f)}_1 \\ \boxed{\ddot{X}_1(f)}_2 \\ \vdots \\ \boxed{\ddot{X}_1(f)}_{18} \end{bmatrix}, \ddot{\boldsymbol{X}}_{\boldsymbol{2}}(\boldsymbol{f}) = \begin{bmatrix} \boxed{\ddot{X}_2(f)}_1 \\ \boxed{\ddot{X}_2(f)}_2 \\ \vdots \\ \boxed{\ddot{X}_2(f)}_{18} \end{bmatrix}, \ldots, \ddot{\boldsymbol{X}}_{\boldsymbol{4}}(\boldsymbol{f}) = \begin{bmatrix} \boxed{\ddot{X}_4(f)}_1 \\ \boxed{\ddot{X}_4(f)}_2 \\ \vdots \\ \boxed{\ddot{X}_4(f)}_{18} \end{bmatrix}.$$

$$\ddot{\boldsymbol{Y}}_{\boldsymbol{1}}(\boldsymbol{f}) = \begin{bmatrix} \boxed{\ddot{Y}_1(f)}_1 \\ \boxed{\ddot{Y}_1(f)}_2 \\ \vdots \\ \boxed{\ddot{Y}_1(f)}_{18} \end{bmatrix}, \ddot{\boldsymbol{Y}}_{\boldsymbol{2}}(\boldsymbol{f}) = \begin{bmatrix} \boxed{\ddot{Y}_2(f)}_1 \\ \boxed{\ddot{Y}_2(f)}_2 \\ \vdots \\ \boxed{\ddot{Y}_2(f)}_{18} \end{bmatrix}, \ldots, \ddot{\boldsymbol{Y}}_{\boldsymbol{4}}(\boldsymbol{f}) = \begin{bmatrix} \boxed{\ddot{Y}_4(f)}_1 \\ \boxed{\ddot{Y}_4(f)}_2 \\ \vdots \\ \boxed{\ddot{Y}_4(f)}_{18} \end{bmatrix}.$$

For each vehicle test, time domain data of 10.24 seconds is used to compute the FFTs. As the sampling frequency is 100 Hz, there are 1024 data points, and there will be 512 points in the one-sided FFT. Each time domain acceleration response can

---

[2]For obtaining the fast Fourier transforms, Matlab's built-in routine `fft` was used.

be reconstructed by 512 pure sinusoids whose magnitude and phase are computed by the `fft` command in Matlab and the frequencies range from 0-50 Hz in steps of 50/512= 0.098 Hz. The size of all of the above column vectors containing eighteen test responses is $18N \times 1$, where $N = 512$.

From the above column vectors, two combined matrices representing the frequency domain acceleration response $\ddot{\boldsymbol{X}}(\boldsymbol{f})$ of all body points B_i and the frequency domain acceleration response $\ddot{\boldsymbol{Y}}(\boldsymbol{f})$ of all axle points A_i were obtained as

$$\ddot{\boldsymbol{X}}(\boldsymbol{f}) = \begin{bmatrix} \ddot{\boldsymbol{X}}_1(\boldsymbol{f}) \\ \ddot{\boldsymbol{X}}_2(\boldsymbol{f}) \\ \ddot{\boldsymbol{X}}_3(\boldsymbol{f}) \\ \ddot{\boldsymbol{X}}_4(\boldsymbol{f}) \end{bmatrix}_{72N \times 1} ; \quad \ddot{\boldsymbol{Y}}(\boldsymbol{f}) = \begin{bmatrix} \ddot{\boldsymbol{Y}}_1(\boldsymbol{f}) \\ \ddot{\boldsymbol{Y}}_2(\boldsymbol{f}) \\ \ddot{\boldsymbol{Y}}_3(\boldsymbol{f}) \\ \ddot{\boldsymbol{Y}}_4(\boldsymbol{f}) \end{bmatrix}_{72N \times 1} \tag{5.1}$$

It may be noted that the FFT of $\ddot{x}$, written here as $\ddot{X}(f)$, is nothing but $-\omega^2$ times the FFT of x, i.e., $-(2\pi f)^2 X(f)$. So $X(f)$ can be found, if needed, from the FFT of $\ddot{x}$ by dividing by $-4\pi^2 f^2$. A Laplace domain reduced order model of the vehicle is obtained from these test data, as follows.

5.3 Vehicle transfer function

In the present study Laplace transforms are used, essentially interchangeably, with the fast Fourier transforms (FFTs) of the measured time domain acceleration responses. The fast Fourier transforms (FFTs) can be thought of as Laplace transforms evaluated at '$s = j\omega$' (imaginary) axis, as will be clearer soon when the actual matrix equations are written down. The frequency will range from zero to half of the sampling frequency, i.e., $\omega_{\text{range}} = 0 - 50$ Hz.

In principle, there are 4 accelerations at body points B_i, whose Laplace transforms can be arranged in a 4×1 matrix

$$s^2\{X(s)\}$$

where the scalar premultiplier s^2 should be dropped when we are interested in displacements rather than accelerations.

Similarly, there are 4 accelerations at axle points A_i, arranged in a 4×1 matrix

$$s^2\{Y(s)\}.$$

The accelerations of A_i determine the accelerations at B_i (in the absence of any other forcing on the system). Assuming a 4×4 transfer function matrix, we write

$$s^2 X(s) = H(s) \left(s^2 Y(s)\right). \tag{5.2}$$

Now we note that if we insert $s = i\omega$ in $s^2 X(s)$ and $s^2 Y(s)$, then we obtain the Fourier transforms, $\ddot{X}(\omega)$ and $\ddot{Y}(\omega)$, each a 4×1 matrix dependent on ω. With some abuse of notation, when we use frequency f instead of angular frequency $\omega = 2\pi f$, we will simply write $\ddot{X}(f)$ and $\ddot{Y}(f)$ to avoid proliferation of symbols.

The next step is to choose a mathematical form for the elements of $H(s)$. $H(s)$ is symmetric from theory (see Chapter 2) and also has other symmetries due to lateral symmetry of the prototype vehicle. So it has 6 independent elements, namely $H_{11}(s), H_{12}(s), H_{13}(s), H_{14}(s), H_{33}(s)$ and $H_{34}(s)$.

Each of these 6 elements is assumed to be well described by an 8th order transfer

169

function (with different numerator and identical denominator coefficients):

$$H_{ij}(s) = \frac{\sum_{k=0}^{7} c_k s^k}{\prod_{n=1}^{4} (s^2 + 2\zeta_n \omega_n s + \omega_n^2)} \qquad (5.3)$$

We repeat that the c's are different for each element H_{ij}.

5.4   Model fitting

The transfer function model is to be fitted using the test data. The coefficients of the numerator of the transfer function are found by linear least squares and the denominator coefficients are obtained by nonlinear optimization. In each fitting iteration the loop below is traversed (see Figure 5.3), and the error norm is reduced iteratively to get a better fit.
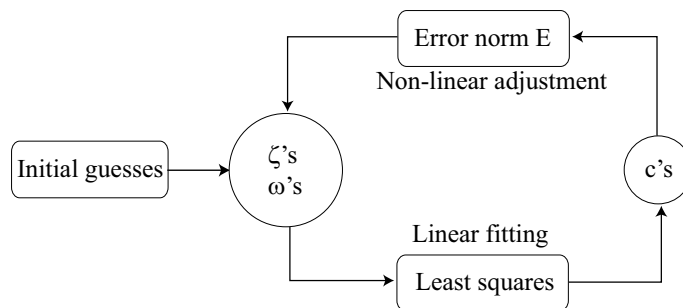
Figure 5.3: Iteration loop used to determine numerator coefficients using linear least squares, and denominator coefficients using nonlinear adjustment.

The procedure to obtain a reduced order model is now discussed in further detail using block ③ in the flow chart of Figure 5.1.

To begin, guessed or estimated values[3] of vehicle natural frequencies ω_i and damping ratios ζ_i are assigned in step **(A)** of ③ in Figure 5.1 These serve the same

---

[3]These initial values were themselves estimated from some simple calculations described in Appendix D.1.

purpose as the decaying exponentials used earlier in Chapter 2.

Given these initial estimates the coefficients d_i of the denominator of the transfer function matrix are obtained from the identity

$$\sum_{i=0}^{8} d_i s^i = \prod_{n=1}^{4} (s^2 + 2\zeta_n \omega_n s + \omega_n^2) \tag{5.4}$$

Note here that d_i for all elements $H_{ij}(s)$ of the transfer function matrix $H(s)$ are the same. Using the denominator coefficients along with candidate numerator coefficients c_i (to be determined by a linear least square calculation very soon), the individual transfer function elements $H_{ij}(s)$ are formulated in (**B**) and the transfer function matrix $H(s)$ is assembled in (**C**).

The c_i are determined as follows.

1. As $H(s)$ is symmetric and the vehicle has left-right symmetry, only 6 scalar transfer functions define $H(s)$ in (**C**). Equation (5.2) can be rewritten as:

$$\underbrace{\begin{bmatrix} \mathbf{X_1(s)} \\ \mathbf{X_2(s)} \\ \mathbf{X_3(s)} \\ \mathbf{X_4(s)} \end{bmatrix}}_{M(s)} = \underbrace{\begin{bmatrix} \mathbf{Y_1(s)} & \mathbf{Y_2(s)} & \mathbf{Y_3(s)} & \mathbf{Y_4(s)} & \mathbf{0} & \mathbf{0} \\ \mathbf{Y_2(s)} & \mathbf{Y_1(s)} & \mathbf{Y_4(s)} & \mathbf{Y_3(s)} & \mathbf{0} & \mathbf{0} \\ \mathbf{0} & \mathbf{0} & \mathbf{Y_1(s)} & \mathbf{Y_2(s)} & \mathbf{Y_3(s)} & \mathbf{Y_4(s)} \\ \mathbf{0} & \mathbf{0} & \mathbf{Y_2(s)} & \mathbf{Y_1(s)} & \mathbf{Y_4(s)} & \mathbf{Y_3(s)} \end{bmatrix}}_{N(s)} \begin{bmatrix} H_{11}(s) \\ H_{12}(s) \\ H_{13}(s) \\ H_{14}(s) \\ H_{33}(s) \\ H_{34}(s) \end{bmatrix} \tag{5.5}$$

where the left hand side matrix $M(s)$ represents measured body point responses and the right hand side big matrix $N(s)$ represents measured axle-point responses. The right-most column vector consists of the six representative scalar transfer functions $H_{ij}(s)$ which includes specified ζ's and ω's as

171

well as numerator coefficients c_{ij} to be determined.

2. Multiplying the left hand side of Equation (5.5) with the *known* common denominator of the transfer function we obtain

$$\left[M(s)\right]_{72N\times 1} \left(\prod_{n=1}^{4} \left(s^2 + 2\zeta_n\omega_n s + \omega_n^2\right)\right) = \left[N(s)\right]_{72N\times 6} \begin{bmatrix} \sum_{k=0}^{7} c_{1k}s^k \\ \sum_{k=0}^{7} c_{2k}s^k \\ \vdots \\ \sum_{k=0}^{7} c_{6k}s^k \end{bmatrix}_{6\times 1} \quad (5.6)$$

3. In Equation (5.6), s can be replaced with $i\omega$, and then $M(s)$ and $N(s)$ will contain known FFT data for a given frequency.

$$\underbrace{\left[M(i\omega)\right]\left(\prod_{n=1}^{4}(i\omega)^2 + 2\zeta_n\omega_n(i\omega) + \omega_n^2\right)}_{[B]_{72\times 1}} =$$

$$\underbrace{\left[N(i\omega) \quad N(i\omega)i\omega \quad N(i\omega)(i\omega)^2 \quad \cdots \quad N(i\omega)(i\omega)^7\right]}_{[A]_{72\times 48}} \underbrace{\begin{bmatrix} \begin{Bmatrix} c_{10} \\ c_{11} \\ \cdots \\ c_{17} \end{Bmatrix} \\ \vdots \\ \begin{Bmatrix} c_{60} \\ c_{61} \\ \cdots \\ c_{67} \end{Bmatrix} \end{bmatrix}}_{[C]_{48\times 1}} \quad (5.7)$$

Note that in Equation (5.7) above the 48 elements of $[C]$, i.e., c_{ij} are (i) from 6 sets of 8 coefficients each and (ii) frequency independent.

172

4. All such matrix equations are vertically stacked for all frequencies, and Equation (5.7) turns into the following matrix equation governing our data and fitted model.

$$[\bar{\mathbf{B}}]_{72N \times 1} = [\bar{\mathbf{A}}]_{72N \times 48}[C]_{48 \times 1} \tag{5.8}$$

5. Since the numerator coefficients of the transfer function are real numbers, the real and imaginary parts of the above complex matrices $[\bar{\mathbf{A}}]$ and $[\bar{\mathbf{B}}]$ are separated and to obtain

$$\underbrace{\begin{bmatrix} \mathbb{R}e([\bar{\mathbf{B}}]) \\ \hline \mathbb{I}m([\bar{\mathbf{B}}]) \end{bmatrix}}_{[\boldsymbol{B}]_{144N \times 1}} = \underbrace{\begin{bmatrix} \mathbb{R}e([\bar{\mathbf{A}}]) \\ \hline \mathbb{I}m([\bar{\mathbf{A}}]) \end{bmatrix}}_{[\boldsymbol{A}]_{144N \times 48}} \underbrace{\begin{bmatrix} \left\{\begin{matrix} c_{10} \\ c_{11} \\ \cdots \\ c_{17} \end{matrix}\right\} \\ \vdots \\ \left\{\begin{matrix} c_{60} \\ c_{61} \\ \cdots \\ c_{67} \end{matrix}\right\} \end{bmatrix}}_{[C]_{48 \times 1}} \tag{5.9}$$

The overall sizes of $[\boldsymbol{A}]$ and $[\boldsymbol{B}]$ matrices are 73728×48 and 73728×1.

6. Finally the above equation containing the acceleration data from all tests is solved in a least square sense in step **(D)** of the flow chart to obtain the

173

numerator coefficient matrix $[C]$ as

$$[C] = [c_{ij}] = (\boldsymbol{A}^T\boldsymbol{A})^{-1}\boldsymbol{A}^T\boldsymbol{B}. \qquad (5.10)$$

Actually, in Matlab we use $\boldsymbol{A}\backslash\boldsymbol{B}$.

Next, these coefficients are used in step $(\mathbf{B})$ to obtain an error norm ε. The model responses $s^2\boldsymbol{X}(\boldsymbol{s})$ for inputs $s^2\boldsymbol{Y}(\boldsymbol{s})$ are compared with the test responses in step $(\mathbf{E})$ to find the total sum of squares error norm between the model and field test responses.

Finally, the error norm ε is adjusted by posing a nonlinear minimization problem in Matlab using `fminsearch`, to obtain the new guesses for the originally guessed parameters ζ's and ω's to be used in step $(\mathbf{A})$. This iteration is continued by `fminsearch` until satisfactory convergence. The entire process takes a few hours on an ordinary desktop PC.

Final values of ζ's and ω's obtained via `fminsearch` are given in Table 5.2.

Identifier	Mode 1	Mode 2	Mode 3	Mode 4
f (Hz)	2.37	4.92	10.41	27.46
ζ	0.31	0.33	0.18	0.73

Table 5.2: Final values of ω's and ζ's obtained from `fminsearch`.

From the values of the numerator coefficients and the refined values of the system natural frequencies and damping ratios, the six transfer functions $H_{ij}(s)$ are finally obtained and assembled to get the transfer function matrix $H(s)$.

The expressions for these transfer functions are given in Appendix D.2.1. The

magnitude plots of the transfer functions $H_{ij}(s)$ are shown in Figure 5.4.

$$H(s) = \begin{bmatrix} H_{11}(s) & H_{12}(s) & H_{13}(s) & H_{14}(s) \\ H_{12}(s) & H_{11}(s) & H_{14}(s) & H_{13}(s) \\ H_{13}(s) & H_{14}(s) & H_{33}(s) & H_{34}(s) \\ H_{14}(s) & H_{13}(s) & H_{34}(s) & H_{33}(s) \end{bmatrix}$$
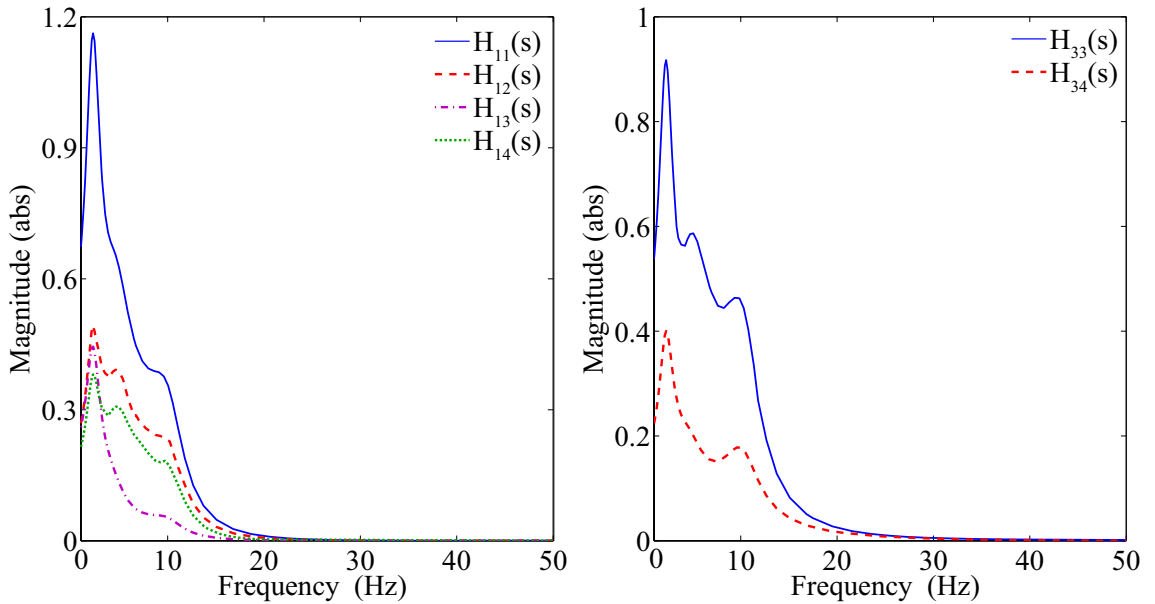
Figure 5.4: Magnitude plots of six transfer functions $H_{ij}(s)$ which are assembled to build the transfer function matrix.

The accelerations at A_i's are inputs to the model. These are pre-multiplied by $H(s)$ to get the model response, i.e., accelerations at B_i's. The transfer functions have eight complex poles (a modeling decision). A discussion of the modes corresponding to these poles and the reasoning used to select the initial guesses for the ζ's and ω's is discussed in Appendix D.1.

5.5   Model validation

For comparing the model response and the test response the test data is filtered using `designfilt` command in Matlab. The cut off frequency is set to 30 Hz. Model and test responses are compared for all four tracks selected for study (see Table 5.1), with eighteen tests in all.

Since the reasonable success of the Adams model in the previous chapter leads us to expect a reasonable match between test and simulation in this chapter as well, we list the various figures below which show graphical results, and then present a brief consolidated discussion at the end. The results are presented in the subsequent figures in the following sequence.

5.5.1   Washboard track

The model response is compared against the test results in Figures 5.5 through 5.8.

5.5.2   Herringbone track

The model response is compared against the test results in Figures 5.9 through 5.14.

5.5.3   Chassis twist track

The model response is compared against the test results in Figures 5.15 through 5.20.

5.5.4   One sided washboard track

The model response is compared against the test results in Figures 5.21 and 5.22.
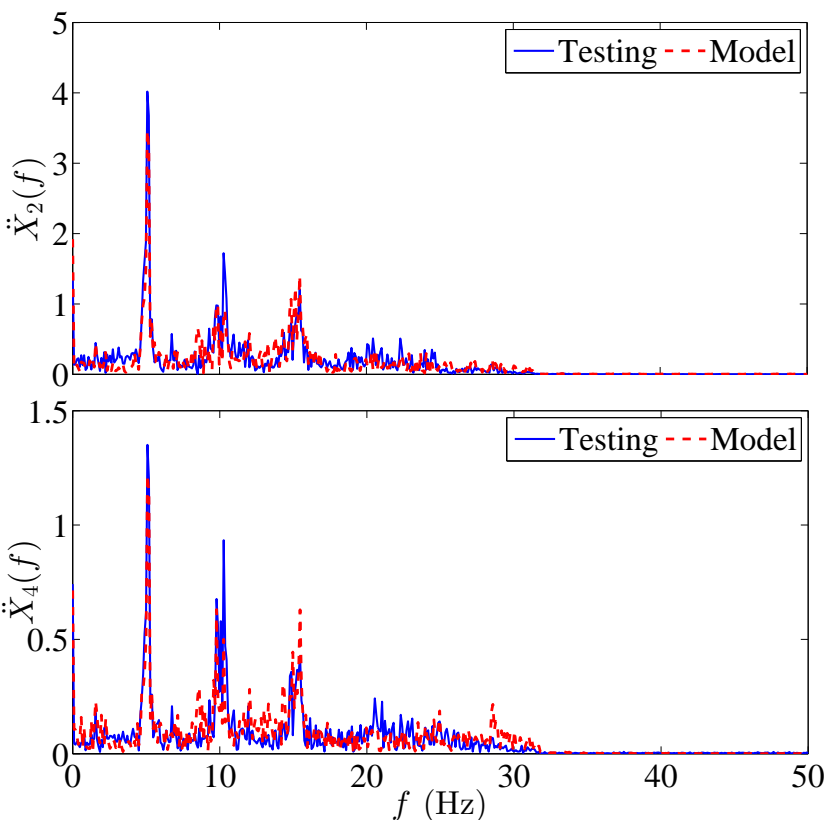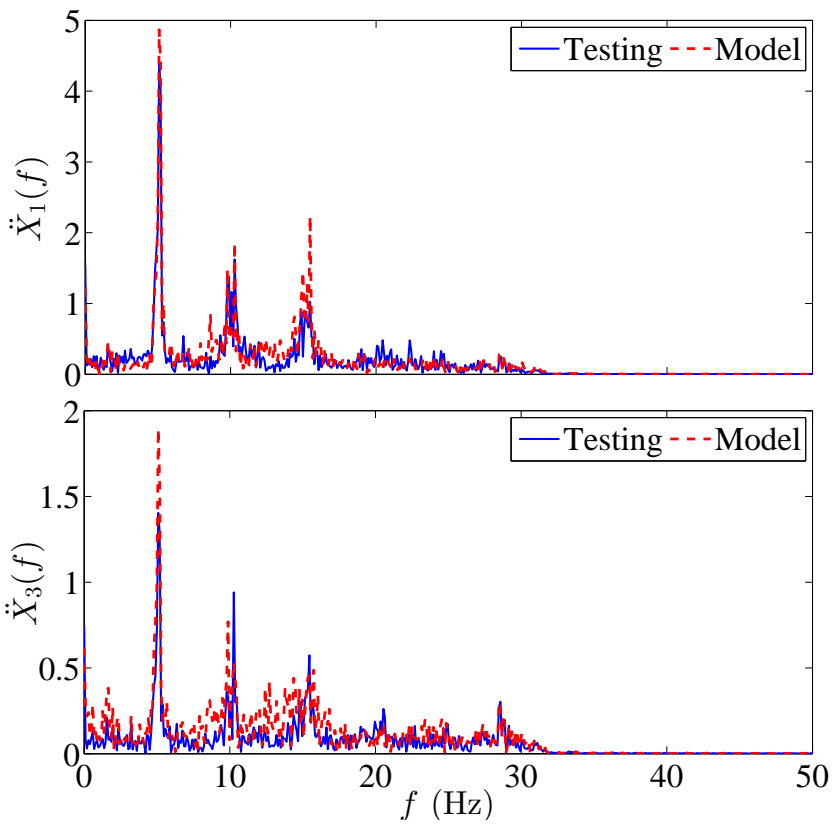
Figure 5.5: Results of low speed test on low-severity washboard track.
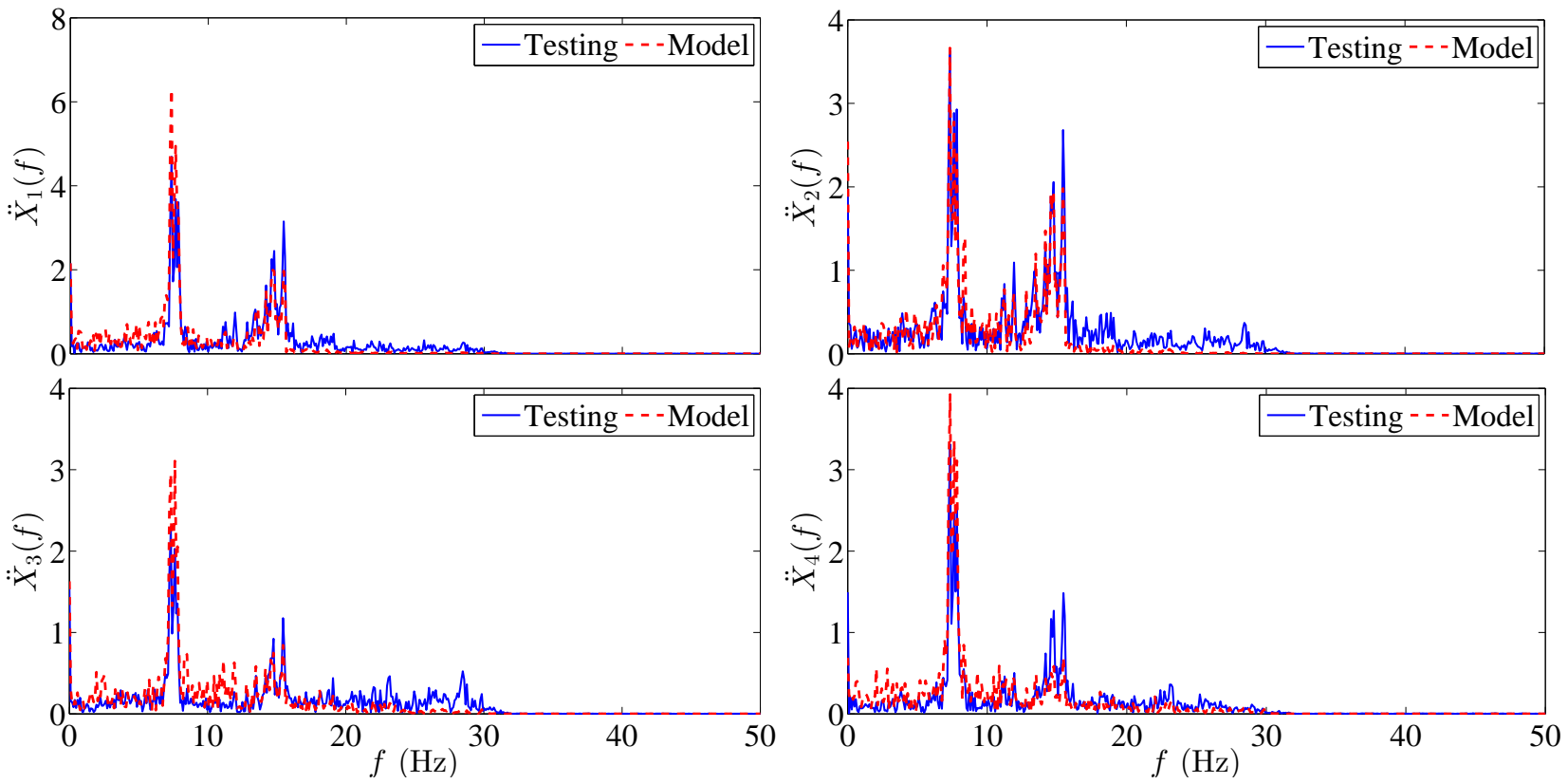
Figure 5.6: Results of high speed test on low-severity washboard track.
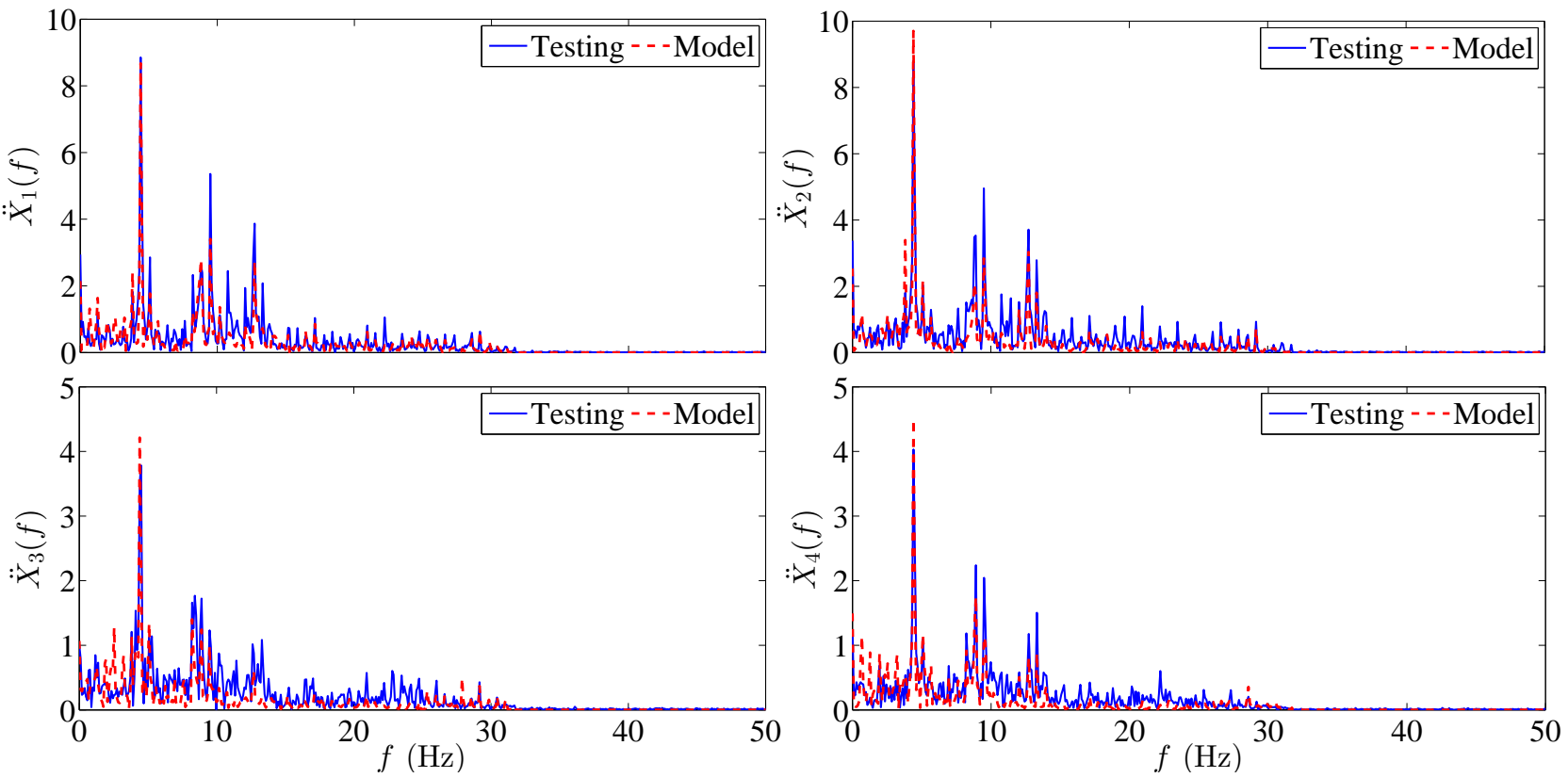
Figure 5.7: Results of low speed test on high-severity washboard track.
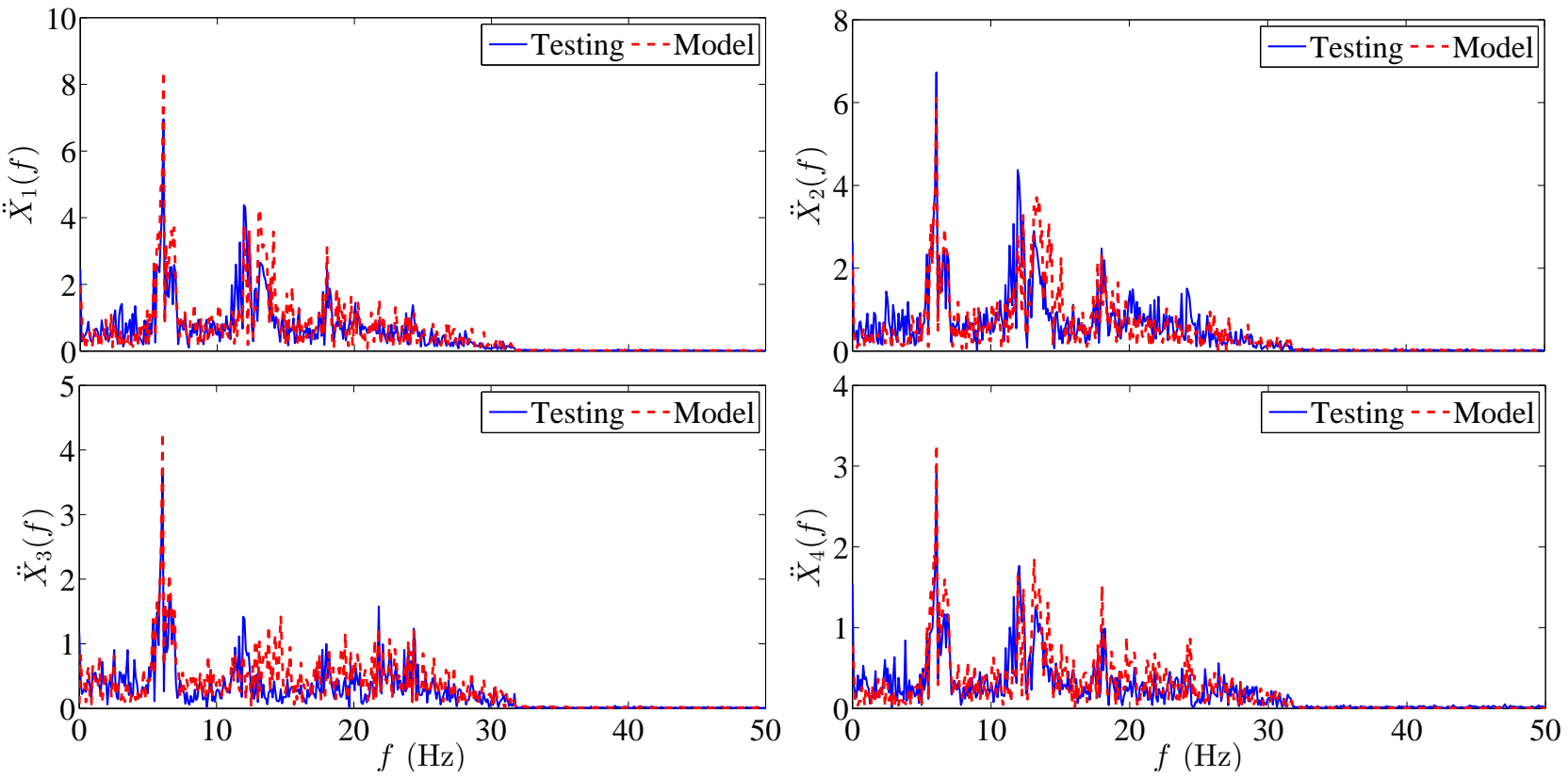
Figure 5.8: Results of high speed test on high-severity washboard track.
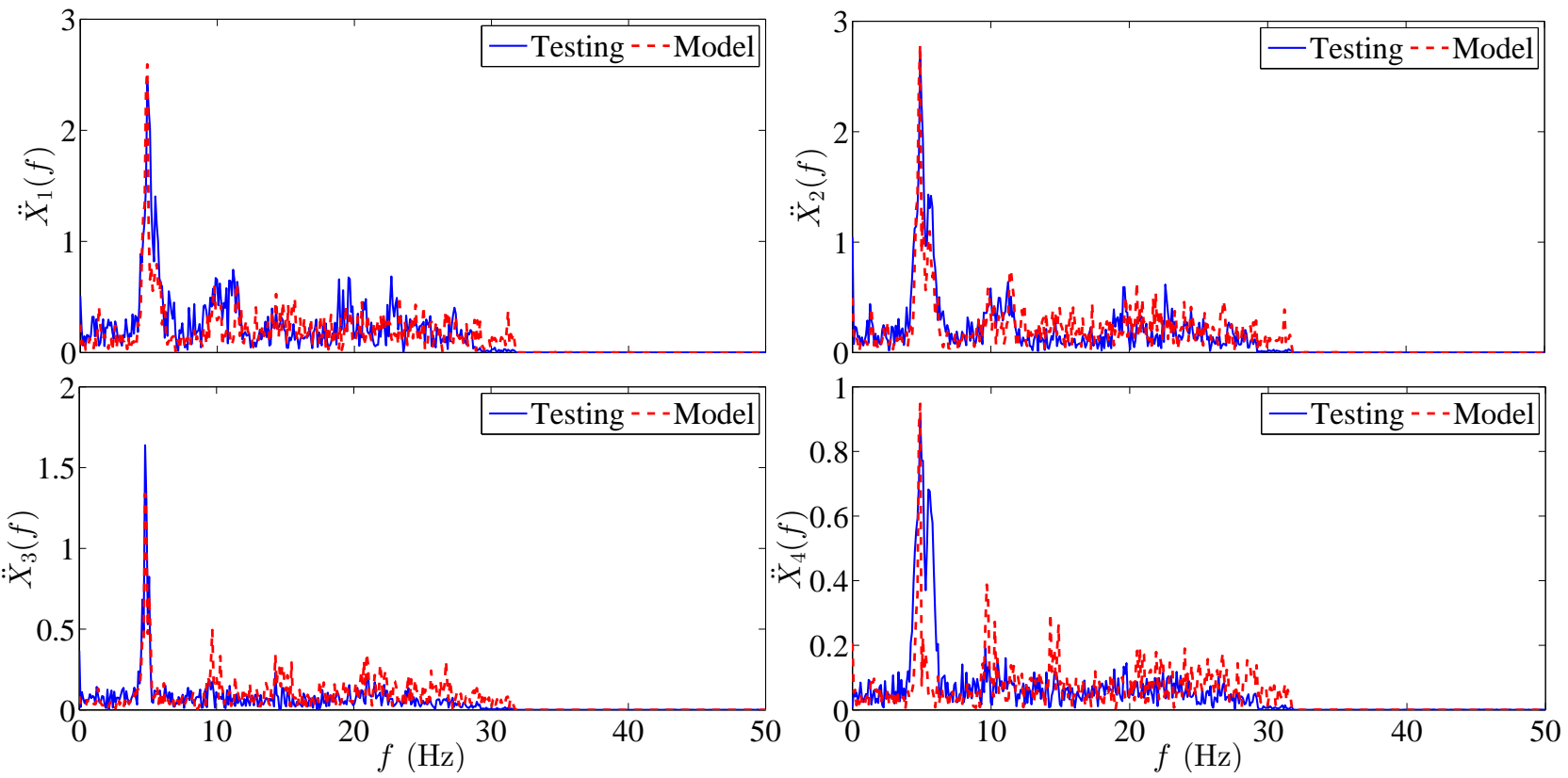
Figure 5.9: Results of low speed test on low-severity herringbone track.
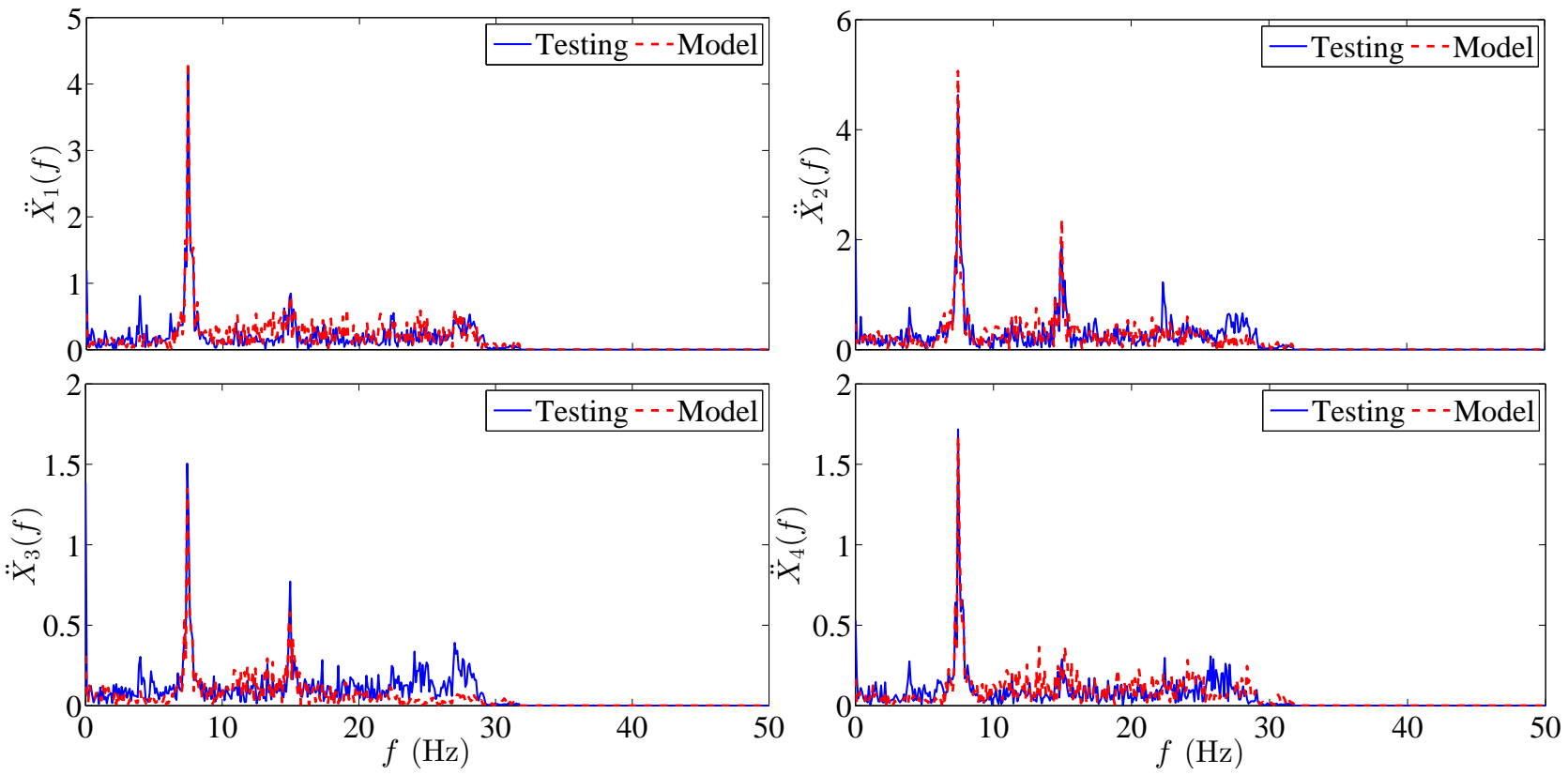
Figure 5.10: Results of high speed test on low-severity herringbone track.
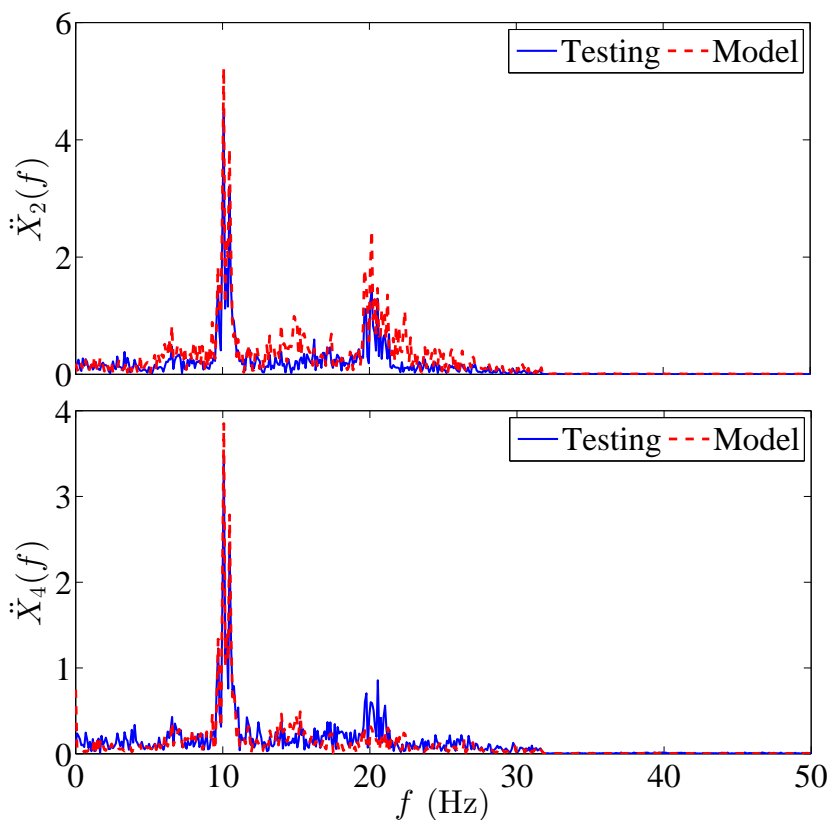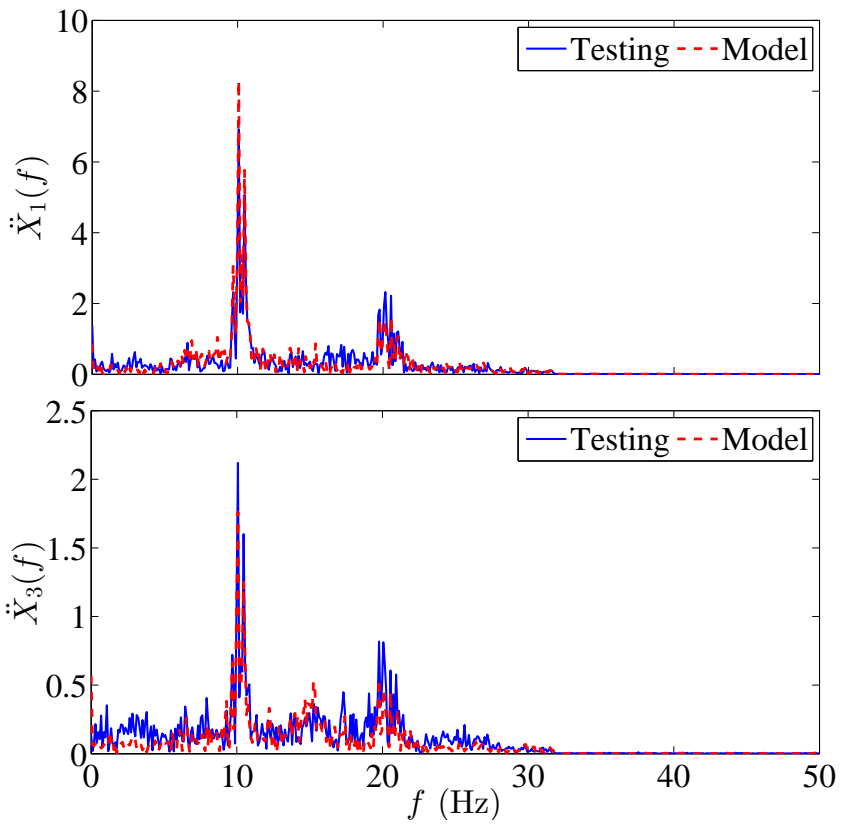
Figure 5.11: Results of low speed test on medium-severity herringbone track.
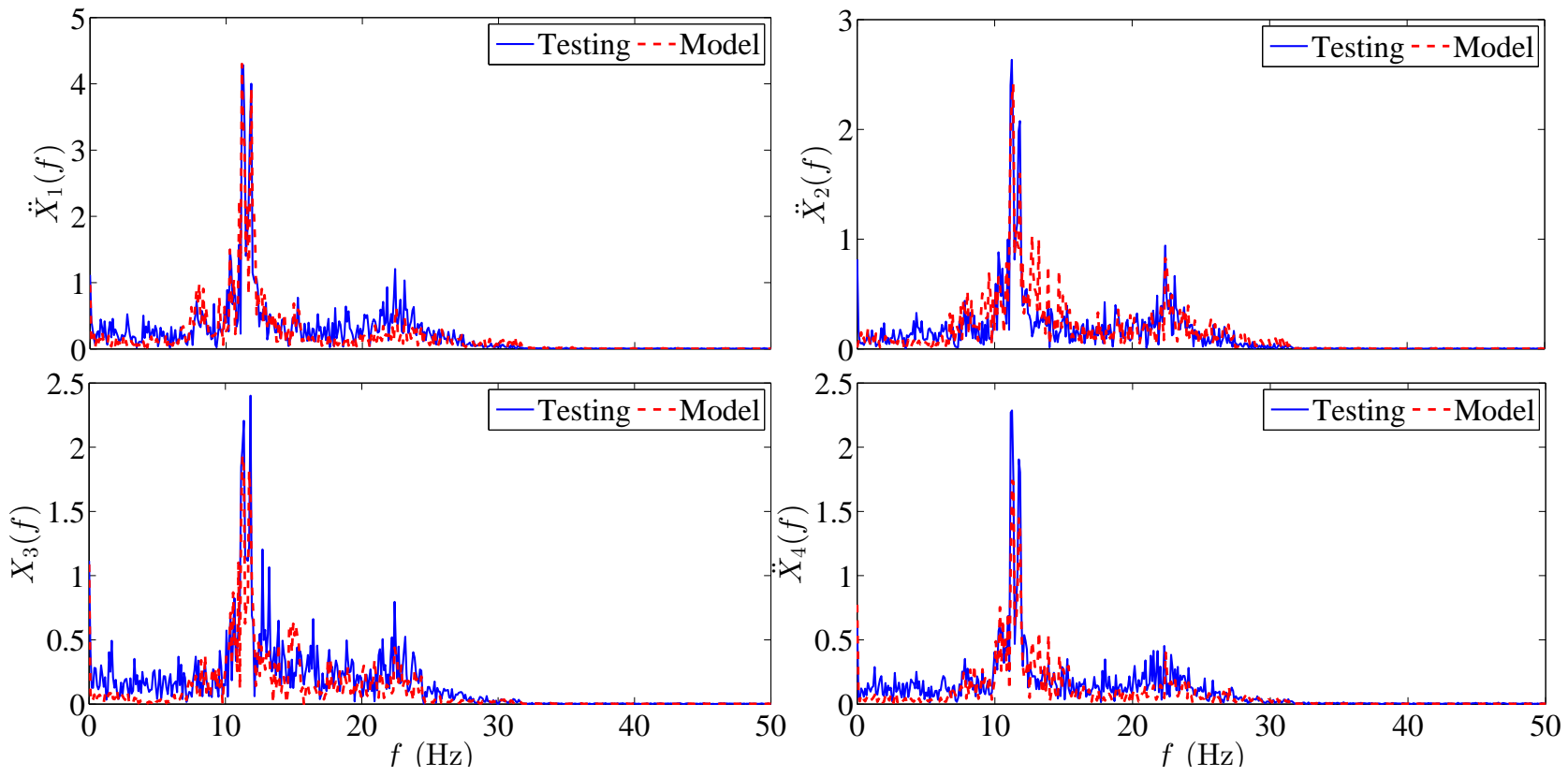
Figure 5.12: Results of high speed test on medium-severity herringbone track.
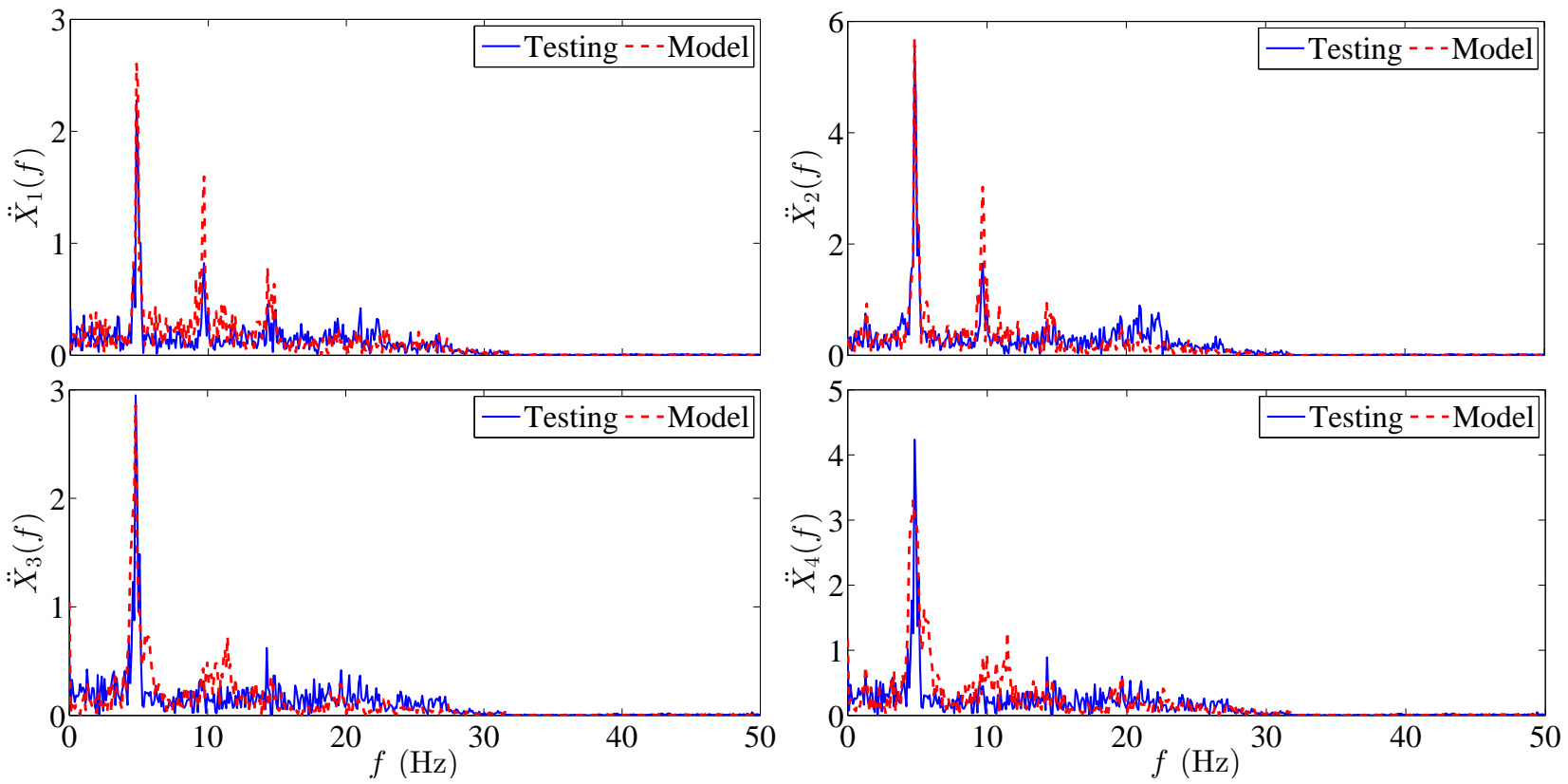
Figure 5.13: Results of low speed test on high-severity herringbone track.
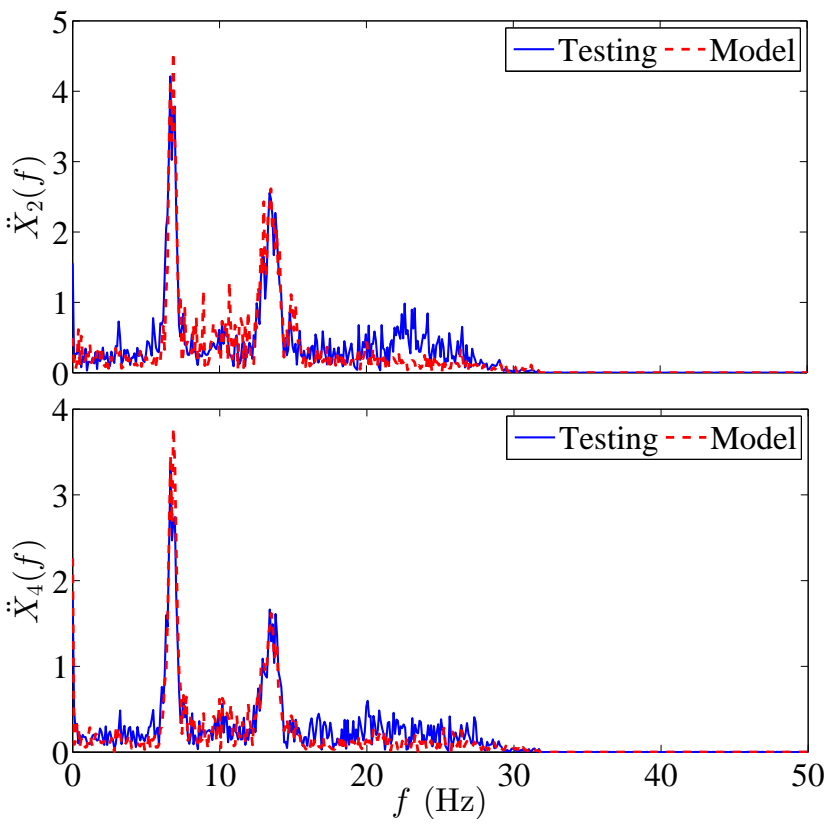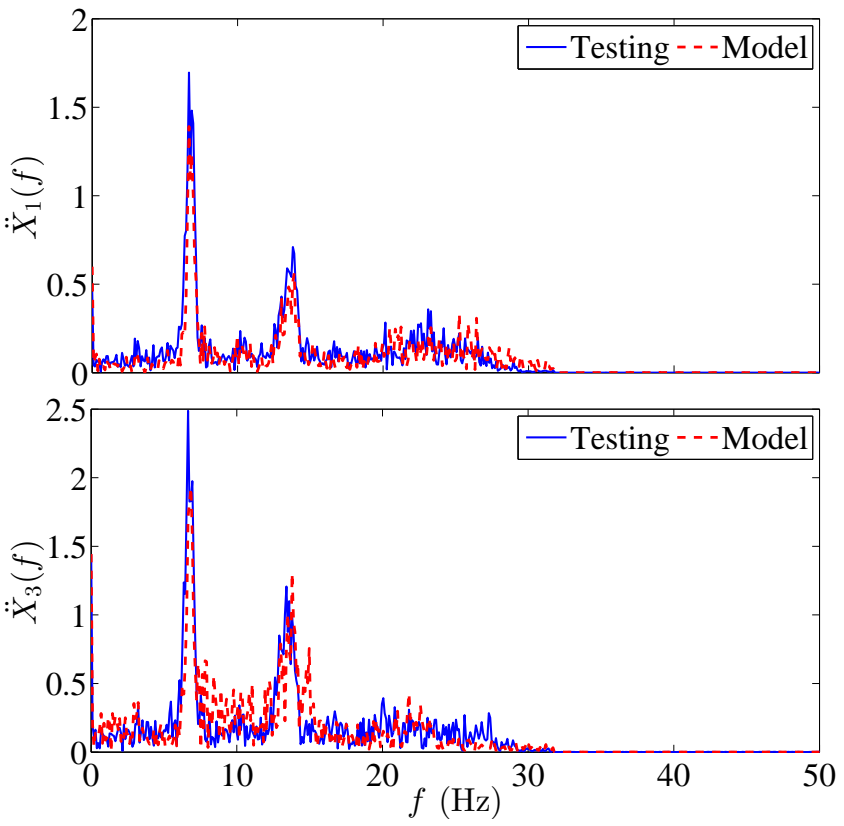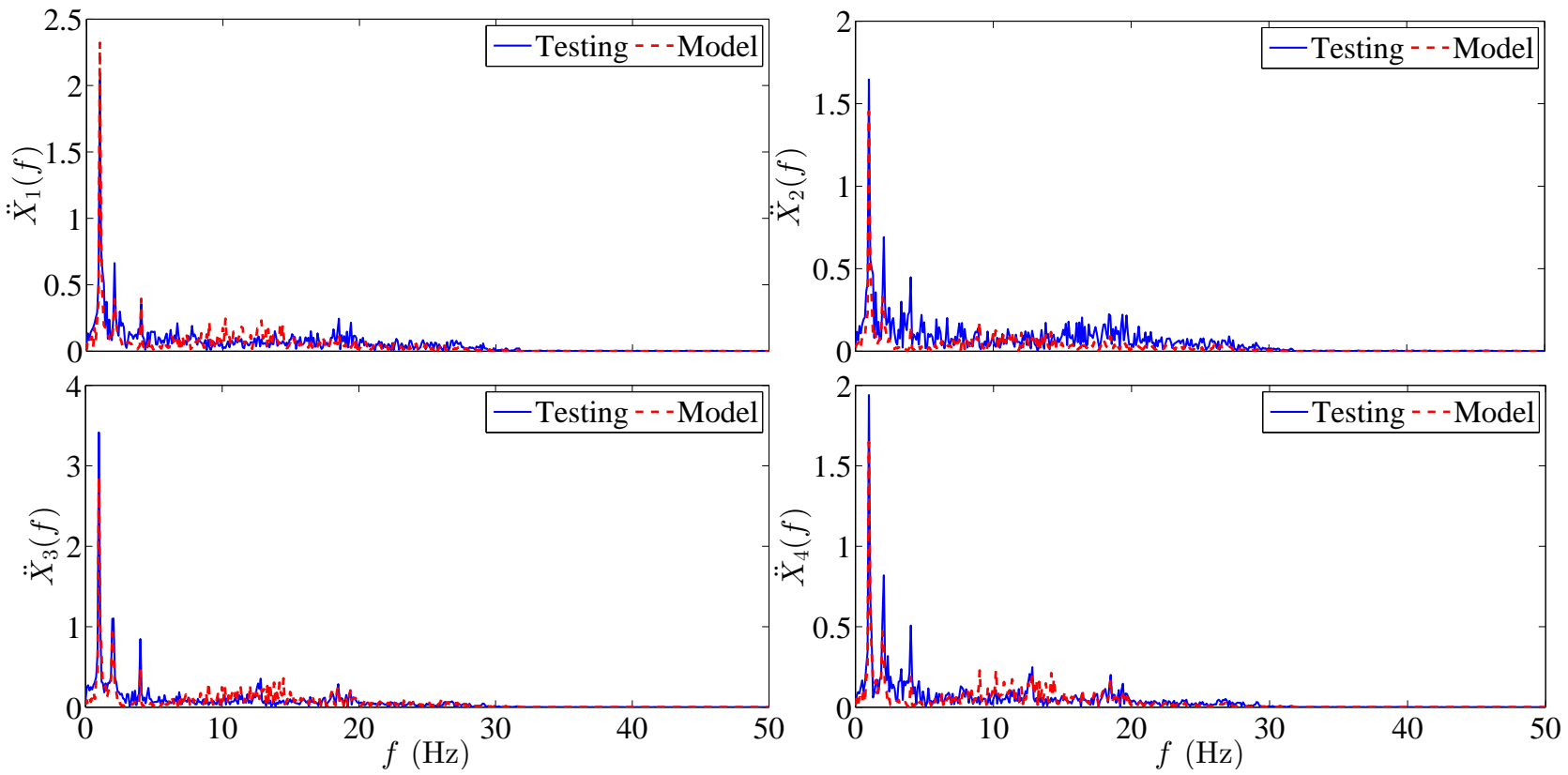
Figure 5.15: Results of low speed test on low-severity chassis twist track.
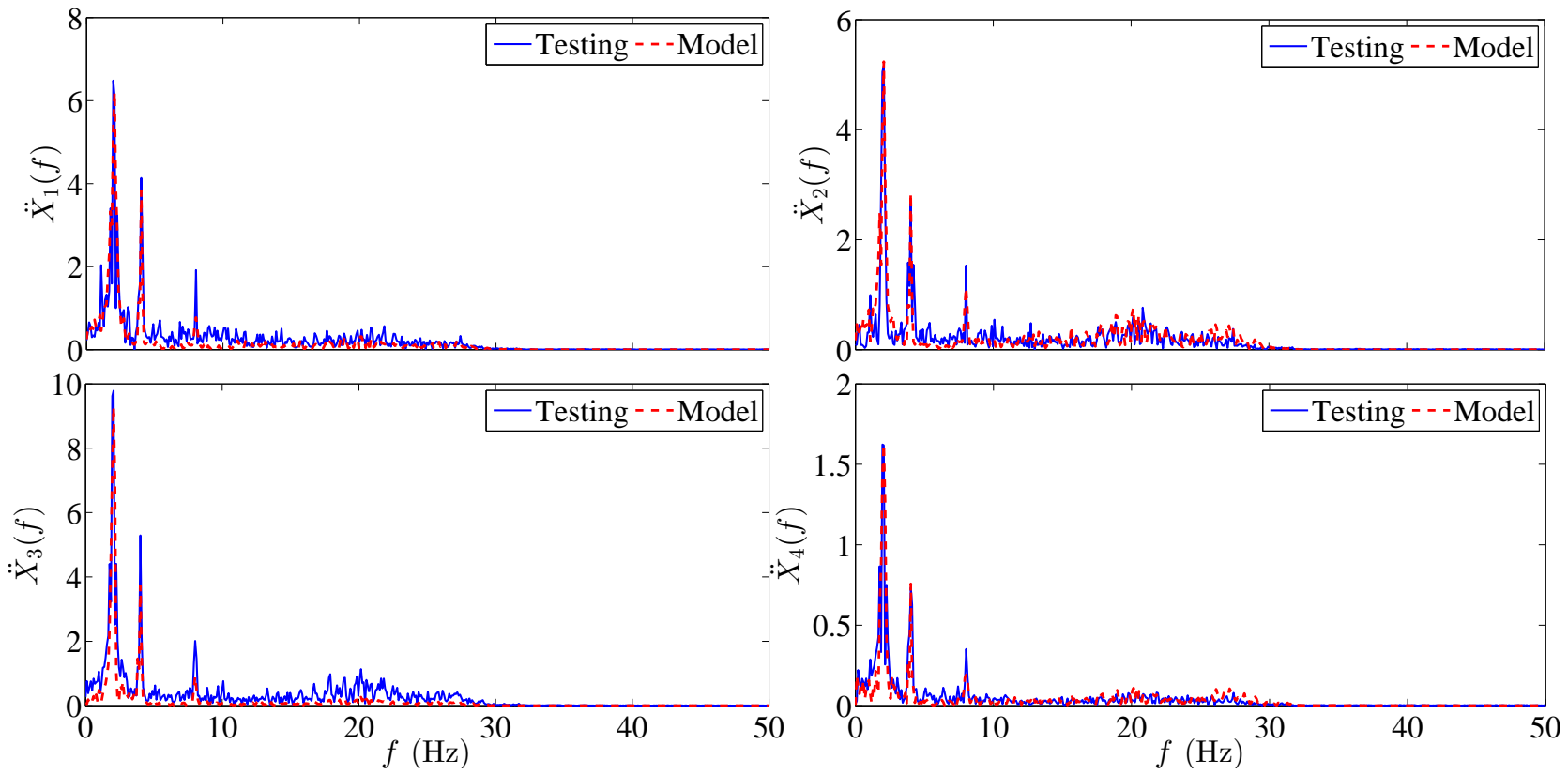
Figure 5.16: Results of high speed test on low-severity chassis twist track.
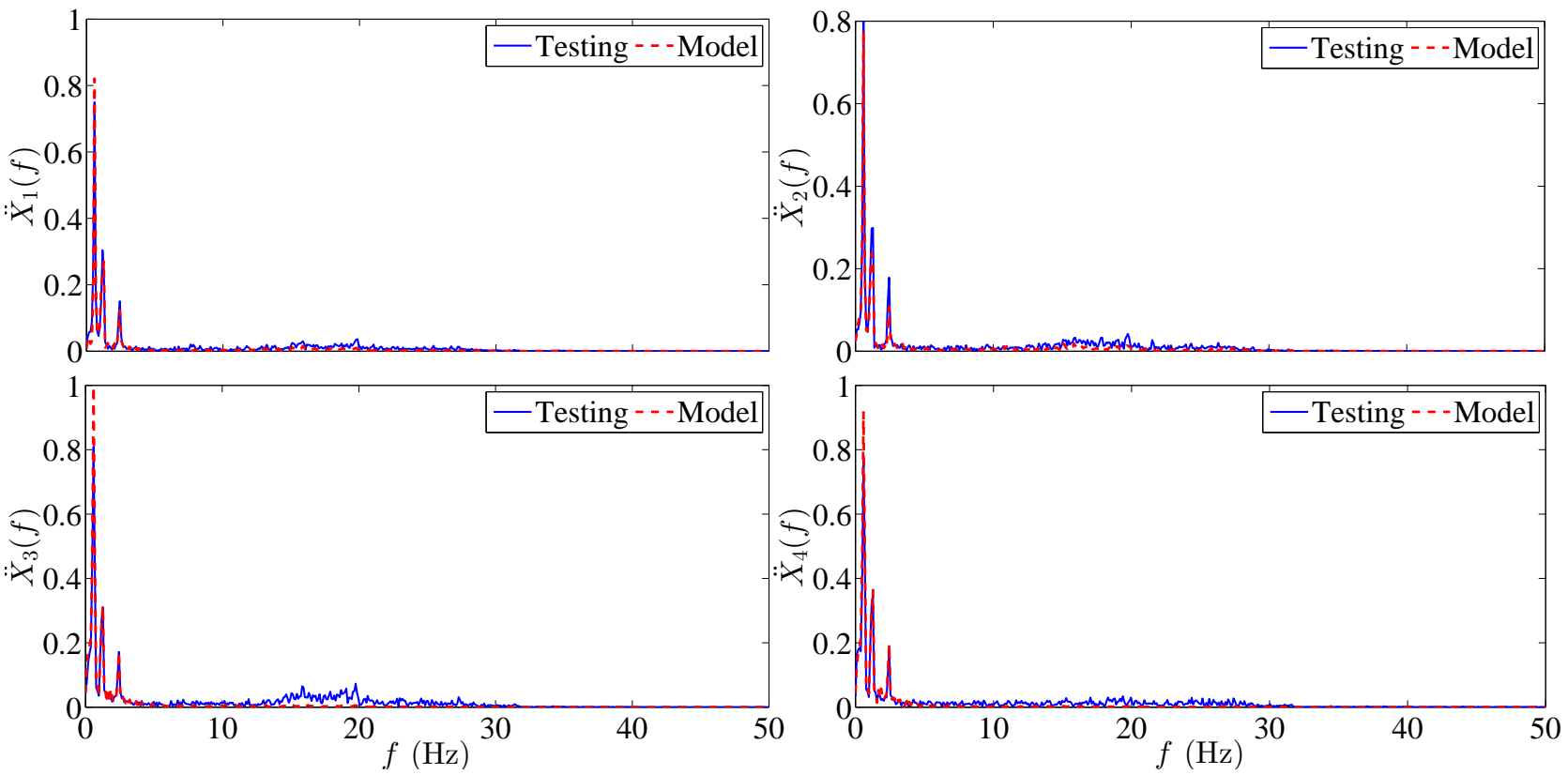
Figure 5.17: Results of low speed test on medium-severity chassis twist track.
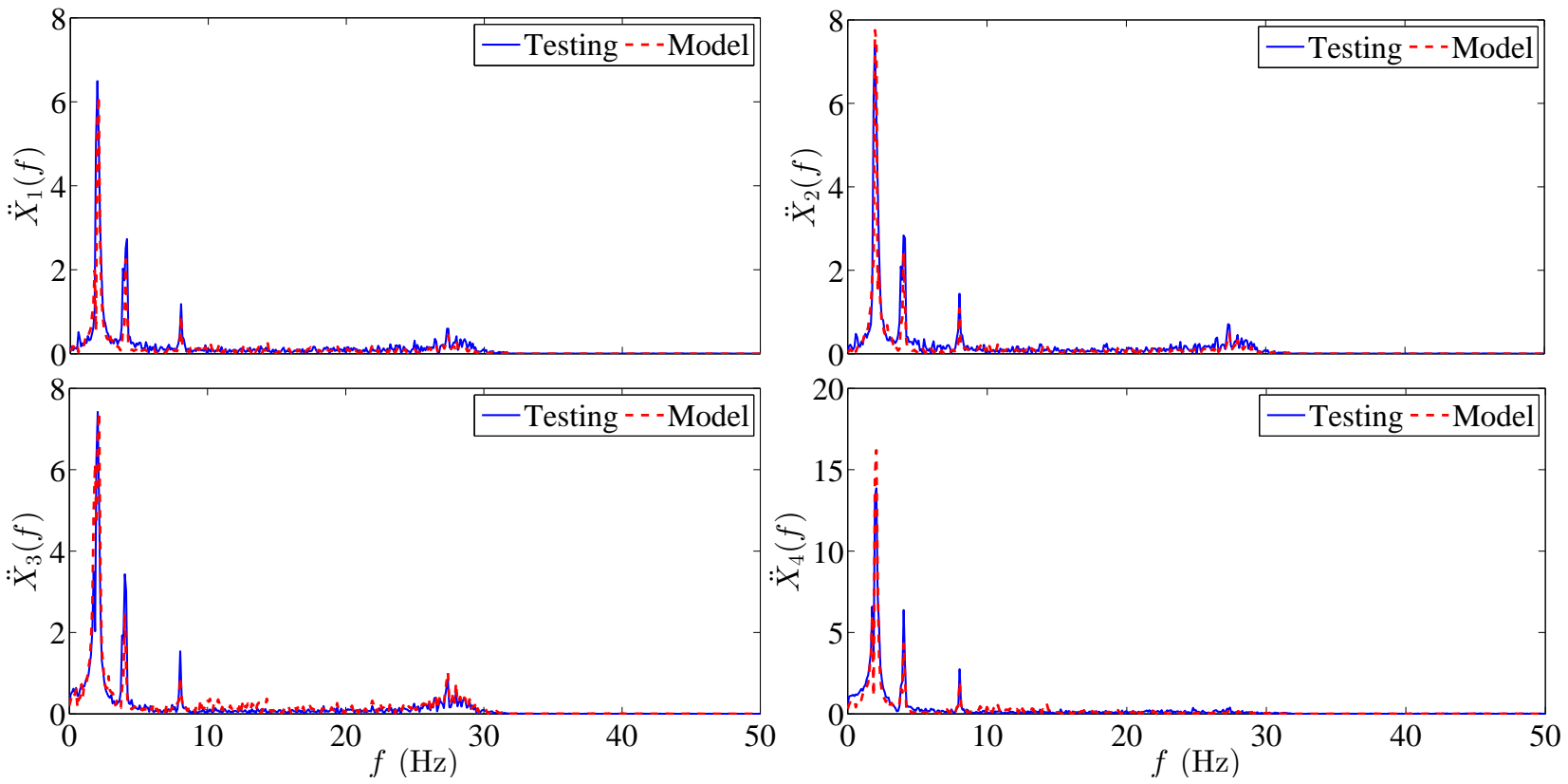
Figure 5.18: Results of high speed test on medium-severity herringbone track.
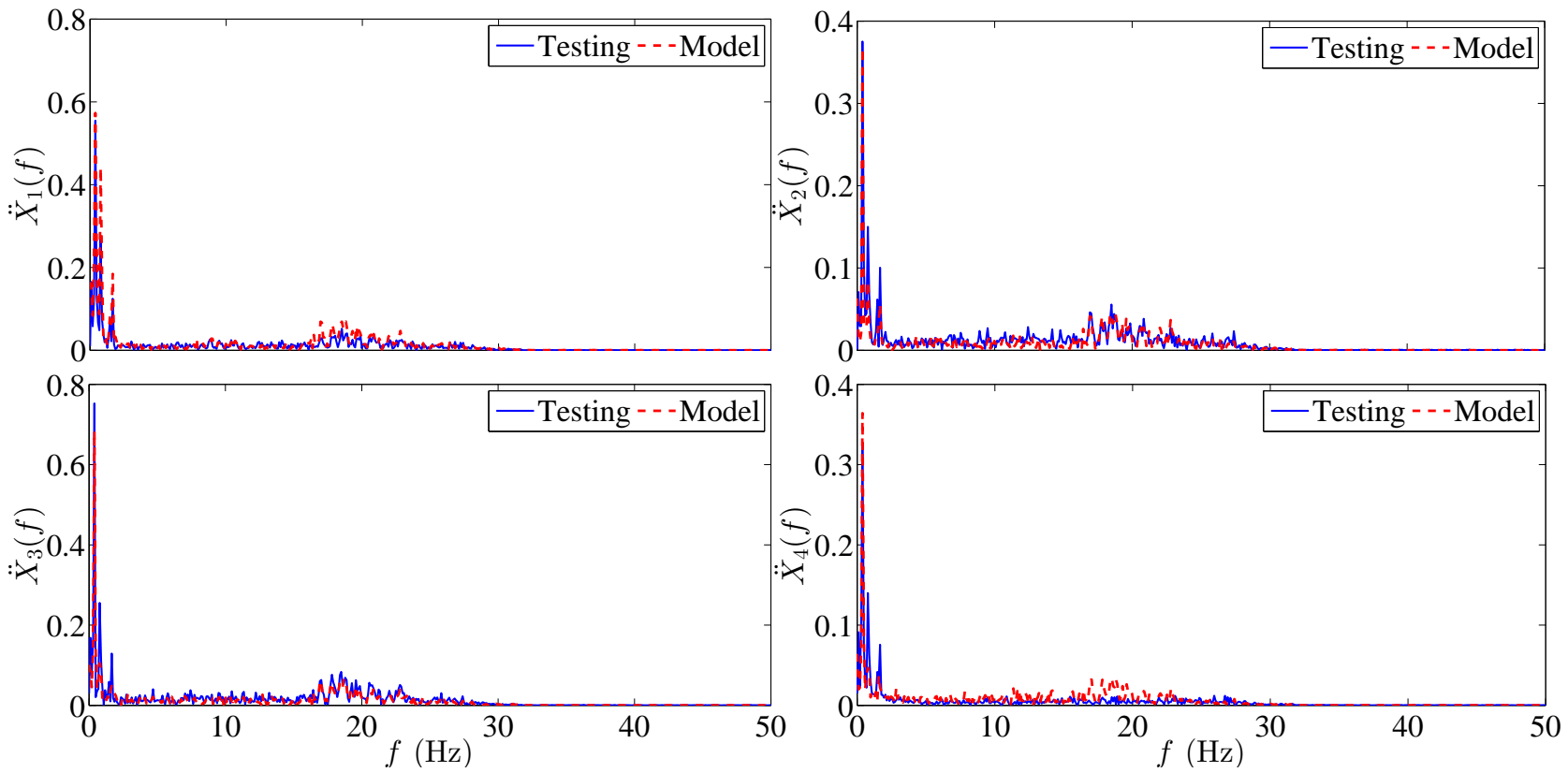
Figure 5.19: Results of low speed test on high-severity chassis twist track.
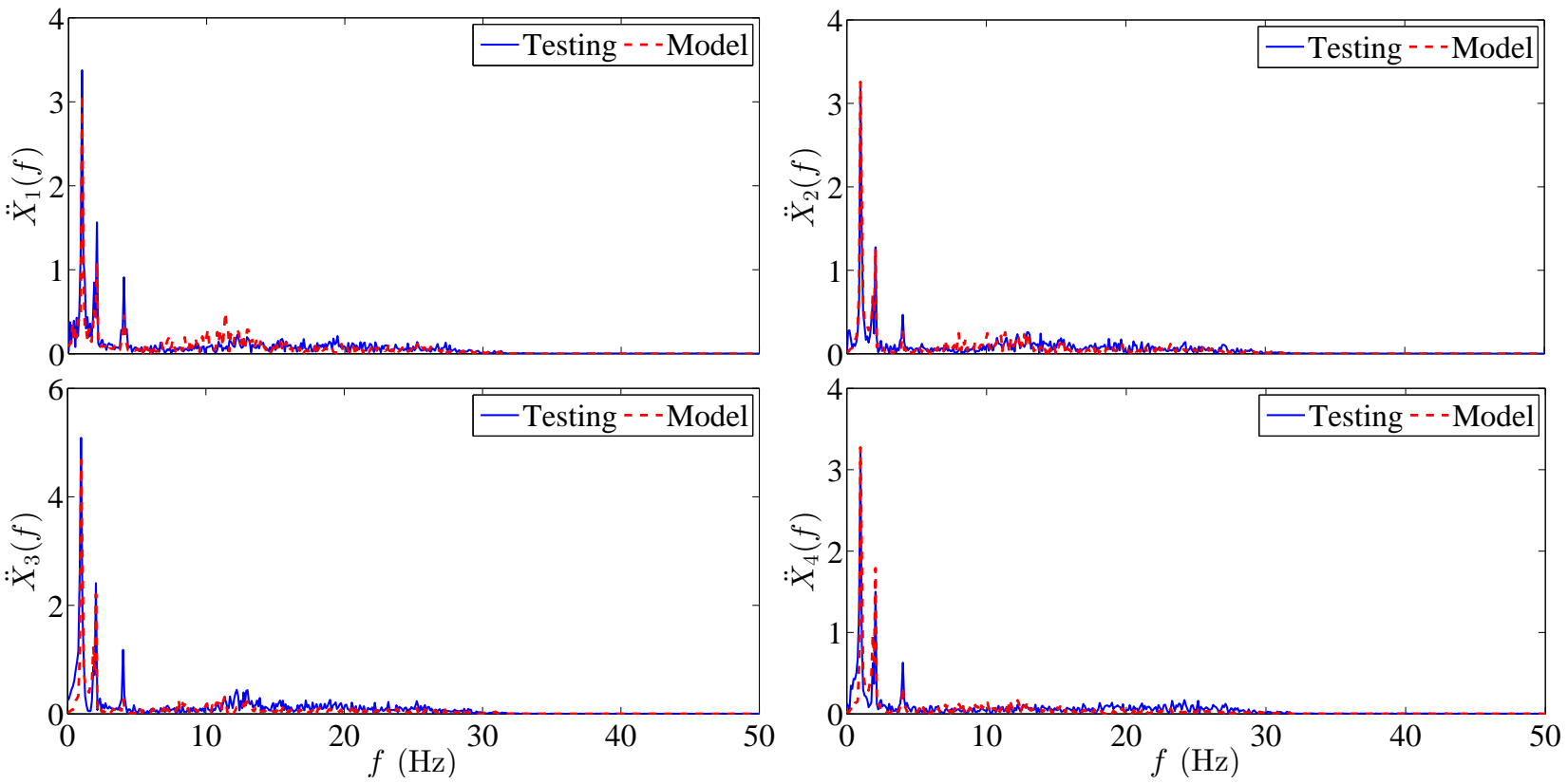
Figure 5.20: Results of high speed test on high-severity chassis twist track.
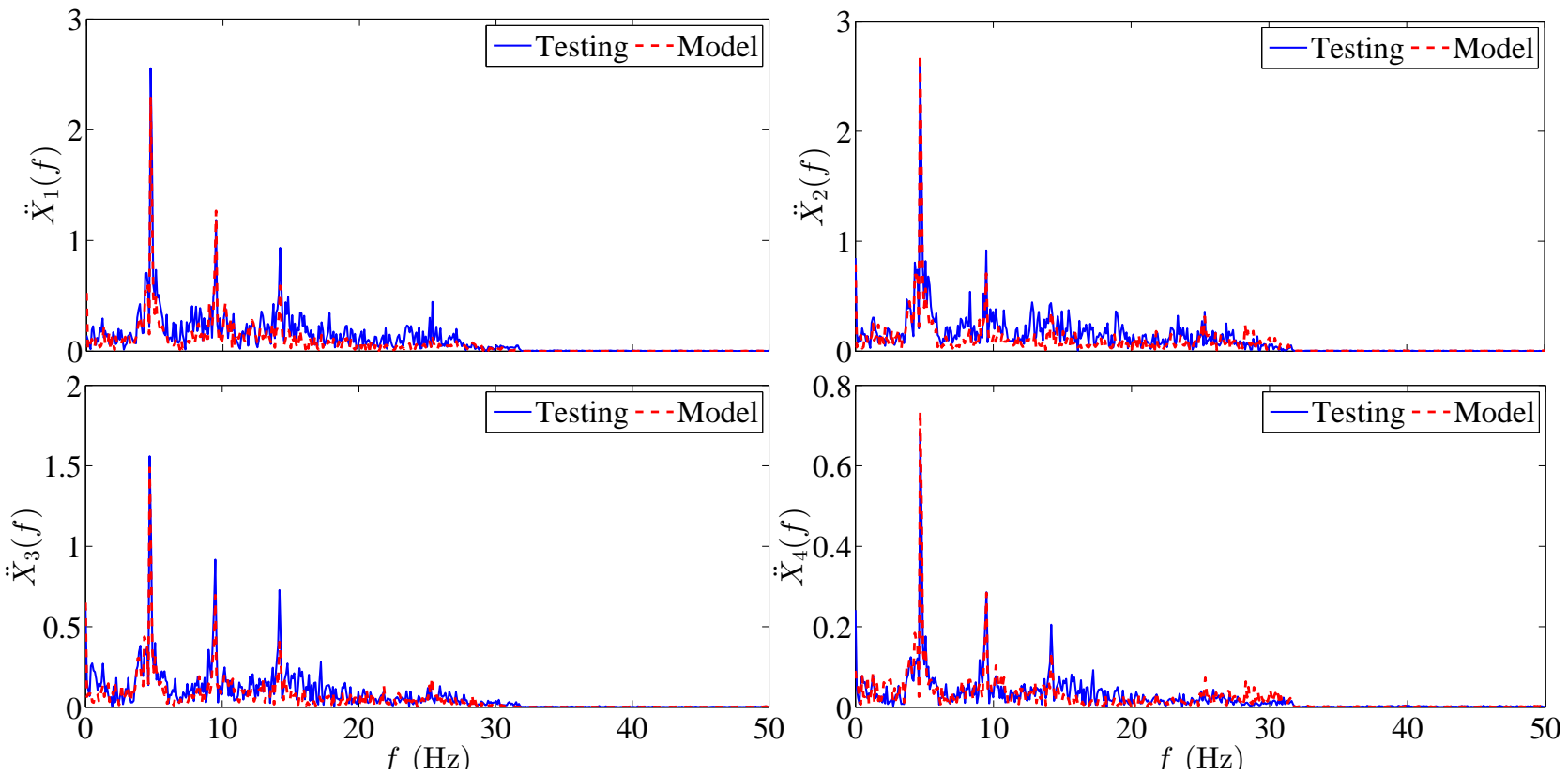
Figure 5.21: Results of low speed test on one sided washboard track.
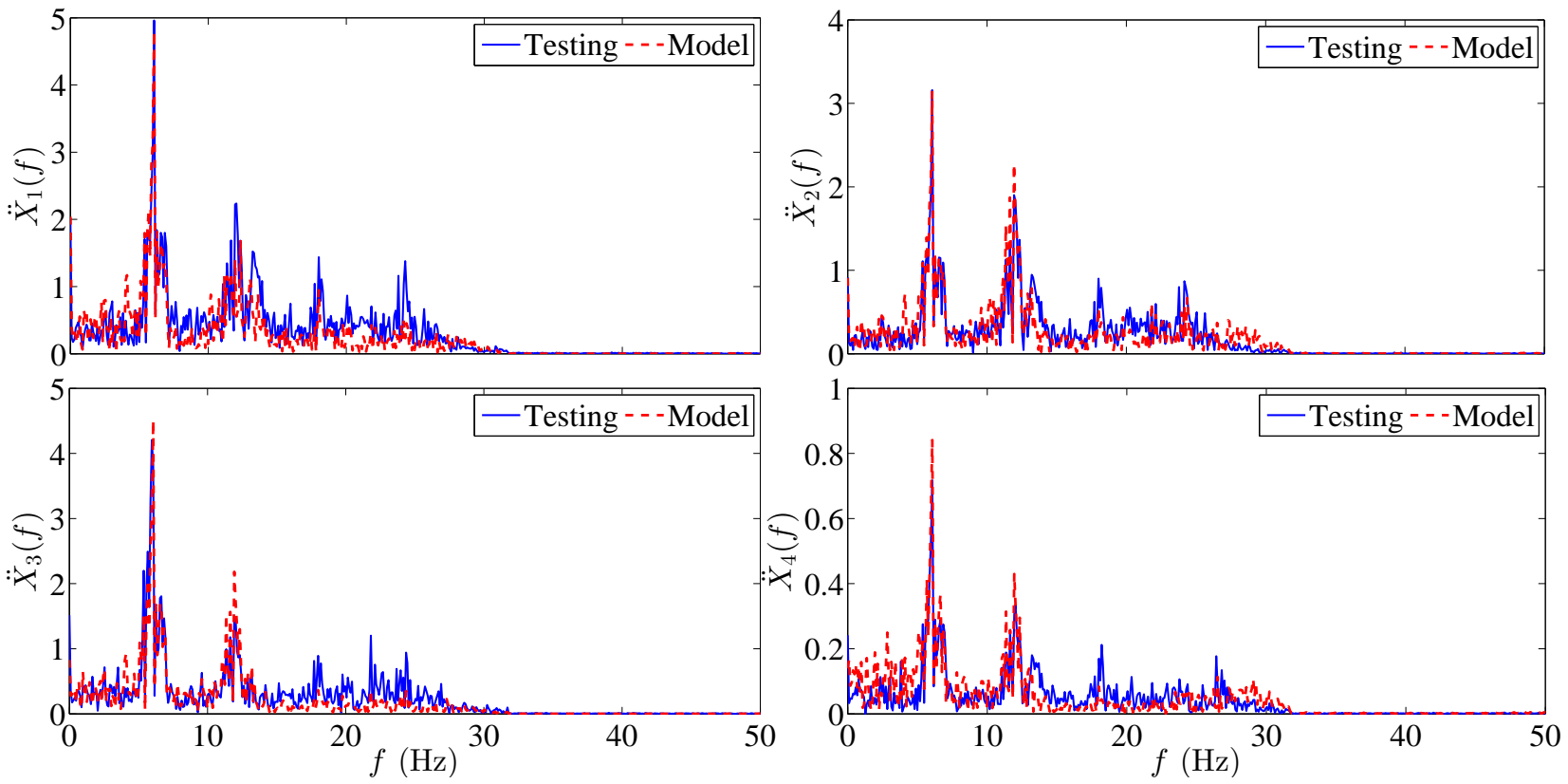
Figure 5.22: Results of high speed test on one sided washboard track.

5.5.5 Discussion of test results

The model and test responses match reasonably well for all vehicle tests. It is emphasized that the plotted quantity is not the magnitude of an element of the transfer function matrix against frequency. Rather, measured axle accelerometer inputs are used by the model to predict body point accelerations, and the FFTs of those predicted quantities are compared to the FFTs of measured accelerations.

1. Washboard track:

   Four vehicle tests were performed at low and high speeds on the washboard track. The model fits all the four tests well. The peak heights in the FFTs are captured and the peak locations match. As a reduced order model is developed, the model responses do not match well beyond 15 Hz, but the working range of vehicle suspensions is also limited to about that same frequency.

2. Herringbone track:

   In this track the left and right wheel excitations were different and for high speed herringbone tests, the time domain responses obtained from the Adams model do not match the time series acceleration measurements well. However, in the frequency domain the match is quite good as some of the limitations of Adams model do not appear here.

3. Chassis twist track:

   In the time domain acceleration measurements there was a high frequency response in addition to the main low frequency response see section 4.35 in Chapter 4. The high frequency response was not captured by the Adams model as in the Adams model the excitation is only from ground (forcing due to engine and driveline vibrations do not appear), but in the frequency domain

the match appears satisfactory. However, if indeed there was a significant ~ 10 Hz effect from the transmission, then the Laplace domain match for this frequency may be misleading. This question, though acknowledged here, is left for resolution to future work on similar vehicles.

4. One-sided washboard track:

   In this track vehicle suffers rocking motions as the ground excitations are acting only on the left wheels. The vehicle used for study did not have a differential which leads to unequal wheel speeds. This difference of speeds was not modeled in the simplified Adams model; also, there is a coupling between driver and steering in the vehicle which was absent in the Adams model. Perhaps, as a result there was substantial mismatch between simulation and test results in the time domain. However, in the frequency domain the model fits the test results well. This part of the improved fit (unlike item 3 above) is probably reliable, because the chain of causality from ground excitation to body response has not been violated.

Some of the FFT plots indicate frequency splitting (and side bands). There was apparently a low frequency fluctuation in amplitude and phase of the measured wheel accelerations. This could be due to a slight asymmetry in suspension parameters, a somewhat weak excitation of a roll mode, or even an approximately periodic fluctuation in the forward speed of the vehicle during testing. The last possibility might explain the widening or apparent splitting of some FFT peaks. Such issues may be investigated more closely in future work if the test conditions are more tightly controlled.

We conclude that, overall, the model reasonably captures the vertical dynamics

of the vehicle. Moreover, it is just an eighth order transfer function model as opposed to a complicated multi-body dynamics Adams model.

So far, a transfer function matrix between accelerations or displacements from A_i to B_i has been obtained. In the next section this transfer function matrix will be used to obtain a more useful transfer function matrix $H_n(s)$ between ground excitations at C_i and displacements at B_i, retaining suspension properties as free parameters.

5.6   Modified transfer function matrix $H_n(s)$

This section closely follows section 2.6 of Chapter 2. The main difference from section 2.6 of chapter 2 is that instead of forces at body points B_i we have displacements inputs at the axle points A_i; we want to develop a new transfer function matrix in terms of displacement inputs at ground contact points C_i.

To obtain $H(s)$, vehicle testing was performed with a set of baseline suspension properties. During subsequent suspension design iterations, it is impractical to build new prototypes and conduct tests for every candidate design change. The aim here, thus, is to obtain a more useful transfer function matrix $H_f(s)$ which incorporates the suspension properties as free parameters[4]. Note that while obtaining the transfer function matrix $H(s)$, the excitations at points A_i were considered, but in reality the excitation comes from the ground at points C_i (see Figure 4.7). Therefore, $H_f(s)$ needs to be modified to determine a transfer function matrix $H_n(s)$ between the displacements at ground contact points C_i and body displacements at B_i.

Thus, there are two steps involved. In the first step, a transfer function matrix

---

[4]the subscript 'f' denotes that the suspension properties are kept as *free* parameters.

$H_f(s)$ is obtained from $H(s)$, and in the second step $H_f(s)$ is used to obtain a transfer function matrix $H_n(s)$. These are discussed in the following subsections.

5.6.1 Incorporating suspension properties as free parameters to obtain $H_f(s)$

We begin with the transfer function matrix $H(s)$ as indicated in ① in Figure 5.23.
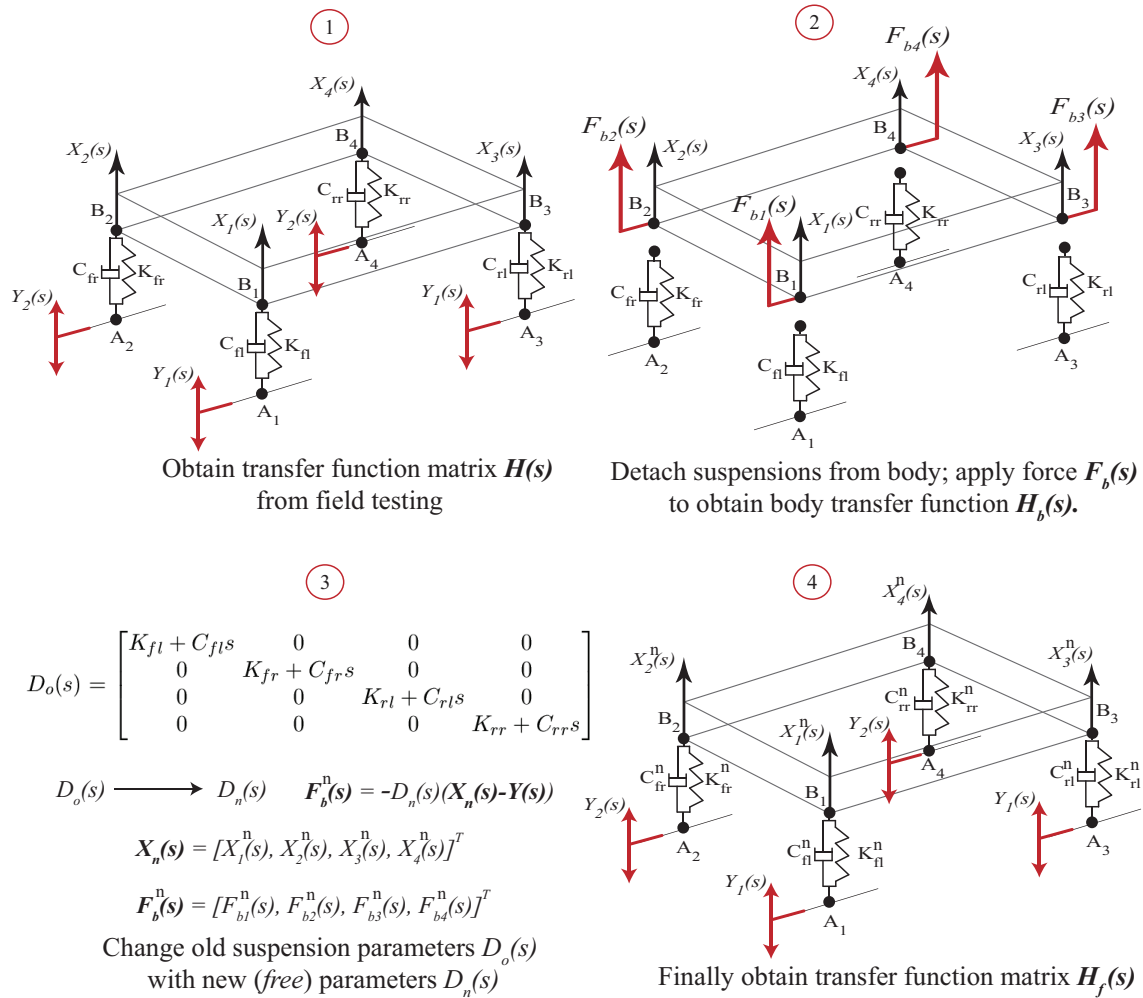
Figure 5.23: Steps involved in obtaining transfer function matrix $H_f(s)$.

First detach the suspensions (spring-dashpots) from the vehicle body (see ②) and apply corresponding spring forces $F_b(s)$ experienced by the suspension-to-body

attachment points B_i as,

$$F_b(s) = -D_o(s)\big[X(s) - Y(s)\big], \tag{5.11}$$

where $D_o(s)$ is a diagonal matrix (subscript "o" denotes old or baseline suspension properties), given by

$$D_o(s) = \begin{bmatrix} K_{fl} + C_{fl}s & 0 & 0 & 0 \\ 0 & K_{fr} + C_{fr}s & 0 & 0 \\ 0 & 0 & K_{rl} + C_{rl}s & 0 \\ 0 & 0 & 0 & K_{rr} + C_{rr}s \end{bmatrix}, \tag{5.12}$$

where $K_{fl}, K_{fr}, K_{rl}, K_{rr}$ are the equivalent stiffnesses and $C_{fl}, C_{fr}, C_{rl}, C_{rr}$ are the corresponding damping coefficients of front left, front right, rear left and rear right wheel-suspension assemblies respectively. The displacements of suspension-to-body attachment points $X_b(s)$ are written as

$$X_b(s) = H_b(s)F_b(s). \tag{5.13}$$

In the above equation $H_b(s)$ may be thought of as a body transfer function matrix (forces to displacements, with suspensions removed). Since the suspension forces are replaced exactly, and the displacements of the same points B_i are considered, therefore in the above equation $X_b(s) = X(s)$. Substituting Equation (5.11) in (5.13) yields

$$X(s) = H_b(s)D_o(s)\big[Y(s) - X(s)\big]. \tag{5.14}$$

199

From Equation (2.6), $X(s) = H(s)Y(s)$, Equation (5.14) reduces to

$$H(s)Y(s) = H_b(s)D_o(s)\Big[I - H(s)\Big]Y(s), \tag{5.15}$$

whence, by the arbitrariness of $Y(s)$, the above equation reduces to

$$H_b(s) = H(s)\Big[I - H(s)\Big]^{-1}D_o(s)^{-1}. \tag{5.16}$$

Now the suspension properties of the front and rear suspensions will be changed (design iteration). Since the vehicle body remains the same, therefore, $H_b(s)$ remains unchanged. The new suspension property matrix is represented by $D_n(s)$ (see ③ in Figure 5.23). With new suspensions the force acting at points B_i changes from $F_b(s)$ to $F_b^n(s)$ indicated by ④ in Figure 5.23. The new set of displacements $X_n(s)$ are obtained as

$$X_n(s) = H_b(s)F_b^n(s), \tag{5.17}$$

where $F_b^n(s) = D_n(s)[Y_n(s) - X_n(s)]$. As similar to the old set of displacements $X(s) = H(s)Y(s)$ the new set of displacements $X_n(s)$ are related to the forces by a transfer function matrix $H_f(s)$ as

$$X_n(s) = H_f(s)Y(s) \tag{5.18}$$

Substituting Equation (5.18) in (5.17) gives

$$H_f(s)Y(s) = H_b(s)D_n(s)\Big[Y(s) - X_n(s)\Big]. \tag{5.19}$$

Simplifying above equation yields

$$H_f(s)Y(s) = H_b(s)D_n(s)\Big[I - H_f(s)\Big]Y(s). \tag{5.20}$$

Again by the arbitrariness of $Y(s)$ the above equation reduces to

$$H_f(s) = I - \Big[I + H_b(s)D_n(s)\Big]^{-1}. \tag{5.21}$$

5.6.2 Obtaining the modified transfer function matrix $H_n(s)$

Using $H_f(s)$ the transfer function matrix from the displacement input $U(s)$ at C_i to the displacement output $X(s)$ at B_i is obtained. For this purpose the unsprung mass model developed in section 2.7 of chapter 2 is used.

The unsprung mass model is given by

$$Y(s) = A(s)X_n(s) - B(s)U(s). \tag{5.22}$$

$A(s)$ and $B(s)$ are obtained from unsprung mass model properties (see Table 5.3).

Identifier	M_u (unsprung)	K_t (tyre)	C_t (tyre)
Front	15 kg	40 N/mm	0.2 N-s/mm
Rear	12.5 kg	40 N/mm	0.2 N-s/mm

Table 5.3: Parameter values used in the unsprung mass compliance model. Note that the unsprung mass is small compared to that of the car sprung mass; both front and rear wheels are identical so the stiffness and damping are the same. Moreover ATV tyres use low inflation pressures (in this vehicle an inflation pressure of 7 psi was used in all four wheels) and as a result these tyres have low stiffness and high damping as compared to the conventional bias-ply tyres.

By definition $X_n(s) = H_n(s)U(s)$, and from Equation (5.21) finally the transfer

function matrix $H_n(s)$ can be obtained as

$$H_n(s) = \left[H_f(s)A(s) - I\right]^{-1} H_f(s)B(s). \tag{5.23}$$

This is the transfer function matrix from ground excitations $U(s)$ at A_i to the response $X(s)$ at suspension to body attachment points B_i. It retains the effects of frame flexibility, mass distribution and other wheel's suspension.

To demonstrate a practical use of this model, a parametric study is performed where both front and rear suspension stiffness is increased by 20% while the damping is kept unchanged[5]. The equivalent suspension properties at the wheel for old and new suspensions are reported in Table 5.4.

Identifier	K_f	K_r	C_f	C_r
Original	10.5 N/mm	6.5 N/mm	0.63 N-s/mm	0.59 N-s/mm
New	12.6 N/mm	7.8 N/mm	0.63 N-s/mm	0.59 N-s/mm

Table 5.4: Original and new equivalent suspension parameters.

The magnitude plots of the diagonal elements $H_{n,11}(s)$ and $H_{n,33}(s)$ of of the new suspension are compared with that of the old suspensions in Figure 5.24.

---

[5]The suspension stiffness can be changed by changing the air pressure of the main air spring chamber. For further details see [72, 73].
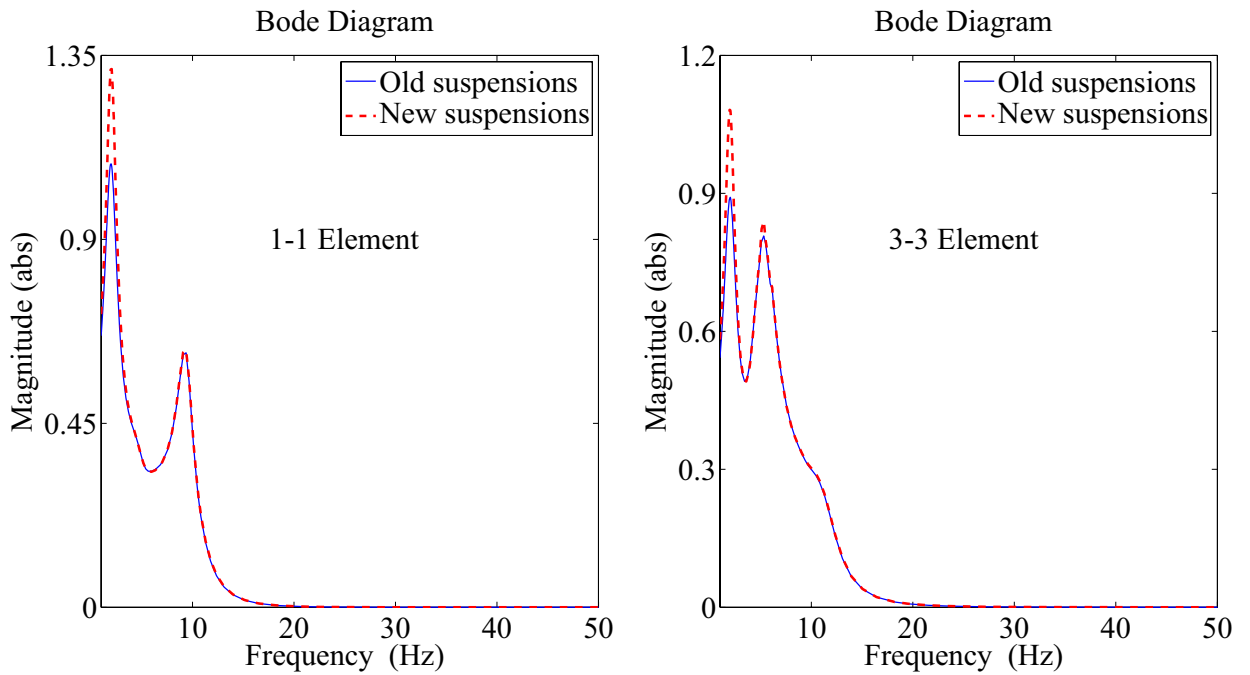
Figure 5.24: Transfer function magnitude plots for old and new suspensions.

5.7 Model order reduction of the final transfer function matrix $H_n(s)$

Initially four values of ω's and ζ's were chosen to obtain the reduced order vehicle transfer function matrix $H(s)$ (see Table 5.2). Each element of $H(s)$ is an 8th order transfer function. Next the suspension properties were changed to obtain a transfer function matrix $H_f(s)$ in Equation (5.21).

Subsequent matrix operations were performed on $H_f(s)$ to incorporate an unsprung mass and wheel compliance to obtain the final transfer function matrix $H_n(s)$. The matrix operations were performed symbolically in Matlab and as a result the order of the transfer function increased from 8 to 44.

For practical work, the order of the transfer function can be reduced without

sacrificing accuracy. For demonstration purpose the model order reduction of one diagonal element of $H_n(s)$, e.g., $H_{n,11}(s)$ (for the front left wheel) will be done. Reduced order models of various orders were obtained using Matlab's built-in function `balred`[6].

A comparison of these reduced order models is shown in Figure 5.25. The results show that an 8th order approximation of the transfer function $H_{n,11}(s)$ preserves the model characteristics accurately.
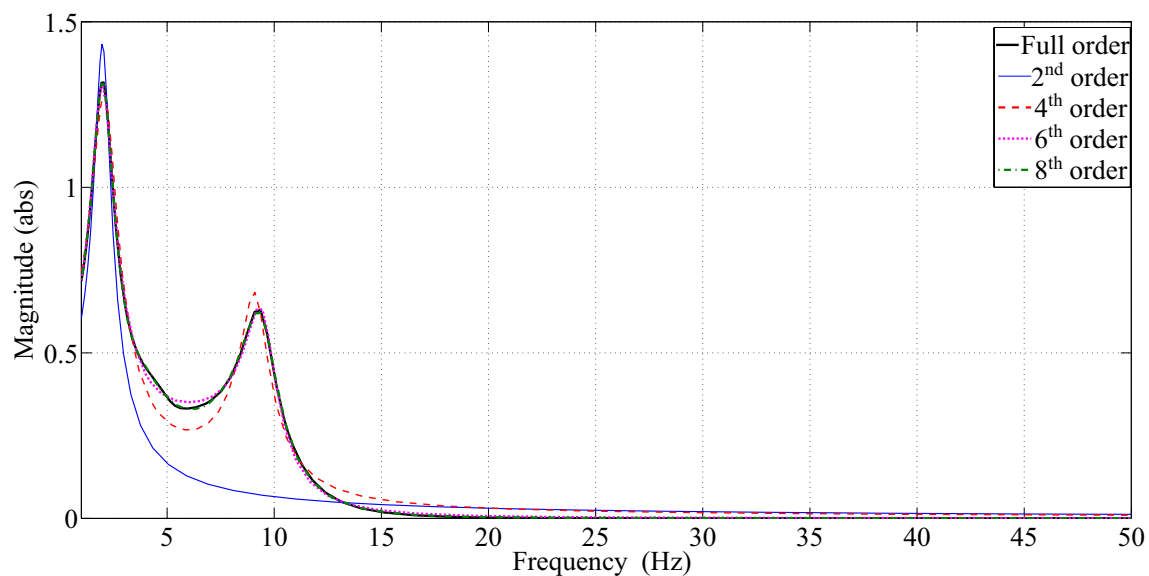
Figure 5.25: Transfer function magnitude plot comparisons of various reduced order models with the full order model.

A similar exercise of model order reduction can be done for all six representative elements (see Equation (5.5)) of the vehicle transfer function matrix $H_n(s)$.

The advantage of this approach is that the suspension properties are kept as free parameters. They can be varied and the response of the vehicle can be predicted without repeated field testing.

---

[6]Options for matching the DC gain and phase should be used.

5.8   Concluding remarks

In this chapter a Laplace domain model development approach from direct field test measurements was demonstrated. The transfer function model was fitted to predict the body points' accelerations in response to measured wheel-axle accelerations. This model was further extended to incorporate an unsprung mass model and retain suspension properties as free parameters, thereby serving as an experimental application of the theory developed in the first part of this work.

The model development requires very little instrumentation and minimal field testing. It is a straightforward way to develop a detailed mathematical model which incorporates vehicle mass, flexibility and damping effects, as well as the effects of stationary ground contacts at other wheels. This approach can be directly used for system identification where an Adams model (or other detailed mathematical model) is not available.

Chapter 6

Conclusions and future work

In this thesis, we have studied four different problems related to vehicle suspension design. The following conclusions are derived from our work:

The vehicle dynamics research literature includes many studies of vehicle suspensions under the quarter-car or half-car simplifications. A fairly simple way was proposed for incorporating vehicle mass, flexibility and damping effects, as well as the effects of stationary ground contacts at other wheels in Chapter 2.

Our approach is of intermediate complexity, between quarter-car or half-car models on the one hand and full-car models on the other. Some expected differences between usual quarter-car model predictions and this more realistic approach can be seen easily. In this model the usual suspension parameters are retained as free parameters to enable parametric optimization studies in the design stage. The model can also be used for the analysis of wheel hop. It is in principle possible to incorporate non-linearities in the local-wheel suspension (where displacements are largest), while retaining linear behavior at other locations.

Elastomers show frequency dependent behavior. In the literature, the *mathematical form* of the empirical fits used have not been fully consistent with linear systems theory. The present work has provided a new and useful contribution in that direction.

We have rationally derived two useful simple mathematical forms with just *three* fitted parameters for modeling the suspension bushings in Chapter 3. In particular, we have ensured the consistency between (a) formulas based on causality, (b) an asymptotic expansion for a regime with slow variations, (c) frequency domain descriptions, and (d) the necessity of real coefficients in Laplace domain descriptions. Experiments with aftermarket automotive bushings have shown that both these mathematical forms can fit the data well. Of these, the modified power law model has more complicated expressions, but fits the data slightly better than does the logarithmic polynomial model.

It is acknowledged that, unlike some models which address very large frequency ranges (e.g., [53, 69]), here a more limited frequency range (about one and a half decades) is considered. However, the selected frequency range is relevant for automotive suspension dynamics simulations, and the small number of fitted parameters along with the consistency with background linear theory makes the two proposed models attractive for practical applications in vehicle dynamics.

Partial validation of a simplified Adams model of a vehicle against field test results has been presented in Chapter 4. Such a model is able to capture the essential vertical suspension dynamic characteristics of the vehicle. The model also retains the effect of frame flexibility (see Figure 6.1), which shows the effect is not insignificant.

The present approach of using test track data to partially validate the model is a practical contribution presenting an inexpensive option that nevertheless provides some useful information and insights. It gives the user an alternative approach for situations where a conventional four post test setup is not available. The simulation results match the experimental results reasonably well for several tests.
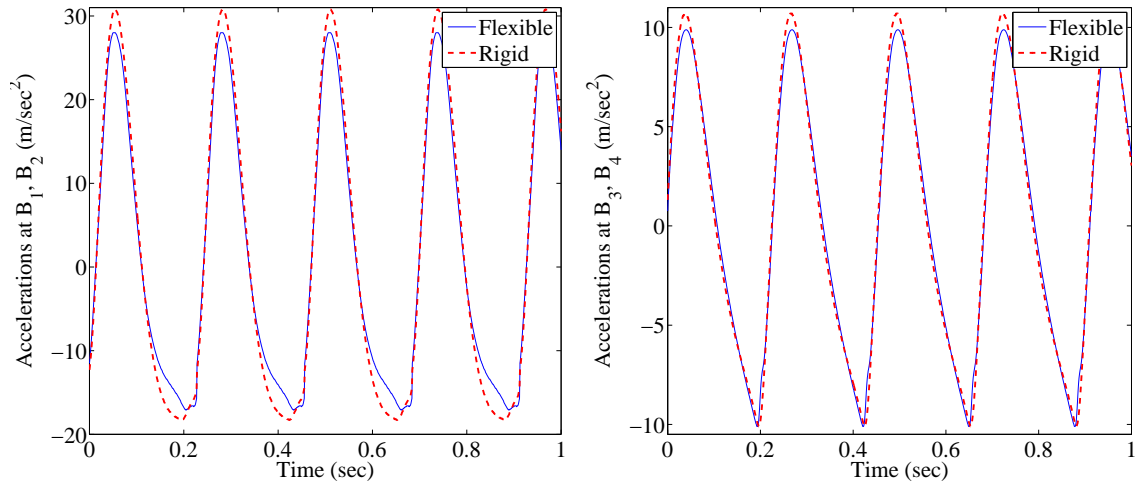
Figure 6.1: Comparison of rigid and flexible frame body point acceleration responses for a vehicle running at low speed on high severity washboard track.

The field test measurements mentioned above are also used for Laplace domain reduced order model development in Chapter 5. This approach requires very little instrumentation and minimal field testing, and no access to professional software like Adams. It is a straightforward way to develop a detailed mathematical model which incorporates effects of vehicle mass, flexibility and damping effects, as well as the effects of stationary ground contacts at other wheels. This approach can be directly used for system identification where an Adams model (or other detailed mathematical model) is not available. The proposed model is simple, gives fairly accurate results for the vertical dynamics of the vehicle, and can be used for suspension design studies at an intermediate level of complexity.

Future work that builds on the approaches and results of this thesis might proceed along one or more of the following lines. First of all, the simplified and generalized quarter car model, with suspension properties retained as free parameters, could be used for suspension optimization and control studies. Additionally, if one were to

treat the near-wheel suspension as nonlinear but the three other-wheel suspensions as linear (because responses are small there), then an explicit reduced -order nonlinear model in the time domain could be developed and investigated.

Secondly, using our new formulas for the frequency domain behavior of suspension bushings, accurate and physically sound characterization of these components could be incorporated in Laplace-domain models or even Adams models along the lines of the generalized quarter-car model (with subsequent model reduction).

Third, in developing and validating Adams models of vehicle using test track data alone, our results have suggested that fore-aft accelerations as well as vibrations excited internally by the engine and transmission, could both potentially be built into the Adams model. Additionally, driver-to-car interactions and wheel compliance in more sophisticated ground contact models [87, 88] could potentially be incorporated.

Finally, a direct extension of the Laplace-domain model building effort of Chapter 5 might include fore-aft motions as well as more points of measurement so as to obtain richer and more detailed models for further study and design improvements.

In this way, the work presented in this thesis has opened up avenues for further developments in inexpensive, simple, yet effective modeling strategies in vehicle suspension dynamics.

Appendices

Appendix A

Supplementary materials for Chapter 2

A.1 Adams suspension model

The vehicle has independent front and rear suspensions. Suspension modeling is done in Adams Car (see Figure A.1).
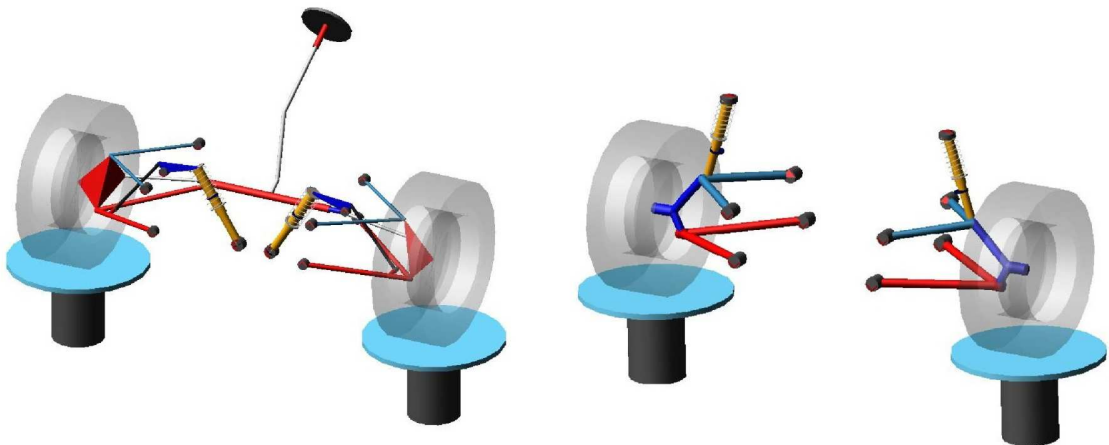
Figure A.1: Front and rear suspension assemblies modeled in Adams Car. Bushings connect the suspension to chassis pivot points.

Essential aspects are described here, and some further details are available in [25]. The front suspension is of double wishbone type along with bi-articulated push rods and bell crank levers. The rear suspension is of double wishbone type.

Both front and rear suspensions have elastic (spring) and dissipative (hydraulic damper)elements.

An equivalent stiffness and damping needs to be estimated for the suspension, accounting for the kinematics of the linkage (i.e., the damper compression differs from actual wheel travel). The equivalent suspension stiffness at wheels (the "wheel rate") was determined directly by a quasi-static wheel travel study of a half car model in Adams. The equivalent damping coefficient was obtained by scaling the manufacturer-supplied damper data by the motion ratio factor (force and velocity were scaled in inverse proportions) to account for linkage kinematics (see Figure A.2).
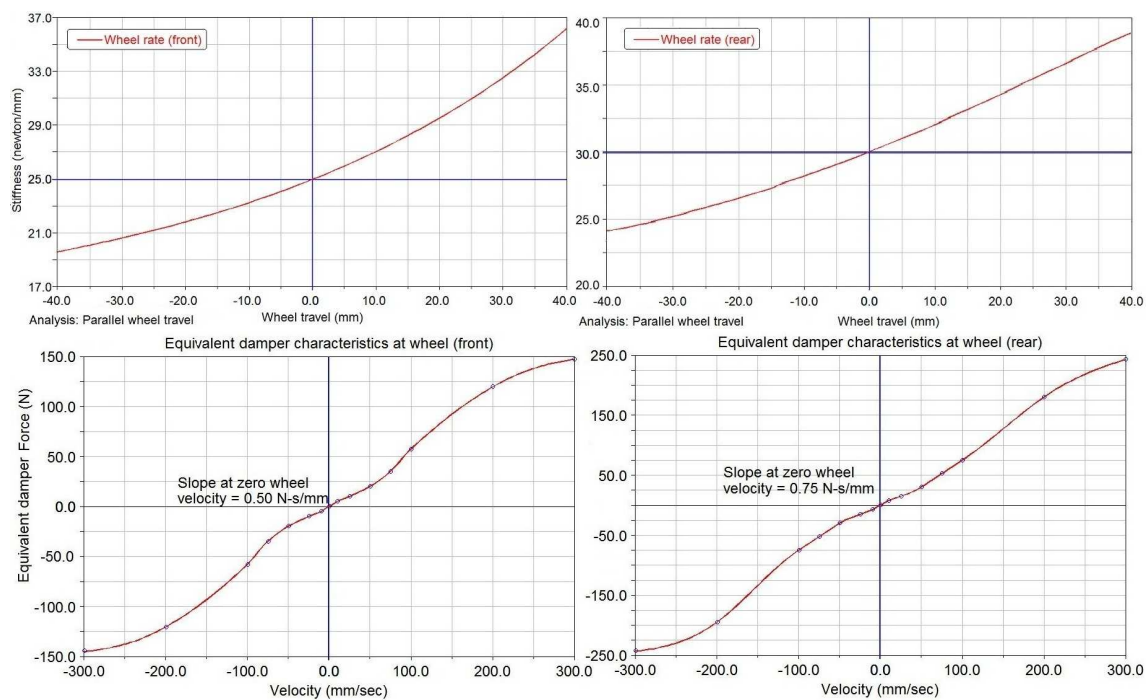
Figure A.2: Equivalent stiffness and damping characteristics of front and rear suspensions.

The baseline suspension properties obtained are shown in Table A.1; see also Table 2.2 in chapter 2.

K_{front}	K_{rear}	C_{front}	C_{rear}
25 N/mm	30 N/mm	0.50 N-s/mm	0.75 N-s/mm

Table A.1: Initial estimates of suspension parameters.

A.2 Initial estimates of σ's and ω's for use in Section 2.4 of Chapter 2

The initial estimates of σ's and ω's for use in Section 2.4 will be obtained in this section.

Consider the incremental model with four-dimensional state vector $\bar{z}_k$ given by

$$\bar{z}_k = x_{k+1} - x_k, \tag{A.1}$$

where x_{k+1} and x_k are the body points' displacements at discrete time intervals $(k+1)T$ and kT respectively. The dimension of the state vector is then extended by considering the values of the increments at multiple time steps as in

$$z_k = \begin{bmatrix} \bar{z}_k \\ \bar{z}_{k+1} \\ \vdots \\ \bar{z}_{k+(j-1)} \end{bmatrix}, \tag{A.2}$$

where j is to be chosen large enough to get a good fit.

An underlying discrete-time model is assumed in the form

$$z_{k+1} = D \ z_k, \tag{A.3}$$

215

where D is a state transition matrix to be fitted, in a least squares sense, from many x-data points.

We know that the underlying continuous time state space model is given by

$$\dot{z} = A\, z; \quad A = 4 \times 4 \text{ system state matrix.} \tag{A.4}$$

Integrating above equation we obtain

$$z(t) = e^{At} z(0). \tag{A.5}$$

The system response at times $t = kT$ and $(k+1)T$ is given by

$$z_k = e^{AkT} z(0);$$

$$z_{k+1} = e^{A(k+1)T} z(0). \tag{A.6}$$

Multiplying the first equation of the Equation (A.6) by e^{AT} and subtracting it from the second we obtain

$$z_{k+1} = e^{AT} z_k \tag{A.7}$$

From Equations (A.7) and (A.3), we get the equivalence between the continuous time and discrete time state space model as,

$$D = e^{AT} \tag{A.8}$$

The eigenvalues of D provide the needed estimates of σ's and ω's, through

$$\sigma + i\,\omega = \frac{\log\Big(\operatorname{eig}(D)\Big)}{T}, \tag{A.9}$$

where T is the time step (in our Adams simulations, $T = 0.02$ seconds).

The exponential rates obtained for various numbers of retained complex eigenvalues are reported in Table A.2.

No. of complex pairs retained	Identifier	σ	ω
One	Single time step model	2.11	14.72
Two	Two time step model	1.88	17.88
		1.90	12.26
Three	Three time step model	1.52	12.28
		2.41	18.29
		4.29	13.40

Table A.2: Initial guesses of σ's and ω's. These need not be very accurate, as subsequent nonlinear fitting is done.

These σ's and ω's were used as initial guesses in nonlinear fitting based on Matlab's built in optimization routine `fminsearch`.

A.3 Balanced reduction

Balanced reduction was introduced in the control community by Moore [89]. The balanced reduction in Matlab is achieved in two steps.

First a balanced realization of the original system is obtained using `balreal` [90]. Next a state elimination algorithm `modred` reduces the order of the balanced state-space model by eliminating the non-significant states. These are discussed in

the following subsections.

A.3.1 Balanced realization

In balanced realization scheme first the transfer function model is converted to a state space model given by

$$
\begin{aligned}
\dot{x} &= Ax + Bu \\
y &= Cx + Du
\end{aligned}
$$

(A.10)

Next the `balreal` algorithm creates a balanced system using a state transformation matrix T given by

$$
\begin{aligned}
\dot{x}_b &= \underbrace{TAT^{-1}}_{A_b} x_b + \underbrace{TB}_{B_b} u \\
y &= \underbrace{CT^{-1}}_{C_b} x_b + Du
\end{aligned}
$$

(A.11)

The syntax for the `balreal` function is:

```
Balanced system = balreal(Original system)
```

A.3.2 Model truncation

Once the balanced system is obtained from the original state space model; truncation is used to eliminate the unimportant state variables to reduce the model order. At first the `modred` function partitions the balanced system states x_b into x_{b1}, to be

218

kept, and x_{b2}, to be eliminated. The number of states to be eliminated 'Elim' is specified by the user. The resultant state space model looks like:

$$\begin{bmatrix} \dot{x}_{b1} \\ \dot{x}_{b2} \end{bmatrix} = \begin{bmatrix} A_{b11} & A_{b12} \\ A_{b21} & A_{b22} \end{bmatrix} \begin{bmatrix} x_{b1} \\ x_{b2} \end{bmatrix} + \begin{bmatrix} B_{b1} \\ B_{b2} \end{bmatrix} u$$

$$y = \begin{bmatrix} C_{b1} & C_{b2} \end{bmatrix} \begin{bmatrix} x_{b1} \\ x_{b2} \end{bmatrix} + Du.$$

(A.12)

Next, the derivative of x_{b2} in the above equation is set to zero and the resulting equation is solved for x_{b1}. The reduced-order model is given by

$$\dot{x}_{b1} = \begin{bmatrix} A_{b11} - A_{b12}A_{b22}^{-1}A_{b21} \end{bmatrix} x_{b1} + \begin{bmatrix} B_{b1} - A_{b12}A_{b22}^{-1}B_{b2} \end{bmatrix} u$$

$$y = \begin{bmatrix} C_{b1} - C_{b2}A_{b22}^{-1}A_{b21} \end{bmatrix} x_{b1} + \begin{bmatrix} D - C_{b2}A_{b22}^{-1}B_{b2} \end{bmatrix} u.$$

(A.13)

The syntax for the modred function is:

```
Reduced system = modred(Balanced system, Elim, 'MatchDC')
```

A.4 Expressions for full and reduced order transfer functions

$G_{11}(s)$ was found to be the following 36th order transfer function:

$$G_{11}(s) =$$

$$\frac{\begin{aligned} &5.9s^{35} + 3\mathrm{e}5s^{34} + 5.5\mathrm{e}9s^{33} + 5.3\mathrm{e}13s^{32} + 1.7\mathrm{e}17s^{31} + 3.1\mathrm{e}19s^{30} + 8.5\mathrm{e}21s^{29} + 1\mathrm{e}24s^{28} \\ &+1.5\mathrm{e}26s^{27} + 1.5\mathrm{e}28s^{26} + 1.3\mathrm{e}30s^{25} + 9.9\mathrm{e}31s^{24} + 6.3\mathrm{e}33s^{23} + 3.4\mathrm{e}35s^{22} + 1.6\mathrm{e}37s^{21} \\ &+6.7\mathrm{e}38s^{20} + 2.3\mathrm{e}40s^{19} + 7.6\mathrm{e}41s^{18} + 2.1\mathrm{e}43s^{17} + 5.3\mathrm{e}44s^{16} + 1.2\mathrm{e}46s^{15} + 2.5\mathrm{e}47s^{14} \\ &+4.7\mathrm{e}48s^{13} + 7.9\mathrm{e}49s^{12} + 1.2\mathrm{e}51s^{11} + 1.7\mathrm{e}52s^{10} + 2.1\mathrm{e}53s^{9} + 2.4\mathrm{e}54s^{8} + 2.5\mathrm{e}55s^{7} \\ &+2.3\mathrm{e}56s^{6} + 1.8\mathrm{e}57s^{5} + 1.3\mathrm{e}58s^{4} + 7.6\mathrm{e}58s^{3} + 3.9\mathrm{e}59s^{2} + 1.3\mathrm{e}60s + 4.1\mathrm{e}60 \end{aligned}}{\begin{aligned} &s^{36} + 6.2\mathrm{e}4s^{35} + 1.4\mathrm{e}9s^{34} + 1.6\mathrm{e}13s^{33} + 9.2\mathrm{e}16s^{32} + 1.3\mathrm{e}19s^{31} + 3.3\mathrm{e}21s^{30} + 3.5\mathrm{e}23s^{29} \\ &+4.7\mathrm{e}25s^{28} + 3.8\mathrm{e}27s^{27} + 3.3\mathrm{e}29s^{26} + 2.1\mathrm{e}31s^{25} + 1.3\mathrm{e}33s^{24} + 6.4\mathrm{e}34s^{23} + 3\mathrm{e}36s^{22} \\ &+1.1\mathrm{e}38s^{21} + 4\mathrm{e}39s^{20} + 1.2\mathrm{e}41s^{19} + 3.3\mathrm{e}42s^{18} + 8.3\mathrm{e}43s^{17} + 1.9\mathrm{e}45s^{16} + 3.9\mathrm{e}46s^{15} \\ &+7.3\mathrm{e}47s^{14} + 1.2\mathrm{e}49s^{13} + 2.0\mathrm{e}50s^{12} + 2.8\mathrm{e}51s^{11} + 3.7\mathrm{e}52s^{10} + 4.3\mathrm{e}53s^{9} + 4.7\mathrm{e}54s^{8} \\ &+4.5\mathrm{e}55s^{7} + 4\mathrm{e}56s^{6} + 3\mathrm{e}57s^{5} + 2\mathrm{e}58s^{4} + 1.1\mathrm{e}59s^{3} + 5.6\mathrm{e}59s^{2} + 1.8\mathrm{e}60s + 5.4\mathrm{e}60 \end{aligned}}$$

This higher order transfer function was reduced, using Matlab's function `balred`, to:

$$G_{red}(s) = \frac{8.3\text{e-}3s^{6} + 1.1s^{5} + 2.1\mathrm{e}2s^{4} + 2.6\mathrm{e}4s^{3} + 1.1\mathrm{e}6s^{2} + 8.9\mathrm{e}6s + 1.9\mathrm{e}8}{s^{6} + 2.9\mathrm{e}1s^{5} + 6.2\mathrm{e}3s^{4} + 7.6\mathrm{e}4s^{3} + 2.8\mathrm{e}6s^{2} + 1.3\mathrm{e}7s + 2.5\mathrm{e}8}.$$

The 's^6' term in the numerator of the above transfer function was dropped to obtain a strictly proper transfer function as

$$G_{red}(s) = \frac{1.1s^{5} + 2.1\mathrm{e}2s^{4} + 2.6\mathrm{e}4s^{3} + 1.1\mathrm{e}6s^{2} + 8.9\mathrm{e}6s + 1.9\mathrm{e}8}{s^{6} + 2.9\mathrm{e}1s^{5} + 6.2\mathrm{e}3s^{4} + 7.6\mathrm{e}4s^{3} + 2.8\mathrm{e}6s^{2} + 1.3\mathrm{e}7s + 2.5\mathrm{e}8}.$$

Appendix B

Supplementary materials for Chapter 3

B.1 Detailed proof of Kramers-Kronig dispersion relations

For a linear and time-invariant (LTI) system the property of causality translates from the requirement of a vanishing impulse response for times smaller than zero directly to the Kramers-Kronig relations in the frequency domain [14, 15].

A short introduction to the Kramers-Kronig relations is provided here for completeness. The present discussion very closely follows [91, 92].

Let $h(t)$ be the impulse response of a linear and time-invariant system. The frequency response of this system is then given by its Fourier-transform as

$$\mathcal{F}[h(t)] = H(\omega) = \int\limits_{-\infty}^{\infty} h(t)\ \mathrm{e}^{-i\omega t}\ dt. \tag{B.1}$$

Now, $h(t)$ does not change if it is multiplied by a unit step function $\Theta(t)$, i.e.,

$$h(t) = h(t)\Theta(t). \tag{B.2}$$

221

Equation (B.2) is substituted in Equation (B.1) to obtain

$$H(\omega) = \int\limits_{-\infty}^{\infty} h(t)\Theta(t)\, e^{-i\omega t}\, dt. \tag{B.3}$$

The right side of the above equation denotes the Fourier transform $\mathcal{F}[h(t)\Theta(t)]$, therefore the convolution theorem can be applied, i.e.,

$$\mathcal{F}[h(t) \cdot \Theta(t)] = \mathcal{F}[h(t)] * \mathcal{F}[\Theta(t)].$$

The Fourier transform of the unit step function is given by

$$\mathcal{F}[\Theta(t)] = \left(\pi\delta(\omega) + \frac{1}{i\omega}\right). \tag{B.4}$$

Substituting Equation (B.4) in Equation (B.3) gives

$$H(\omega) = \left[H(\omega) * \left(\pi\delta(\omega) + \frac{1}{i\omega}\right)\right].$$

The convolution of two functions $A(\omega), B(\omega)$ is defined as

$$A(\omega) * B(\omega) = \frac{1}{2\pi} \int\limits_{-\infty}^{\infty} A(\omega') \cdot B(\omega - \omega')\, d\omega'.$$

Executing the convolution we obtain

$$H(\omega) = \frac{1}{2\pi} \left(\int\limits_{-\infty}^{\infty} \pi H(\omega') \cdot \delta(\omega - \omega') + \int\limits_{-\infty}^{\infty} \frac{H(\omega')}{i(\omega - \omega')} \right) d\omega',$$

which reduces to

222

$$H(\omega) = \frac{1}{2\pi} \left(\pi H(\omega) + \int_{-\infty}^{\infty} \frac{H(\omega')}{i(\omega - \omega')} \, d\omega' \right),$$

where the singular integral is to be taken in the Cauchy Principal value (CPV) sense [60, 92].

The above can be further simplified to obtain

$$H(\omega) = \frac{1}{\pi} \int_{-\infty}^{\infty} \frac{H(\omega')}{i(\omega - \omega')} \, d\omega'. \tag{B.5}$$

The right hand side of the above integral is split up as

$$\frac{1}{\pi} \int_{-\infty}^{\infty} \frac{H(\omega')}{i(\omega - \omega')} \, d\omega' = \frac{1}{\pi} \int_{-\infty}^{0} \frac{H(\omega')}{i(\omega - \omega')} \, d\omega' + \frac{1}{\pi} \int_{0}^{\infty} \frac{H(\omega')}{i(\omega - \omega')} \, d\omega'. \tag{B.6}$$

Substituting $\omega' = -\omega''$, the negative-domain integral can be rewritten as

$$\frac{1}{\pi} \int_{-\infty}^{0} \frac{H(\omega')}{i(\omega - \omega')} \, d\omega' = \frac{1}{\pi} \int_{0}^{\infty} \frac{H(-\omega'')}{i(\omega + \omega'')} \, d\omega''.$$

By the definition of Fourier integral, $H(-\omega'') = H^*(\omega'')$, Equation (B.6) can be written as

$$H(\omega) = \frac{1}{\pi} \left(\int_{0}^{\infty} \frac{H(\omega')}{i(\omega - \omega')} \, d\omega' + \int_{0}^{\infty} \frac{H^*(\omega'')}{i(\omega + \omega'')} \, d\omega'' \right). \tag{B.7}$$

By definition

$$H(\omega) = H_1(\omega) + iH_2(\omega); \quad H^*(\omega) = H_1(\omega) - iH_2(\omega). \tag{B.8}$$

Substituting Equation (B.8) in Equation (B.7) and combining both integrals gives

$$H(\omega) = \frac{1}{\pi} \int\limits_{0}^{\infty} \left(\frac{(\omega + \omega')(H_1(\omega') + iH_2(\omega')) + (\omega - \omega')(H_1(\omega') - iH_2(\omega'))}{i(\omega'^2 - \omega^2)} \right) d\omega'. \tag{B.9}$$

Simplification of the above equation yields

$$H(\omega) = \frac{1}{\pi} \int\limits_{0}^{\infty} \left(\frac{2H_2(\omega')\omega' - i2H_1(\omega')\omega}{\omega^2 - \omega'^2} \right) d\omega'. \tag{B.10}$$

The real and imaginary parts of Equation (B.10) are separated to obtain

$$H_1(\omega) = \frac{2}{\pi} \int\limits_{0}^{\infty} \frac{\omega' H_2(\omega')}{\omega^2 - \omega'^2} \, d\omega'; \qquad H_2(\omega) = -\frac{2}{\pi} \int\limits_{0}^{\infty} \frac{\omega H_1(\omega')}{\omega^2 - \omega'^2} \, d\omega'. \tag{B.11}$$

These are the well known Kramers-Kronig relations. The fundamental implication in the context of this thesis is that the real and imaginary parts of $H(\omega)$ cannot be independently assigned and fitted.

B.2 Asymptotic approximation to be used in model development

In the present study, the frequency response function $H(\omega)$ corresponds to the complex modulus of the viscoelastic material $M^*(\omega) = M_d(\omega) + iM_1(\omega)$. Moreover, in the original Kramers-Kronig application, an allowance was made for an instantaneous component of response $M_0\delta(t)$, where M_0 is the value at high ("infinite") frequency. The causality condition was applied to the remainder of the total response, given by $[M(t) - M_0\delta(t)]$.

$$M_{\mathrm{d}}(\omega) - M_0 = \frac{2}{\pi} \int\limits_0^\infty \frac{\omega' M_1(\omega')}{\omega^2 - \omega'^2}\, d\omega', \qquad M_1(\omega) = -\frac{2}{\pi} \int\limits_0^\infty \frac{\omega[M_{\mathrm{d}}(\omega') - M_0]}{(\omega^2 - \omega'^2)}\, d\omega'$$

(B.12)

Using the second equation of Equation (B.12), a more useful representation was obtained by Bode [93].

Rewriting Equation (B.12) as

$$M_1(\omega) = -\frac{2}{\pi} \int\limits_0^\infty \frac{\omega[M_d(\omega') - M_0]}{\omega^2 \left(1 - (\frac{\omega'}{\omega})^2\right)}\, d\omega', \tag{B.13}$$

a change of variable $x = \ln\left(\dfrac{\omega'}{\omega}\right)$ gives

$$dx = \frac{1}{\omega'}d\omega', \text{ therefore, } d\omega' = \omega' dx = \omega \mathrm{e}^x dx,$$

which yields (note the change in integration limits)

$$M_1(\omega) = -\frac{2}{\pi} \int\limits_{-\infty}^\infty \frac{\cancel{\omega}\mathrm{e}^x[G(x) - G_0]}{\cancel{\omega^2}(1 - \mathrm{e}^{2x})}\, dx$$

where $G(x) = M_d(\omega'), G_0 = M_0$.

Taking e^x common from the denominator gives

$$M_1(\omega) = -\frac{2}{\pi} \int\limits_{-\infty}^\infty \frac{\cancel{\mathrm{e}^x}[G(x) - G_0]}{\cancel{\mathrm{e}^x}(\mathrm{e}^{-x} - \mathrm{e}^x)}\, dx \tag{B.14}$$

Equation (B.14) is to be integrated in order to obtain dispersion relations. Substituting $\mathrm{e}^x = z$, therefore, $\mathrm{e}^x dx = dz, G(x) = \tilde{G}(z)$, and thereby changing the limit

225

of integration to 0 to ∞ gives.

$$
\begin{aligned}
M_1(\omega) &= -\frac{2}{\pi} \int_0^\infty \frac{[\tilde{G}(z) - G_0]}{z^2 - 1} \, dz \\
&= \frac{1}{\pi} \int_0^\infty [\tilde{G}(z) - G_0]\left(\frac{1}{z+1} - \frac{1}{z-1}\right) dz,
\end{aligned}
$$

where the singularity at $z = 1$ is to be interpreted in the CPV sense, i.e.,

$$
M_1(\omega) = \lim_{\varepsilon \to 0} \frac{1}{\pi}\Bigg[\int_0^{1+\varepsilon} [\tilde{G}(z) - G_0]\left(\frac{1}{z+1} - \frac{1}{z-1}\right) dz \\
+ \int_{1+\varepsilon}^\infty [\tilde{G}(z) - G_0]\left(\frac{1}{z+1} - \frac{1}{z-1}\right)\Bigg] dz
$$

The above integral is evaluated to obtain

$$
M_1(\omega) = \lim_{\varepsilon \to 0} \frac{1}{\pi}\Bigg[\underbrace{(\tilde{G}(z) - G_0)\ln\left(\frac{z+1}{z-1}\right)\Bigg|_0^{1+\varepsilon} + (\tilde{G}(z) - G_0)\ln\left(\frac{z+1}{z-1}\right)\Bigg|_{1+\varepsilon}^\infty}_{1}
$$

$$
+ \underbrace{\int_0^\infty \frac{d\tilde{G}(z)}{dz} \ln\left(\frac{z+1}{z-1}\right) dz}_{2}\Bigg]
$$

The first term vanishes and second term is transformed back to

$$
M_1(\omega) = \frac{1}{\pi} \int_{-\infty}^\infty \underbrace{\frac{dG(x)}{dx}}_{F(x)} \ln \underbrace{\left(\frac{e^x + 1}{e^x - 1}\right)}_{\coth \frac{|x|}{2}} dx.
$$

The above integral is symmetric about $x = 0$ and therefore it can be re-written as

226

$$M_1(\omega) = \frac{2}{\pi} \int_0^\infty F(x) \ln \left(\coth \frac{|x|}{2} \right) \, dx, \tag{B.15}$$

Equation (B.15) was primarily used by Bode to develop simplified relations between attenuation and phase of amplifiers [16]. Furthermore, using Equation (B.15), O'Donnell et al. [64] obtained simple localized approximate series expansions. To that end, $F(x)$ is expanded in a Taylor series about $x = 0$ to obtain

$$M_1(\omega) = \frac{2}{\pi} \sum_{n=0}^\infty \frac{F^n(0)}{n!} \int_0^\infty x^n \ln \left(\coth \frac{|x|}{2} \right) \, dx,$$

Note that $\coth \dfrac{|x|}{2}$ is an even function (see Figure B.1), and the integral vanishes for odd powers of x.
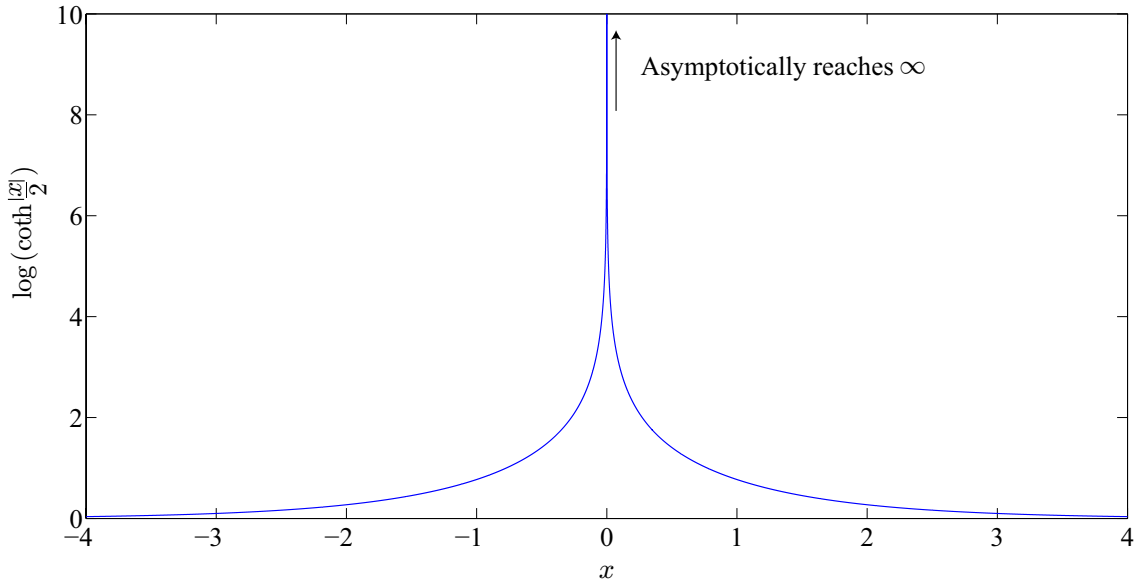
Figure B.1: Behaviour of function $\ln \coth(\frac{|x|}{2})$ in the neighborhood of $x = 0$.

So we write

$$M_1(\omega) = \frac{2}{\pi} \sum_{n=0}^\infty \frac{F^{2n}(0)}{(2n)!} \int_0^\infty x^{2n} \ln \left(\coth \frac{|x|}{2} \right) \, dx, \tag{B.16}$$

Next $\ln\left(\coth\dfrac{|x|}{2}\right)$ is expanded in a power series in terms of e^{-x} to obtain

$$\ln\left(\coth\frac{|x|}{2}\right) = \ln\left(\frac{1+e^{-x}}{1-e^{-x}}\right) = \sum_{m=0}^{\infty}\frac{2e^{-(2m+1)x}}{2m+1} \tag{B.17}$$

Substitute Equation (B.17) in Equation (B.16) yield

$$M_1(\omega) = \frac{4}{\pi}\sum_{n=0}^{\infty}\frac{F^{2n}(0)}{(2n)!}\sum_{m=0}^{\infty}\frac{1}{2m+1}\underbrace{\int_0^{\infty}x^{2n}e^{-(2m+1)x}\,dx}_{Q} \tag{B.18}$$

The integral Q is $\Gamma(2n+1)(2m+1)^{-(2n+1)}$. From the definition of the gamma function,

$$\Gamma(2n+1) = (2n)!.$$

Substituting this in Equation (B.18) finally yields

$$M_1(\omega) = \frac{4}{\pi}\sum_{n=0}^{\infty}\frac{F^{2n}(0)}{(2n)!}\sum_{m=0}^{\infty}\frac{1}{(2m+1)^{2n+2}} \tag{B.19}$$

When the dynamic properties in the frequency range of interest are far from resonance, so that variations are slow, the above series expansion and can be truncated after a small number of terms.

Substituting $F^{2n}(0) = \dfrac{d^{2n+1}G(x)}{dx^{2n+1}}\bigg|_{x=0}$ gives

$$M_1(\omega) =$$

$$\frac{4}{\pi}\left(\frac{\pi^2}{8}\frac{dG(x)}{dx}\bigg|_{x=0} + \frac{\pi^4}{96}\frac{d^3G(x)}{dx^3}\bigg|_{x=0} + \frac{\pi^6}{960}\frac{d^5G(x)}{dx^5}\bigg|_{x=0} + \frac{17\pi^8}{161280}\frac{d^7G(x)}{dx^7}\bigg|_{x=0} + \dots\right) \tag{B.20}$$

By changing the independent variable[1] x to ω' and retaining the leading order and

---

[1]Note that at $x=0$, $\omega' = \omega$ and $G(x)\big|_{x=0} = M_d(\omega)$.

228

the first correction term the above equation reduces to

$$M_1(\omega) = \frac{\pi}{2}\omega\frac{dM_\mathrm{d}(\omega)}{d\omega} + \frac{\pi^3}{24}\Big(\omega\frac{dM_\mathrm{d}(\omega)}{d\omega} + 3\omega^2\frac{d^2M_\mathrm{d}(\omega)}{d\omega^2} + \omega^3\frac{d^3M_\mathrm{d}(\omega)}{d\omega^3}\Big) + \ldots \quad \text{(B.21)}$$

This approximation is valid only when the frequency range of interest is far from resonances. Also, the correction term in Equation (B.21) has to be much smaller than the leading order term for the approximation to be good. This approximate equation was used for the model development in Chapter 3.

B.3   Test rig, bushing and fixtures details

We have used an MTS 370.10 elastomer test system for dynamic material characterization of suspension bushings. Test-rig details are shown in Figure B.2.
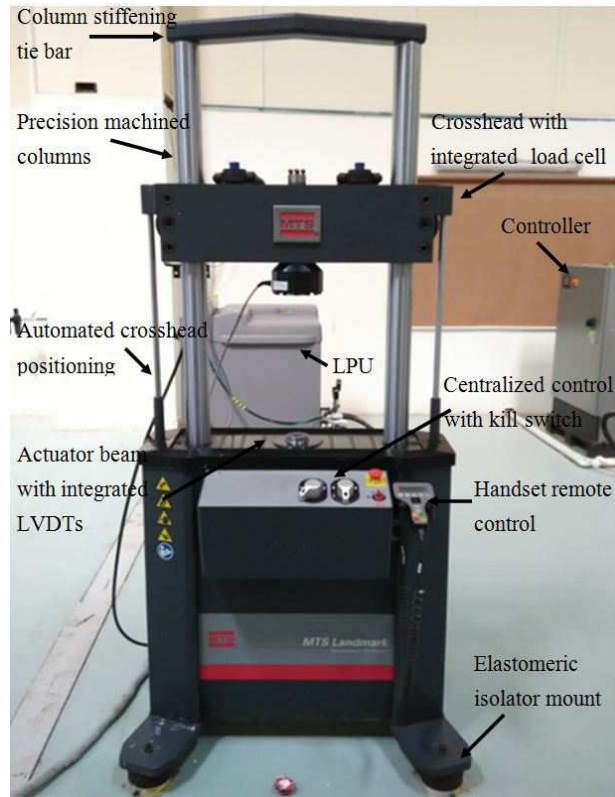
Figure B.2: MTS 370.10 elastomer test system. Image Source: NATRiP, India [63].

The dimensional details of four different bushings are shown in Figures B.3 and B.4.
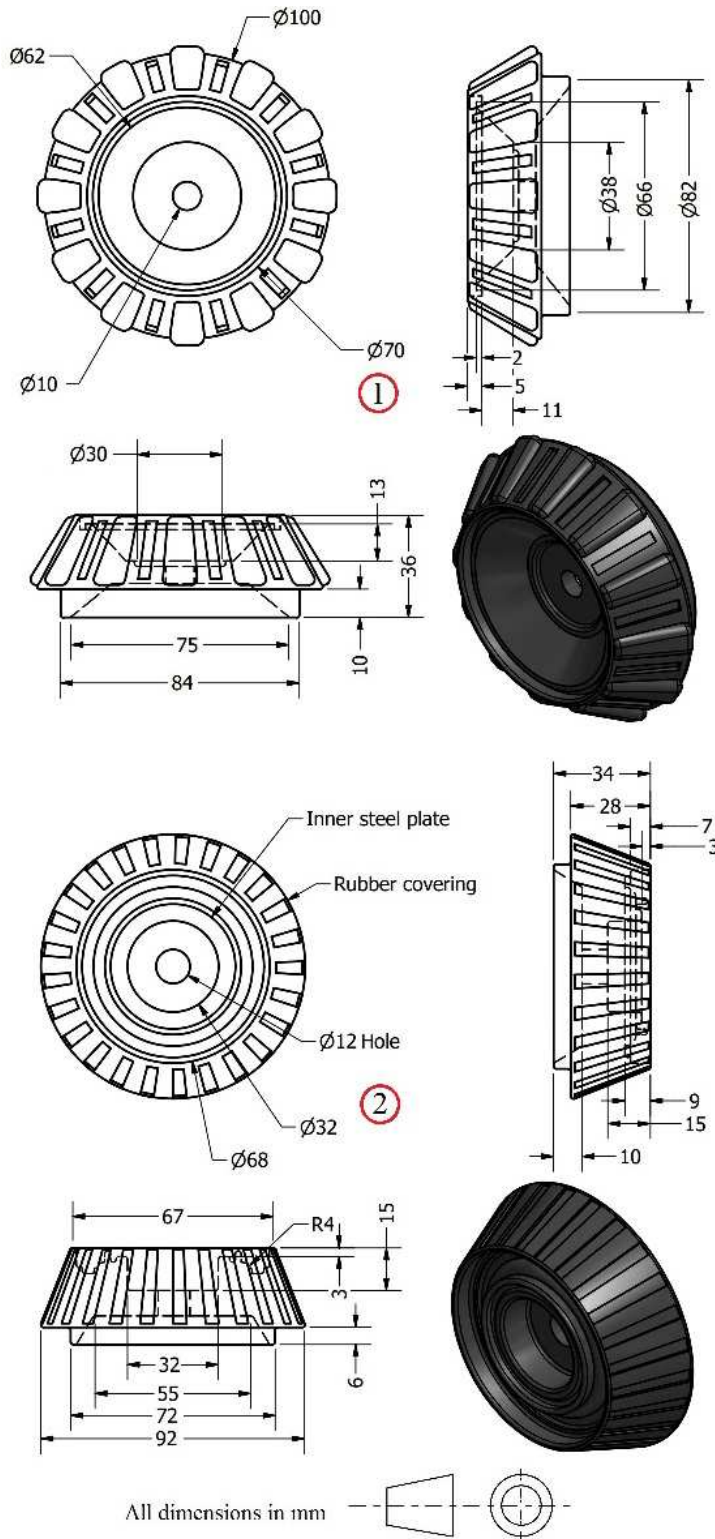
Figure B.3: Dimensional details of bushing 1 and 2.
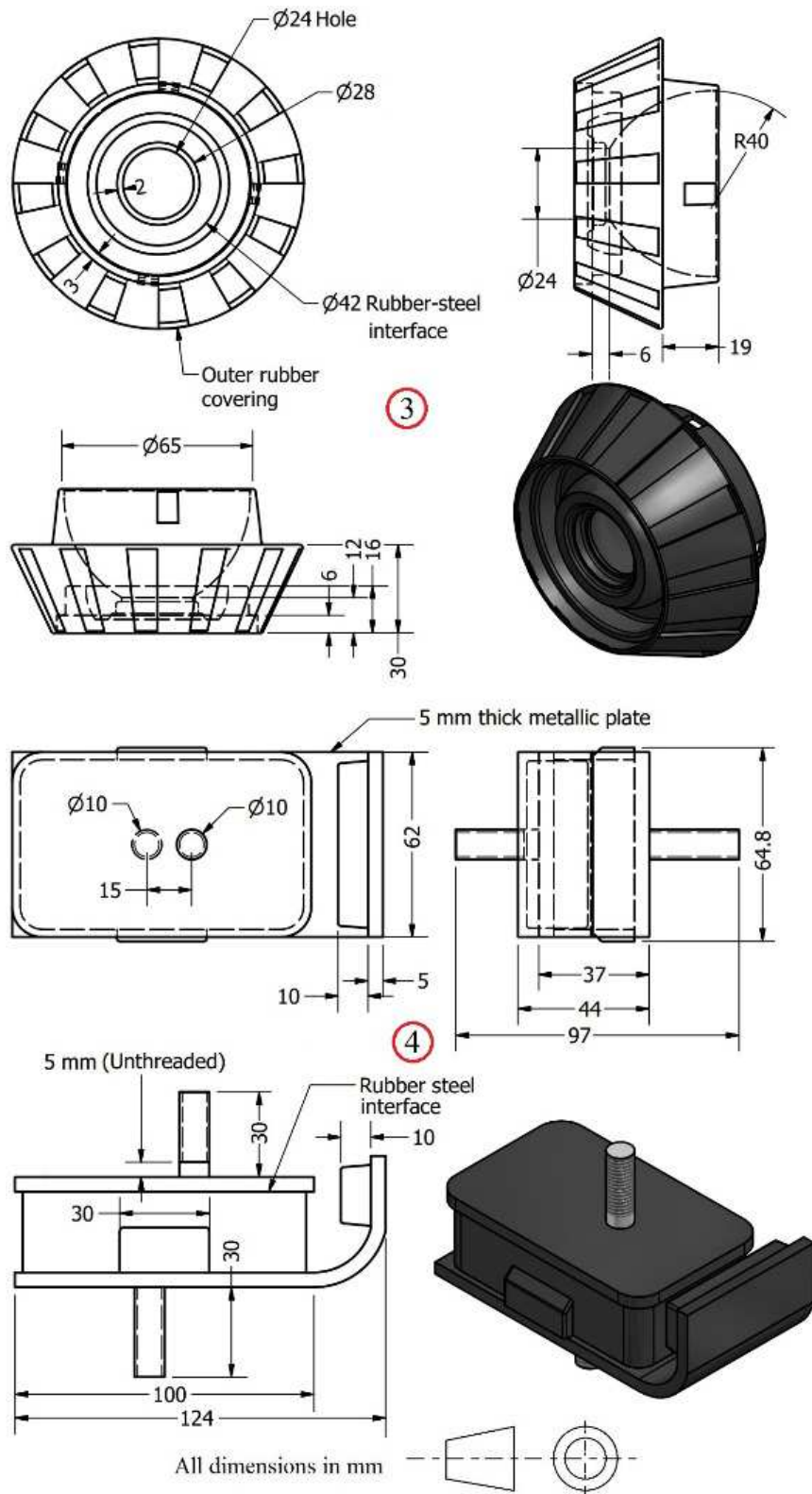
Figure B.4: Dimensional details of bushing 3 and 4.

Depending on the dimensions and the shapes of these bushings, fixtures were prepared for mounting these bushings on the MTS 370.10 test rig. Moreover, in order to apply a distributed load on bushings 1, 2 and 3 a sleeve plate was chosen from the aftermarket. The fixtures used during the testing for different bushings are shown in Figure B.5.
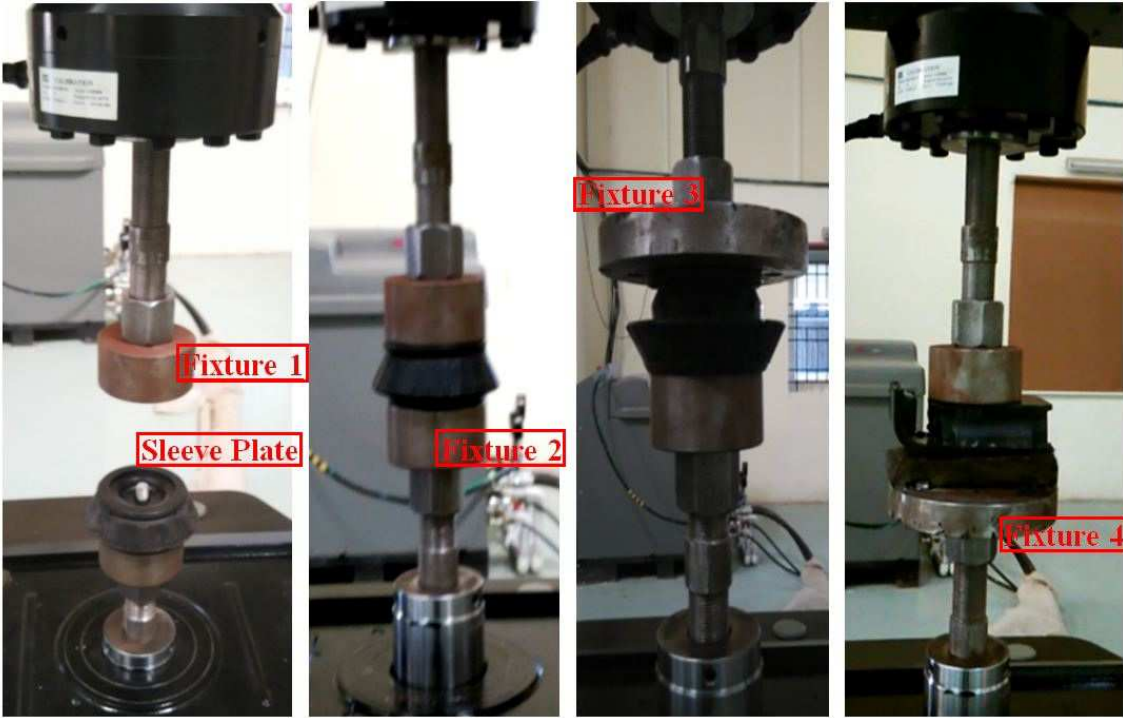
Figure B.5: Different fixtures used to mount various bushings on the test-rig. The four subfigures show the mounting arrangements of four different bushings used for the dynamic material characterization study.

Appendix C

Supplementary materials for Chapter 4

C.1 Vehicle instrumentation and accelerometer calibration

In this section, vehicle instrumentation and accelerometer calibration will be discussed. We have used the capacitor-based ADXL 326 accelerometer for vehicle testing. It is light weight (1.3 gm), compact (2cm×2cm); see Figure C.1, requires low current (350μA), has a wide measurement range ($\pm16g$), a broad temperature range ($-40°$ to $125°$C), and can be easily interfaced with a 5V micro controller such as the Arduino.
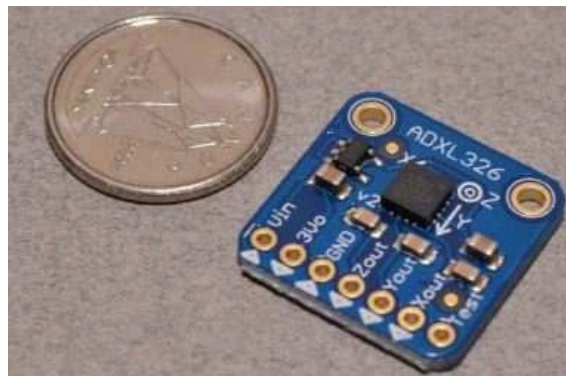
Figure C.1: Size of ADXL 326 accelerometer as compared to a small coin. Image source: BC Robotics [94].

The details of the accelerometer are shown in Figure C.2(a). The data acquisition system used consists of a FAT32 Micro SD card module (see Figure C.2(b)) and an Arduino ATMega328P micro-controller board (see Figure C.2(c)). These systems are compatible with a breadboard, making it easy to connect them together (see Figure C.2(d)). The circuit is powered by a standard 9V battery.

The accelerometers need to be calibrated before using them for measurements. Though these are triple axis accelerometers, only the Z-axis output channel is used for measuring vertical accelerations, therefore the calibration is done only for the Z-axis output measurements.

For calibration the output from each accelerometer was first compared against a standard Brüel & Kjær (B&K) Type-4382 piezoelectric accelerometer [95] using a rigid beam-spring-damper system (see Figure C.3(a)) already present in a teaching laboratory in IIT Kanpur.
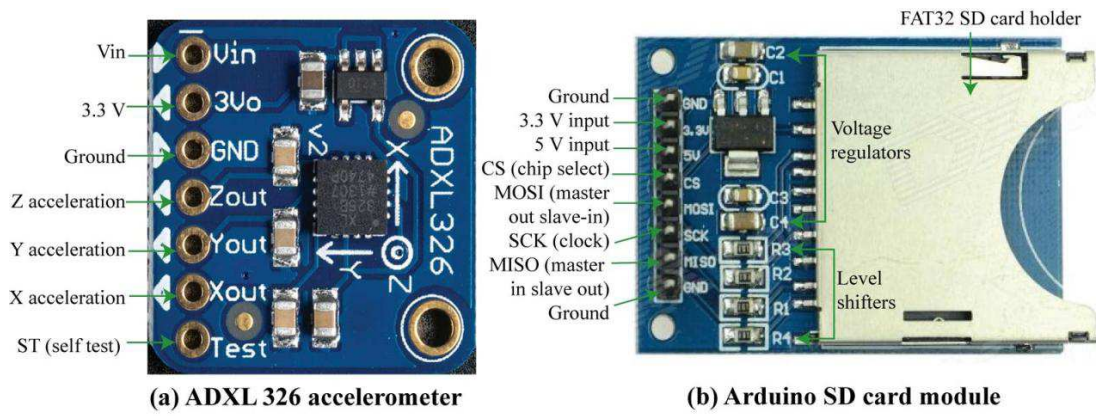
(a) ADXL 326 accelerometer

(b) Arduino SD card module
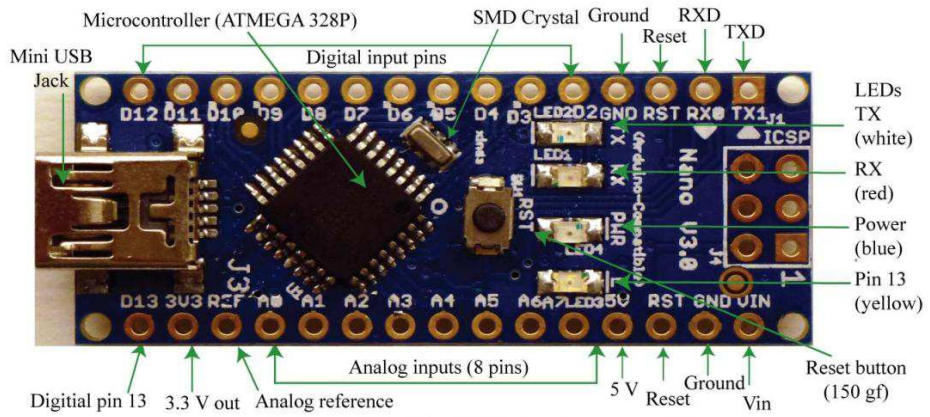
(c) Arduino ATMEGA 328P developmental board
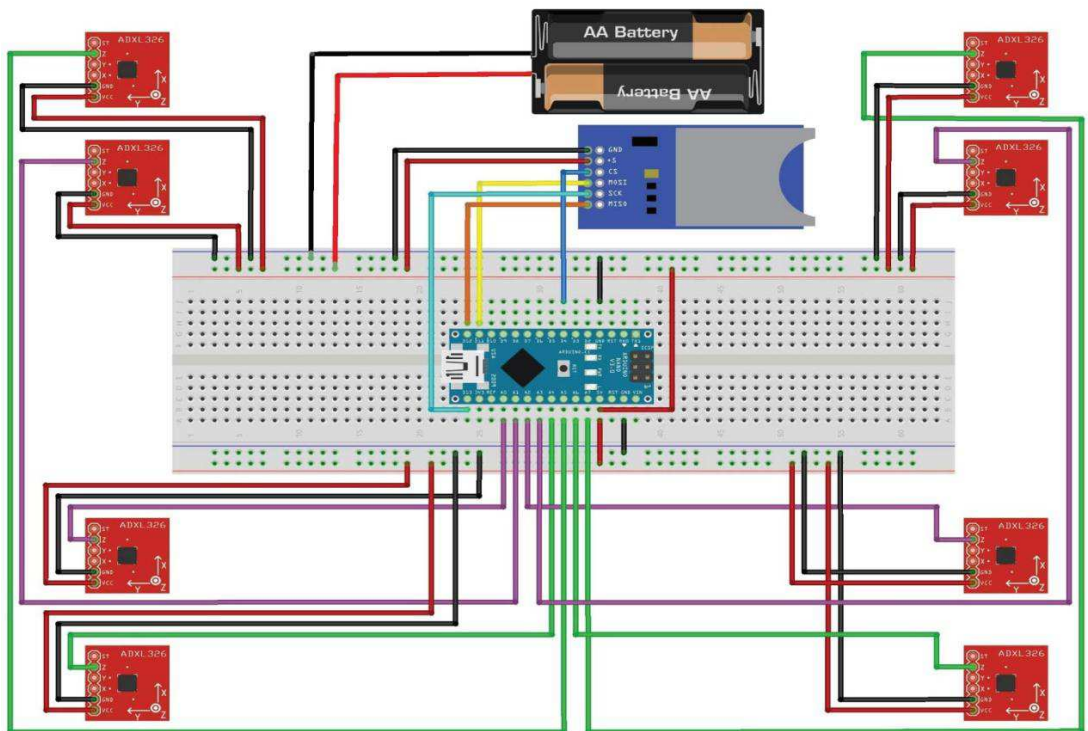
(d) Hook up diagram to connect various MEMS devices

Figure C.2: Details of the vehicle instrumentation and the data acquisition system.
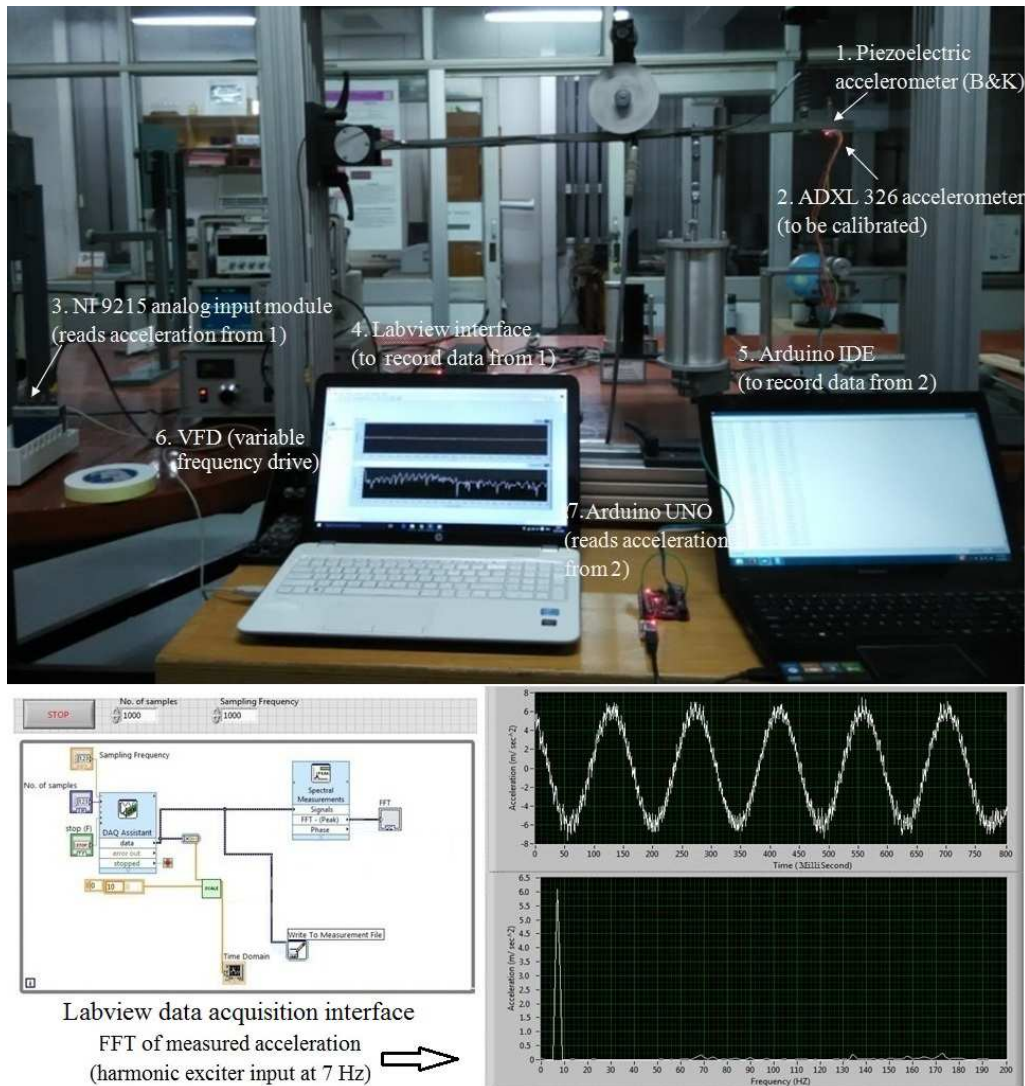
Figure C.3: Calibrating individual accelerometers using rigid beam vibration apparatus.

The forced vibrations are generated by an electrical motor-driven imbalance exciter. The exciter frequency is set using a variable frequency drive (VFD) with digital display. The vertical accelerations of rigid beam were measured by the previously calibrated B&K accelerometer, and recorded by NI 9215 analog input module using Labview interface (see Figure C.3(b)) [96].

The ADXL326 accelerometer which is to be calibrated is mounted at the same location as that of the B&K accelerometer and the accelerations are recorded using

Arduino Uno developmental board. The outputs of both the accelerometers are compared at various frequencies in our frequency range of interest (1-50 Hz) and the calibration constants are determined for all eight accelerometers. The comparison of output from both accelerometers for beam vibrating at 7 Hz is shown in Figure C.3(c).

After calibrating all accelerometers individually, the data from a set of accelerometers was simultaneously recorded to check for synchronicity in measurements. For this purpose, four ADXL326 accelerometers were mounted on a flexible cantilever beam (see Figure C.4-top). The beam is a slender mild steel ruler scale of length 24 inch, width 1 inch and thickness 1/40 inch.

The free end of the beam is attached to an electrodynamic actuator (B&K 4809) which is driven by a function generator (GW Instek 2104) using the signal amplifier (B&K 2718). A sinusoidal force input of frequency 15Hz and magnitude of 100gf is applied by the actuator[1]. The beam vibration response is recorded at 15 Hz using Arduino Mega developmental board and a FAT32 SD card module and is compared with simulation results (see Figure C.4 (middle and bottom)). It has been ensured that the excitation frequency is not close to one of the beam natural frequency so that there is no resonances and damping is unimportant.

---

[1]Digital display: 100gf $\approx$ 1 N.
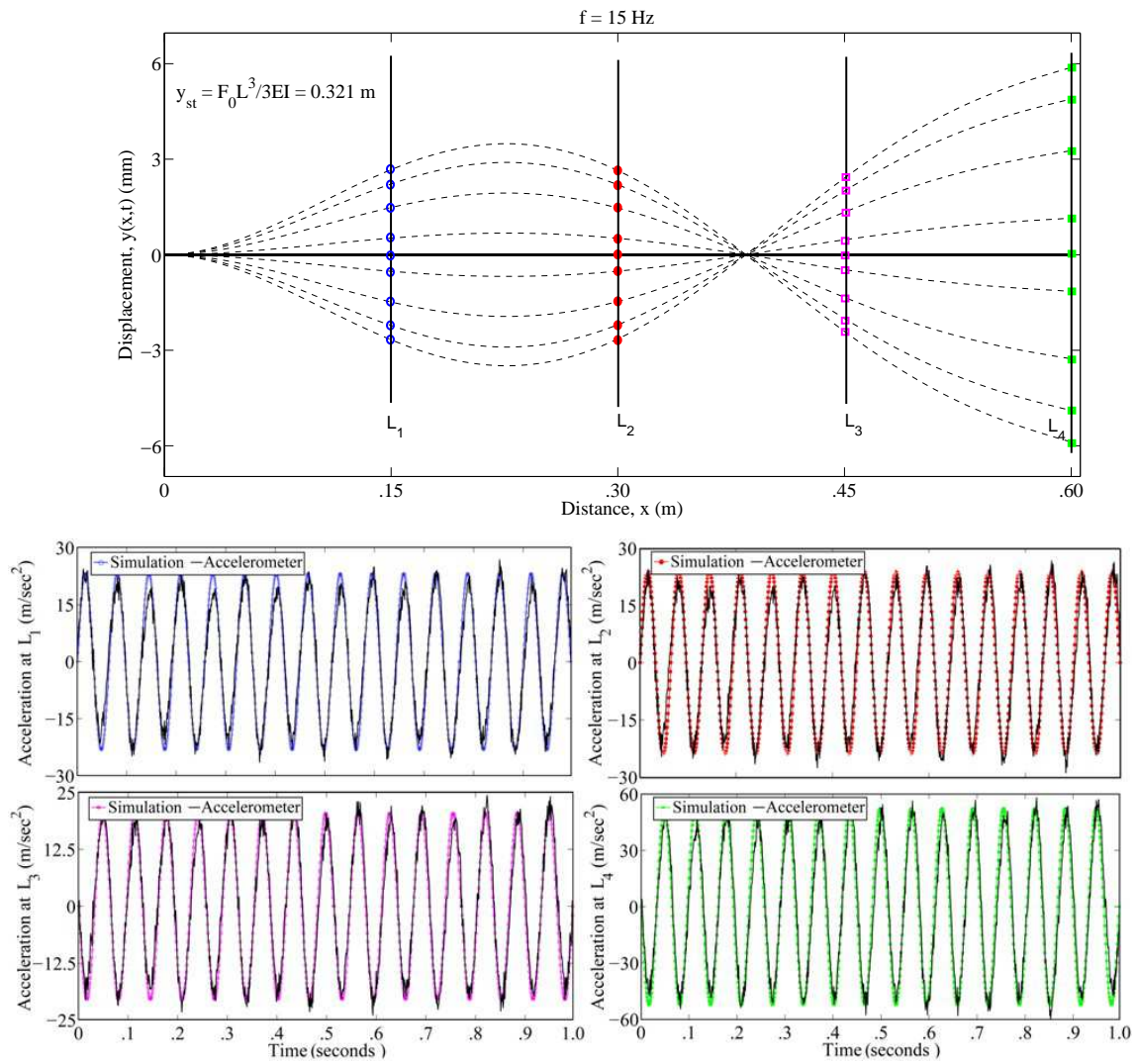
Figure C.4: Top: four ADXL326 accelerometers mounted on a cantilever beam; middle: beam deflection versus time plotted analytically; bottom: comparison of accelerations measured at four locations L_1, L_2, L_3 and L_4 with analytical simulation results.

238

Appendix D

Supplementary materials for Chapter 5

D.1 Initial estimates of ω's and ζ's for use in Section 5.4 of Chapter 5

The initial estimates of ω's and ζ's in the model fitting of Chapter 5 are to be supplied by the user to the `fminsearch` subroutine. Different vehicle vibration modes considered for the study are shown in Figure D.1.

We will now use simple models for these modes to obtain initial guesses for the ω_n.

1. **Vehicle pitch and bounce modes:**

    The vehicle pitch and bounce modes are shown in Figure D.1(a) and (b). The pitch and bounce frequencies are calculated by simple theory as below.

    The differential equations for the vehicle bounce, Z, and pitch, θ, motions of a simple vehicle (ignoring damping) can be written as:

$$M_s\ddot{Z} + (K_f + K_r)Z + (K_r l_r - K_f l_f)\theta = 0$$

$$I_{yy}\ddot{\theta} + (K_r l_r - K_f l_f)Z + (K_f l_f^2 + K_r l_r^2)\theta = 0 \tag{D.1}$$
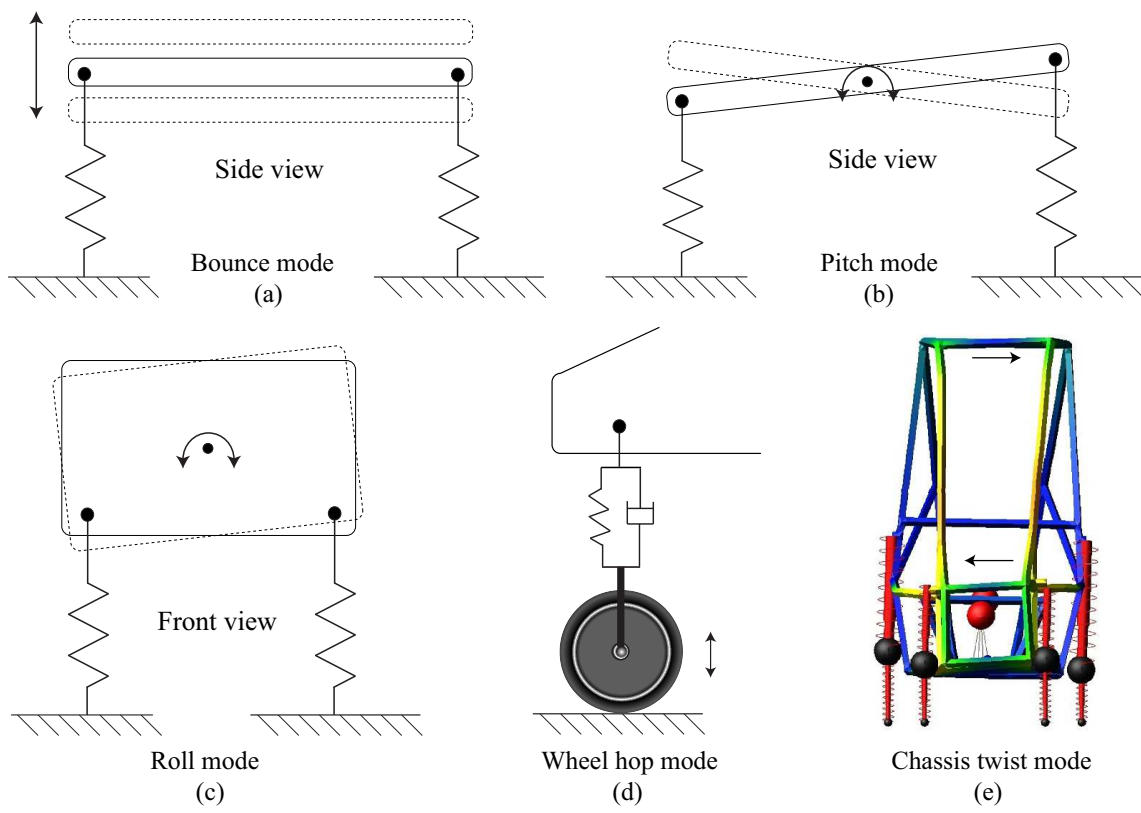
Figure D.1: Vehicle vibration modes.

where M_s is the vehicle sprung mass, K_f and K_r are equivalent stiffness of front and rear suspensions and I_{yy} is the pitch moment of inertia of the vehicle.
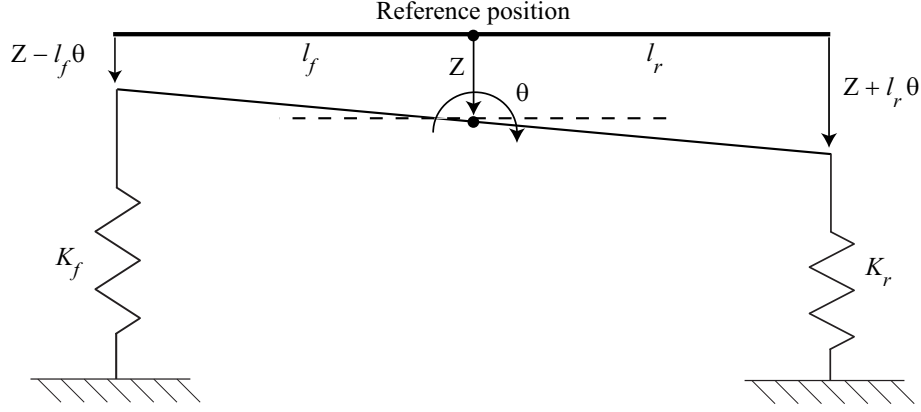
Figure D.2: Vehicle coupled bounce and pitch motions.

Simplifying Equation (D.1) and written the same in matrix form gives

$$
\begin{bmatrix} 1 & 0 \\ 0 & 1 \end{bmatrix} \begin{bmatrix} \ddot{Z} \\ \ddot{\theta} \end{bmatrix} + \begin{bmatrix} \alpha & \beta \\ \dfrac{M_s\beta}{I_{yy}} & \gamma \end{bmatrix} \begin{bmatrix} Z \\ \theta \end{bmatrix} = \begin{bmatrix} 0 \\ 0 \end{bmatrix} \tag{D.2}
$$

where

$$
\alpha = \frac{K_f + K_r}{M_s}; \quad \beta = \frac{K_r l_r - K_f l_f}{M_s}; \text{and } \gamma = \frac{K_f l_f^2 + K_r l_r^2}{I_{yy}}.
$$

The above eigenvalue problem is solved to obtain the natural frequencies as

$$
\omega_1 = \sqrt{\frac{\alpha + \gamma}{2} + \sqrt{\left(\frac{\alpha - \gamma}{2}\right)^2 + \frac{M_s\beta^2}{I_{yy}}}}; \quad \omega_2 = \sqrt{\frac{\alpha + \gamma}{2} - \sqrt{\left(\frac{\alpha - \gamma}{2}\right)^2 + \frac{M_s\beta^2}{I_{yy}}}}. \tag{D.3}
$$

of which ω_1 is the bounce natural frequency ω_{bounce} and ω_2 is the pitch natural frequency ω_{pitch}.

2. **Vehicle roll mode:**

The vehicle roll mode is shown in Figure D.1(c).

The vehicle roll frequency can be simply calculated as

$$\omega_{\text{roll}} = \sqrt{\frac{K_{\text{roll}}}{I_{xx}}} \tag{D.4}$$

where K_{roll} is the suspension roll stiffness given by, $K_{\text{roll}} = K_s w^2$; $K_s = $ summation of the front and rear stiffness and $w = $ lateral separation between the springs (see Figure D.3).
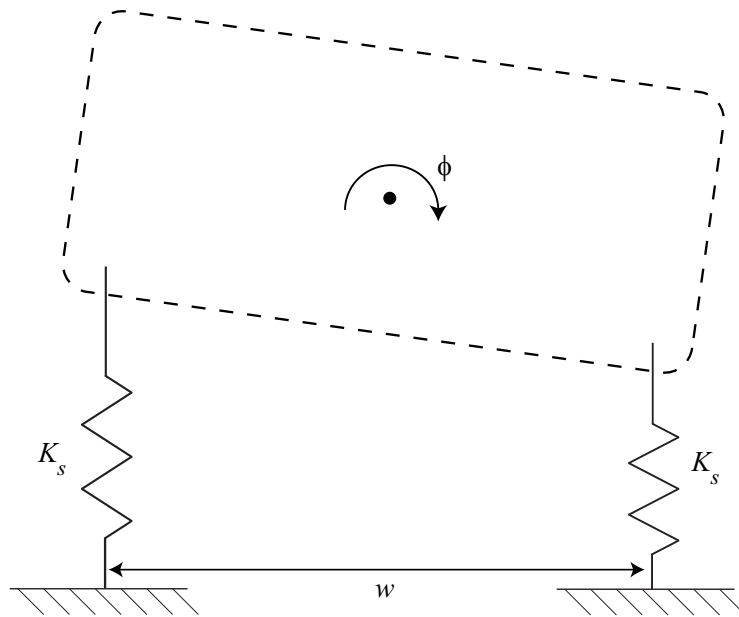
Figure D.3: Vehicle roll mode.

3. **Wheel hop:**

The wheel hop mode is shown in Figure D.1(d).

Wheel hop is a strong vertical oscillation of the wheels of a car. Wheel hop is discussed in detail in Section 2.10.2 of Chapter 2. The wheel hop frequency

can be calculated as

$$\omega_{\text{hop}} = \sqrt{\frac{K_t + K_s}{M_u}}, \tag{D.5}$$

where K_t is the tyre stiffness, K_s is the suspension stiffness and M_u is the unsprung mass.

4. **Chassis twist mode:**

   The last mode considered is the chassis twist mode (see Figure D.1(e)).

   As we have considered a flexible chassis model, this mode is reatined as it is the first flexible body mode. The chassis twist frequency is obtained from the simplified Adams model of the vehicle developed in Chapter 4 [97, 98]. Mode shape is indicated by the deflected shape of the vehicle in Figure D.1 (e); the natural frequency computed is 26.49 Hz.

The different modal frequencies obtained from the above analysis are reported in Table D.1.

Identifier	Pitch mode	Bounce mode	Roll mode	Wheel hop	Twist mode
f (Hz)	3.03	4.93	4.95	10.56	26.49
ζ	0.1	0.1	0.1	0.1	0.1

Table D.1: Values of ω's and ζ's to choose initial guesses for `fminsearch`.

We have seen that the vehicle bounce and roll frequency are nearly equal, so only one of these frequencies is used as an initial guess to the model. Therefore, there are four initial estimates of ω's. The value of ζ's are assigned as 0.1 for all the modes which will be adjusted by `fminsearch`.

These values need not to be very accurate, as subsequent nonlinear fitting will be done.

D.2 Expressions for the transfer function elements obtained from test data

The expressions of the six representative elements of the original transfer function matrix $\boldsymbol{H}(s)$ are presented here. Subsequently the expression of the 1-1 element $(\boldsymbol{H_{n,11}}(s))$ of the new transfer function matrix $\boldsymbol{H_n}(s)$ and the reduced order transfer function $\boldsymbol{H_{\mathrm{red}}}(s)$ of the 44th order transfer function will be given.

D.2.1 Original transfer function expressions

The general expression of one scale transfer function element of the transfer matrix $H(s)$ is given in terms of the numerator and denominator coefficients as

$$\frac{c_7 s^7 + c_6 s^6 + c_5 s^5 + c_4 s^4 + c_3 s^3 + c_2 s^2 + c_1 s + c_0}{s^8 + \left(2\sum \omega_i \zeta_i\right)s^7 + \left(\sum_{i\neq j}\omega_i^2 + 4\zeta_i\zeta_j\omega_i\omega_j\right)s^6 + \left(2\prod_{i\neq j}\omega_j^2\sum\zeta_j\omega_j + 8\sum_{i\neq j,k}\zeta_i\omega_i\zeta_j\omega_j\zeta_k\omega_k\right)s^5 + \left(\sum_{i\neq j}(\omega_i\omega_j)^2 + 4\prod_{k\neq i,j}\omega_k^2\sum_{i\neq j}\zeta_i\zeta_j\omega_i\omega_j + 16\prod\zeta_i\omega_i\right)s^4 + \left(2\prod_{k\neq i,j}\sum\zeta_k\omega_k\sum_{i\neq j}(\omega_i\omega_j)^2 + 8\prod_{i\neq j}\sum\omega_i^2\prod_{j=1}^{3}\zeta_j\omega_j\right)s^3 + \left(4\sum_{i\neq j,k,l}\zeta_i\omega_i\zeta_j\omega_j\sum_{k\neq l}(\omega_k\omega_l)^2\right)s^2 + \left(2\sum_{i\neq j,k,l}\zeta_i\omega_i\sum\omega_j\omega_k\omega_l\right)s + \prod\omega_i^2}$$

In the above expression i, j and k range from 1 to 4 corresponding to the four values of system modes of vibration.

The expressions of the six transfer functions $H_{ij}(s)$ that are used to construct the transfer matrix $H(s)$ are given below,

$$\boldsymbol{H_{11}}(s) =$$
$$\frac{-0.4s^7 + 72.1s^6 - 3.9e4s^5 + 3.9e06s^4 - 9.1e8s^3 - 3.6e5s^2 + 5.5e4s + 1.5e13}{s^8 + 305.1s^7 + 5e4s^6 + 3.3e6s^5 + 2.3e8s^4 + 6.8e09s^3 + 2e11s^2 + 2e12s + 2.7e13}$$

$$\boldsymbol{H_{12}}(s) =$$
$$\frac{-0.3s^7 + 47.8s^6 - 3.1e4s^5 + 2.6e6s^4 - 6.5e8s^3 + 1.7e4s^2 + 5.6e4s + 6e12}{s^8 + 305.1s^7 + 5e4s^6 + 3.3e6s^5 + 2.3e8s^4 + 6.8e09s^3 + 2e11s^2 + 2e12s + 2.7e13}$$

$$\boldsymbol{H_{13}}(s) =$$
$$\frac{-0.1s^7 - 11.1s^6 - 7.1e3s^5 - 4.3e5s^4 - 1.4e8s^3 - 1.6e6s^2 + 1e4s + 5.8e12}{s^8 + 305.1s^7 + 5e4s^6 + 3.3e6s^5 + 2.3e8s^4 + 6.8e09s^3 + 2e11s^2 + 2e12s + 2.7e13}$$

$$H_{14}(s) =$$

$$\frac{0.3s^7 + 72.2s^6 + 4.5e4s^5 + 2.4e6s^4 + 5.8e8s^3 - 5e6s^2 - 6e4s - 4.8e12}{s^8 + 305.1s^7 + 5e4s^6 + 3.3e6s^5 + 2.3e8s^4 + 6.8e09s^3 + 2e11s^2 + 2e12s + 2.7e13}$$

$$H_{33}(s) =$$

$$\frac{-0.2s^7 - 87.1s^6 + 3.6e4s^5 - 1e7s^4 + 1e9s^3 + 4.2e6s^2 - 1.6e5s + 1.2e13}{s^8 + 305.1s^7 + 5e4s^6 + 3.3e6s^5 + 2.3e8s^4 + 6.8e09s^3 + 2e11s^2 + 2e12s + 2.7e13}$$

$$H_{34}(s) =$$

$$\frac{0.4s^7 + 38.7s^6 + 3.5e4s^5 + 6e6s^4 + 16e07s^3 - 4.1e3s^2 - 6.7e4s + 5e12}{s^8 + 305.1s^7 + 5e4s^6 + 3.3e6s^5 + 2.3e8s^4 + 6.8e09s^3 + 2e11s^2 + 2e12s + 2.7e13}$$

D.2.2 Expressions for the 1-1 element of the full order and the reduced order new transfer function

$H_{n,11}(s)$ was found to be a 44th order transfer function given by

$$H_{n,11}(s) =$$

$$\frac{\begin{aligned}
&1.4e34s^{42} + 1.7e37s^{41} + 1e40s^{40} + 5e42s^{39} + 1.9e45s^{38} + 6e47s^{37} + 1.6e50s^{36} + 4e52s^{35} \\
&+8.2e54s^{34} + 1.6e57s^{33} + 2.6e59s^{32} + 3.9e61s^{31} + 5.1e63s^{30} + 6e65s^{29} + 6.3e67s^{28} \\
&+5.9e69s^{27} + 4.9e71s^{26} + 3.7e73s^{25} + 2.4e75s^{24} + 1.4e77s^{23} + 7.9e78s^{22} + 3.8e80s^{21} \\
&+1.6e82s^{20} + 6e83s^{19} + 2e85s^{18} + 5.4e86s^{17} + 1.1e88s^{16} + 1.7e89s^{15} - 7e89s^{14} \\
&-1.5e92s^{13} - 6.4e93s^{12} - 1.9e95s^{11} - 4.4e96s^{10} - 8.7e97s^9 - 1.4e99s^8 - 2e100s^7 \\
&-2.4e101s^6 - 2.4e102s^5 - 2e103s^4 - 1.3e104s^3 - 6.7e104s^2 - 2.3e105s - 4.2e105
\end{aligned}}{\begin{aligned}
&2.7e33s^{44} + 4e36s^{43} + 3.1e39s^{42} + 1.6e42s^{41} + 6e44s^{40} + 1.8e47s^{39} + 4.5e49s^{38} \\
&+9.4e51s^{37} + 1.7e54s^{36} + 2.6e56s^{35} + 3.6e58s^{34} + 4.4e60s^{33} + 5e62s^{32} + 5e64s^{31} \\
&+4.4e66s^{30} + 3.7e68s^{29} + 2.8e70s^{28} + 2e72s^{27} + 1.2e74s^{26} + 7.2e75s^{25} + 3.9e77s^{24} \\
&+2e79s^{23} + 8.9e80s^{22} + 3.8e82s^{21} + 1.4e84s^{20} + 5.2e85s^{19} + 1.7e87s^{18} + 5.1e88s^{17} \\
&+1.4e90s^{16} + 3.5e91s^{15} + 8.1e92s^{14} + 1.7e94s^{13} + 3.1e95s^{12} + 5.4e96s^{11} + 8.2e97s^{10} \\
&+1.1e99s^9 + 1.3e100s^8 + 1.4e101s^7 + 1.31e102s^6 + 1e103s^5 + 7.3e103s^4 + 4e104s^3 \\
&+1.7e105s^2 + 5e105s + 7.9e105
\end{aligned}}$$

The order of $H_{n,11}(s)$ is reduced to obtain a tenth order transfer function $H_{\text{red}}(s)$ given by

$$H_{\text{red}}(s) =$$

$$\frac{-0.1s^7 + 46.7s^6 - 4.6e3s^5 + 1.9e5s^4 + 3.9e7s^3 - 3.2e8s^2 + 1.1e10s - 8.3e11}{s^8 + 75.1s^7 + 9.6e3s^6 + 4e5s^5 + 2.4e7s^4 + 4.9e8s^3 + 1.4e10s^2 + 1e11s + 1.5e12}$$

Bibliography

[1] RN Jazar. *Vehicle Dynamics: Theory and Application*, pages 931–975. Springer US, Boston, MA, 2008.

[2] H Frahm. Device for damping vibrations of bodies., April 18 1911. US Patent 989,958.

[3] JP Den Hartog. *Mechanical Vibrations*. McGraw-Hill Book Company, Inc., New York, 1934.

[4] D Hrovat. Optimal active suspension structures for quarter-car vehicle models. *Automatica*, 26(5):845–860, 1990.

[5] J Levitt and NG Zorka. The influence of tire damping in quarter car active suspension models. *ASME Journal of Dynamic Systems, Measurement and Control*, 113(1):134–137, 1991.

[6] S Türkay and H Akçay. A study of random vibration characteristics of the quarter-car model. *Journal of Sound and Vibration*, 282(1):111–124, 2005.

[7] LVV Gopala Rao and S Narayanan. Preview control of random response of a half-car vehicle model traversing rough road. *Journal of Sound and Vibration*, 310(1):352–365, 2008.

[8] M Bouazara and MJ Richard. An optimization method designed to improve 3-D vehicle comfort and road holding capability through the use of active and semi-active suspensions. *European Journal of Mechanics-A/Solids*, 20(3):509–520, 2001.

[9] C Kim and PI Ro. An accurate full car ride model using model reducing techniques. *Journal of Mechanical Design*, 124(4):697–705, 2002.

[10] T Ersal, B Kittirungsi, HK Fathy, and JL Stein. Model reduction in vehicle dynamics using importance analysis. *Vehicle System Dynamics*, 47(7):851–865, 2009.

[11] K Li, S Zheng, D Yang, X Lian, and M Nagai. Modeling and control of active suspensions for MDOF vehicle. *Tsinghua Science and Technology*, 8(2):224–230, 2003.

[12] IM Ibrahim, DA Crolla, and DC Barton. Effect of frame flexibility on the ride vibration of trucks. *Computers & Structures*, 58(4):709–713, 1996.

[13] C Lewitzke and P Lee. Application of elastomeric components for noise and vibration isolation in the automotive industry. Technical report, SAE Technical Paper, 2001.

[14] RL Kronig. On the theory of dispersion of X-rays. *Journal of the Optical Society of America*, 12(6):547–557, 1926.

[15] H A Kramers. La diffusion de la lumiere par les atomes. *Transactions of Volta Centenary Congress*, 2:545–557, 1927.

[16] HW Bode. Relations between attenuation and phase in feedback amplifier design. *Bell System Technical Journal*, 19(3):421–454, 1940.

[17] D Hrovat. Survey of advanced suspension developments and related optimal control applications. *Automatica*, 33(10):1781–1817, 1997.

[18] CY Liang and H Peng. Optimal adaptive cruise control with guaranteed string stability. *Vehicle System Dynamics*, 32(4-5):313–330, 1999.

[19] P Yih and JC Gerdes. Modification of vehicle handling characteristics via steer-by-wire. *IEEE Transactions on Control Systems Technology*, 13(6):965–976, 2005.

[20] H Kanchwala, J Wideberg, CB Alba, and D Marcos. Control of an independent 4WD electric vehicle by DYC method. *International Journal of Vehicle Systems Modelling and Testing*, 10(2):168–184, 2015.

[21] A Alleyne. Improved vehicle performance using combined suspension and braking forces. *Vehicle System Dynamics*, 27(4):235–265, 1997.

[22] K Yi, J Yoon, and D Kim. Model-based estimation of vehicle roll state for detection of impending vehicle rollover. In *American Control Conference, 2007*, pages 1624–1629. IEEE, 2007.

[23] MD-Adams. http://web.mscsoftware.com/Products/CAE-Tools/MD-Adams.aspx. Accessed on: 2015-11-10.

[24] GT: Grand Tourer. http://en.wikipedia.org/wiki/Grand_tourer. Accessed on: 2015-11-10.

[25] J Wideberg, C Bordons, P Luque, DA Mántaras, D Marcos, and H Kanchwala. Development and experimental validation of a dynamic model for electric vehicle with in hub motors. *Procedia-Social and Behavioral Sciences*, 160:84–91, 2014.

[26] MSC-Nastran. http://www.mscsoftware.com/product/msc-nastran. Accessed on: 2015-11-10.

[27] C Papalukopoulos and S Natsiavas. Nonlinear biodynamics of passengers coupled with quarter car models. *Journal of Sound and Vibration*, 304(1):50–71, 2007.

[28] EJ Davison. A method for simplifying linear dynamic systems. *IEEE Transactions on Automatic Control*, 11(1):93–101, 1966.

[29] M Aoki. Control of large-scale dynamic systems by aggregation. *IEEE Transactions on Automatic Control*, 13(3):246–253, 1968.

[30] CF Chen and LS Shieh. A novel approach to linear model simplification. *International Journal of Control*, 8(6):561–570, 1968.

[31] BC Moore. Principal component analysis in linear systems: Controllability, observability, and model reduction. *IEEE Transactions on Automatic Control*, 26(1):17–32, 1981.

[32] C Kim and P I Ro. Reduced-order modelling and parameter estimation for a quarter-car suspension system. *Proceedings of the Institution of Mechanical Engineers, Part D: Journal of Automobile Engineering*, 214(8):851–864, 2000.

[33] Dan Negrut and Andrew Dyer. Adams/solver primer. *Ann Arbor*, 2004.

[34] JR Barber. The reciprocal theorem. In *Elasticity*, volume 107 of *Solid Mechanics and Its Applications*, pages 393–404. Springer Netherlands, 2004.

[35] Lord Rayleigh. *The theory of sound*, volume 1. Macmillan, 1877.

[36] S Adhikari and J Woodhouse. Identification of damping: part 1, viscous damping. *Journal of Sound and Vibration*, 243(1):43–61, 2001.

[37] S Adhikari and J Woodhouse. Identification of damping: part 3, symmetry-preserving methods. *Journal of Sound and Vibration*, 251(3):477–490, 2002.

[38] A Healey. The tyre as part of the suspension system. *Proceedings of the Institution of Automobile Engineers*, 19(1):26–128, 1924.

[39] J Dixon. *The shock absorber handbook*. John Wiley & Sons, 2008.

[40] Kelly Controls, LLC. http://www.kellycontroller.com/car-hub-motor-72v-7kw-p-711.html. Accessed on: 2016-02-15.

[41] BC Nakra. Vibration control in machines and structures using viscoelastic damping. *Journal of Sound and Vibration*, 211(3):449 – 466, 1998.

[42] MD Rao. Recent applications of viscoelastic damping for noise control in automobiles and commercial airplanes. *Journal of Sound and Vibration*, 262(3):457–474, 2003.

[43] SW Park. Analytical modeling of viscoelastic dampers for structural and vibration control. *International Journal of Solids and Structures*, 38(44):8065–8092, 2001.

[44] RH Zhang and TT Soong. Seismic design of viscoelastic dampers for structural applications. *Journal of Structural Engineering*, 118(5):1375–1392, 1992.

[45] ML Williams, RF Landel, and JD Ferry. The temperature dependence of relaxation mechanisms in amorphous polymers and other glass-forming liquids. *Journal of the American Chemical society*, 77(14):3701–3707, 1955.

[46] JD Ferry. *Viscoelastic properties of polymers.* John Wiley & Sons, 1980.

[47] MA Trindade, A Benjeddou, and R Ohayon. Modeling of frequency-dependent viscoelastic materials for active-passive vibration damping. *Journal of Vibration and Acoustics*, 122(2):169–174, 2000.

[48] HT Banks, S Hu, and ZR Kenz. A brief review of elasticity and viscoelasticity for solids. *Advances in Applied Mathematics and Mechanics*, 3(1):1–51, 2011.

[49] SPC Marques and GJ Creus. *Computational viscoelasticity.* Springer, Heidelberg, Germany, 2012.

[50] JE Soussou, F Moavenzadeh, and MH Gradowczyk. Application of prony series to linear viscoelasticity. *Transactions of The Society of Rheology*, 14(4):573–584, 1970.

[51] RL Bagley and PJ Torvik. A theoretical basis for the application of fractional calculus to viscoelasticity. *Journal of Rheology*, 27(3):201–210, 1983.

[52] SWJ Welch, RAL Rorrer, and RG Duren. Application of time-based fractional calculus methods to viscoelastic creep and stress relaxation of materials. *Mechanics of Time-Dependent Materials*, 3(3):279–303, 1999.

[53] RL Bagley and PJ Torvik. Fractional calculus-a different approach to the analysis of viscoelastically damped structures. *AIAA Journal*, 21(5):741–748, 1983.

[54] MTS Systems Corporation: Dynamic Mechanical Analysis. https://www.mts.com/en/products/application/materials-testing/composites/dynamiccharacterization/index.htm. Accessed on: 2016-11-12.

[55] T Pritz. Transfer function method for investigating the complex modulus of acoustic materials: rod-like specimen. *Journal of Sound and Vibration*, 81(3):359–376, 1982.

[56] M Alcoutlabi and JJ Martinez-Vega. Modeling of the viscoelastic behavior of amorphous polymers by the differential and integration fractional method: the relaxation spectrum $H(\tau)$. *Polymer*, 44(23):7199–7208, 2003.

[57] NW Tschoegl. *The phenomenological theory of linear viscoelastic behavior: an introduction.* Springer, Berlin, 1989.

[58] W Kuhn. Elastizität und viscosität hochpolymerer verbindungen. *Angewandte Chemie*, 52(16):289–301, 1939.

[59] BYK Hu. Kramers-Kronig in two lines. *American Journal of Physics*, 57(9):821–821, 1989.

[60] T Pritz. Frequency dependences of complex moduli and complex Poisson's ratio of real solid materials. *Journal of Sound and Vibration*, 214(1):83–104, 1998.

[61] DC Hutchings, M Sheik-Bahae, DJ Hagan, and EW Van Stryland. Kramers-Krönig relations in nonlinear optics. *Optical and Quantum Electronics*, 24(1):1–30, 1992.

[62] V Mangulis. Kramers-Kronig or Dispersion Relations in Acoustics. *The Journal of the Acoustical Society of America*, 36(1):211–212, 1964.

[63] NATRAX Indore. http://www.natrip.in/index.php/natrax-about-testing-centers. Accessed on: 2016-11-10.

[64] M O'Donnell, ET Jaynes, and JG Miller. Kramers-Kronig relationship between ultrasonic attenuation and phase velocity. *The Journal of the Acoustical Society of America*, 69(3):696–701, 1981.

[65] L Fredette and R Singh. Estimation of the transient response of a tuned, fractionally damped elastomeric isolator. *Journal of Sound and Vibration*, 382:1–12, 2016.

[66] SA Noll, B Joodi, J Dreyer, and R Singh. Volumetric and dynamic performance considerations of elastomeric components. *SAE International Journal of Materials and Manufacturing*, 8(2015-01-2227):953–959, 2015.

[67] L Fredette, J Dreyer, and R Singh. Dynamic analysis of hydraulic bushings with measured nonlinear compliance parameters. *SAE International Journal of Passenger Cars-Mechanical Systems*, 8(2015-01-2355):1128–1136, 2015.

[68] YC Lu. Fractional derivative viscoelastic model for frequency-dependent complex moduli of automotive elastomers. *International Journal of Mechanics and Materials in Design*, 3(4):329–336, 2006.

[69] T Pritz. Five-parameter fractional derivative model for polymeric damping materials. *Journal of Sound and Vibration*, 265(5):935–952, 2003.

[70] SGSITS Indore. http://www.sgsits.ac.in/. Accessed on: 2017-03-03.

[71] S Mishra and V K Goyal. Vehicle #007. Team GS Racers Design Report. https://tinyurl.com/yamvxuhy, 2016.

[72] FOX Float 3. Factory series owners manual. https://www.ridefox.com/fox_tech_center/owners_manuals/605-00-111-revA.pdf. Accessed on: 2017-03-03.

[73] FOX Float 3 EVOL R. Factory series owners manual. http://www.ridefox.com/fox_tech_center/owners_manuals/605-00-119-revA.pdf. Accessed on: 2017-03-03.

[74] MTS 850.25. Model 850 load unit product manual. http://www.mts.com/cs/groups/public/documents/library/mts_2013265.pdf. Accessed on: 2017-03-03.

[75] Rollcage. Material testing report. https://tinyurl.com/yb84k6zc, 2015.

[76] MD ADAMS Exchange. Exporting parasolid model using ADAMS/Exchange. http://www.mscsoftware.com/assets/MSC_DS_MD_Adams.pdf.

[77] Ernest P Hanavan Jr. A mathematical model of the human body. Technical report, DTIC Document, 1964.

[78] RF Chandler, Charles E Clauser, John T McConville, HM Reynolds, and John W Young. Investigation of inertial properties of the human body. Technical report, DTIC Document, 1975.

[79] BKT ATV Tyres. https://www.bkt-tires.com/en/pattern/w-207. Accessed on: 2017-03-03.

[80] MD Adams Guide. 2010 version. *Ann Arbor, Michigan*.

[81] J Y Wong. *Theory of ground vehicles*. John Wiley & Sons, 2008.

[82] Anupam Saxena and Birendra Sahay. *Computer aided engineering design*. Springer Science & Business Media, 2007.

[83] Carl Martin Becker and Pieter Schalk Els. Profiling of rough terrain. *International Journal of Vehicle Design*, 64(2-4):240–261, 2014.

[84] A González, EJ O'brien, YY Li, and K Cashell. The use of vehicle acceleration measurements to estimate road roughness. *Vehicle System Dynamics*, 46(6):483–499, 2008.

[85] ISO 8608:2016 Mechanical vibration - road surface profiles - reporting of measured data. International standards organisation, 2016.

[86] Adams/3D Road. 3D Road modeling in adams. http://www.mscsoftware.com/assets/1718_ADAM3O3Z3DRDZLTDAT.pdf.

[87] AJC Schmeitz. *A semi-empirical three-dimensional model of the pneumatic tyre rolling over arbitrarily uneven road surfaces.* PhD thesis, TU Delft, Delft University of Technology, 2004.

[88] AJC Schmeitz, IJM Besselink, J De Hoogh, and H Nijmeijer. Extending the magic formula and swift tyre models for inflation pressure changes. *VDI BERICHTE*, 1912:201, 2005.

[89] BC Moore. Principal component analysis in linear systems: Controllability, observability, and model reduction. *IEEE Transactions on Automatic Control*, 26(1):17–32, 1981.

[90] AJ Laub, MT Heath, CC Paige, and RC Ward. Computation of system balancing transformations and other applications of simultaneous diagonalization algorithms. *IEEE Transactions on Automatic Control*, 32(2):115–122, 1987.

[91] VS Galishev. A simple derivation of the kramers-krönig relations. *Optics and Spectroscopy*, 8:217, 1960.

[92] J Bechhoefer. Kramers–kronig, bode, and the meaning of zero. *American Journal of Physics*, 79(10):1053–1059, 2011.

[93] HW Bode. Amplifier, July 12 1938. US Patent 2,123,178.

[94] ADXL 326. MEMS accelerometer. http://www.bc-robotics.com/shop/adxl326-tripple-axis-accelerometer-breakout/. Accessed on: 2017-03-03.

[95] Brüel & Kjær. Type 4382 piezoelectric accelerometer. https://www.bksv.com/en/products/transducers/vibration/Vibration-transducers/accelerometers/4382. Accessed on: 2017-03-03.

[96] National Instruments. Ni-9215 (c series voltage input module). http://www.ni.com/en-in/support/model.ni-9215.html. Accessed on: 2017-03-03.

[97] VN Sohoni and J Whitesell. Automatic linearization of constrained dynamical models. *Journal of Mechanisms, Transmissions, and Automation in Design*, 108(3):300–304, 1986.

[98] David J Ewins. *Modal testing: theory and practice*, volume 15. Research studies press Letchworth, 1984.